Technische Universität Wien

DISSERTATION

Real–Time Smart Antenna Processing for GSM1800

ausgeführt zum Zwecke der Erlangung des akademischen Grades eines Doktors der technischen Wissenschaften

eingereicht an der
Technischen Universität Wien
Fakultät für Elektrotechnik

von

Dipl.–Ing. Alexander KUCHAR
Matrikelnummer 9025786
A–2232 Deutsch–Wagram, Friedhofallee 4a/11
geboren in Wien am 10. März 1971

Wien, im Dezember 1999 .....

First supervisor: Prof. Dipl.–Ing. Dr. Ernst BONEK
Institut für Nachrichtentechnik und Hochfrequenztechnik
Technische Universität Wien
Fakultät für Elektrotechnik, Austria

Second supervisor: Prof. Dipl.–Ing. Dr. Peter LEUTHOLD
Institut für Kommunikationstechnik
Eidgenössische Technische Hochschule (ETH) Zürich, Switzerland

ZUSAMMENFASSUNG

Diese Arbeit beschreibt eine auf Richtungsschätzung basierende Intelligente Antenne für GSM1800. Dabei konzentriere ich mich auf den für eine Basisstation entwickelten Prozessor $\mathbf{A}^3\mathbf{P}$ (Adaptive Antenna Array Processor). $\mathbf{A}^3\mathbf{P}$ ermöglicht eine adaptive Strahlformung in der Aufwärts- als auch in der Abwärtsstrecke in Echtzeit. Die Intelligente Antenne besteht aus einer linearen Antennengruppe mit $M = 8$ Elementen, acht Sende–Empfangszügen und dem $\mathbf{A}^3\mathbf{P}$.

Die Signalverarbeitung von $\mathbf{A}^3\mathbf{P}$ gliedert sich in vier Schritte:

- Richtungsschätzung
  Mit einem hochauflösenden Schätzer werden aus den in der Aufwärtsstrecke empfangenen Daten die Richtungen der einfallenden Wellen geschätzt.

- Klassifizierung der Einfallsrichtungen
  Die einfallenden Wellen werden von einem räumlichen Filter getrennt bereitgestellt. Eine Benutzeridentifizierung, basierend auf einem Detektor, ordnet die Wellen dem Benutzer oder den Störern zu.

- Tracking und Richtungsauswahl
  Ein sogenannter Tracker folgt jeder vom Benutzer ausgehenden, räumlich getrennten Einfallsrichtung (Ausbreitungspfad). Das Trackingkonzept mittelt nicht nur die Einfallsrichtungen über der Zeit, sondern misst auch die Zuverlässigkeit der Signale der einzelnen Ausbreitungspfade. Die Hauptkeule wird nun in die Richtung des stärksten Pfades gelenkt, was einer auswahlbasierten Winkeldiversität entspricht. Ein Pfad wird jedoch nur ausgewählt, wenn seine Zuverlässigkeit ausreichend ist. Erst diese Strategie garantiert eine robuste Signalverarbeitung. Ein separater, von der Aufwärtsstrecke unabhängiger Tracker wird für die Abwärtsstrecke verwendet, damit man dort mit größeren Zeitkonstanten mitteln kann.

- Signalrekonstruktion — Strahlformung
  Im letzten Schritt liefert ein Strahlformungsalgorithmus ein Antennendiagramm, dessen Hauptkeule in Richtung des ausgewählten Benutzerpfades zeigt, während Störsignale möglichst unterdrückt werden. Verwendet man zum Unterdrücken der Störer *breite Nullstellen*, wird die Robustheit gegen Störsignale mit großer Winkelaufspreizung erhöht.

Als Schlüsselelemente in einer richtungsbasierten Intelligenten Antenne stellten sich heraus: die Benutzeridentifikation und der Tracker. Zusammen ermöglichen sie eine zuverlässige Auswahl der Hauptstrahlrichtung, die in einer exzellenten Störunterdrückung selbst dann resultiert, wenn der Störabstand gering ist.

A^3**P**'s Rechenzeit von der Größenordnung von $1ms$ erlaubt in einem GSM–System eine Echtzeitverarbeitung. **A**^{3}**P** ist für räumliche Filterung (Spatial Filtering for Interference Reduction) entwickelt und optimiert worden. **A**^{3}**P** kann aber ohne großen Aufwand für den Einsatz in einem räumlichen Multiplexverfahren (Spatial Division Multiple Access) erweitert werden. Dann mußmit einer Rechenzeitverlängerung von zirka 35% für jeden zusätzlichen Benutzer gerechnet werden.

Experimente mit **A**^{3}**P** haben die erwarteten Verbesserungen in vielerlei Hinsicht bestätigt. Es wurden aber auch überraschende Ergebnisse gefunden.

Der Gewinn im Störabstand ist $25dB$, wenn das Störsignal nur aus einem kleinen Winkelbereich, in der Größenordnung von 1°, einfällt. Selbst wenn sich die Signale von Benutzer und Störer *teilweise* überlappen, kann **A**^{3}**P** den Störer um $18dB$ unterdrücken.

Zusätzliches Nullen des Störers erhöht den Gewinn im Störabstand nur um $4dB$. Simulationen ließen hier mehr erwarten. Die Strategie, die zum Nullen verwendet wird, hat keinen Einflußauf den optimalen Störabstand. Auch *breite* Nullstellen, anstatt der üblichen scharfen Nullstellen, erhöhen den Gewinn im Störabstand nicht, jedoch wird das System in zweierlei Hinsicht robuster: Erstens müssen die Richtungen der einfallenden Störsignale nicht so genau bekannt sein, und zweitens können die Signale der Störer auch aus einem größeren Winkelbereich einfallen, ohne daßdie Störunterdrückung maßgeblich reduziert wird.

Die Auswertung der Meßergebnisse ergab, daßder Gewinn im Störabstand durch zwei Faktoren beschränkt ist: Erstens, durch eine unzureichende räumliche Trennung von Benutzer- und Störsignal. Das Benutzersignal kann nicht mit ausreichender Signalqualität gewonnen werden, wenn aus *jeder* Richtung, aus der die Nutzsignale empfangen werden, auch starke Störsignale einfallen. Jedoch reicht bereits ein Pfad *ohne* Überlappung aus, um die Störung unterdrücken zu können. Wenn sich Benutzer- und Störsignale jedoch räumlich gut unterscheiden, beschränkt ein zweiter Faktor die Störunterdrückung: Nicht–ideale Eigenschaften der Hardware bewirken verschobene und gefüllte Nullstellen.

A^3**P** ist kompatibel mit Frequenzsprungverfahren (frequency hopping), weil bei den Störsignalen keine Mittelung verwendet wird (kein Tracking der Störsignale). Daher kann **A**^{3}**P** auf plötzliche Änderungen der Störsignale reagieren, auch wenn sich die Interferenzsituation von einem Burst zum nächsten ändert.

Der große Gewinn im Störabstand bleibt bestehen, solange die Richtungsauflösung größer als 5° ist. Eine hochauflösende Richtungsschätzung ist daher *nicht* notwendig, womit die Anforderungen an die Komplexität der Algorithmen verringert wird.

Die Schätzgenauigkeit eines Richtungsschätzers ist in Intelligenten Antennen nicht von Bedeutung. Daher habe ich einen alternative Größe definiert, den *Richtungsschätzbereich*. Im Gegensatz dazu steht die *Variation der geschätzten Richtungen*, die die Schätzgenauigkeit beim Einfallen einer ebenen Welle beschreibt. Nur der Richtungsschätzbereich erlaubt Rückschlüsse auf die Einsatzfähigkeit eines Richtungsschätzers in einer Intelligenten Antenne.

Neben dem bereits erwähnten Gewinn im Störabstand, definiere ich verschiedene Gewinne im Signal–zu–Rauschstand (Signal–to–Noise Ratio, SNR). Den mittlere SNR–Gewinn nenne ich den *Strahlformungsgewinn*. Weiters ist der *Diversitätsgewinn* die Differenz zwischen dem SNR–Gewinn und dem Strahlformungsgewinn bei einer bestimmten Wahrscheinlichkeit (zB. 1%). Im Fall einer rauschbegrenzten Verbindung und wenn das Benutzersignal aus einem schmäleren Winkelbereich einfällt als die Hauptkeule breit ist, erreicht **A**^{3}**P** einen maximalen Strahlformungsgewinn von $7dB$. Die $2dB$ Verlust, die man im Vergleich zum theoretischen Maximum in Kauf nehmen muß, sind auf das Erzwingen der hohen Nebenkeulendämpfung zurückzuführen. In interferenzbegrenzten Situationen reduziert sich der Strahlformungsgewinn

auf $4 - 6dB$.

Mit der Winkeldiversität kann **A**^{3}**P** bemerkenswerte Diversitätsgewinne erzielen. Der Diversitätsgewinn, gemessen bei einer Wahrscheinlichkeit von 1%, erreicht in rauschbegrenzten Situationen Werte von bis zu $6dB$. Natürlich ist so ein großer Gewinn nur in Ausbreitungsszenarien mit mehreren Pfaden möglich.

Im allgemeinen stehen dem Strahlformungsalgorithmus $M-1$ Freiheitsgrade zur Verfügung. Diese können entweder zur Unterdrückung von Störsignalen oder zum Maximieren des Diversitätsgewinns in rauschbegrenzten Situationen verwendet werden. Ich habe **A**^{3}**P** für interferenzbegrenzte Anwendungen optimiert. Dabei garantiert vor allem der Tracker eine von der Störleistung unabhängige, hohe Störunterdrückung auch dann, wenn die Störsignale bis zu $30dB$ stärker sind als das Benutzersignal. Ist **A**^{3}**P** jedoch am Ausgang rauschbegrenzt, liefert er beste Ergebnisse, wenn man den Tracker ausschaltet. Um ein optimales Verhalten unabhängig von der aktuellen Störsituation zu erhalten, schlage ich eine Deaktivierung des Trackers vor, sobald der Ausgang von Rauschbegrenzung zu Interferenzbegrenzung wechselt.

ABSTRACT

This work describes a direction–of–arrival (DOA) –based smart antenna system for GSM1800. The focus lies on the developed antenna array processor that performs real–time adaptive beamforming in every GSM frame. The smart antenna consists of a uniform linear array with $M = 8$ elements, eight transceiver trains and the Adaptive Antenna Array Processor (**A**^{3}**P**). The system allows digital beamforming in uplink and in downlink.

The **A**^{3}**P** performs four main tasks:

- DOA estimation
  From the received input data in the uplink, the directions of the incoming waves are estimated with a high–resolution estimator.

- DOA classification
  This step identifies the wavefronts of the user: First, **A**^{3}**P** spatially resolves the wavefronts from the input data with a spatial pre–filter. A user identification, based on a detector, classifies the DOAs and decides whether a wavefront (DOA) belongs to a user or to an interferer.

- Tracking and DOA selection
  A tracker follows each nominal DOA (multipath component) of the user. This does not only include averaging of the DOAs, but also measures the reliability of each multipath. The main beam points into the direction of the strongest multipath, which corresponds to angular selection diversity. Selecting a multipath only when its reliability is large enough guarantees robust smart antenna processing. Separate trackers are used for uplink and for downlink because the downlink requires averaging.

- Signal reconstruction — beamforming
  Finally a beamforming algorithm forms an antenna pattern with a main beam steered into the direction of the selected user multipath, while simultaneously minimizing the influence of the interfering wavefronts. Placing *broad nulls* increases the robustness against a large angular spread and against inaccurate DOA estimates.

The key elements of a DOA–based smart antenna are: user identification and tracking. Together they provide very reliable decisions, where the main beam should aim at, resulting in an excellent interferer suppression, even in low carrier–to–interference ratio (C/I) environments.

The run–time of **A**^{3}**P** is in the order of $1ms$, thus suitable for real–time operation. **A**^{3}**P** is optimized for spatial filtering for interference reduction (SFIR) operation, but can be easily extended for space division multiple access (SDMA) operation. The run–time will only increase by 35% for each additional user that is served in SDMA mode.

Experiments bear out the viability of DOA–based processing. **A**^{3}**P** achieves the expected enhancements, but there are also find some surprising results.

The gain in C/I is $25dB$, if the interferer signal is incident with a small angular spread (on the order of 1°). Even if the user and interferer signals are *partly* overlapping, **A^{3}P** achieves an interferer suppression of $18dB$.

Interferer nulling increases the C/I gain, but not to the expected extent. The additional C/I gain by forcing nulls into the direction of interferers is only $4dB$. The nulling strategy does not influence the optimum C/I gain. Placing *broad* nulls instead of conventional sharp nulls does not improve C/I gain, but it does increase the robustness against a reduced angular resolution of the DOA estimates and against a large angular spread.

From the measurement evaluation I conclude that the C/I gain is limited by two factors: First, the interference suppression is limited by the angular separability of user and interferer. User and interferer signals cannot be separated when *all* directions where the user signal can be received also include severe interference. But as long as there is a user multipath component *without* angular overlap, the interferer signal can be suppressed. Second, shifted and filled nulls, caused by hardware imperfections, limit the C/I gain if angular separability is high.

A^{3}P is compatible to frequency hopping, because it does not track the interferer DOAs. It can instantaneously adapt to the current interferer situation, even if this changes from one burst to the next.

The C/I gain does not degrade as long as the angular resolution is larger than 5°. DOA estimation with angular resolution in the sub–degree range is *not* required. The relaxed requirements on the DOA estimation reduce the complexity of the system.

The estimation accuracy of a DOA estimator is not of concern in a smart antenna application. Thus I defined an alternative indicator, the *DOA estimation range* that allows judgement of the suitability of a DOA estimator in a smart antenna system.

As quality measures I defined the signal–to–noise ratio (SNR) gain, besides the mentioned C/I gain. The average gain in SNR is called *beamforming gain*. At a given probability level, the *diversity gain* is the difference between the *SNR gain* at that level and the beamforming gain. In noise–limited environments and when the angular spread of the user signal is smaller than the beam width, **A^{3}P** achieves a maximum beamforming gain of $7dB$. The loss of $2dB$ compared to the theoretical optimum is a result of tapering to achieve low sidelobe level. In interference–limited environments the beamforming gain reduces to $4-6dB$.

The angular diversity concept of **A^{3}P** realizes a remarkable diversity gain. The diversity gain is up to $6dB$ when measured at the 1% probability level in a noise–limited environment. Such a large diversity gain can be achieved in scenarios where more than one nominal DOA exist simultaneously.

In general, an adaptive beamformer uses its $M-1$ degrees of freedom either to suppress interference in interference limited environments, or to maximize the diversity gain in noise–limited environments. I optimized **A^{3}P** for interference–limited situations. Here the tracker plays a key role and guarantees a C/I gain independently from the input C/I, even when interference is by $30dB$ stronger than the user signal. If **A^{3}P** is noise–limited at the output, *deactivating* the tracker gives best performance. To reach the best results independently of the interference situation, I proposed to add another level of adaptivity to **A^{3}P**: When the situation at the output changes from the noise– to the interference–limited case, **Hybrid A^{3}P** activates the tracker.

Asynchronism may degrade the system performance, when not all interferers can be sensed. Here I suggested two possible solutions to improve the robustness of **A^{3}P** against asychronous interference.

PREFACE

Never before in the field of mobile communication has so much been changed by so many. Not only has the penetration of mobile services turned the most optimistic forecasts obsolete, also the telecommunication industry has set high aims for the future [Joh98]. Substantial technological progress is needed as never before.

Today second generation systems like the Global System for Mobile Communications (GSM) already exploit available capacity enhancing techniques, like Frequency Hopping (FH) and Hierarchical Cell Structures (HCS), but still are running into capacity limits due to the rapid increase in the number of users. Efficient use of the limited available spectral resources is crucial. A transition to the next generation of mobile communication systems via High–Speed Circuit–Switched Data (HSCSD), Generalized Packet Radio System (GPRS), and Enhanced Data rates for GSM Evolution (EDGE) will increase spectral efficiency by more efficient signaling, modulation and coding schemes. Data rates from 14.4kbit/s (GSM, single timeslot), up to 170kb/s (GPRS) up to 400kb/s (EDGE) in the same bandwidth will be possible.

Although the second generation already offers a wireless access on the Internet, the Third Generation Mobile Systems, also referred as 3G systems, will go a step further: data rates of up to 2Mb/s are envisaged. Most of these future mobile communication standards, like the Universal Mobile Telecommunication System (UMTS), with their extremely high data rate requirements, already exploit the time/frequency and code domain to optimize spectral efficiency. The last domain that is not yet fully exploited is the *spatial* domain.

Smart antennas exploit the space dimension. They are a strong candidate to overcome the capacity limits of 2G systems, as well as helping 3G systems to achieve data rates up to 2Mb/s. Furthermore smart antennas can enhance coverage. This fact will additionally drive the integration of smart antennas in future wireless systems, because smart antennas positively affect the link budget. Extending the coverage from outdoor to indoors systems is an essential requirement of today's as well as of tomorrow's systems and smart antennas are a candidate to achieve this goal. Standardization bodies of 3G systems have recognized the potential that the spatial dimension offers and thus adapt the standard to guarantee a less costly and more effective deployment of smart antennas.

Multiple Input/Multiple Output systems with several antennas at both ends of the link will raise the limits of spectral efficiency to multiples of that of conventional single antenna systems [FG98], [MH99], [And98b], [And98a]. Spectral efficiencies of 10–20b/s/Hz in indoor "fixed" wireless systems have already been demonstrated in the lab by exploiting smart antenna technology [LT98].

A smart antenna system that is applicable to all systems is not yet discovered. The application makes all the difference. Whether Time Division Multiple Access (TDMA) or Code Division Multiple Access (CDMA), whether narrowband or broadband, the smart antenna signal processing has to be tailored to the specific system needs. Although during the last years

the number of publications in the field of smart antenna technology has grown steadily, there is no generally applicable solution available. Numerous sophisticated theoretical concepts are under study and various approaches have been taken to optimize reception and transmission with multiple antennas.

Smart antenna technology is on the brink of commercial realization. Proving concepts either by theoretical analysis or by simulation is not enough anymore. Today smart antenna technology must be proven practically. For several reasons it is important to build smart antenna testbeds:

- Optimize reception and transmission with multiple antennas for a certain system including all real–world problems, e.g. calibration.
- Study implementation issues, i.e. embed the smart antenna in an existing base station concept, find requirements on hardware, like necessary processing power and transceiver parameter (e.g. allowed phase and gain imbalances).
- Validate theoretical concepts.
- Measure the achievable benefits in an implemented smart antenna system. This will bring the technology to the potential customers, the network operators, and in turn motivate further development.
- Study the effect of the mobile radio channel on the system performance.

The *Institut für Nachrichtentechnik und Hochfrequenztechnik* has formed a cooperation with the *Alcatel Corporate Research Center Stuttgart* to develop and implement a smart antenna array processor for real–time application. In this particular work the array processor is developed to upgrade a GSM/DCS1800 base station with a smart antenna. This work presents the results of the project and focuses on the developed real–time smart antenna processor. This processor was integrated into a demonstrator and a field trial investigated the system in real–world environments.

Chapter 1 gives an overview of today's state of smart antenna technology.

Chapter 2 introduces the smart antenna processor and the cooperation project. I will briefly outline the hardware of the smart antenna demonstrator and show how the developed array processor is embedded in the base station.

The signal model used throughout this work will be presented in Chapter 3.

In Chapter 4, I will describe the developed adaptive antenna array processing scheme. I will discuss each individual element of the processing scheme, including the performance of each individual subtask. Critical points that may influence the overall system performance are high–lighted and referred to the next chapter.

The evaluation of the adaptive antenna array processor focuses on the uplink. It is based on measurements with the smart antenna demonstrator. At the beginning of Chapter 5 I will define the quality measures that quantify the benefits of the developed smart antenna system. The main part of this chapter studies the role of each subtask and how it affects those quality measures. Here I will also find an optimum configuration for the algorithms.

In Chapter 6 I will evaluate the adaptive antenna array processor in typical applications: 1) I will investigate the sensitivity enhancement of $\mathbf{A}^3\mathbf{P}$ in scenarios where no interference is present. In contrast to Chapter 5, where I only study interference limited environments, I here will quantify the diversity gain of the system. 2) I will study environments with intercell

interference. The effect of non-synchronous interference is here essential. 3) I will include frequency hopping and I will show that the smart antenna is compatible with this GSM feature.

Chapter 7 presents an outlook and concludes this work.

ACKNOWLEDGEMENTS

A friend once said to me that the acknowledgement is the most important part of a thesis; another one said that he does not like long praises at all. I will try to satisfy both of them . . . .

Before I list you who made this work possible and who supported me the one way or the other, I start with the most important: **I thank you all. I owe you a lot**.

A company that supports your work — Alcatel Stuttgart Michael Tangemann for making this cooperation so fruitful. I learned a lot from him about managing a technical project. Cornelis Hoek, a most gifted engineer, who together with Michael is responsible for a great deal of the project's success. Michael Hother, Guillaume de Lattre, Günter Köhler and many other colleagues from Alcatel for their support during the project and especially during the measurement campaign in Stuttgart. Dr. Bostelmann for his continuous efforts to convince the management of Alcatel Stuttgart to invest money in a young research team.

My safe place and dear friend — Prof. Ernst Bonek There are many things to thank him and undoubtedly in my professional life he is the most important person, but I will keep it short: Thank you for always believing in me and for all you have done for me!

My second supervisor — Prof. Peter Leuthold Prof. Leuthold for his willingness to supervise my thesis and his patience in waiting for the actual document. Finally he was fast in reviewing my work and very flexible in setting up the date for the exam. His comments considerably improved the quality of my thesis.

My companion — Andreas Molisch A dear friend and loyal supporter, an unbelievably knowledgeable man, a wizard in mobile communications.

My inspiration — Josef Fuhl Beside Ernst, he was my first colleague, teacher, and mentor at the INTHF. I admire you in many respects. Many thanks!

My kick in the behind — Per Ödling I met this guy rather late, only a few months ago, but soon it was clear that he will become a close friend. Thank you for making *once more* sure that this thesis came to an end.

My team — Manfred Taferner, Günther Pospischil, Wolfgang Rauscher, and Martin Strasser They participated in the project that lead to this thesis. Without them, the project would have been impossible to carry out. *Manfred Taferner and Günther Pospischil* were more than just team members, they became close friends. They were very patient with the many requests for help. I could not think of working without their support.

My working environment — the INTHF There are many people, especially the Mobile Communications Group, who made the four years at the INTHF a wonderful experience. I will name just a few, but I won't forget any of you.

Juha Laurila with whom I shared a room during the last year. We had a tremendous amount of discussions and shared many ideas. Mrs. Svejda helped me to keep an eye on our budget. Mrs. Manuela Heigl who always had a smile for me and Mrs. Jarosch who so often made sure that I got a slot of Ernst's precious time. And finally, Walter Schüttengruber, who was always there when I needed help in a fight with hardware and the software of Bill Gates.

My source of energy — Elke My wife, the love of my life, the most important person in my life. She had a lot to take, because of my sometimes late working hours. Still, she supported me with her love and understanding throughout the years of this work[1]. Especially during the hotter periods of the project and the final writing of the thesis, my life would have been difficult without her patience and active support.

[1] During the last years I began to realize what "There is always a strong woman behind a successful man." can mean.

I dedicate this work to Hannah and Elke.

CONTENTS

ZUSAMMENFASSUNG **1**

ABSTRACT **1**

PREFACE **i**

ACKNOWLEDGEMENTS **v**

1 INTRODUCTION **1**
1.1 What makes the "Smart Antenna" smart? 1
1.2 State–of–the–Art 3
1.2.1 Smart antenna structures for uplink 3
1.2.2 Uplink smart antenna algorithms 7
1.2.3 Uplink algorithms and structures 9
1.2.4 Downlink 10
1.2.5 Multiple antenna elements on both ends of the link 12
1.2.6 Channel models 12
1.2.7 Testbeds and demonstrators 12

2 GSM1800 SMART ANTENNA DEMONSTRATOR **15**
2.1 Hardware architecture 16
2.2 User interface 18

3 DATA MODEL **21**
3.1 Notation 21
3.2 Signal model of smart antenna base station 21
3.3 Channel modeling 24

4 ADAPTIVE ANTENNA ARRAY PROCESSOR $\mathbf{A}^3\mathbf{P}$ **29**
4.1 Array processing scheme 29
4.2 $\mathbf{A}^3\mathbf{P}$'s concept 30
4.3 DOA estimation 32
4.3.1 Unitary ESPRIT with subspace *estimation* 33
4.3.2 Unitary ESPRIT with subspace *tracking* 36
4.3.3 Estimating the number of DOAs 38
4.3.4 Minimum Variance Method 39
4.3.5 Run–time of DOA estimation 42

4.3.6 DOA estimation accuracy 43
4.3.7 DOA estimation robustness 47
4.3.8 Summary DOA estimation 54
4.4 Spatial pre–filtering — Uplink beamformer 57
4.4.1 Conventional beamforming 57
4.4.2 Broad null beamforming 58
4.4.3 Run–time of uplink beamformer 58
4.4.4 Summary uplink beamformer 58
4.5 User identification 60
4.5.1 Post–correlation 60
4.5.2 Run–time of user identification 63
4.6 Tracker 63
4.6.1 Tracking scheme 64
4.6.2 Selection of DOAs for final beamforming 69
4.6.3 Summary tracker 71
4.7 Signal reconstruction – beamforming 73
4.7.1 Broad null beamforming 73
4.7.2 Conventional beamforming 75
4.7.3 Run–time of uplink post beamformer 75
4.7.4 Measured antenna pattern of **SmearR** 76
4.8 **A^{3}P** run–time 76

5 QUANTIFYING BENEFITS 79
5.1 Measurements in a controlled environment 80
5.1.1 BER performance in an AWGN channel 80
5.1.2 Interference suppression capabilities 82
5.2 Measures for performance evaluation 82
5.2.1 Measurement modeling — generating scenarios 83
5.2.2 Definition of SNR and C/I 84
5.2.3 Definition of C/I gain and SNR gain 87
5.3 DOA estimation resolution and robustness 90
5.3.1 Resolution of DOA estimator 95
5.3.2 Conclusions 98
5.4 Effect of nulling strategy in spatial pre–filter 100
5.5 Influence of user identification 102
5.6 Effect of tracking 103
5.6.1 Is tracking just averaging? 104
5.6.2 Summary 106
5.7 Effect of the nulling strategy 106
5.7.1 Interferer nulling — does it work? 108
5.7.2 Broad nulling versus sharp nulling 111
5.7.3 Broad nulls and the DOA estimation 111
5.7.4 Null width and null depth 115
5.7.5 Broad nulls and angular spread 115
5.7.6 Conclusions 117
5.8 Summary and conclusions 117

6 APPLICATIONS **119**
6.1 Sensitivity enhancement 119
6.1.1 **A**^{3}**P** dual beam 121
6.1.2 Scenario Urban 1 122
6.1.3 Scenario Highway 125
6.1.4 Scenario Urban 2 127
6.1.5 Summary 129
6.2 Interference to noise limited environments 131
6.2.1 Environment I⟶N 131
6.2.2 Interference or noise — what is the limiting factor? 133
6.2.3 Tracking — or not? 135
6.2.4 Summary 138
6.3 Asynchronous networks 138
6.3.1 **A**^{3}**P** and the GSM timeslot structure 138
6.3.2 Environment SFIR 141
6.3.3 **A**^{3}**P** in Scenario SFIR 1 141
6.3.4 **A**^{3}**P** in Scenario SFIR 2 145
6.3.5 **A**^{3}**P** in Scenario SFIR 3 149
6.3.6 Summary 151
6.3.7 Improvements 153
6.4 Frequency hopping 153
6.4.1 Scenario SFIR 4 155

7 OUTLOOK **159**
7.1 Downlink 159
7.2 SDMA 160
7.2.1 **A**^{3}**P**'s architecture and SDMA 161
7.3 Refinements of **A**^{3}**P** 164
7.3.1 Beamforming and calibration 164
7.3.2 Hybrid **A**^{3}**P** 165

A REAL–VALUED TRANSFORMATION OF COVARIANCE MATRIX **169**

B LIST OF FREQUENTLY USED ACRONYMS **171**

C LIST OF FREQUENTLY USED SYMBOLS **173**

BIBLIOGRAPHY **177**

CURRICULUM VITAE **185**

Chapter 1

INTRODUCTION

A good scientist is a person with original ideas. A good engineer is a person who makes a design that works with as few original ideas as possible.
There are no prima donnas in engineering.

Freemon Dyson (1923-, theoretical physicist)

In the introduction I will briefly describe the term "smart antenna" and then present the state–of–the–art of smart antenna technology. As I develop a smart antenna processor at a GSM1800 base station in this work, this chapter focuses on *base station* smart antenna technology.

1.1 What makes the "Smart Antenna" smart?

In truth, antennas are not smart; antenna *systems* are; to be precise, they are *adaptive*. A smart antenna consists of the antenna, a radio frequency (RF) part and a signal processing part, with the *signal processing* part being *smart*. The focus of smart antenna technology lies on this signal or array processing. In the following I will put the terms "smart antenna" and "array processing" into context.

Array processing[1] includes techniques that process signals from several spatially distributed sensors. Basically this allows exploiting the spatial domain, because the antenna signals are sensed at different spatial locations. In radar or sonar applications, array processing is used to detect and find signal sources. In mobile communications array processing aims at the detection of a communication signal with improved quality. We call such a system a "smart antenna".

By combining the outputs of multiple antenna elements with signal processing capabilities to transmit and/or receive RF signals in an adaptive manner, a smart antenna can dramatically increase the performance characteristics (such as capacity) of a wireless system. Simply speaking, a smart antenna system can automatically change the transmission and/or reception pattern in response to the signal environment. Actually we use this principle in this work, but

[1]The term "array" might be replaced by "multi sensor" if one argues that an array antenna is only a regular antenna structure with rather closely spaced single elements. In my terminology an antenna array includes any system with multiple sensors, regardless of the elements' locations in space. We use in this work only a uniform linear array with an element spacing of half a wavelength. The *IEEE Standard Dictionary* [Boo93] notes that "array antennas" is also applied to cases where the elements are not arranged in a regular fashion.

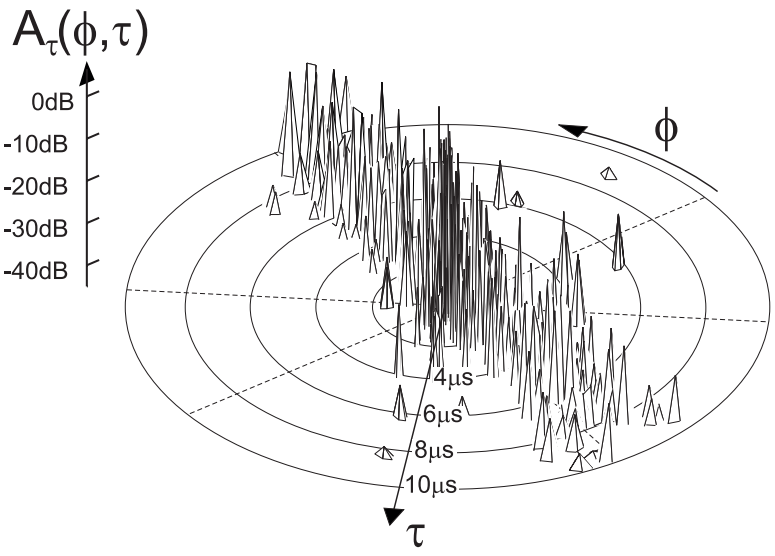

Figure 1.1. Azimut–delay power distribution at the mobile station in urban Paris [KRB99]. The result demonstrates the directional nature of the mobile radio channel. Here a street canyon forces the energy to arrive at the mobile from basically two directions (street directions).

as you will notice in the next section, this is not the whole story.

What are the potential gains of smart antennas? In a cellular wireless communication system a smart antenna:

- Mitigates the effect of co–channel interference: The spatial dimension enables interference suppression that is not possible with processing in time domain only. Often the desired signal and the co–channel interference (CCI) arrive at the receiver with well separated spatial signatures, thus allowing the smart antenna to extract the desired signal and suppress CCI. In the transmit case the smart antenna can focus the energy to the desired user and so reduce the interference for other users.

- Increases range: The array gain improves the power at the receiver. Similarly, beamforming in the transmitter increases the radiated power of the system thus extending the range of the base station.

- Reduces delay spread: Reception (transmission) from (to) limited angular ranges reduces the delay spread when severe multipath is present. Especially in high–data rate applications, like wireless local–area networks (WLAN), the receiver might then be able to operate without an equalizer.

- Combats fading: Exploiting diversity in reception as well as in transmission improves the resistance against small–scale fading.

The signal processing in a smart antenna system is matched to the specific characteristic of the mobile radio system and the mobile radio channel: the air interfaces and the demanding time–varying multipath propagation. An example of the angular power distribution, $A_tau(\phi,\tau)$, at the mobile station in an urban environment demonstrates the complex characteristic of the directional mobile radio channel (Fig. 1.1).

1.2 State–of–the–Art

Various overview papers present introductions to smart antenna technology: [Win98b] gives a short introduction to smart antennas, their benefits and application. A more comprehensive study with extensive references is [God97a] and [God97b], where Part II focuses on beamforming. In [PP97], [PN98] the focus lies on space–time processing for TDMA and CDMA systems. An introduction of smart antenna arrays for CDMA systems is presented in [TGM96]. Reference [KV96] presents an overview on parametric direction–of–arrival (DOA) estimators for array signal processing. [Bon98] discusses current issues of smart antenna technologies.

A comprehensive treatment of smart antenna technology is [Fuh97b], including a system concept for upgrading a second generation TDMA system with smart antennas and an analysis of various uplink and downlink algorithms. Basically we can integrate base station smart antenna technology into a GSM/DCS network in three main steps [THR94]:

- High sensitivity reception: Here the smart antenna is applied only in uplink, which increases the BS sensitivity. This concept depends on an increased transmit power in downlink to achieve balanced links.

- Spatial filtering for interference reduction (SFIR): Beamforming is applied also in downlink, so that both links can exploit the advantages of smart antennas. The main idea is to reduce the co–channel interference level in a cellular mobile communications system by focussing the energy into the direction of the desired user. This will allow improvements in spectral efficiency by a factor of $2-3$ [FKB97], [KFB97], [AB99] compared to conventional sector systems.

- Space division multiple access (SDMA): In contrast to SFIR, SDMA serves more users on the *same* frequency at the *same* time within one cell. An additional gain of 80% in spectral efficiency compared to SFIR is predicted [KFB97].

A considerable difference exists in the uplink and the downlink situation. In the uplink, the signal received by the smart antenna has passed the channel, and thus it is possible to estimate not only transmitted data but also the channel. In downlink, smart antenna processing is carried out *prior* to transmission and therefore *before* the signal passes the channel.

I will first take a look at smart antenna structures that can be used in the uplink and then point out the difference to the downlink.

1.2.1 Smart antenna structures for uplink

A smart antenna system contains an RF part and a signal processing part (Fig. 1.2). In the uplink RF part the received signals from the M array elements are filtered, amplified and down–converted and sampled. The analog–digital converter separates the RF part from the signal processing part. The following smart antenna processor extracts from the M signals the K user signals (for SFIR $K=1$, and for SDMA $K>1$). In most systems, the smart antenna processor output signals are the complex received baseband signals that have to be detected in the baseband unit.

Basically a smart antenna processor may include a:

- Spatial processor: In the straightforward approach an adaptive beamformer realizes a spatial filter (Fig. 1.3), i.e. a single weight vector $\mathbf{w}$ is applied to the M antenna signals,

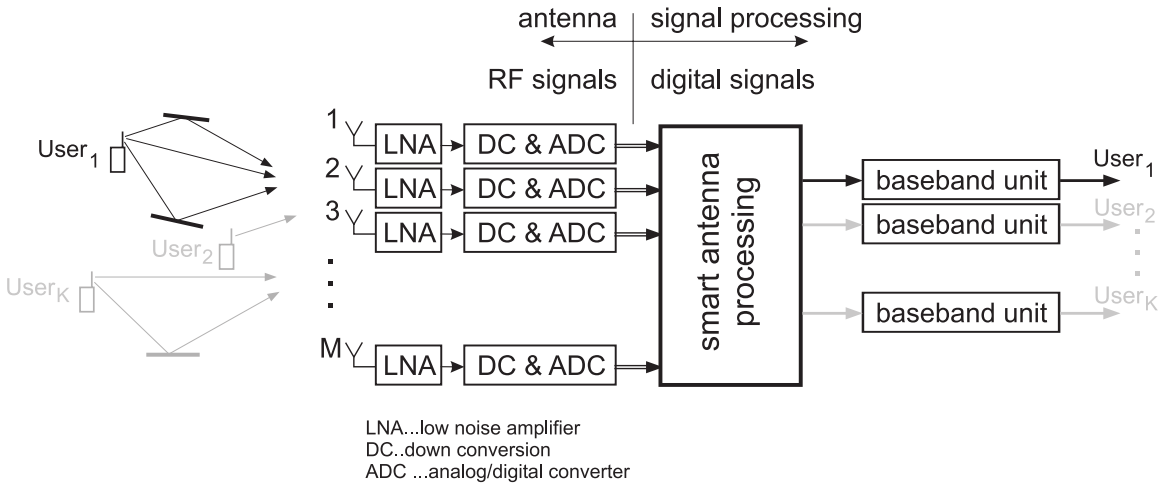

Figure 1.2. Principle of a smart antenna array at the uplink. The smart antenna extracts the user signals, which are equalized and detected in a baseband processing unit.

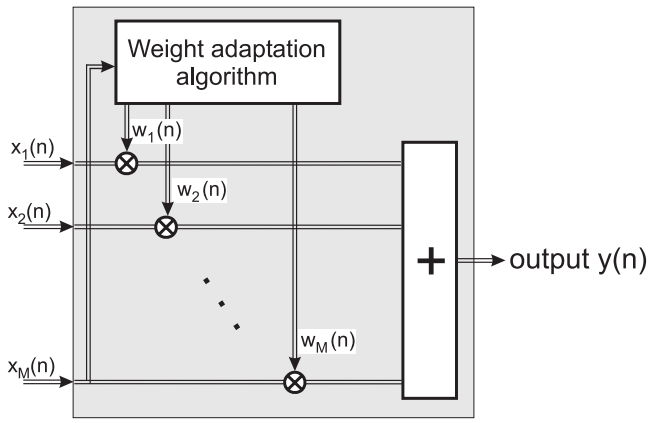

Figure 1.3. Space–only processing. The smart antenna processor includes only a spatial processing structure, which is followed by an temporal equalizer (Fig. 1.2).

$x_m(n)$, $m = 1 \ldots M$, to combine the received signals which results in the user signal, $y(n)$. The smart antenna processor is followed typically by a conventional baseband processor that includes equalizer and detector. Thus this approach utilizes a spatial filter and a subsequent *independent* temporal filter (equalizer).

- Space/time equalizer: An extension of the above concept is to combine the spatial filter with the temporal filter (Fig. 1.4) [Fuh97b]. The output of the space–time filter is directly put into a detector without further equalization, because temporal equalization is already carried out in the space/time equalizer. Combined spatio–temporal processing will improve the performance especially in systems with large delay spread. It will not boost performance significantly compared to the previous approach when no significant variation of the angular power distribution over delay occurs, because then temporal and spatial equalization can be done serially without loss of performance. In [PP97] the concept of space–only and space–time processing are discussed, both for TDMA and CDMA systems.

- Space/time detector: In the most elaborate approach the space–time equalization and detection is combined (Fig. 1.5). Such systems show in general superior performance, but most are today computationally too demanding for real–time implementation [LKB99]. However, first steps are taken to reduce the complexity and so allow a real–time implementation [LTB99]. Here the smart antenna processor already includes the detector and thus it includes also the baseband processing unit. A drawback is that there is no equivalent of this concept for transmission.

  In the first two concepts — spatial processor and space/time equalizer — we can think of antenna patterns that are implicitly or explicitly formed[2] to optimize reception/transmission. In the case of the space/time detector *no* weight vector is calculated anymore and thus the concept of beamforming is not applicable here. Actually the intermediate step of extracting a user–specific complex baseband signal is omitted. Instead the final user symbol stream is extracted in a single procedure, hence the name space/time detector.

[2]In such approaches one or more weight vectors are calculated. With the known array geometry we can calculate for each weight vector an antenna pattern.

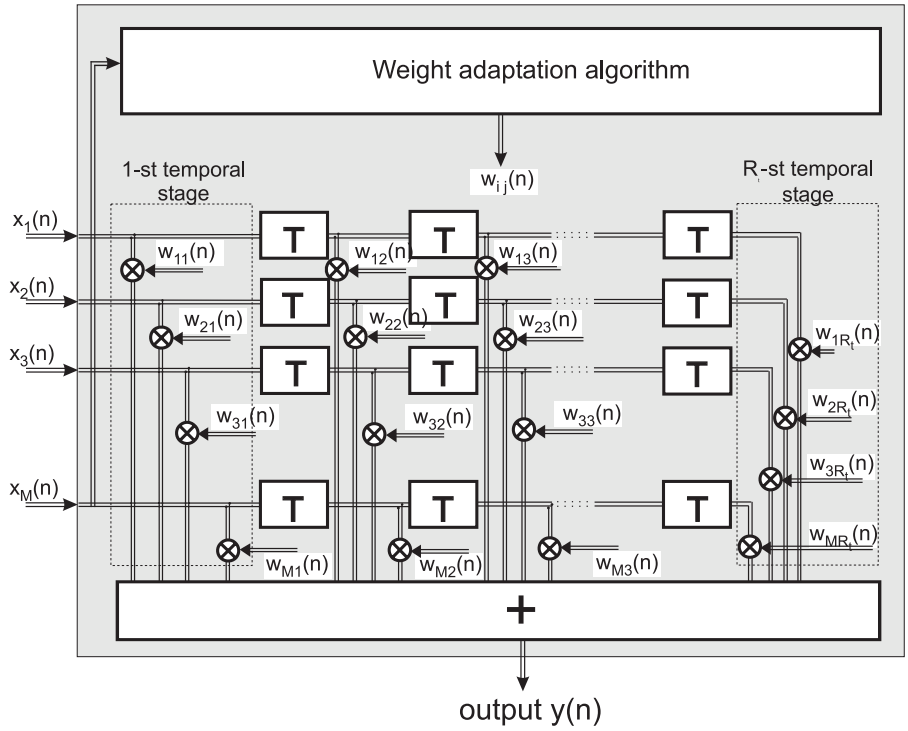

Figure 1.4. Space/time equalization. The smart antenna processor includes a spatio–temporal processing structure. The output of the smart antenna processor can be detected without further equalization.

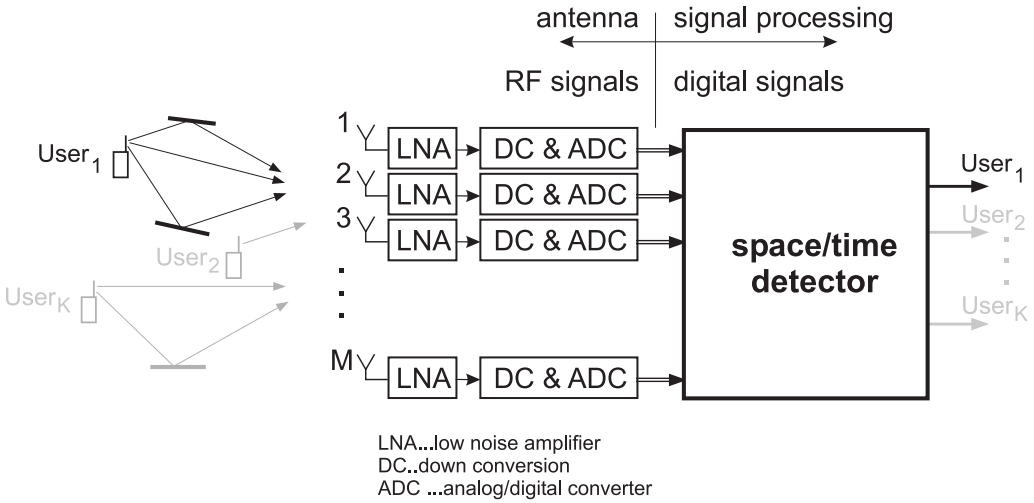

Figure 1.5. A space–time detector combines the spatio–temporal equalization with the detection process.

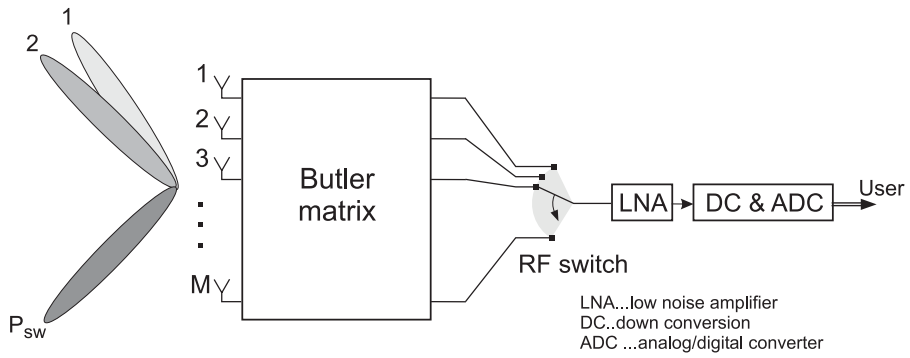

Figure 1.6. Principle of a switched beam.

A different category of smart antenna comprises traditional, analog beamforming.

- Switched beam system: In contrast to the previous fully adaptive approaches, a switched beam system [NNK98] does not require digital array processing. Rather, more effort is spent in the RF part to realize the smart antenna. A switched beam system consists of an RF beamforming network that forms P_{sw} beams to cover the angular range of interest (typically a sector of 120°). Often the number of beams is equal to the number of antenna elements, $P_{sw} = M$. Typically a Butler matrix [NNK99], which represents a Fourier transform network, is used for beamforming. Its P_{sw} outputs provide the received signal from each of the fixed antenna beams. The reception system selects the output with the best performance (typically the strongest signal, but more elaborate schemes go for minimum BER [KNKB97], [Nov99]). Clearly a switched beam system is an economical solution, because it does not need extensive signal processing power and, most important, only a single transceiver.

Sometimes the term "adaptive antenna" is used as synonym for "smart antenna". However the adaptivity of the receiver/transmitter characteristics is limited in the case of the switched beam system.

1.2.2 Uplink smart antenna algorithms

The tremendous variety of algorithms for smart antenna processing makes it nearly impossible to categorize them unequivocally. However, most of the algorithms in the literature follow one of the listed strategies:

- Combining: The strategy is to combine the antenna signals to optimize a measure for signal quality, e.g. signal–to–interference–plus–noise ratio (SNIR). In contrast to maximum ratio combining (MRC) [Jak74], these methods take interference into account. Optimum combining (OC) [Win84] maximizes SNIR. It reduces to MRC if no interference is present. In a practical implementation of the optimum combiner the *knowledge of a reference symbol sequence* to calculate the weights in a time–variant channel is exploited [Win84], [Win93]. Algorithms that exploit a known part of the transmitted symbol sequence to extract the antenna weights are called *temporal reference algorithms* [Fuh97b]. An efficient computation of the weights of a wideband structure requires only the computational complexity in the order of the complexity of a narrowband approach [Fuh97a]. Here the

complexity is independent of the temporal filter length. Still the output SNIR is better than in the case of the narrowband system. In [BPW99] subspace implementations of the OC and a *minimum mean–square error* (MMSE) approach, which minimizes the error between the beamformer output signal and the known training sequence, are compared. Here the weighted subspace implementation of the OC worked better than its MMSE counterpart. Temporal reference algorithms tend to exploit the space diversity offered by the channel, or in other words: they combat fading effectively while simultaneously suppressing interference [Win94].

- DOA–based beamforming: The strategy is to form an antenna pattern that extracts the individual message from each user. To do so one estimates the DOAs of the incident signals and uses this information for beamforming. I call this strategy in short "beamforming". The DOA estimators and the subsequent beamforming algorithms typically belong to the class of *spatial reference algorithms*, because they assume the knowledge of some properties of the array manifold. The *array manifold* is the set of array response vectors for all possible DOAs. It includes the effect of array geometry, element patterns, mutual coupling, and scattering from objects near the base station. When the array manifold is measured at the receiver baseband after digitization, it also includes effects of receiver imperfections, like I–Q imbalances [KFK97]. When we assume certain ideal properties of the manifold, calibration becomes crucial. In [WTFH98] the beamforming performance is measured with a testbed, and calibration issues are addressed.

  An excellent overview of parameter estimation with emphasis on DOA estimation is [KV96]. There DOA estimators are divided into two main categories, namely *spectral–based* and *parametric* approaches. The first class of algorithms forms an angular power spectrum. The locations of the peaks correspond to the estimated DOAs. In this work we apply the Minimum Variance Method (MVM) or Capon's beamformer [CGK67], [JD91]. Parametric techniques fully exploit the underlying data model and estimate the parameters (DOAs) simultaneously. Especially for uniform linear arrays (ULA) the ESPRIT algorithm [RPK86] has recently gained importance. An alternative algorithm to estimate the DOAs is the space–alternating generalized expectation-maximization (SAGE) [FTHD98].

  [AMVW91] compares an adaptive array based on beamforming to a combining approach. The DOA–based beamforming method shows superior SNIR gain for small angular spread, but performance degrades, although only "gracefully", when signal energy is incident from larger angular ranges. The method is more flexible than the combining approach. DOA tracking can be included, which prevents the DOA estimates from changing too much between two consecutive bursts. Additional information about the mobile locations is available through the DOA estimates. This knowledge can be of great use for the handover and is also of interest by itself for mobile station location information (emergency service, law enforcement). The authors note that the beamforming technique does not solve the problem of fading and thus propose to utilize e.g. polarization diversity. Furthermore, they assume knowledge about which of the estimated DOAs are the intended user DOAs.

  A comment on terminology. In contrast to my notation, some authors, e.g. [AMVW91], use the term "beamforming" for both combining and DOA–based beamforming. What both schemes have in common is that they linearly combine the antenna signals (reception). This can also be interpreted as an artificially formed beam in the antenna pattern

into the direction of the user, while minimizing the influence of interferers. While the DOA–based beamforming accomplishes this beam steering explicitly, the combining approach rather places nulls implicitly into the directions of the interferers. However there is the significant difference in the two schemes: DOA–based beamforming exploits the correlation between antenna signals, while the combining approach also exploits diversity (=decorrelation of signals). In other words, combining will perform in general better than beamforming when the antenna signals are decorrelated.

When the antenna pattern is adjusted "on–line" by either a combining scheme or DOA–based beamforming scheme, the technique is often referred to as *adaptive beamforming* or *adaptive arrays*.

- Blind algorithms: Blind algorithms do not need reference signals, but rather exploit structural information of the transmitted signals, like the finite alphabet or constant modulus property. They can either be used for beamforming [OSMS93] or for space–time detection. In the latter, the transmitted data sequences (or a soft detector output) is directly estimated omitting the intermediate step of complex baseband signal estimation. Additionally such algorithms are typically able to extract the signals of *all* received users, thus belonging to the class of multiuser blind space–time methods [PP97][3]. Such algorithms have in general better performance than single user algorithms and are not sensitive to calibration errors. However, these advantages must be paid for by a significantly increased computational complexity. A way to reduce complexity is to exploit known user identifiers for initialization of iterative procedures in the algorithm [LKB99].

1.2.3 Uplink algorithms and structures

Finally by mapping the algorithms onto the structures, I will make clear which algorithms are used in which structures:the spatial processor, the space–time equalizer, and the space–time detector.

A *spatial processor* exploits the space domain. In a spatial processor both the combining and DOA–based beamforming algorithms can be applied. Thus a spatial processor is often referred to as "adaptive beamformer" or "adaptive array". It is a narrowband structure. By connecting a temporal equalizer in cascade, the spatial processor can be combined to obtain a structure that can better cope with wideband channels. Of course the temporal equalizer can exploit only multipath components that pass the spatial filter. Not necessarily these multipath components have to be incident from the same direction. The algorithm implemented in the spatial process and the temporal equalizer do not exchange information, they work independent from each other.

The *space–time equalizer* is a wideband structure. An algorithm carries out the equalization in space and time in a single step. Here, in principle, all multipath components can be exploited. In such a structure typically combining algorithms are used.

The most elaborate structure, the *space–time detector* (Fig. 1.5), can only be realized with algorithms that combine equalization in space and time and detection. Thus blind algorithms are applicable.

In this work I implement a spatial processor including angular diversity. By forming more than a single weight vector, we can apply different beamformers thus collecting energy not only from a single direction but from all available multipaths. Of course, this means that energy

[3]Note that there are also nonblind multiuser space–time algorithms.

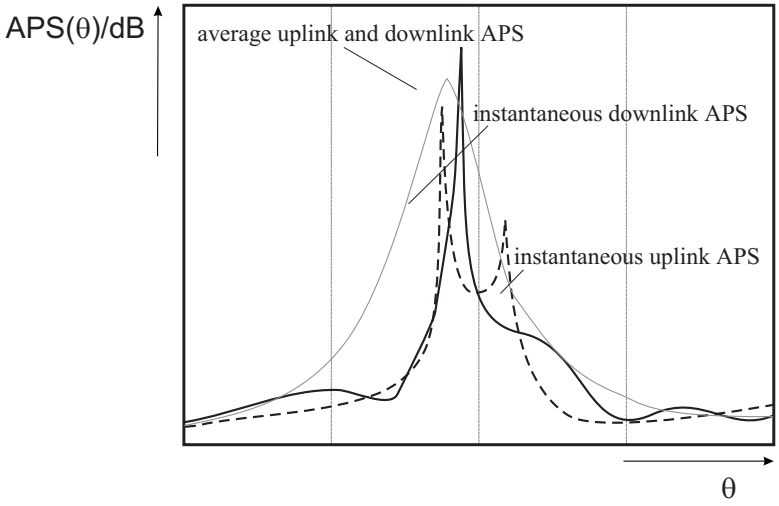

Figure 1.7. Sketch of instantaneous and averaged azimuthal power spectra.

is in general collected from arbitrary and different delays. In other words, the array exploits all the signal energy available, thus also including signal components with larger delay in the processing. The resulting structure is not strictly the same as the space–time equalizer (Fig. 1.4), but it includes definitely more than the one of Fig. 1.3. Instead of applying weight vectors regularly spaced in delay by a symbol period, the weight vectors are applied to signals with the same delay, but different directions. For example, a maximum ratio combiner can then be used to sum up the signal contributions from the different directions.

1.2.4 Downlink

Up to now I discussed the uplink case. In uplink we can estimate the channel parameters from the received data, because we have sensed the signals *after* they have passed the channel. An uplink smart antenna algorithm can therefore adapt to the instantaneous channel situation.

This is not the case in downlink. In typical mobile communication systems, uplink and downlink are strictly speaking *not* reciprocal. In a frequency division duplex (FDD) system, like GSM, the assumption of identical carrier frequencies is not fulfilled. In practice this means that small–scale fading in uplink and downlink is uncorrelated[4]. The uncorrelated fading results in different instantaneous uplink and downlink azimuthal power spectra (APS). Figure 1.7 demonstrates two *instantaneous* APSs that differ significantly in uplink and downlink. However, the *average* APSs are the same.

The uplink and downlink channel are quasi–reciprocal. Here quasi–reciprocity means that the *average* APS and the *average* path loss are equal in both links. Recent measurements [MPFF99] have confirmed that the mean DOAs are exactly the same when measured at two frequencies around $1800MHz$ with a frequency spacing of about $70MHz$.

What are the consequences of the quasi–reciprocity on the applicability of the various adaptation strategies?

- Reusing the uplink weights in downlink is not recommended [Fuh97b].

[4]The correlation depends on the frequency spacing and the channel [Fuh97b]. Uplink and downlink are uncorrelated if the duplex distance is larger than the coherence bandwidth.

- Combining algorithms and blind algorithms are not directly applicable to the downlink. This is a consequence of the missing instantaneous channel estimates. But if such algorithms are applied in uplink, the resulting uplink channel estimates can be exploited for the downlink beamforming.

- DOA–based algorithms are applicable, because they can also use averaged information (DOAs, path loss) extracted on the uplink.

A DOA–based smart antenna with a simple DOA estimation, based on the above mentioned assumptions, is considered in [Yli99]. Simulations reveal that a DOA–based approach for the downlink yields in an AWGN channel a BER performance close to the one of the uplink.

Other downlink algorithms

Transmit diversity schemes can be used to provide diversity benefits at the mobile station receiver with multiple transmit antennas when the channel is not known at the transmitter. [Win98a] showed that transmit diversity with M antennas provides a diversity gain within $0.1dB$ of that with M receive antennas. In this delay transmit diversity scheme multiple antennas transmit delayed versions of the same signal to create frequency–selective fading at a single antenna at the receiver, which uses equalization to obtain diversity gain against fading.

A more general framework for linear transmit antenna diversity is described in [PW98]. There, the ability to exploit diversity is created by processing the symbol stream to be transmitted with a different linear filter at each antenna element. This processing is referred to as *linear antenna precoding*. It includes delay transmit diversity as a special case.

Space-time coding generalizes the transmit diversity scheme by including also coding aspects (see e.g. [TSC98]). Here, typically, the data stream is encoded by a channel coder and then split into M parallel data streams and then simultaneously transmitted over the M antenna elements. It is possible to construct space-time codes that increase spectral efficiency over that of the single antenna case while simultaneously providing a diversity gain. In [TSC98] a fundamental tradeoff between code complexity, diversity gain, and the spectral efficiency[5] is discussed.

Transmit diversity schemes couple the energy into the spatial channel without regard to the interference. [HP99] alleviates these problems by applying several beam steering arrays. The proposed scheme combines the advantages of DOA–based downlink beamforming with a spatial diversity scheme.

Other schemes that take the effect of interference into account are downlink beamforming algorithms. The algorithms studied in [Hug98] assume the knowledge of the downlink covariance matrix. The best method to estimate the downlink covariance in an FDD system is to use the uplink estimated DOAs. A recently developed algorithm transforms the uplink covariance matrix into a downlink covariance matrix [HLB99]. [MSH99] applies a slow power control scheme to a fixed multibeam antenna and shows an improvement in average carrier–to–interference ratio (C/I) of $2-3$dB. By minimizing the transmit power under the constraint of a target C/I or BER for each user, the average interference level is reduced.

[5] To achieve the full diversity gain when M_T transmit and M_R receive antennas are used, the spectral efficiency is upper bounded by the spectral efficiency of the single antenna case. However, when higher spectral efficiency is the goal, it can be achieved at lower diversity gains. In other words, a fraction of the number of degrees of freedom $M_R + M_T$ can be used to improve the system performance (diversity gain) while the remaining degrees of freedom allow to achieve higher spectral efficiencies.

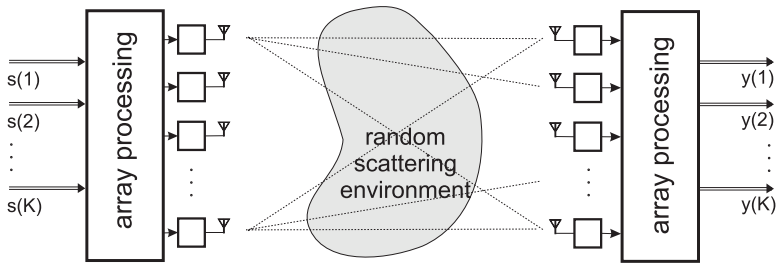

Figure 1.8. Multiple input multiple output system [And98b].

Downlink structures

The straightforward solution for the downlink is to use the space–only filter, i.e. a DOA–based solution. In downlink, of course, the input and the output of the space–only filter (Fig. 1.3) are exchanged, because the user sequence is transmitted over M antennas.

A simpler possibility is to apply a switched beam system at the downlink. Here, the beam selection is based on information derived in the uplink.

A more complex space–time coder is required especially if the potential capacity gain of multiple input/multiple output systems is to be exploited (see next subsection). Here the transmit signals differ not only by complex antenna weights, but in general also by the sent information. The information bit stream is encoded by a space–time encoder, then serial–to–parallel converted to split the encoded data stream into parallel data streams. Each stream of data is used as the input to a pulse shaper followed by a modulator. The modulated signals are then sent simultaneously.

1.2.5 Multiple antenna elements on both ends of the link

Future systems will include smart antennas in both the base station and the mobile station (Fig. 1.8). Exploiting multiple antennas at both ends of the link will boost the offered capacity [FG98], [MH99], [And98b], [And98a]. In [FG98] such a system in a Rayleigh fading environment is addressed when the channel characteristic is unknown at the transmitter but is known (tracked) at the receiver. When the number of antenna elements is equal at both links, the information theoretic capacity grows linearly (rather than logarithmically) with the number of antennas for fixed power and bandwidth. This clearly demonstrates the ultimate potential of spatial processing.

1.2.6 Channel models

Channel models for smart antennas have to include the directional component of the mobile radio channel. An introduction to channel models is presented in [ECS+98]. An extensive survey of the relevant literature is presented in [MFG+99]. In this work the Geometry–based Stochastic Channel Model (GSCM) [FMB98], [MKL+ed], [MKL+99], [LMB98] is used that is based on *local scatterers around the mobile*[BBJ95], [LR96] and far scatterers.

1.2.7 Testbeds and demonstrators

Implementing smart antenna technology for real–time operation is a challenge for hardware as well as for array processing. Several approaches have been studied to introduce smart

antenna technology into GSM [FKJ+94], [MPLE+97], IS–136 [WMZ98], [HÖMB97], and third generation systems [MFD+96], [TMB98]. Most of these schemes either include uplink processing only, or apply algorithmic solutions in uplink and downlink separately. In our proposal both uplink and downlink are treated in a single homogenous approach.

A smart antenna demonstrator and field trial results are presented in [AFK+97]. The demonstrator uses an MLSE receiver in uplink[BJ95] that jointly performs diversity combining, equalization, and interference rejection. The downlink is based on a simple DOA estimation from uplink data, followed by beamforming. The scheme suffers from unbalanced performance, i.e. a better uplink performance than that of the downlink. Especially the uplink scheme utilizes diversity and thus works best in urban environments, where the downlink DOA–based scheme showed the worst results.

[MTC+98] describes an SDMA demonstrator that utilizes a multichannel MLSE receiver in temporal white noise at the uplink. The downlink is again based on DOA estimation. However, they apply a special signaling scheme that allows interference–free DOA estimation. Thus the identification of DOAs is not required. The system is not compatible with an existing mobile communications standard.

[APC+98], [GBe98], [MFD+96], [MPLE+97] reports about field trials with the TSUNAMI (II) testbed. The testbed compares various algorithms: on the uplink switched beams, temporal reference algorithms and spatial reference algorithms; on the downlink, switched beams. The field trial measurements indicated that algorithms with the ability to differentiate between wanted and unwanted signals performed most successfully. High–resolution DOA estimation algorithms appeared to work well only in macrocell environments. A robust uplink algorithm combined a switched beam approach with a training–sequence–based beam selection criterion.

[JXLV98] reports about the measurement of spatial signature variation at 900MHz using a smart antenna testbed with eight antenna elements. Other measurements with testbeds are reported in [Pet96], [SWR+97].

Chapter 2

GSM1800 SMART ANTENNA DEMONSTRATOR

Within a research cooperation with the Alcatel Corporate Research Center Stuttgart, the Mobile Communiciations Group of the *Institut für Nachrichtentechnik und Hochfrequenztechnik* developed a *Real–Time Smart Antenna Processing for GSM1800 Base Stations*. The aim was to upgrade a conventional GSM1800 base station with a smart antenna demonstrator. The demonstrator hardware (RF part, baseband processing, ...) was developed by Alcatel. The smart antenna processor, named **Adaptive Antenna Array Processor** or in short **A**^{3}**P** , was developed in our group in Vienna and finally integrated in the demonstrator in Stuttgart [KTT+99b], [KTT+99a], [KTT+99c], [KTTH99], [HKTT99].

In this work we implement a smart antenna at the base station, but do not try to implement multiple antennas at the mobile station. This has a simple reason: Only this approach allows a seamless integration of smart antenna technology into existing mobile communication systems like GSM, because there is no need for exchanging the user terminals already in use.

The project was structured in the following phases:

- Literature survey and layout of array processing concept: After scanning the literature we decided to use a concept that is based on a high–resolution DOA estimator, a signal identification procedure to distinguish between user and interferer signals based on the GSM training sequence, a tracking algorithm and a final beamforming algorithm. The downlink differs from the uplink basically by a modified tracking scheme.

- Estimation of the computational demand: Based on this information, and because a flexible programming environment was sought, we selected a powerful general purpose processor — the DEC Alpha with 500MHz clock frequency — as a hardware platform.

- Algorithm development and evaluation: In this phase we developed the array processing in MATLAB including several approaches for each subtask. From the algorithm evaluation we selected the best–suited algorithms for final real-time implementation.

- Real–time implementation of the array processing code on the DEC Alpha.

- Integration of **A**^{3}**P** into the smart antenna hardware demonstrator.

- Performance measurements: The measurements included functional tests in a controlled environment and extensive field measurements.

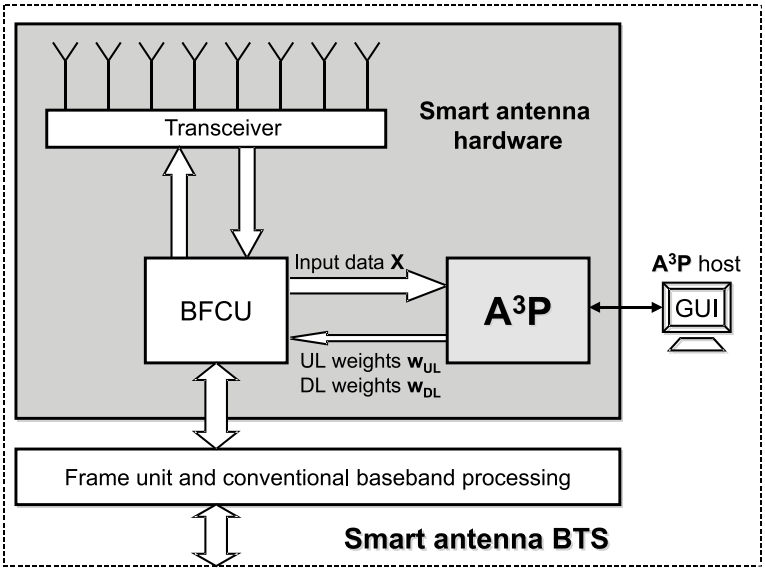

Figure 2.1. Hardware concept of the GSM1800 smart antenna BTS. The BTS consists of a conventional BTS frame unit, and smart antenna relevant hardware components, including the **A**^{3}**P** and a beamforming control unit (BFCU). A graphical user interface (GUI), on the **A**^{3}**P** host, controls the operation of the **A**^{3}**P**.

2.1 Hardware architecture

The demonstrator is based on a standard GSM1800 base station (Fig. 2.1 and Fig. 2.2). To limit the changes required in the base transceiver station (BTS) hardware, a conventional frame unit (FU) is used and only the front end hardware has to be upgraded for array processing. The smart antenna relevant hardware contains the antenna array with the transceivers, a beamforming control unit (BFCU), and an array processor.

Physical antenna array The antenna array (Fig. 2.3) is a commercial 8–element linear antenna array with half wavelength element spacing and a gain of $13.5dB$. Each single array elements consist of 6 vertically polarized stacked dipoles in front of a reflector plane. The single elements are sector antennas with a half–power beamwidth of 120°. To have similar antenna characteristics for all eight elements, the array actually consists of ten elements — one dummy antenna element at each end.

Transceiver The antenna array is connected to a diplexer that combines the transmitted and received signals. In the receiving part of the transceivers (Fig. 2.4) the filtered and amplified signals are downconverted to baseband. The Analog/Digital Converter has a resolution of 14 bits. To cover the entire dynamic range two automatic gain ranges are implemented. In the transmission part the digital signals are converted to analog signals which are then upconverted to the carrier frequency and amplified. The maximum output power of each power amplifier is $35W$. The allocated carrier frequency for measurements and field trials is in uplink (downlink) $1755.8MHz$ ($1845.8MHz$).

Embedded array processor The sampled received I– and Q–signals in uplink are collected by the beamforming control unit (BFCU). When a burst is received, the BFCU transferes the data of a single timeslot, $\mathbf{X}$, to the Adaptive Antenna Array Processor **A**^{3}**P**. The real–time processing by

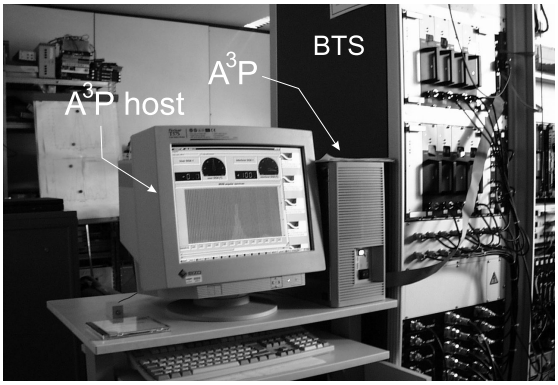

Figure 2.2. **A^{3}P**, the **A^{3}P** host and the BTS.

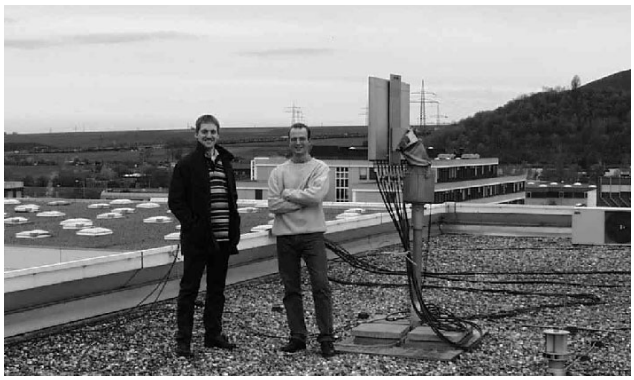

Figure 2.3. The array with feeder cables (left: Alexander Kuchar, right: Guillaume de Lattre).

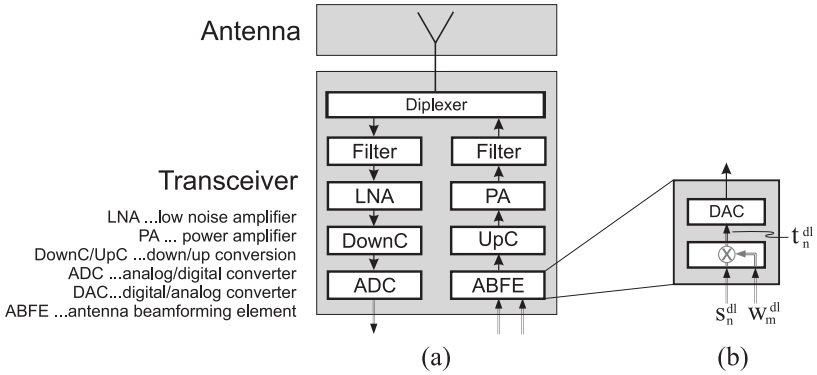

Figure 2.4. Transceiver hardware. (a) Single transceiver and antenna. (b) Antenna beamforming element.

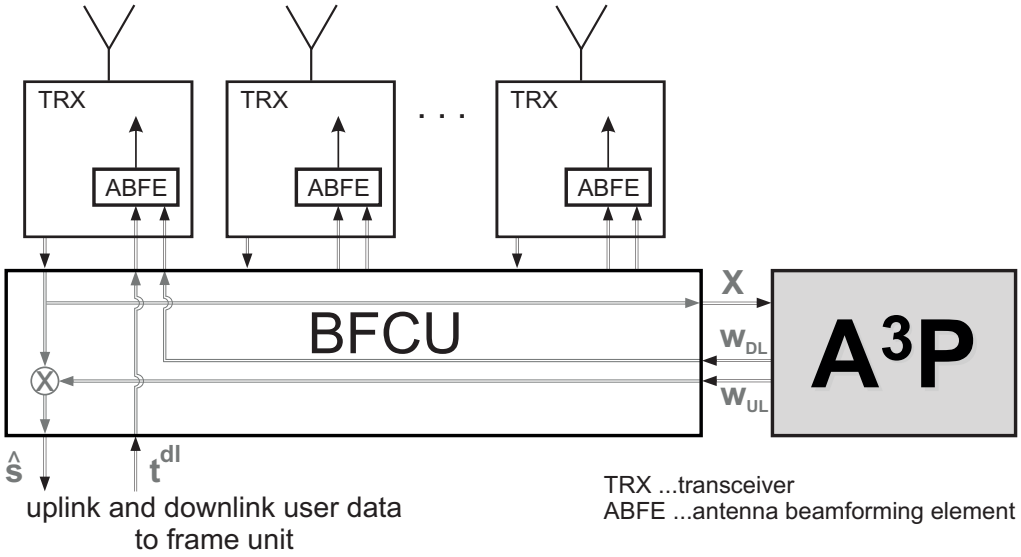

Figure 2.5. Embedded **A**^{3}**P**. The BFCU collects and distributes the uplink and downlink signals. The physical uplink beamforming (multiplication) is implemented in the BFCU. The ABFE performs the physical downlink beamforming. As example the functionality for a single element is plotted in gray.

A^3**P** results in an *uplink* beamforming weight vector, $\mathbf{w}_{ul}$, and a *downlink* beamforming weight vector, $\mathbf{w}_{dl}$. The physical *uplink* beamforming, (see Section 3.2, Eq. 3.2.6), is implemented in the BFCU (Fig. 2.5). The resulting user signal, $\hat{\mathbf{s}}$, is transferred to the baseband detector integrated in the Frame Unit (FU).

The BFCU receives the downlink baseband signal, $\mathbf{t}^{dl}$, from the FU and transfers it to the m–th row of $\mathbf{T}$ to the m–th antenna beamforming element (ABFE). The m–th ABFE performs its part of the physical beamforming (see Section 3.2, Eq. 3.2.9), and thus guarantees the excitation of the transmit array for the downlink beamforming.

In the BFCU several simpler array processing algorithms are implemented that allow real–time comparison during the measurements. In the demonstrator the data of timeslot 4 is processed by **A**^{3}**P** . It is possible to feed exactly the *same* received uplink data into timeslot 5 which is processed by the simple BFCU algorithms. Thus the same data is available in another timeslot for a fair comparison of **A**^{3}**P** with other schemes. There it is possible to use a single antenna element as a reference as well.

2.2 User interface

The operation of the **A**^{3}**P** can be fully controlled by the **A**^{3}**P** host (Fig. 2.1 and Fig. 2.2)[KTRS97b], [KTP98]. A graphical user interface (Fig. 2.6) allows detailed configuration of the smart antenna processing algorithms. The **A**^{3}**P** host also allows rudimentary data logging.

The system is also able to log raw data directly from the BFCU. We made extensive use of this feature, which resulted in many logged raw data files.

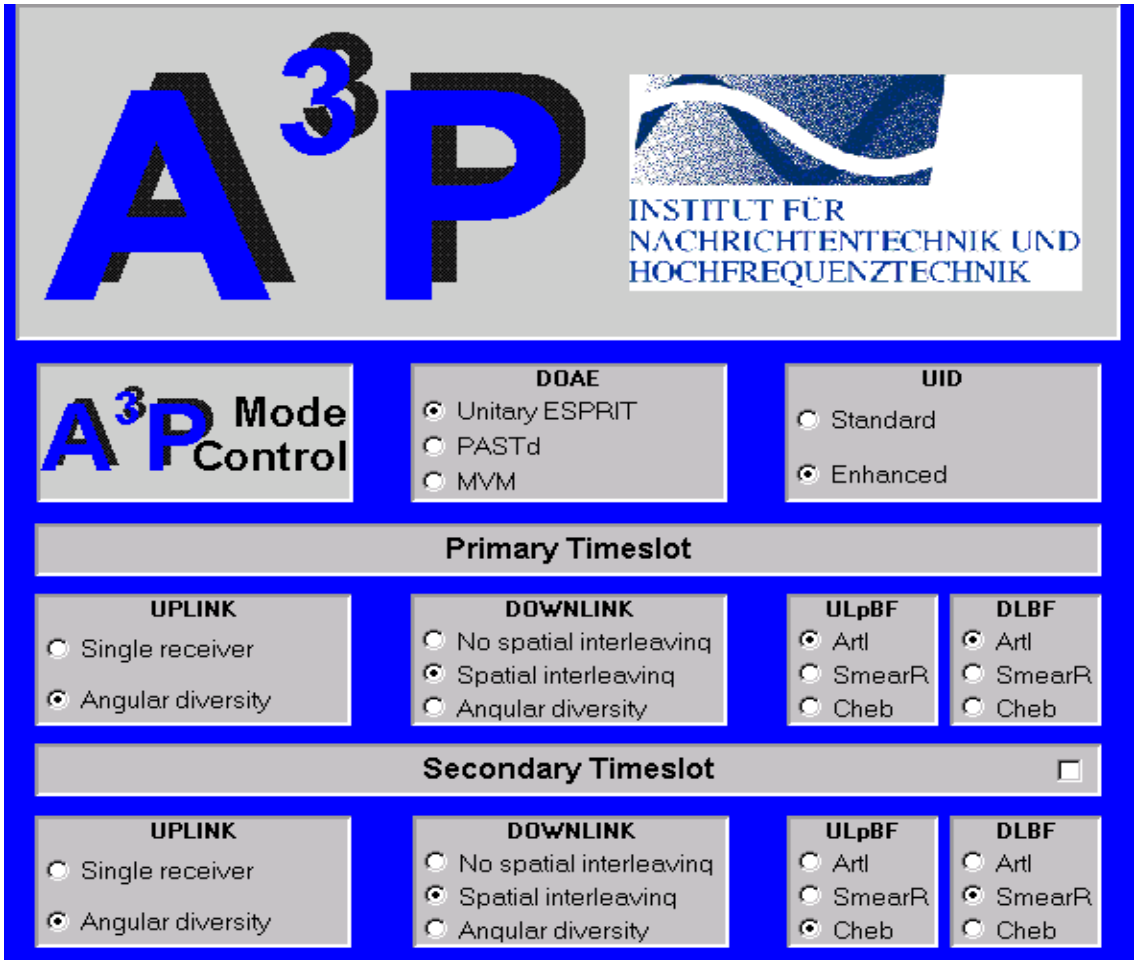

Figure 2.6. User interface of **A^{3}P** .

Chapter 3

DATA MODEL

In this chapter I will describe the signal model of the smart antenna base station, as well as the channel model. The model focuses on the uplink.

3.1 Notation

In this work, I will use the following notation:

- *Scalar* values are denoted by lower or uppercase italic letters, like $x(t)$ or C.
- *Vectors* are column vectors and denoted by bold lowercase letters, like $\mathbf{x}$.
- *Matrices* are written in uppercase bold letters, like $\mathbf{X}$.
- Matrices and vectors can be *conjugated*, like $\mathbf{X}^*$, transposed, like $\mathbf{X}^T$, or Hermitian transposed, like $\mathbf{X}^H$. The Moore–Penrose Pseudo Inverse [JD91] of the matrix $\mathbf{X}$ is $\mathbf{X}^\dagger$.
- An *estimate* of a quantity has a hat, like $\hat{\phi}$.
- $\mathbf{z} = \mathbf{x} \odot \mathbf{y}$ denotes the element–wise multiplication of the vectors $\mathbf{x}$ and $\mathbf{y}$, where $\mathbf{z}$ as well as $\mathbf{x}$ and $\mathbf{y}$ have the same dimension.
- $\Re\{x\}$ ($\Im\{x\}$) returns the real (imaginary) part of x.
- $\min\limits_x f(x)$ ($\max\limits_x f(x)$) returns the smallest (largest) $f(x)$.
- $ln\{x\}$ denotes the natural logarithm of x.

Appendix C lists all used symbols and their explanation.

3.2 Signal model of smart antenna base station

The signal model includes all quantities available in the GSM smart antenna BS. We use $M = 8$ antenna elements for array processing at the BS. The signal model focuses on the reception in the BS, i.e. the uplink. All quantities without a subscript are in uplink. Downlink quantities are denoted with the superscript $(.)^{dl}$.

Let $\mathbf{x}_{uncal}(t)$ be the received (uplink) array output data vector collected at time t

$$\mathbf{x}_{uncal}(t) = [x_1(t), x_2(t), \ldots, x_M(t)]^T. \tag{3.2.1}$$

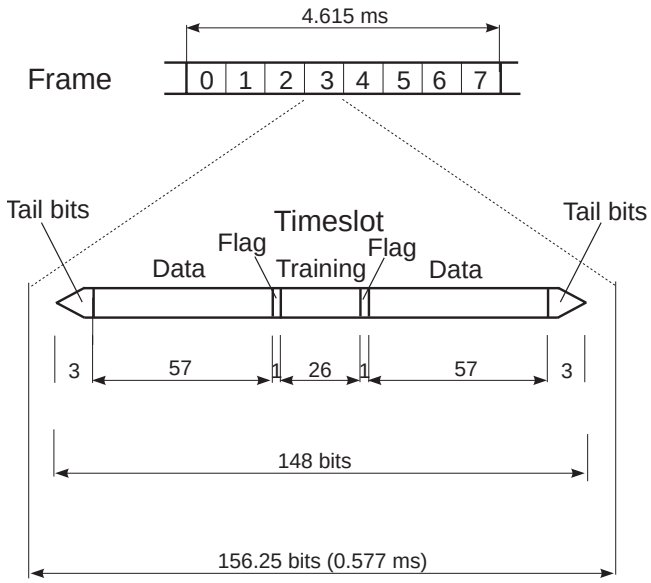

Figure 3.1. GSM burst structure [MP92]. The 26 bit midamble is surrounded by 1 flag bit, 57 data bits, and 3 tail bits on each side.

$\mathbf{x}_{uncal}(t) \in \mathbb{C}^{M\times 1}$ contains the *un*calibrated downconverted complex RF signals at each of the M antenna elements at time t. The signals are sampled at the GSM symbol rate $T = 3.7\mu s$

$$\mathbf{x}_{uncal}(n) = \mathbf{x}_{uncal}(nT) = \mathbf{x}_{uncal}(t)\mid_{t=nT} . \tag{3.2.2}$$

The BFCU (see Fig. 2.5) collects the continuous incoming data samples and calibrates the input data with a calibration vector $\mathbf{c}$

$$\mathbf{x}(n) = \mathbf{x}_{uncal}(n) \odot \mathbf{c} . \tag{3.2.3}$$

In practice, $\mathbf{c}$ was kept constant over a series of measurements (typicaly a day), but $\mathbf{c}$ may change as fast as from burst to burst (at least it has to be constant over a single burst). It accounts for the phase and amplitude imbalances of the eight receivers and is measured by the BS on a regular basis. In a TDMA system the signals are processed burst–by-burst. A burst in GSM is typically an entire frame. Because the array processor is applied only to a single timeslot, we understand as a burst the data of a single timeslot of a GSM frame. In this sense burst–by–burst processing is equivalent to frame–by–frame processing. The BFCU transfers the calibrated data corresponding to one timeslot[1]

$$\mathbf{X}(n) = [\mathbf{x}(n+1)\, \mathbf{x}(n+2), \ldots, \mathbf{x}(n+N)] \in \mathbb{C}^{M\times N}, \tag{3.2.4}$$

where $N = 156$ (Fig. 3.1) to the $\mathbf{A}^3\mathbf{P}$. For convenience I will sometimes drop the time index n in my notation henceforth.

[1] In our system always the 4th timeslot is used for adaptive array processing.

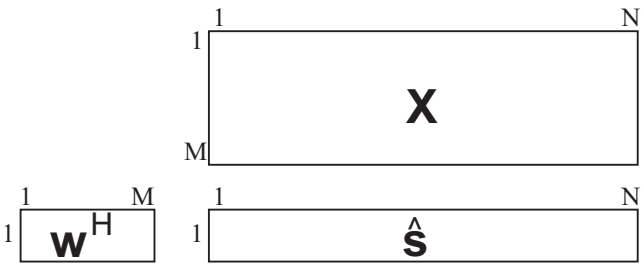

Figure 3.2. Structure of vectors and matrices $\mathbf{w}$, $\hat{\mathbf{s}}$, and $\mathbf{X}$.

Note that since I apply SFIR, the smart antenna processing will finally lead to a *single* user signal, i.e. the number of users to be served is $K = 1$. However, interfering signals are present from other co–channel users, typically located in neighboring cells.

A^3**P**'s burst–wise processing results in an uplink weight vector for the user,

$$\mathbf{w} = [w_1\ w_2, \ldots, w_M]^T, \tag{3.2.5}$$

where w_m is the complex weight applied to the m–the antenna element. The uplink beamforming results in an estimate for the baseband user signal $\hat{\mathbf{s}}$.

To this end, the weight vector is transferred to the BFCU, where the physical uplink beamforming

$$\hat{\mathbf{s}} = \mathbf{w}^H \mathbf{X} \tag{3.2.6}$$

is carried out (Fig. 3.2). $\hat{\mathbf{s}}$ contains an estimate of the transmitted baseband signal sequence. We apply a *constant* weight matrix for the entire burst, assuming that the channel is stationary within the timeslot duration of $0.577ms$.

From $\hat{\mathbf{s}}$ the frame unit (FU) recovers the sent user bit sequence with an equalizer and detector. The vectors and matrices have the dimensions $\mathbf{w} \in \mathbb{C}^{M\times 1}$, $\hat{\mathbf{s}} \in \mathbb{C}^{1\times N}$, and $\mathbf{X} \in \mathbb{C}^{M\times N}$.

A^3**P**'s processing results in up to two weight vectors for the uplink beamforming. If two weight vectors are calculated, also two data sequences, $\hat{\mathbf{s}_1}$ and $\hat{\mathbf{s}_2}$, are available. A diversity receiver will exploit the additional information to detect the user data sequence with reduced BER. $\hat{\mathbf{s}}_1$ and $\hat{\mathbf{s}}_1$ are fed to a combining diversity receiver available in the FU. The weight vectors, $\mathbf{w}_1$ and $\mathbf{w}_2$, define two spatial filters that allow to collect the signal energy from two propagation paths with different DOAs and, in general, different times–of–arrival (TOA). In contrast to the wideband array (Fig. 1.4 on p. 6), where the diversity is sought from beginning in *delay* domain, the spatial filters allow exploitation of the *angle* domain diversity.

A^3**P** does not only compute the *uplink* weight matrix, $\mathbf{W}$, but also a single *downlink* weight vector

$$\mathbf{w}^{dl} = [w_1^{dl}\ w_2^{dl}, \ldots, w_M^{dl}]^T. \tag{3.2.7}$$

In general, **A**^{3}**P** is able to calculate, similarly to the uplink, more weight vectors for the downlink. The transmission hardware in the base station, specifically the antenna beamforming elements (ABFEs), can use up to four weight vectors, which allows the implementation of

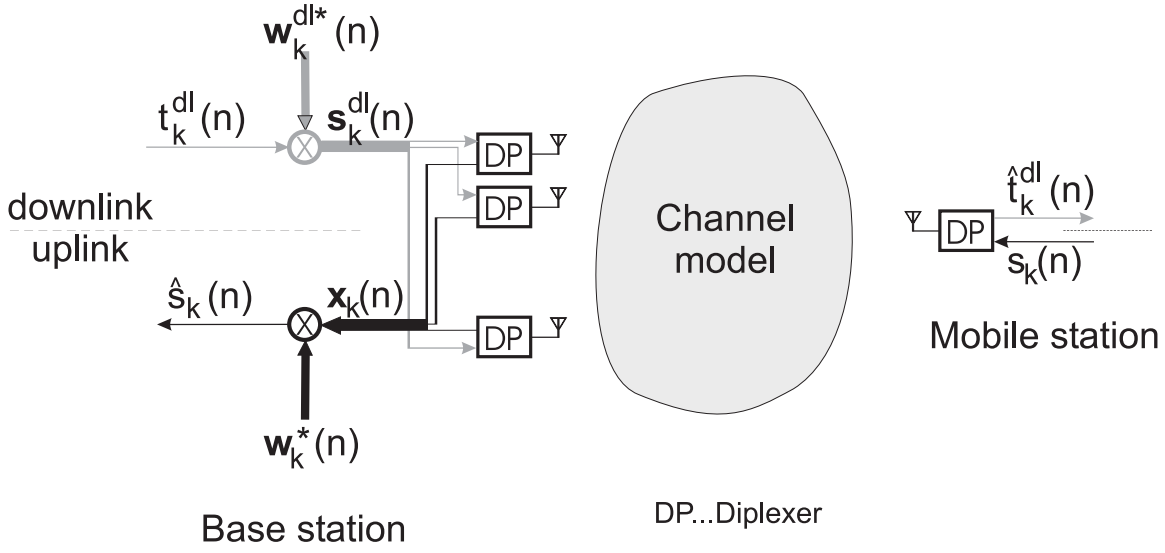

Figure 3.3. Signal model of smart antenna system. The model for the uplink and downlink includes both, BS and MS.

transmit (angle and/or delay) diversity schemes. Here, I do not apply transmit diversity, because I focus on the uplink. The m–th complex downlink weight w_m^{dl}, $1 \leq m \leq M$, is transferred to the m–th ABFE. There the user specific downlink baseband signal, $\mathbf{t}^{dl}$, is weighted

$$\mathbf{s}_m^{dl,m} = w_m^{dl,m}\mathbf{t}^{dl}, 1 \leq m \leq M. \tag{3.2.8}$$

Taking all M ABFEs into account the transmitted data matrix, $\mathbf{S}^{dl}$, is defined by

$$\mathbf{S}^{dl} = [\mathbf{s}_1^{dl}\ \mathbf{s}_2^{dl}, \ldots, \mathbf{s}_M^{dl}]^T = \mathbf{w}^{dl}\mathbf{t}^{dl^T}, \tag{3.2.9}$$

where $\mathbf{S}^{dl} \in \mathbb{C}^{M\times N}$, $\mathbf{w}_{dl} \in \mathbb{C}^{M\times 1}$, $\mathbf{t}^{dl} \in \mathbb{C}^{N\times 1}$, and $\mathbf{s}^{dl} \in \mathbb{C}^{N\times 1}$. The n–th column of $\mathbf{S}^{dl}$ holds the transmitted complex baseband vector at time instant n. Figure 3.3 summarizes the signal model.

3.3 Channel modeling

Up to now I have modeled the signals within the base station. For the development of the signal processing and for the evaluation of the **A**^{3}**P** I need a full signal model including the entire communication link: the transmitter, the channel and the receiver. The channel model focuses on the uplink. It is an equivalent baseband model, i.e. I do not consider upconversion and downconversion.

I assume a narrowband system, in the sense that the maximum propagation time of a wave over the array, τ_{array}, is much smaller than the inverse of the system bandwidth, B:

$$\tau_{array} = \frac{(M-1)}{f_c}\frac{\Delta}{\lambda} << \frac{1}{B} \tag{3.3.1}$$

or

$$\frac{B}{f_c} << (M-1)\frac{\Delta}{\lambda} \tag{3.3.2}$$

This condition assures a negligible baseband (information) phase difference between the first and the last antenna element, when an incident wave travels along the array (worst case: wave incident from endfire direction). Thus a GSM1800 system with a bandwidth of $B = 200kHz$, a carrier frequency of $f_c = 1800MHz$, and an eight element uniform linear array with an element spacing, Δ, of about half a wavelength is a narrowband system:

$$\frac{0.2}{1800} << \frac{7}{2} \tag{3.3.3}$$

I assume that all mobile stations have a single antenna. The transmitter is not described in detail, because we apply modulator and data format according to the GSM standard.

To model the communication between the signal sources and the receiver I apply the Geometry–based Stochastic Channel Model (GSCM) [FMB98], [LMB98], [MLKS98], [MKL$^+$ed]. In this semi–stochastic approach the statistical distribution of *scatterers* is prescribed, but not their exact location, as in a deterministic approach. For the actual simulation a specific realization of scatterers is selected at random from this distribution, and the angularly resolved impulse response is extracted by simple ray tracing. Of course, the scatterer distributions have to be chosen in such a way that the resulting power delay profiles, angular power spectra, etc. agree reasonably well with typical measurement results [LMB98], [MKL$^+$99].

Compared to the purely stochastic approach, where the average power delay profile (PDP), angular power spectrum (APS), etc. and their statistical distributions are specified, the GSCM has several advantages: (i) The model reflects physical propagation mechanisms, which allows simple determination of the scatterer distribution from geometrical considerations. (ii) All necessary information is inherent in the distribution of the scatterers. Therefore, possible correlations between PDP and APS do not lead to a complication of the model. (iii) The movement of a mobile station can be included in a straightforward way. Furthermore shadowing can be easily implemented. Compared to a purely deterministic channel model, where a complete geometrical specification is required, the GSCM requires only specification of the scatterer distribution. [MKL$^+$99]

GSCM is based on local and far scatterers (Fig. 3.4). The mobile is surrounded by local scatterers. Additionally a far scattering area may be present. These far scatterers are far away from both the mobile and the base station, typically fixed at an absolute position in space to model high–rise buildings, mountains, etc. The received signal at the BS is a superposition of many rays incident via reflections from those scattering sources. The distribution of these scatterers determines channel parameters as angular spread (AS), non–ideal correlation of individual antenna signals as a result of the finite AS, power delay profiles, and delay spread. The scatterer distribution can be set to match realistic propagation environments [LMB98]. A thorough discussion on the latest developements of the GSCM are presented in [MKL$^+$99].

The complex baseband signal originated from the signal source k and received by the m–th antenna element is

$$x_{k,m}(n) = \sum_{l=1}^{L_k} \rho_{k,l,m} e^{-j[2\pi nTf_{d,l,k} + 2\pi(f_c + f_{d,l,k})\tau_{k,l,m}]} s_k(n - n_{\tau_{k,l,m}}), \text{ with} \tag{3.3.4}$$

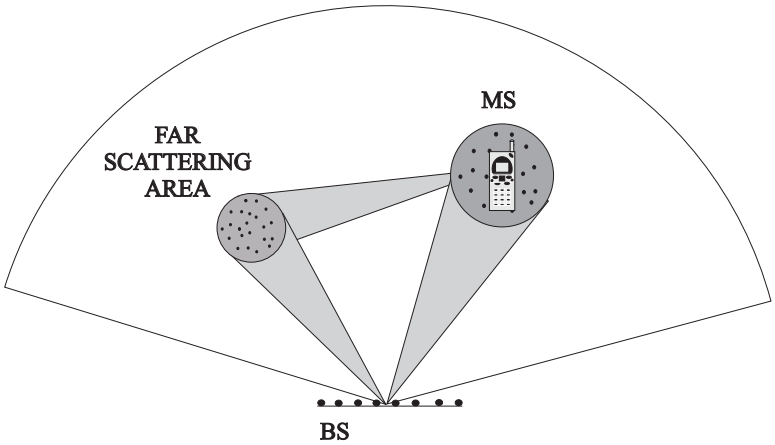

Figure 3.4. Basic concept of the Geometry–based Stochastic Channel Model. BS ... base station, MS ... mobile station.

$$n_{\tau_{k,l,m}} = [\frac{\tau_{k,l,m}}{T}], \tag{3.3.5}$$

where L_k is the number of scatterers for the k–th user, and $\rho_{k,l,m}$ is the complex path coefficient of the l–th scatterer to the m–th antenna, including the complex scattering coefficient and the path loss. [.] rounds the real–valued number to the nearest integer value[2]. The signal $s_k(n - n_{\tau_{k,l,m}})$ is a time–shifted version of the transmitted baseband signal $s_k(n)$ of the k–th user. The Doppler shift $f_{d,l,k}$ of the wave originated from the k–th mobile and reflected at the l–th scatterer is

$$f_{d,l,k} = \frac{v_k \cos \phi_{v,l,k}}{c} f_c, \tag{3.3.6}$$

where v_k is the mobile's velocity and $\phi_{v,l,k}$ the direction of the velocity relative to the propagation direction. The delay $\tau_{k,l,m}$ and $\phi_{v,l,k}$ of each wave results from simple ray tracing (for details see [FMB98]).

The general model of Eq. (3.3.4) can be simplified to the well known array processing model

$$\begin{aligned} \mathbf{x}_k(n) &= [x_{k,1}(n), x_{k,2}(n), \ldots, x_{k,M}(n)]^T \\ &= \sum_{l=1}^{L_k} \mathbf{a}_{k,l} \rho_{k,l} s_{k,l}(n) \\ &= \boldsymbol{A}_k \tilde{\mathbf{s}}_k(n), \end{aligned} \tag{3.3.7}$$

where

$$\tilde{\mathbf{s}}_k = [\rho_{k,1} s_{k,1}, \rho_{k,2} s_{k,2}, \ldots, \rho_{k,L} s_{k,L},]^T. \tag{3.3.8}$$

This model relies on two approximations: First, $s_{k,l}(n) \equiv s_k(n - n_{\tau_{k,l,m}})$ or $n_{\tau_{k,l,m}} \equiv n_{\tau_{k,l}}$, $m = 1 \ldots M$, i.e. the delay of the l–th wave is constant for all antenna elements. Second, $\rho_{k,l,m} \equiv \rho_{k,l}$, $m = 1 \ldots M$, i.e. the path loss between the l–th scatterer and the m–th antenna is the same. Both approximations will be valid if the scatterers are, compared to the array aperture, far away from the BS. Note that in the simulations we use the exact formulation.

$\mathbf{a}_{k,l}$ is the so–called *steering vector* corresponding to the l–th wave of the k–th user, $\mathbf{A}_k = [\mathbf{a}_{k,1}, \ldots, \mathbf{a}_{k,L}]$ is the *array steering matrix* of user k. In case of a uniform linear array with element spacing Δ, the steering vector is

$$\mathbf{a}_{k,l} = f(\phi_{k,l})[1\ e^{-jk\Delta cos\phi_{k,l}}, \ldots, e^{-(M-1)jk\Delta cos\phi_{k,l}}]^T, \tag{3.3.9}$$

where k is the wave number, $f(\phi_{k,l})$ the element pattern of the identical elements, and $\phi_{k,l}$ is the azimuth of the l–th wave of user k. Equation (3.3.7) and Eq. (3.3.9) require the antenna elements to be uncoupled and identically directed.

The communication environment includes a single wanted user, and K_I interferer. All transmitted signals are GMSK modulated sequences. Thus our uplink model includes $K =$

[2]In the implementation of the GSCM we do not have $s_k(t)$ available for arbitrary t, but only a sampled version $s_k(n - n_{\tau_{k,l,m}})$. This introduces an error, because we have to round the delay. To reduce the error, we apply eight times oversampling to the channel.

$1 + K_I$ signal sources, i.e. the user signal and K_I interferer. Finally we sum up all K signal components and add noise

$$\mathbf{x}(n) = \sum_{k=1}^{K} \mathbf{x}_k(n) + \mathbf{n}(n), \tag{3.3.10}$$

where $\mathbf{n}(n)$ is additive white Gaussian noise.

I collect N snapshots of the user–specific array output vector at times $t = nT, 1 \leq n \leq N$ and get the data of a GSM burst for the k–th user

$$\mathbf{X}_k(n) = [\mathbf{x}_k(n+1)\, \mathbf{x}_k(n+2), \ldots, \mathbf{x}_k(n+N)] \in \mathbb{C}^{M \times N}. \tag{3.3.11}$$

In an SFIR system only a single user is connected to the BS under consideration. All interferers are assumed to communicate in neighboring co–channel cells therefore I assume intercell interference only. In contrast, if I model in an SDMA system only the intracell interferers, they will dominate the interference. The only difference between the two systems, except of course the interference level, is that in an SFIR system interference is in general asynchronous, if the base stations are not synchronized[3]. This leads to an additional arbitrary shift of delays for the interferers in Eq. (3.3.4).

[3]To the best of my knowledge, base stations are not synchronized in a GSM system.

Chapter 4

ADAPTIVE ANTENNA ARRAY PROCESSOR A^{3}P

In this chapter I present the signal processing of the developed array processor. **A^{3}P**'s processing is structured in several subtasks, which I discuss individually and in detail. Here, I will not only describe each individual subtask, but also, when possible, its individual performance. In general, I will focus on properties of the algorithms that affect the entire system. Some parts of the processing are designed to cope with insufficiencies of other algorithms. I will explain how these parts, as soon as put together, result in a robust array processing.

When it makes sense, the assessment will rely on measurement data. This allows to judge the algorithms behavior in a *real* system, with data from *real* channels, and not only on a theoretical basis. Whenever possible, I will compare the simulated performance with measured performance. Sometimes the evaluation is not possible with measured data, then I will rely on computer simulations.

From the investigation of the individual algorithms arises a list of questions that follow the same line: What is the influence of an algorithm's key feature on the overall system performance? Answers to those question will be presented in Chapter 5.

I will start with a summary of the goals set at the beginning of the project and how **A^{3}P** is designed to reach them. Before presenting the details of the various algorithms, I will present an overview of **A^{3}P**'s smart antenna processing concept.

4.1 Array processing scheme

The goal in this work was to design a smart antenna processor for a GSM system. It was decided to adopt a spatial reference approach under the following constraints:

- Base the processing on the *estimation of DOAs in uplink*: This allows to use similar algorithms for uplink and for downlink to get *balanced links*.
- Implement a *space–only* filter: The existing standard baseband processing unit is utilized for temporal equalization. This shall minimize the necessary change in hard– and software in the base station, when upgraded with a smart antenna.
- Suppress co–channel interference, i.e. apply *SFIR*. Still always keep in mind that the scheme can, in principle, be upgraded to an SDMA scheme.
- Develop a processing scheme that works *within the GSM standard*. Address the combination of smart antennas and frequency hopping.
- For identification of the user signal, exploit the 26 bit long GSM *training sequence*.

- Implement the array processing on a *single* processor.
- For *real–time* application the developed smart antenna algorithms have to be run–time optimized. A weight adaptation *every* GSM frame (frame duration is $4.6ms$) for a single timeslot is envisaged.

I put the focus on the optimization of the DOA–based approach to mobile radio environments. Thus **A**^{3}**P** includes:

- A *tracking* scheme that can cope with far–off DOA estimates and with severe interference.
- *Broad nulls* in the beamforming to increase the robustness against interfering signals that are incident with large angular spread.
- *Angular diversity* to increase robustness against small–scale fading. Although a scheme based on beam steering works best in situations with small angular spread, e.g. macro-cells, we make use of the diversity offered by environments with many multipath components present.

The approach taken with **A**^{3}**P** differs from [AFK+97], because **A**^{3}**P** will give more balanced links. Particularly, this will result in similar performance on both links in a certain class of environments, e.g. urban or rural environment. In contrast to [MTC+98], [AMVW91], I relax the assumption of knowing the user DOAs *a priori* and instead integrate a user identification. Only this allows utilizing the scheme in a real system.

In this work I use an approach similar to the one in [AMVW91], although with a main difference: I apply different algorithms for both the DOA estimation and the beamforming, which also includes a DOA tracking scheme. The tracking scheme is essential to increase the link robustness in typical radio channels, as I will show in Chapter 5.

Today's challenge is to bridge the gap that still exists between the chances theory offers and real world applications. Multipath caused by building or hill reflections introduce problems for conventional adaptive array processing concentrating on the strongest path only [TBHH97]. In **A**^{3}**P** additional nominal DOAs, if present, are exploited to increase the diversity gain, thus improving the performance compared to channels with a single nominal DOA. I employ *angular* diversity. Instead of seeking diversity in time or frequency domain, the angle domain is exploited here.

4.2 **A**^{3}**P**'s concept

GSM is a TDMA system and therefore the data is processed burst–wise. **A**^{3}**P** receives data in the uplink corresponding to a single GSM timeslot, or $N = 156$ so–called temporal snapshots, each consisting of $M = 8$ complex values (Eq. (3.2.4), p.22). For each of these data bursts, $\mathbf{X}(n)$, **A**^{3}**P** calculates at least a single beamforming weight vector for each link, uplink and downlink. Thus, **A**^{3}**P** optimizes reception and transmission by adapting the antenna pattern to the instantaneous channel situation.

A^3**P**'s processing is structured in four main sections (Fig. 4.1):

- DOA estimation
  From the received input data in uplink a DOA estimation (**DOAE**) estimates the number of incoming wavefronts and their DOAs.

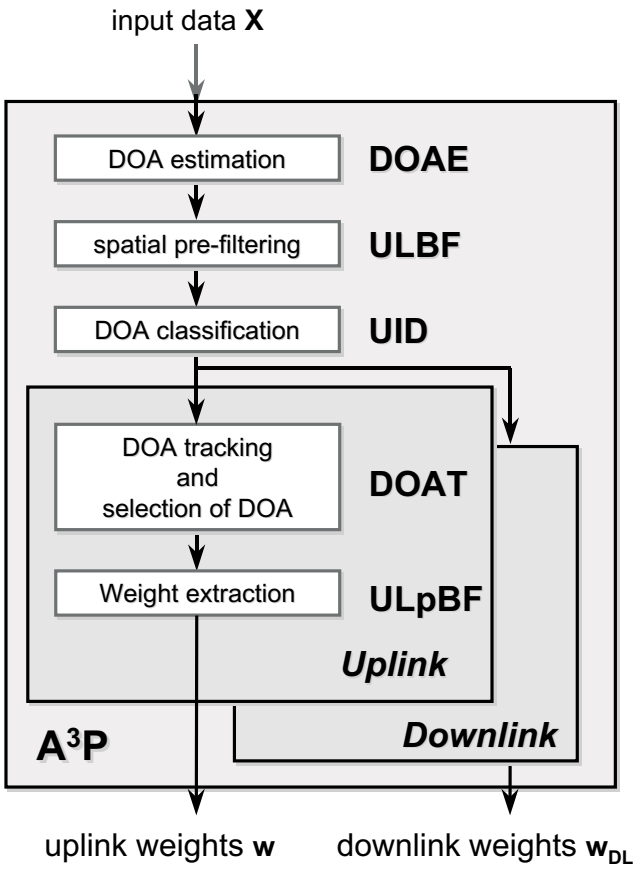

Figure 4.1. Adaptive Antenna Array Processor **A**^{3}**P**. **DOAE** ... DOA estimation, **ULBF** ... uplink beamformer, **UID** ... user identification, **DOAT** ... DOA tracking, **ULpBF** ... uplink post beamformer, **DLBF** ... downlink beamformer.

- DOA classification
  In a next step I identify those wavefronts that originate from the user: First, **A³P** extracts, from the input data with a spatial pre–filter, the spatially resolved wavefronts, each incident from an estimated DOA. I will call the spatial pre–filter the uplink beamformer (**ULBF**). A user identification (**UID**) classifies the DOAs, i.e. it decides whether a wavefront (DOA) belongs to a user or to an interferer.

- Tracking and DOA selection
  The user DOAs are tracked to increase the reliability of the DOA estimates. From the tracked DOAs, I select the ones that will maximize the signal quality. The DOA tracking (**DOAT**) increases the system robustness.

- Signal reconstruction — beamforming
  Finally a beamforming algorithm, the uplink post beamformer (**ULpBF**), forms an antenna pattern with a main beam steered into the direction of the user, while simultaneously minimizing the influence of the interfering wavefronts.

In downlink, we need a weight vector that defines the excitation of the transmit antennas. The downlink weight calculation differs from the uplink processing only in the fact that I apply separate tracking and downlink beamforming (**DLBF**) algorithms.

In the following I will discuss each of the subtasks (**DOAE**, **ULBF**, **UID**, **DOAT**, **ULpBF**, and **DLBF**) in detail.

4.3 DOA estimation

Estimating the DOAs is a well known problem in signal processing [KV96]. There are various approaches to estimate the DOAs of the wavefronts incident at an array. High–resolution estimators provide a resolution that exceeds the traditional resolution limit of $2\pi/M$. The Rayleigh criterion states that two incoherent plane waves incident from two slightly different directions can only be resolved with a uniform linear array of M identical sensors, if the difference of their spatial frequencies is at least $2\pi/M$ ([Haa91], p.3) or in case of $M = 8$ about $15°$. Here, I apply several high–resolution parameter estimation techniques.

In [KV96] parameter estimation techniques are classified into two main categories, namely *parametric* and *spectral–based* approaches. The parametric approach, also called model–based approach, fully exploits the assumed signal model, e.g. typically that a limited number of uncorrelated plane waves is incident. Of course those methods perform well when the assumptions are fulfilled, and have problems otherwise. In the latter approach an angular spectrum is calculated and the DOAs are estimated by a subsequent one–dimensional peak search.

We selected two different high–resolution algorithms. The first approach has two variants:

- Unitary ESPRIT
  - with subspace *estimation*
  - with subspace *tracking*

- Minimum Variance Method or Capon's beamformer

4.3.1 Unitary ESPRIT with subspace *estimation*

Unitary ESPRIT [HN95] is a signal subspace–based algorithm and belongs to the family of parametric estimators. In the first variant, the subspace is *estimated* by an eigenvalue decomposition, while in the second variant the subspace is *tracked* by an subspace tracking algorithm. Unitary ESPRIT is an improved variation of ESPRIT. Before I will discuss Unitary ESPRIT in detail, I will mention the main characteristic of ESPRIT.

The ESPRIT (Estimation of Signal Parameters via Rotational Invariance Techniques) algorithm was developed by Roy, Paulraj, and Kailath [RPK86]. The algorithm relies on several assumptions:

- Narrowband data model: In Chapter 1 I discussed, in context of array processing, the definition of a narrowband system. ESPRIT assumes that the baseband signals' amplitudes and phases vary slowly with respect to the propagation time across the array. Thus the signals at each sensor are the same, in principle, and differ only by a DOA–dependent phase shift.

- Far–field data model: I assume that the array is in the far–field of the signal sources, which results in plane waves incident at the array.

- Array geometry: All ESPRIT–type algorithms rely on the so–called *shift invariance property* of the array steering vector $\mathbf{a}$. This translates in terms of array geometry to an array composed of two identical, but displaced, subarrays (Fig. 4.2(a)) with negligible mutual coupling.

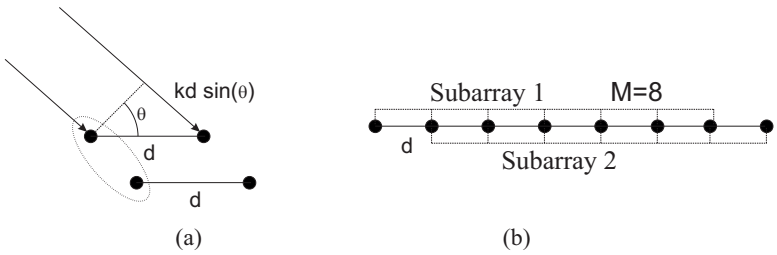

Figure 4.2. Planar array composed of two pairwise identical, but displaced sensors (doublets) required for ESPRIT–type algorithm. (b) Subarray configuration for a centro–symmetric line array (uniform linear array) of $M = 8$ identical sensors.

Since I assume two identical, but spatially displaced subarrays, the steering vector of the second subarray is just a scaled version of the corresponding steering vector of the first subarray. This property is exploited to setup the *Invariance Equation* (see Eq. (4.3.5) on p. 35) that allows to estimate the DOAs of multiple incident waves.

Unitary ESPRIT exploits the centro–symmetry of a uniform linear array (Fig. 4.2). This allows transforming the complex input data matrix into a real–valued data matrix. As a consequence the algorithm is computationally less demanding, and the estimation accuracy is increased [Haa91].

The transformation that results in real–valued data is equivalent to forward–backward averaging [Haa91]. By this averaging two coherent waves will be decorrelated, and Unitary ESPRIT is then fit to estimate the DOAs correctly, if not more than two DOAs are correlated.

Unitary ESPRIT	Unitary ESPRIT with subspace tracking
Subspace estimation (EVD)	Subspace tracking (PASTd)
Solution of the Invariance Equation	
Spatial frequency estimation	

Table 4.1. Summary of the subspace–based DOA estimators. (EVD ... eigenvalue decomposition, PASTd ... Projection Approximation Subspace Tracking and Deflation
)

1. **Transform the complex input data matrix into real–valued covariance matrix:**
   Compute the forward-backward averaged covariance matrix

$$\mathbf{R}_{FB} = \mathcal{T}(\mathbf{X})\mathcal{T}(\mathbf{X})^H \in \mathbb{C}^{M\times M}. \tag{4.3.1}$$

   as defined in Appendix A.

2. **Signal Subspace Estimation:**

   - Compute the eigenvectors, $\mathbf{U}$, and eigenvalues, Λ, by means of an eigenvalue Decomposition of $\mathbf{R}_{FB}$:

$$\mathbf{R}_{FB} = \mathbf{U}\,\Lambda\,\mathbf{U}^H \tag{4.3.2}$$

     The diagonal matrix $\Lambda \in \mathbb{R}^{M\times M}$ holds the eigenvalues, λ_m, in its diagonal.
   - Estimate from the M eigenvalues, λ_m, the model order $\hat{L}$ (Sect. 4.3.3).
   - The $\hat{L}$ eigenvectors corresponding to the $\hat{L}$ dominant eigenvalues present an estimate,

$$\hat{\mathbf{U}}_s \in \mathbb{C}^{M\times\hat{L}}, \tag{4.3.3}$$

     of the basis of the signal subspace.

3. **Solution of the Invariance Equation:**

   - Build up a basis of the signal subspace for each of the two subarrays. $\mathbf{A}^3\mathbf{P}$ applies the subarray configuration as defined in Fig. 4.2(b).

$$\underbrace{\mathbf{U}_i}_{\mathbb{C}^{M-1\times L}} = \mathbf{K}_i\hat{\mathbf{U}}_s, \text{where } i = 1, 2, \tag{4.3.4}$$

     where $\mathbf{K}_i$ are sparse selection matrices defined in Eq. (4.3) in ([Haa91], p. 38).
   - Solve the Invariance Equation, $\mathbf{U}_2 \approx \mathbf{U}_1\Psi$, by means of least squares:

$$\Psi = (\mathbf{U}_1^H\,\mathbf{U}_1)^{-1}\,\mathbf{U}_1^H\,\mathbf{U}_2 \in \mathbb{C}^{\hat{L}\times\hat{L}} \tag{4.3.5}$$

4. **DOA extraction:**
   Calculate the eigenvalues ψ_l of the resulting complex matrix Ψ, where the $\hat{L}$ DOAs are resulting in

$$\phi_l = -\arcsin\left(\frac{2\,\text{atan}\,\Re(\psi_l)}{2\pi\frac{\Delta}{\lambda}}\right), \quad l = 1, \ldots, \hat{L}. \tag{4.3.6}$$

Table 4.2. Summary of Unitary ESPRIT.

Unitary ESPRIT estimates the signal subspace by means of an eigenvalue decomposition. From this estimated signal subspace the DOAs are calculated by solving the Invariance Equation and a subsequent spatial frequency estimation (Tab. 4.1). In the following I will refer to this algorithm as **Unitary ESPRIT**, which is summarized in detail in Tab. 4.2.

4.3.2 Unitary ESPRIT with subspace *tracking*

Instead of *estimating* the signal subspace, the subspace tracker PASTd (Projection Approximation Subspace Tracking and Deflation) [Yan95b], [Yan95a] recursively *tracks* the signal subspace. A detailed presentation of the update procedure of the eigenvalues and eigenvectors is presented in [Yan95b].

Reducing the computational complexity was the main motivation to apply this algorithm. In quasi–stationary channels the signal subspace is only slowly time–varying. It is therefore more efficient to track those changes than to perform a full subspace estimation every burst [Haa91]. To be more precise: It is the projection matrix of the signal subspace that changes only slowly, while the basis of the signal subspace, $\hat{\mathbf{U}}_s$, changes rapidly, i.e. from one burst to the next. The basis of the signal subspace is the output of the signal subspace estimation. From $\hat{\mathbf{U}}_s$ the DOAs are estimated. Actually Unitary ESPRIT does not require the signal eigenvectors, but any orthonormal basis of the signal subspace is sufficient[1]. To estimate the signal subspace, $\hat{\mathbf{U}}_s'$, Yang applies a novel interpretation of the signal subspace, where the basis of the signal subspace is a solution of the following unconstrained minimization problem [Yan95b]

$$\hat{\mathbf{U}}_s' = \arg\min_{\mathbf{Z}}\{J(\mathbf{Z}) = E\,||\mathbf{x} - \mathbf{Z}\mathbf{Z}^H\mathbf{x}||^2\}. \tag{4.3.7}$$

It turns out that the scalar function $J(\mathbf{Z})$ allows a new interpretarion of the signal subspace. For us the most important property of $J(\mathbf{Z})$ is that it possesses a global minimum at which the column span of $\mathbf{Z}$ equals the signal subspace [Yan95b]. Instead of minimizing the cost function $J(\mathbf{Z})$, PASTd applies a modified cost function. First the expectation in Eq. (4.3.7) is replaced with an exponentially weighted sum

$$J(\mathbf{Z}(n)) = \sum_{i=1}^{n} \beta^{n-i}||\mathbf{x}(i) - \mathbf{Z}(n)\mathbf{y}(i)||^2, \tag{4.3.8}$$

and second, the approximation

$$\mathbf{y}(i) = \mathbf{Z}(i-1)^H\mathbf{x}(i) \tag{4.3.9}$$

is applied. β is a "decaying factor" that determines the convergence rate. The effective window length for $\beta < 1$ is $1/(1-\beta)$ when $n \gg 1$. Furthermore a sequential estimation of the principal components is applied, hence the "d" in "PASTd" for deflation technique.

The PASTd algorithm is schematically summarized in Tab.4.3. This signal subspace tracker replaces Step 2 (**Signal subspace estimation**) in Tab.4.2 of the Unitary ESPRIT algorithm. I will call the resulting DOA estimator **PASTd** as compared to the previously described **Unitary**

[1] Any matrix $\hat{\mathbf{U}}_s'$ that is related to the signal eigenvectors, $\hat{\mathbf{U}}_s$, by a unitary transformation $\hat{\mathbf{U}}_s' = \mathbf{Q}\hat{\mathbf{U}}_s$, where $\mathbf{Q} \in \mathbb{C}^{\hat{L}\times\hat{L}}$ is a unitary matrix, forms an orthonormal basis of the signal subspace.

1. **Initialize the tracked values:**
   Initialize the M eigenvalues, $\lambda_m(0)$, $0 < m \leq M$, and the eigenvectors, $\hat{\mathbf{U}}_s'(0)$.

2. **Track for each snapshot, $\mathbf{x}(n)$, $n = 0, \ldots, N_{PASTd}$:**
   - Update the eigenvalues, $\lambda_m(n)$, and eigenvectors, $\hat{\mathbf{U}}_s'(n)$ by applying PASTd [Yan95b].
   - From the eigenvalues, estimate the number of DOAs, $\hat{L}(n)$ (Sect. 4.3.3).

Table 4.3. Summary of the signal subspace tracking algorithm PASTd.

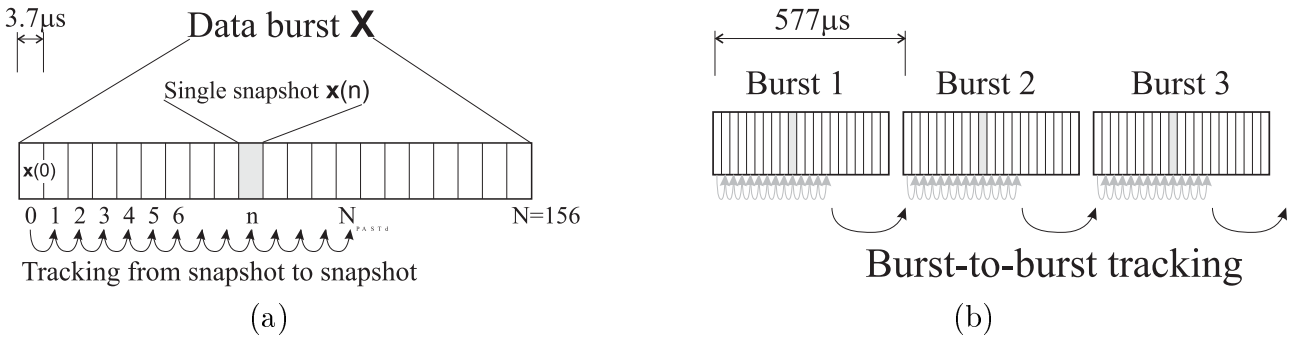

Figure 4.3. Signal subspace tracking. (a) Tracking within a data burst. (b) Burst–to–burst tracking.

ESPRIT. As estimator for the number of DOAs, I apply the same criteria as with **Unitary ESPRIT**. For more details on further complexity reduction techniques and implementation refer to [KTRS98].

The main difference to the signal subspace estimation by means of eigenvalue decomposition is that **PASTd** does not require a covariance matrix calculation. Instead, only the input data is processed snapshot by snapshot[2]. Figures 4.3(a) demonstrates the subspace tracking within a GSM data burst. The *tracking* of the signal subspace is performed over a specified number of snapshots, N_{PASTd}, *within each data burst*. By choosing the parameter N_{PASTd} the computational complexity of **PASTd** can be traded against the estimation accuracy. When $N_{PASTd} < N$ the variation will decrease, because not the entire available information (all snapshots of a burst) is used.

Burst–to–burst tracking To increase the estimation accuracy **PASTd** may be initialized with the state of the signal subspace of the previous burst (Fig. 4.3b). For that purpose, the tracked values from the previous burst, i.e. the signal subspace basis, the eigenvalues, and the number of DOAs, are used as initialization for the current burst. However, it is also possible to reset

[2]One snapshot is a single sample of the antenna array. Therefore we get a vector $[1 \times M]$ and each vector element represents one sample at each antenna element.

the tracker at every burst, i.e. initialize the function with new start values at every burst. Then **PASTd** is applied *without* burst–to–burst tracking. This is necessary when frequency hopping is applied, and the interference situation, and thus the signal subspace, changes significantly from burst to burst.

The decaying factor, β, must be chosen appropriately. It determines how fast PASTd converges. The closer β to unity, the more snapshots are taken into consideration for updating the signal subspace, and the longer it will take until the algorithm converges. The smaller β is, the less snapshots are taken into account, and the more inaccurate the estimated DOAs will be. More details about the decaying factor are available in [Str98]. Depending on whether burst–to–burst tracking is applied or not, I define two sets of parameters for **PASTd** (Tab. 4.4). In the standard **PASTd** configuration I will apply burst–to–burst tracking. While in case of burst–to–burst tracking the variation will be superior, this configuration will not be applicable for a system with frequency hopping (Tab. 4.6). On the other hand, **PASTd** *without* burst–to–burst tracking has a significantly larger run–time, because the algorithm must use all available data within a burst to guarantee convergence.

PASTd configuration	N_{PASTd}	β
PASTd (standard, with burst–to–burst tracking)	50	0.97
PASTd without burst–to–burst tracking	140	0.75

Table 4.4. Configurations of **PASTd** . The standard configuration *with* and another configuration *without* burst–to–burst tracking.

4.3.3 Estimating the number of DOAs

The parametric estimators **Unitary ESPRIT** and **PASTd** require an estimate of the number of sources, L, because L is not known in advance. The model order estimation (also "rank estimation" or "estimation of the number of DOAs") determines the rank of $\mathbf{X}$ from the estimated eigenvalues of the data matrix, λ_m.

MDL and AIC The first two criteria are based on information theory [WK85]. The criteria named "An Information Criterion" (AIC) [Aka74] and "Minimum Description Length" (MDL) are given by

$$\begin{aligned} AIC(\hat{L}) &= W(\hat{L}) + p_f(\hat{L}), \\ MDL(\hat{L}) &= W(\hat{L}) + \frac{1}{2} p_f(\hat{L}) \ln(N), \end{aligned} \tag{4.3.10}$$

where $\hat{L}$ is the estimated number of sources, $\ln(\cdot)$ denotes the natural logarithm, and $p_f(\hat{L})$ denotes the free (adjustable) parameters in the estimate of the covariance matrix $\hat{\boldsymbol{R}}$, assuming that there are $\hat{L}$ sources. The minimizers of the AIC and MDL criteria are chosen as the AIC and MDL estimates of L [WK85].

The statistic $W(\hat{L})$ follows as

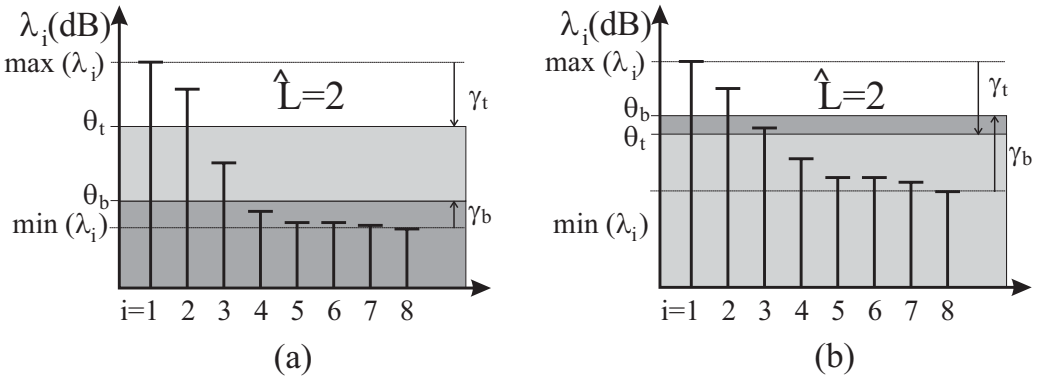

Figure 4.4. Threshold Criterion. (a) $\theta_t > \theta_b$. (b) $\theta_t < \theta_b$.

$$W(\hat{L}) = -156(M-\hat{L})\ln\left\{\frac{\left(\prod_{l=\hat{L}+1}^{M}\lambda_l\right)^{1/(M-\hat{L})}}{\frac{1}{M-\hat{L}}\sum_{l=\hat{L}+1}^{M}\lambda_l}\right\}, \tag{4.3.11}$$

where λ_l are the eigenvalues of the input data and $p_f(\hat{L})$ is given by

$$p_f(\hat{L}) = \frac{1}{2}\hat{L}(2M-\hat{L}+1). \tag{4.3.12}$$

Threshold Criterion The third criterion is a simple, heuristic criterion that applies two thresholds to the eigenvalues:

- a top threshold in dB, defined as the level that is γ_t smaller than the largest eigenvalue, $\max(\lambda_i)$.
- a bottom threshold in dB, defined as the level that is γ_b larger than the smallest eigenvalue, $\min(\lambda_i)$.

The Threshold Criterion estimates the rank L as the number of eigenvalues that are larger than the top threshold level *and* are larger than the bottom threshold level(Fig. 4.4). In other words, the applied threshold level, θ_a, is

$$\theta_a = \begin{cases} \theta_t = \max_i(\lambda_i) - \gamma_t & \text{if } \theta_t > \theta_b, \\ \theta_b = \min_i(\lambda_i) + \gamma_b & \text{otherwise.} \end{cases} \tag{4.3.13}$$

4.3.4 Minimum Variance Method

The third algorithm belongs to the class of spectral–based parameter estimators. Such techniques can be further subdivided into *beamforming* techniques and *subspace–based* methods [KV96]. *Capon's Beamformer* [CGK67], also known as Minimum Variance Method, is a beamforming technique. It alleviates the limitation of the conventional beamformer (Fourier–based

spectral analysis) to resolve only two sources spaced more than the beamwidth apart. Capon's beamformer minimizes the power contribution by noise and any signals coming from other directions than ϕ, while maintaining a fixed gain into the direction ϕ:

$$\mathbf{w}_{Capon} = \min_{\mathbf{w}} P(\mathbf{w}) \tag{4.3.14}$$

subject to $\mathbf{w}^H \mathbf{a}(\phi) = 1$, where

$$P(\mathbf{w}) = \mathbf{w}^H \, \hat{\mathbf{R}} \, \mathbf{w}. \tag{4.3.15}$$

$\hat{\mathbf{R}}$ is the estimate of the covariance matrix of $\mathbf{X}$, i.e. the sample covariance matrix

$$\hat{\mathbf{R}}(n) = \frac{1}{N}\mathbf{X}(n)\mathbf{X}(n)^H \tag{4.3.16}$$

$$= \frac{1}{N}\sum_{n=1}^{N} \mathbf{x}(n)\mathbf{x}(n)^H \tag{4.3.17}$$

Inserting the optimum weight vector

$$\mathbf{w}_{Capon} = \frac{\hat{\mathbf{R}}^{-1}\,\mathbf{a}(\phi)}{\mathbf{a}(\phi)^H \, \hat{\mathbf{R}}^{-1} \, \mathbf{a}(\phi)} \tag{4.3.18}$$

into Eq. (4.3.15) leads to Capon's spatial spectrum

$$P_{Capon}(\phi) = \frac{1}{\mathbf{a}^H(\phi)\hat{\mathbf{R}}^{-1}\mathbf{a}(\phi)}, \tag{4.3.19}$$

where $\mathbf{a}(\phi)$ is the uniform linear array steering vector and $\hat{\mathbf{R}}$ is the sample covariance matrix.

A 1D–search in the spatial power spectrum $P_{Capon}(\phi)$ is necessary to find the DOAs. In Fig. 4.5 I demonstrate the high–resolution capability resulting from a spectrum with steep spectral peaks.

To reduce the computational effort I apply a two-level search. First, peaks are searched in a spectrum that is calculated only with coarse resolution, typically $R_c = 1°$. Around the found peaks a second refined search with a fine resolution, $R_f < R_c$, allows to improve the resolution without increasing the run–time extensively. For **MVM** I select a standard configuration with reasonable run–time, and a configurations with highest possible resolution (Tab. 4.5). The fine resolution of **A**^{3}**P** is limited by the memory available in the processor.

Configuration	R_c (°)	R_f (°)
standard	1	0.1
MVM, high resolution	0.1	0.02

Table 4.5. Parameter settings of Minimum Variance Method (**MVM**).

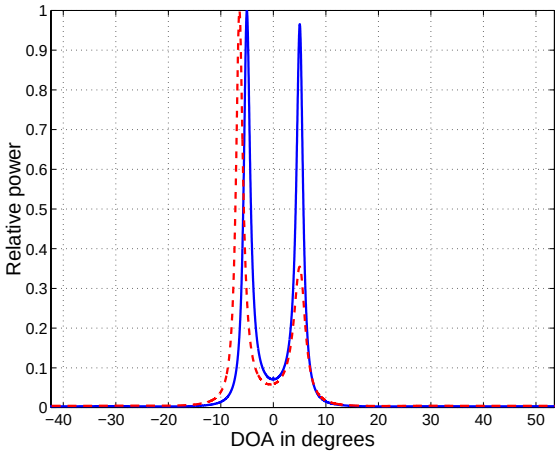

Figure 4.5. Minimum Variance Method (MVM) sample spectra when two equi–powered signal sources are present at $\phi_1 = -5°$ and $\phi_2 = +5°$. The solid line represents a scenario where each sources results in a single plane wave at the receiver. In the second scenario, signal source 2 has an angular spread of about $5°$ (dashed line).

Configuration	Accuracy	Average run–time (μs)	Frequency hopping
Unitary ESPRIT	high	452	compatible
PASTd with burst–to–burst tracking	high	340	not possible
PASTd without burst–to–burst tracking	low	570	compatible
MVM	low	511	compatible
MVM, high resolution	high	2000	compatible

Table 4.6. Properties of different parameter settings of the **DOAE**.

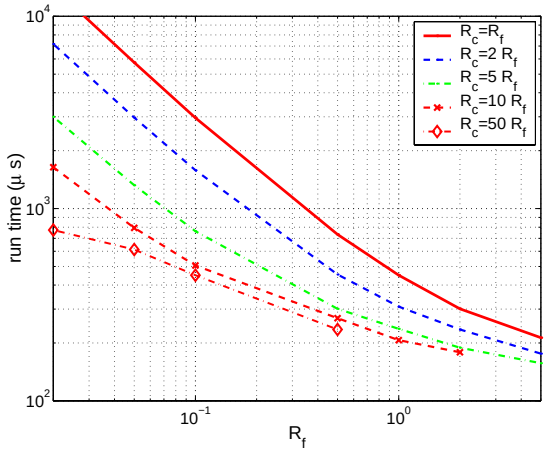

Figure 4.6. Average run–time of **MVM** versus the fine resolution, R_f. The coarse resolution is a multiple of the fine resolution, R_f, varying from $R_c = R_f$ to $R_c = 50R_f$.

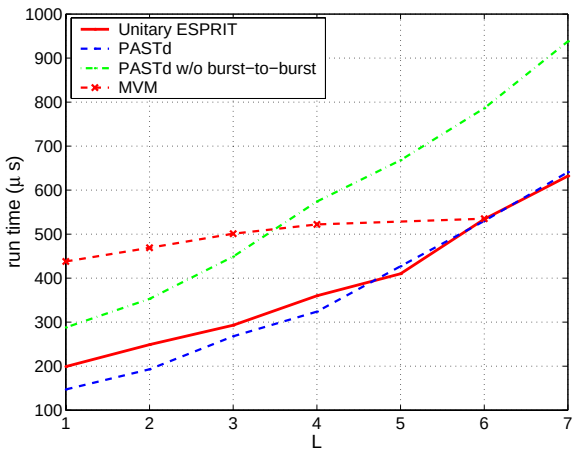

Figure 4.7. Average run–time of the various **DOAE** algorithms versus number of DOAs, L.

4.3.5 Run–time of DOA estimation

Before I present the measured run–time of the various DOA estimators, I take a closer look on the run–time of **MVM**. The run–time of **MVM** strongly depends on the chosen angular resolution (Fig. 4.6). The larger R_c is compared to R_f, the less the run–time depends on R_f (curves are more level). Of course, we are interested to find a configuration that will give optimum *fine* resolution at possibly small run–time. I select $R_c = 10\,R_f$, with $R_f = 0.1°$, as the standard configuration. Decreasing R_c further does not change the run–time. Selecting a fine resolution that is 5 times worse ($R_f = 0.5°$) will reduce the run–time only by about 45%.

Finally I present the measured run–time of the different implemented DOA estimators. Here I investigated their dependence on L, the number of DOAs (Fig. 4.7). The surprising result is that **Unitary ESPRIT** has nearly the smallest run–time. Only **PASTd** in its standard configuration beats **Unitary ESPRIT** for $L < 5$, but the difference is not significant. **MVM**, in principle, has a larger run–time, but it is less dependent on L. Additionally, **MVM** is the only algorithm where run–time can be simply traded against angular resolution. When **PASTd** without burst–to–burst tracking is applied, the run–time is the largest for $L > 3$. The large difference between the two **PASTd** configurations is a consequence of the different number of data samples, which is $N_{PASTd} = 50$ for the standard configuration and $N_{PASTd} = 140$ otherwise (Tab. 4.4).

4.3.6 DOA estimation accuracy

In the following subsections I will assess the **DOAE**. First I will define a quantity that allows quantification of the estimation accuracy and present the theoretical and measured accuracy of the implemented DOA estimators.

Definition of the DOA estimate variation: The *DOA estimate variation*, σ_{DOAE}, is the second central moment of the estimated DOAs, when a *single plane* wave is incident:

$$\sigma^2_{DOAE} = \int_{\phi} (\phi - E\{\phi\})^2 pdf_{\phi}\, d\phi, \tag{4.3.20}$$

where pdf_{ϕ} is the probability density function (PDF) of the estimated DOAs.

The DOA estimate variation[3] is the standard deviation (square root of the variance) of the DOA estimates. In practice, I apply this definition to a finite number of sample estimates, measured in different bursts. Of course I assume ergodicity. In the discrete case Eq. (4.3.20) reduces to

$$\sigma^2_{DOAE} = \frac{1}{N_{samples}} \sum_{n=1}^{N_{samples}} (\hat{\phi}_n - \overline{\hat{\phi}})^2, \tag{4.3.21}$$

with

$$\overline{\hat{\phi}} = \frac{1}{N_{samples}} \sum_{n=1}^{N_{samples}} \hat{\phi}_n, \tag{4.3.22}$$

where $N_{samples}$ estimated DOAs ϕ_n are available.

I measured the estimate variation and compared it to computer simulations. For the measurements I used a continuous wave (CW) generator with LOS to the BS (Fig. 4.8); there is no interfering signal source active. The BTS antenna array is mounted on a rotor to allow measurements for different DOAs. It is standing on the roof of a three–storey high building that is surrounded by buildings with similar — but not significantly larger — height. I measured the estimated DOAs in $N_{bursts} = 3000$ bursts, for different transmit powers of the CW generator.

The measured variation (Fig. 4.9(a)) decreases monotonously with SNR for all estimators. But at large SNR values the estimation variation does not decrease any further with increasing signal power. For example the minimum estimation variation of **Unitary ESPRIT** is in the order of $0.01°$. In case of the **MVM** the variation is limited because of the finite spectral resolution of $R_f = 0.02°$.

In Fig. 4.9(b) I present the results of computer simulations with the exactly the same configurations as in the measurements. The estimate variation of the estimators goes to zero for an infinite SNR. Of course, this is not the case for **MVM**, where the spectral resolution is limited. (Here I applied the high–resolution configuration of **MVM** .)

Although **MVM** has the best theoretical performance, this is not the case in practice. The measured curve of **MVM** is shifted by $20dB$ compared to the theory. For **Unitary ESPRIT** the degradation in the measurements is about $8dB$, in case of **PASTd** only $5dB$. That **Unitary ESPRIT** shows a stronger degradation from the theory than **PASTd** has the following reason. When **PASTd** is applied to finite data, i.e. if the number of iterations is not large enough, the

[3]Naming σ_{DOAE} the estimation accuracy has the disadvantage that a "low accuracy" sounds negative, although it is of course desirable.

(a) (b)

Figure 4.8. Controlled measurement environment on the roof top of the Alcatel building. The antenna array is mounted on a rotor. A GSM mobile station (MS) with LOS to the BS present. (a) Principal setup. (b) Photo of measurement setup.

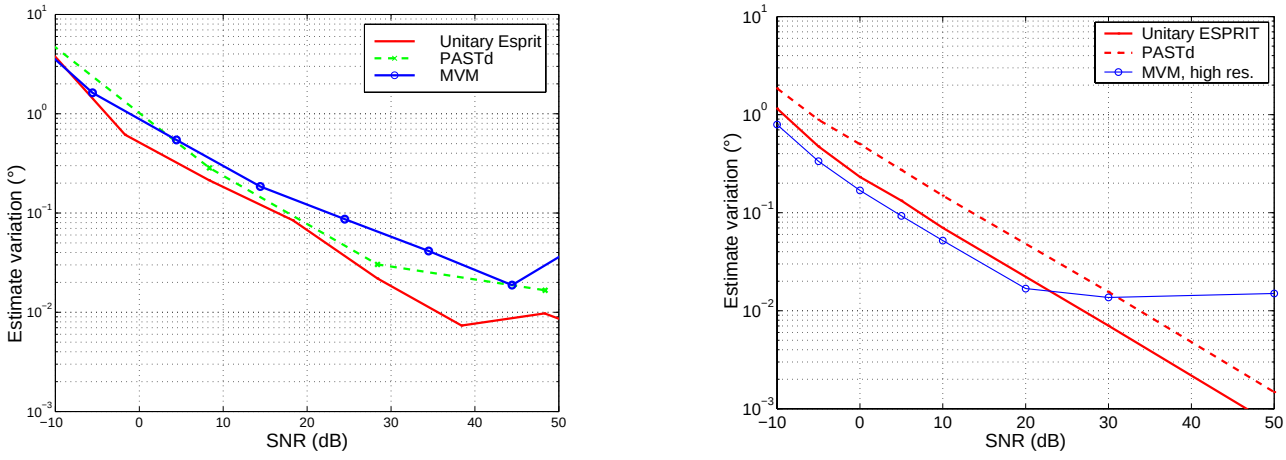

(a) (b)

Figure 4.9. Estimate variation of the **DOAE** versus SNR when a single plane wave is incident from $\phi = 0°$. (a) Measurement. (b) Simulation. For **Unitary ESPRIT** and **PASTd** the standard configurations are applied.

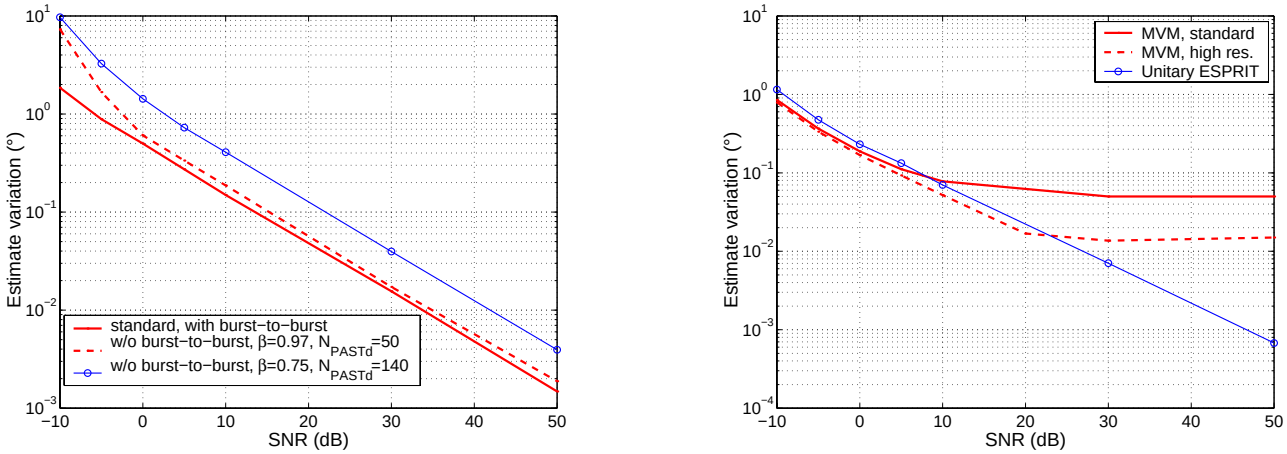

(a) (b)

Figure 4.10. Estimate variation of various **DOAE** configurations versus SNR when a single plane wave is incident from $\phi = 0°$. (a) Three **PASTd** configurations, and (b) **MVM** with standard resolution (0.1°) and high resolution (0.02°), with **Unitary ESPRIT** as reference.

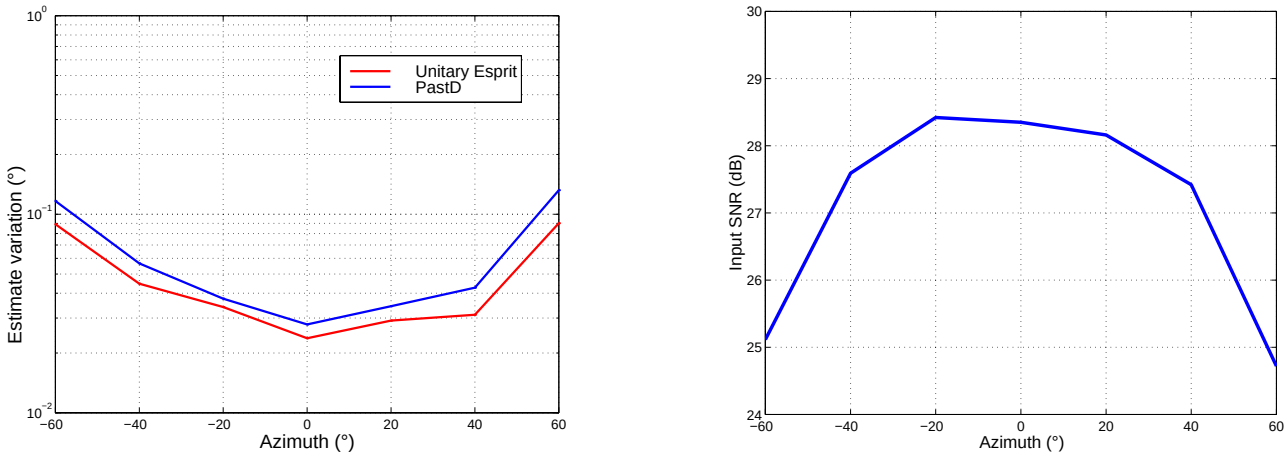

(a) (b)

Figure 4.11. Measured estimate variation of the **DOAE** versus angle when a single plane wave is incident. (a) Estimate variation. (b) Average input SNR.

signal subspace basis estimated by **PASTd** is not totally orthogonal. But this is the case for **Unitary ESPRIT**. Imperfections of the hardware, like calibration errors and mutual coupling, cause a degradation from the ideal result. As long as the imperfections are small, the finite amount of data will limit the performance of **PASTd**. Here, of course, the imperfections set the limits, but still this explains why the degradation is smaller for **PASTd**. In case of **Unitary ESPRIT** already the smallest imperfections will degrade the performance.

Another fact may cause the deviation of measurements and theory: the measurement environment. On the roof top some scatterers are close to the array that may cause additional, albeit weaker, waves incident at the array. Additionally the transmit MS antenna has a finite aperture so that is seen under an angle of about 0.5° at the array. In summary, **MVM** is most sensitive against all imperfections in this scenario. **Unitary ESPRIT** and **PASTd** are more robust. Most significant , however, is the similar behavior of all implemented algorithms: To measure a DOA estimate variation of 1° all algorithms require an input SNR in the range of $0dB$[4]. Note that these conclusions are drawn from an assessment when only a discrete wave is incident. In the following I will assess the algorithms under more general assumptions and this will lead to different conclusions.

Dependence of DOA estimate variation on the absolute angle I also measured the variation for different incident angles ϕ while the transmit power of the mobile stayed constant. The individual antennas are sector antennas and not omnidirectional antennas. Therefore the receiver input power, and thus the input SNR, is smaller for angles far off the broadside direction. Moving to directions far off broadside results in a smaller array aperture, which additionally increases the estimate variation. Thus there are two effects that increase the estimation variation compared to the one at broadside direction. These effects are not separable with the available measurement data. Figure 4.11(a) presents the resulting DOA estimate variation. Figure 4.11(b) demonstrates the variation of the input SNR.

[4] An input SNR of $0dB$ is a worst–case assumption, because conventional GSM detectors require an SNR in the order of $7-9dB$ for proper BER performance, which corresponds to an input SNR in the order of $0dB$ considering a maximum SNR gain of $10\log_{10} M = 9dB$.

Comments The presented results for the variation assumed that there is only a single discrete wave incident and that the number of DOAs is known, $L = 1$. Relaxing this assumption, i.e. applying estimators for the number of DOAs will degrade the estimate variation. However, an assessment is then not so easy anymore. If, for example, the **DOAE** would return two DOA estimates, which one of these should then enter the statistics? The DOA closest to the correct one, or both? To find a way out of this dilemma, my approach is to define the DOA estimate variation only for the case that the number of DOAs is known to the estimator and equal to unity. This will not give information about the applicability of DOA estimators to the mobile radio channel that, in general, includes more propagation paths than only one. However, measuring the DOA estimate variation indicates how well the hardware is implemented, because this can easily be compared with simulation results. From the agreement between measured and simulated accuracies that we achieve with our base station, and the optimum variation in the order of a hundreds of a degree, I conclude that the calibration of the system is sufficient.

4.3.7 DOA estimation robustness

After describing the DOA estimation performance in an idealized environment, and thus setting the limits of the DOA estimation, I will relax the assumptions step by step and finally assess the **DOAE** in a mobile radio channel.

A DOA estimator is influenced by many factors, among which the most important are: the angular spread of the environment, the number of signal sources present, and the number of estimated DOAs. To assess an estimator under realistic, but challenging, assumptions a more general concept than the estimate variation is required. Thus I define a new quantity, the *DOA estimation range*. It will allow the quantification of the estimator's performance in more realistic situations than in the case of a single incident discrete DOA. With the concept of the estimation range I want to provide a rather practical tool to assess an estimator.

Definition of the estimation range To quantify the estimation range I compute the cumulative distribution function (CDF), cdf_ϕ of the estimated DOAs.

In the case of a single wave incident, $L = 1$, the *estimation range* is defined as the minimum size of the angular range around a nominal DOA, ϕ_0, that includes $\alpha = 38.3\%$ of the estimated DOAs.

$$Q_{DOAE} = \min_{\zeta}\{\phi(cdf_\phi = \zeta) - \phi(cdf_\phi = \zeta - \alpha)\}, \tag{4.3.23}$$

where

$$\phi(cdf_\phi = \zeta) < \phi_0 < \phi(cdf_\phi = \zeta - \alpha) \tag{4.3.24}$$

This condition assures that the nominal DOA stays *within* the defined angular range. It does not require a symmetry around ϕ_0.

Some comments:

- The definition allows a calculation from sample data, either measured or simulated, under the assumption of ergodicity.
- Implementation: Of course we cannot measure the exact probability density function

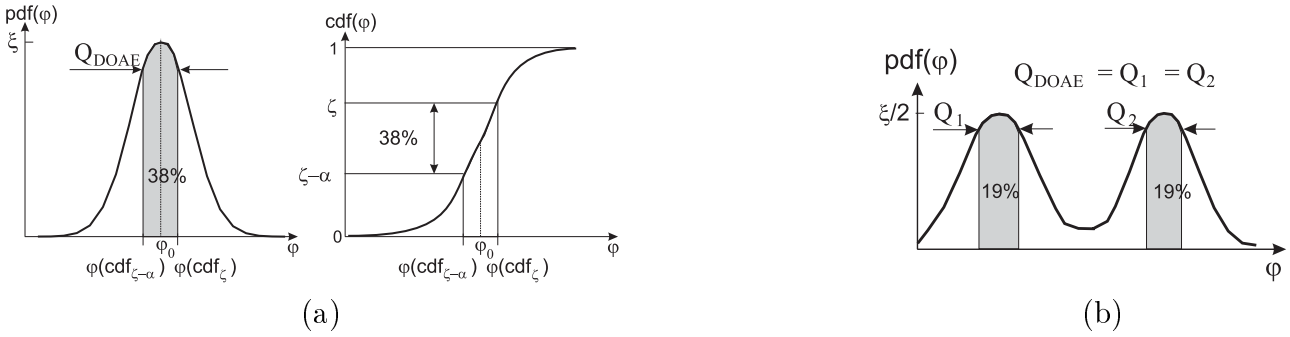

Figure 4.12. Definition of the estimation range. (a) Single DOA with standard deviation σ. (b) Generalized definition: Two DOAs, each with a standard deviation of σ.

(PDF), pdf_ϕ, or cdf_ϕ. But from sample data it is easy to compute a histogram, i.e. an estimate for the pdf_ϕ. Starting with the histogram value closest to the nominal DOA, I just have to increase the interval in both directions around the starting point, and sum up all PDF values within an interval. Finally I will stop, when the sum of the PDF values is larger than 38%. The corresponding value of the angular range is Q_{DOAE}.

- If a single DOA is incident and the estimated DOAs are Gaussian distributed, $Q_{DOAE} = \sigma_{DOAE}$, i.e. the estimation range is equal to the estimate variation. This is the reason why I have chosen $\alpha = 0.383$.
- Computing Q_{DOAE} requires, additionally to the sample estimates, only the knowledge of a nominal DOA.
- The estimation range is a concept that shall *not* replace the theoretical assessment of an estimator, e.g. whether it is unbiased or not. Instead it should allow to assess an estimator under more complex situations and therefore in realistic environments.
- The concept can be easily generalized to the case of more incident DOAs. In that case the estimator, in general, will yield also more than one DOA. Because only a histogram needs to be calculated, it is not required to relate an estimate to the corresponding signal source — a nontrivial task, if more DOAs are present. This is especially true if the number of estimated DOAs varies from one experiment to the next.

Generalized estimation range To define the generalized estimation range, I apply the definition 4.3.23 to each nominal DOA. In the case of L waves incident, L *generalized estimation ranges* are defined.

The l–th generalized estimation range $Q_{DOAE,l}$ is defined as the minimum size of the angular range around the l–th nominal DOA, ϕ_l, that includes $\alpha = \frac{38.3\%}{L}$ of the estimated DOAs.

$$Q_{DOAE,l} = \min_{\zeta}\{\phi(cdf_\phi = \zeta) - \phi(cdf_\phi = \zeta - \alpha)\}, \tag{4.3.25}$$

where

$$\phi(cdf_\phi = \zeta) < \phi_l < \phi(cdf_\phi = \zeta - \alpha) \tag{4.3.26}$$

Thus we get several estimation qualities, all for the same DOA estimator, but each valid for a certain nominal DOA. The estimation range is a quantity that describes the behavior of a DOA estimator in a specific environment (or better for a specific multipath component). It tells how robust a nominal DOA can be estimated by the DOA estimator under consideration. The estimation range of a certain estimator will be different in case of a nominal DOA when a discrete wave is incident than in the case when a large angular spread around the nominal DOA is present.

- In the generalized definition I look for the angular range that includes $\frac{38}{L}\%$. If e.g., two nominal DOAs are incident, each with the same spread of estimation errors around the correct DOA, the two estimation qualities (for each DOA) will give

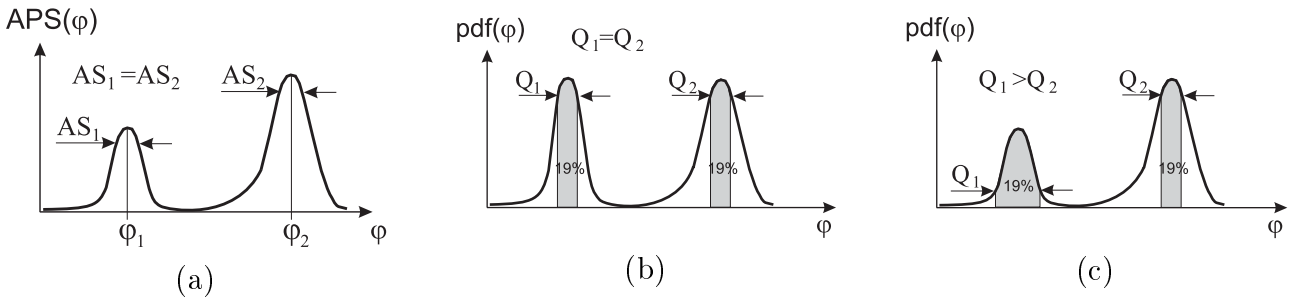

Figure 4.13. Scenario with two multipaths, each having the same angular spread, but different powers. (a) Angular power spectrum. (b) PDF of estimated DOAs for Estimator 1. (c) PDF of estimated DOAs for Estimator 2.

the same value as in the case of a single DOA (Fig. 4.12). Then the generalized estimation range is equal to the estimation range.

– The reader might wonder, why in the case of several DOAs, the level α is not depending on the power of the signals. Assume a situation as illustrated in Fig. 4.13: two multipaths are present, Signal 1 and Signal 2, each with the same angular spread (Fig. 4.13(a)), but with different signal power. Let us assume that there are two DOA estimators: *Estimator 1* and *Estimator 2*. In such a situation, the PDF of the estimated DOAs for *Estimator 1* may look like in Fig. 4.13(b).

  Estimator 1 is an excellent estimator, because although the power of Signal 1 is smaller, the estimator finds as many DOAs around the nominal DOA, ϕ_1, as for the second multipath component. Correspondingly, the estimation qualities for the two multipaths are the same $Q_1 = Q_2$ (Fig. 4.13(b)).

  If *Estimator 2* (Fig. 4.13(c)) is not able to find the first multipath component so often, the estimation range would increase. Thus, with a constant α, the estimation range accounts not only for the *spread* of the DOA estimates, but also for the *frequency* of the estimates. The frequency of the estimates includes two effects: First, how often a nominal path is estimated in comparison to others and second estimates far off the nominal DOAs. Such a far–off estimate means one "good" estimate less that falls within the close range around the nominal DOA, which results in an increase of the estimation range.

  Would we choose a threshold value α separately for each multipath, depending on the power of the signals (larger power — larger α), the outcome would be different. Then the estimation qualities would be the different for *Estimator 1*, $Q_1 < Q_2$ and the same for *Estimator 2*, $Q_1 = Q_2$. We may not forget that we then would make the following assumption: That the frequency of the multipath to be estimated depends linearly on the signal power. Who says that this is a correct — or better a practical — choice? Another disadvantage is that I do not always know the signal powers, especially not during measurements.

Influence of the estimated rank on the estimation range measured in a LOS environment Having defined the estimation range I will assess the **DOAE** in more realistic environments. In a first step I relax the assumption that the number of DOAs is correct, $\hat{L} = L$. Instead I will measure, still in the controlled LOS environment (Fig. 4.8), with only a single incident wave, the influence of the applied number of DOAs, $\hat{L}$, on the estimation range. Because the rank estimation is

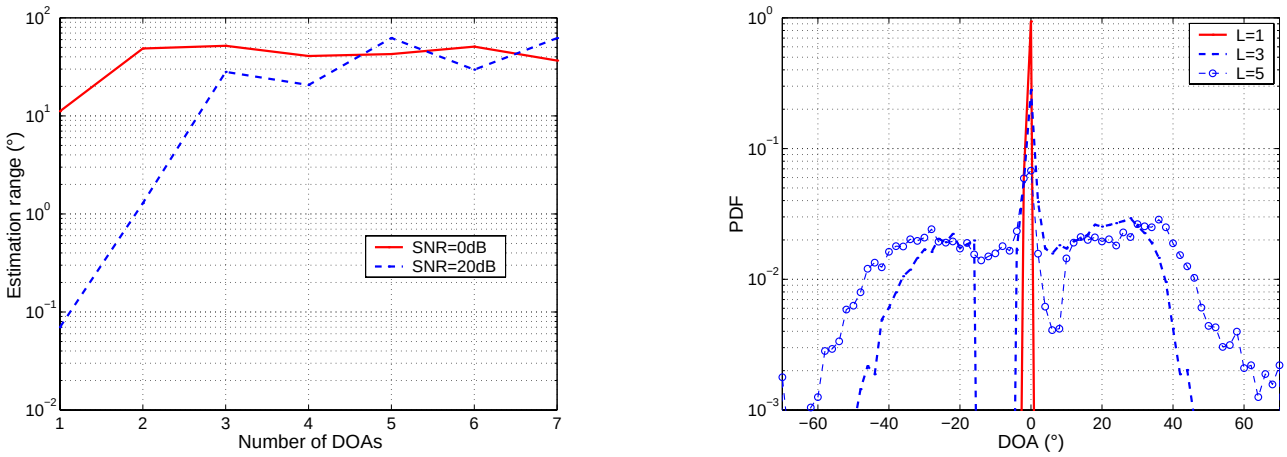

(a) (b)

Figure 4.14. Estimation range, Q_{DOAE}, as a function of the number of DOAs, $\hat{L}$, and the average input SNR. (a) Estimation range. (b) Sample PDFs for $SNR = 0dB$.

only applied to the parametric estimators **Unitary ESPRIT** and **PASTd** , and the influence is in principle the same on both estimators, I will study **Unitary ESPRIT** only. Thus during this measurement I vary the number of DOAs from $\hat{L} = 1 \ldots 7$ for **Unitary ESPRIT** . Note that for all measurements only a *single* wave is incident. With this measurement I evaluate the robustness of **Unitary ESPRIT** against a *false* estimate of L. The result indicates a significant degradation of estimation range with increasing number of additionally estimated waves (Fig. 4.14(a)). The situation becomes more severe when the input SNR is low. Some sample PDFs (Fig. 4.14(b)) demonstrate that too large a number of $\hat{L}$ significantly increases the number of far–off estimates. Overestimating the number of incident waves thus results in a significant degradation of the **DOAE** performance in a LOS environment.

Influence of the rank estimation criterion on the estimation range Having demonstrated the principal influence of $\hat{L}$ on the **DOAE**, I will assess the different rank estimators. I now apply a synthetic channel model, the GSCM [LMB98]. I assume that two signal sources are active, each having local scatterers, Gaussian distributed around the MS. This results in an angular spread of 2.5° for each MS. Table 4.7 summarizes the channel parameters. The two mobiles transmit with the same power, resulting in an average input C/I of 0dB. The average input SNR was varied.

Parameter	Mobile 1	Mobile 2
nominal DOA	45°	−10°
number of local scatterers	50	50
local scatterer radius	100m	100m
distance MS—BS	2000m	2000m
angular spread of each multipath	2.5°	2.5°

Table 4.7. GSCM channel parameters. Two mobiles are present.

The resulting estimation range for each nominal DOA (MS) follows the same trend, thus I only present the result for MS1 located at $\phi = 45°$ (Fig. 4.15). For small SNR values,

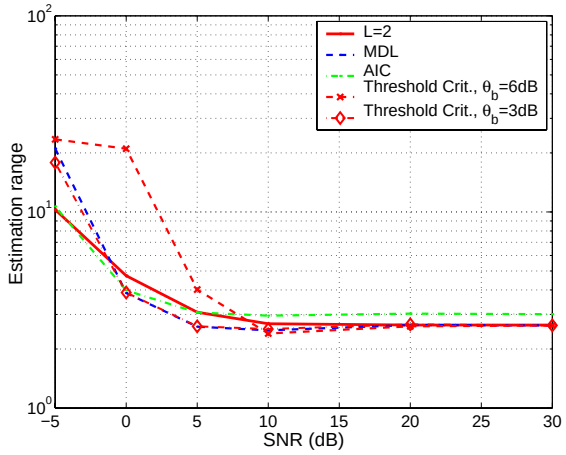

Figure 4.15. DOA estimation range, Q_{DOAE}, as a function of the average input SNR for different rank estimators.

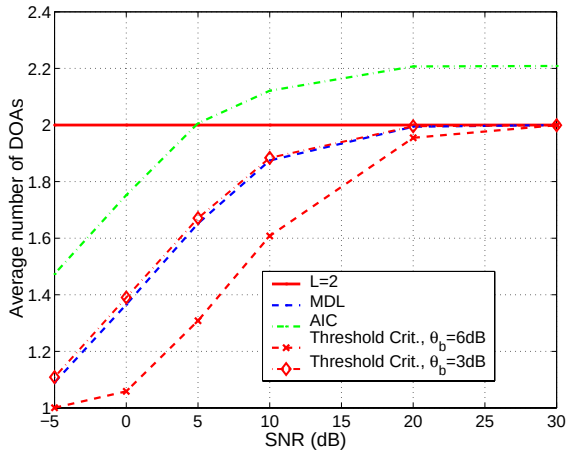

Figure 4.16. Average estimated number of DOAs, $\hat{L}$, for different rank estimators.

MDL and **AIC** are more robust than the Threshold Criterion (dashed line with crosses), where **AIC** gives slightly better estimation range. For large SNR, **MDL** and the Threshold Criterion perform equally well. Only **AIC** overestimates L significantly. This is illustrated by the average estimated number of DOAs (Fig. 4.16).

That the Threshold Criterion is not so robust against noise is a result of the *bottom threshold*, θ_b, which was set to $6dB$. I thus reduced the bottom threshold to $\theta_b = 3dB$ and the resulting estimation range is now the same as for **MDL**. However, this will increase the number of estimated DOAs in general, because now every eigenvalue that is only $3dB$ larger than the noise floor is considered as a signal. In the field trial this turned out to be disadvantageous. Important is the fact that with θ_b I can easily adjust the sensitivity for signals with small SNR.

Estimation range of the DOA estimators Finally I will compare the different DOA estimators. I apply the same scenario as in the previous simulation, but now I vary the power of the transmitted signals, thus varying the input C/I. The number of estimated DOAs is fixed to $\hat{L} = 2$, thus this assessment does not include the effect of non–ideal rank estimation. Note that for **MVM** $\hat{L}$ cannot be fixed, because it is implicitly estimated.

The estimation range of **MVM** is the best, closely followed by **PASTd** *with* burst–to–burst tracking. **Unitary ESPRIT** and **PASTd** *without* burst–to–burst tracking perform equally, but worse than the other two (Fig. 4.17).

The superior robustness of **MVM** is even clearer when we consider different angular spreads. Figure 4.18 presents the estimation range for the same scenario, but when the angular spread of each nominal DOA is varied. Especially when the angular spread is small, **Unitary ESPRIT** and **PASTd** often fail, produce far–off estimates, and thus the estimation range is larger. In contrast, **MVM** can cope even with large angular spreads.

Estimation range of a sample measurement Finally I show an example of estimated DOAs from a field measurement (Sample Measurement 1). The mobile had LOS to the BS with a nominal DOA of $\phi \approx 45°$. Sample Measurement 1 included 5000 bursts; the MS moved with an velocity of about $v = 10km/h$. The distance between MS and BS was large (about 1km) resulting in a nearly constant DOA during the measurement period. To get an idea of the channel situation, I compute the angular power spectrum at time index n, $P_{APS}(\phi, n)$ (Fig. 4.19),

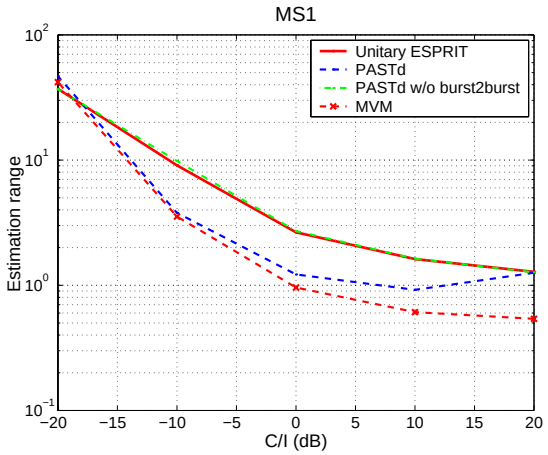

Figure 4.17. DOA estimation range, Q_{DOAE}, as a function of the average input C/I for different DOA estimators.

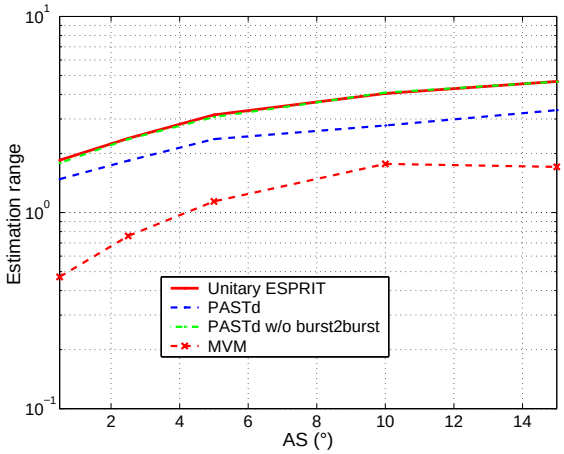

Figure 4.18. DOA estimation range, Q_{DOAE}, as a function of the angular spread, AS. The average input C/I is 0dB.

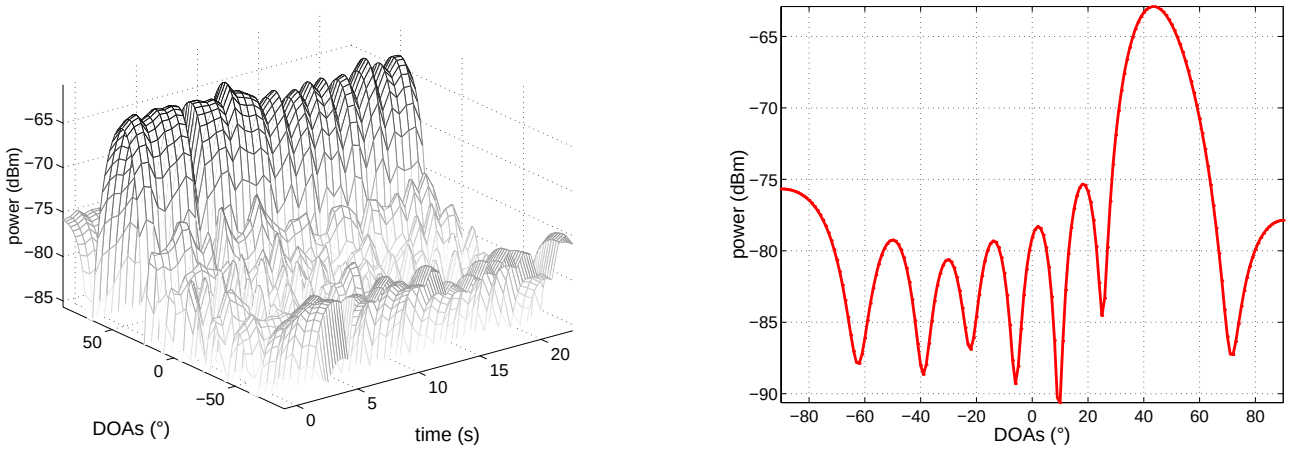

Figure 4.19. Sample Measurement 1. (a) Angular power spectrum for the $N_{sample} = 5000$ sample bursts. Note that the plot shows only every 200–th burst. (b) Averaged APS.

$$P_{APS}(\phi, n) = \mathbf{a}(\phi)\,\hat{\mathbf{R}}(n)\mathbf{a}(\phi)^H, \tag{4.3.27}$$

where $\mathbf{a}(\phi)$ is the steering vector for angle ϕ and $\hat{\mathbf{R}}(n)$ is the sample covariance matrix of the n–th burst.

I applied **Unitary ESPRIT** as DOA estimator. First I ran **Unitary ESPRIT** with $L = 1$, i.e. I estimate only the dominant DOA. The resulting PDF of the estimated DOAs has a sharp peak around $\phi = 45°$ (Fig. 4.20). As soon as I relax the assumption of knowing L in advance and apply instead an estimator for L, the PDF broadens significantly. I call the estimated DOAs significantly away from the LOS direction *far–off estimates*. In the range of $-50° \ldots 50°$ the PDFs look similar for all criteria, but outside that range the Threshold Criterion results in significantly less far–off estimates. Note that, here, I have applied the Threshold Criterion with a bottom threshold of $\theta_b = 6dB$, i.e. a less sensitive and thus more robust configuration (compare with Fig. 4.16). Figure 4.21 supports the conclusion that the Threshold Criterion shows a better estimation range than **MDL** or **AIC** .

In this evaluation I assumed that only a single multipath component exists. This is just a working assumption. I could also have assumed more nominal DOAs and calculated the corresponding estimation qualities. However, it would have been hard to decide where those nominal DOAs were. It should be stressed that, although I have assumed only a single nominal DOA, I am able to compare the estimation qualities of two different estimators to judge their performance.

4.3.8 Summary DOA estimation

The **DOAE** estimates $\hat{L}$ directions of arrival, $\hat{\phi}_l$, $l = 1 \ldots \hat{L}$, from the input data (Fig.4.22).

By applying an appropriate definition, a quantification of the estimate variation allows finding the limits of the estimators under ideal conditions. Measuring the estimate variation and comparing it with simulation results allows to assess the principal functionality of the algorithms. Additionally, the comparison with simulation allows drawing conclusions about the

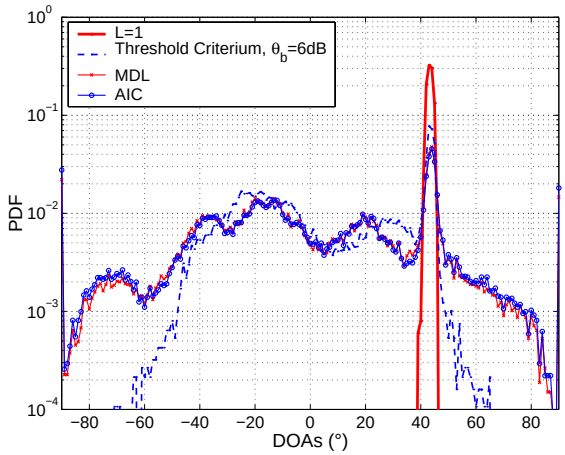

Figure 4.20. Sample Measurement 1. PDF of estimated DOAs for different rank estimators.

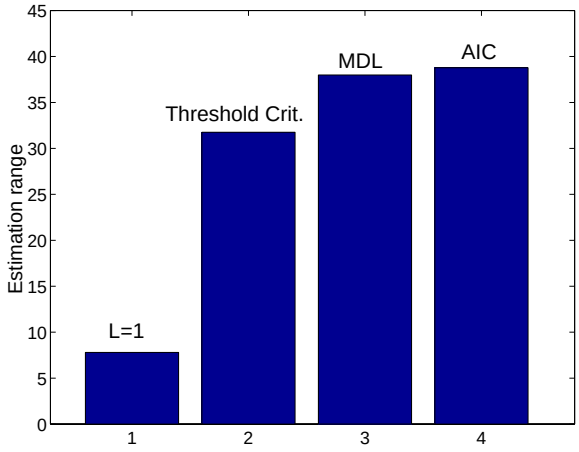

Figure 4.21. Sample Measurement 1: DOA estimation range, Q_{DOAE}, for different rank estimators.

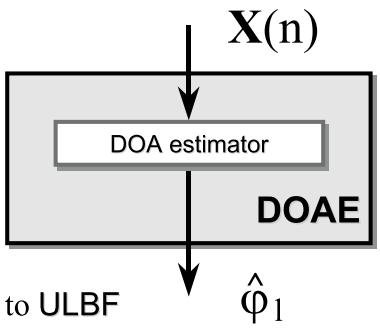

Figure 4.22. Schematic of the DOA estimation (**DOAE**).

quality of the calibration. The estimate variation quantifies the *accuracy* of a DOA estimator, i.e. how accurate a DOA can be estimated under optimum conditions. However, the estimate variation has little meaning in mobile radio channels, thus an additional measure for the *robustness* of the estimator is needed: the estimation range. An estimator with excellent accuracy but small robustness is not needed (lots of far–off estimates will cause outages), instead it is better to get a successful estimate every trial that might be less accurate.

Estimate variation:
The estimate variation quantifies the estimation accuracy of an estimator. The estimate variation is inverse proportional to the accuracy. It is defined under ideal conditions, i.e. a single wave incident at the array.

Estimation range:
The estimation range quantifies the robustness of an estimator. The estimation range is inverse proportional to the robustness. The estimation range can be measured in practical mobile radio channels.

Quantifying the robustness of a DOA estimator is a challenging task. Different properties influence the performance of an estimator, like the angular spread, the number of signal sources present, and the number of estimated DOAs. I have developed and applied a concept to quantify the robustness by defining an estimation range to assess the influence of various parameters on the **DOAE**.

From the assessment of the **DOAE** I conclude:

- The measured estimate variation is smaller than $1°$ for an input SNR larger than $0dB$ when a discrete wave is incident from broadside.
- The measured estimate variation is similar for all estimators, but is best for **Unitary ESPRIT**, although in theory **MVM** should outperform **Unitary ESPRIT**.
- A DOA estimation with high accuracy is realizable. The optimum accuracy is for all three estimators in the order of $0.01°$.
- Rank estimation:
  - Overestimating the rank, $\hat{L} > L$, in a LOS scenario significantly degrades the estimation performance, and more and more far-off estimates occur.
  - In a synthetic scenario with finite angular spread, the **AIC** overestimates L, while **MDL** and the Threshold Criterion give best results.
- Based on the estimation range I conclude that **MVM** is the most *robust* estimator, when the signals are incident with a finite angular spread.
- **PASTd** with burst–to–burst tracking gives similar robustness as **MVM**. **Unitary ESPRIT** and **PASTd** without burst–to–burst tracking are significantly less robust.
- **Unitary ESPRIT** showed the best variation, while it had the worst estimation range. In Chapter 5 I will prove that the most robust estimator guarantees the best overall results and not the most accurate one.

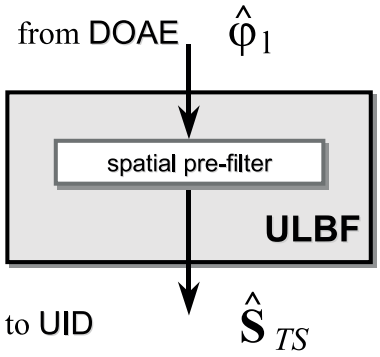

Figure 4.23. Schematic of the uplink beamformer (**ULBF**).

At the end of this section some questions remain unanswered: What is the influence of the estimate variation on the overall system performance? What variation is necessary? Or in other words, do we really need high–resolution DOA estimation? An answer to these questions will be presented in Chapter 5.

4.4 Spatial pre–filtering — Uplink beamformer

The uplink beamformer **ULBF** extracts from $\mathbf{X}$ a spatially resolved signal for each of the $\hat{L}$ estimated DOAs, $\hat{\phi}_l$, $l = 1 \ldots \hat{L}$ (Fig. 4.23). Thus I have to derive $\hat{L}$ weight vectors, $\mathbf{w}_l$, $1 \leq l \leq \hat{L}$, whose patterns steer a beam each into the wanted direction $\hat{\phi}_l$, while nulling all other directions. The resulting spatially resolved signal matrix, $\hat{\mathbf{S}}_{TS}$, is then

$$\hat{\mathbf{S}}_{TS} = \mathbf{W}_{ULBF}^{H}\, \mathbf{X}_{TS}, \tag{4.4.1}$$

where

$$\hat{\mathbf{S}}_{TS} = [\ \hat{\mathbf{s}}_{TS,1}^{T} \quad \hat{\mathbf{s}}_{TS,2}^{T} \quad \cdots \quad \hat{\mathbf{s}}_{TS,L}^{T}\ ]^{T}, \tag{4.4.2}$$

and

$$\mathbf{W}_{ULBF} = [\ \mathbf{w}_{ULBF,1} \quad \mathbf{w}_{ULBF,2} \quad \cdots \quad \mathbf{w}_{ULBF,L}\ ]. \tag{4.4.3}$$

$\mathbf{X}_{TS}$ is the part of the baseband measurement matrix $\mathbf{X}$ that contains the training sequence (midamble). The reconstructed signal vectors $\hat{\mathbf{s}}_{TS,l}$, $1 \leq l \leq \hat{L}$, contain the spatially resolved midambles corresponding to the l–th DOA. To compute the weight matrix, I can choose from two algorithms.

4.4.1 Conventional beamforming

The straight forward solution is to apply the Moore–Penrose Pseudo Inverse [JD91] of the estimated steering matrix.

$$\mathbf{W}_{ULBF}^{H} = \hat{\mathbf{A}}^{\dagger}, \tag{4.4.4}$$

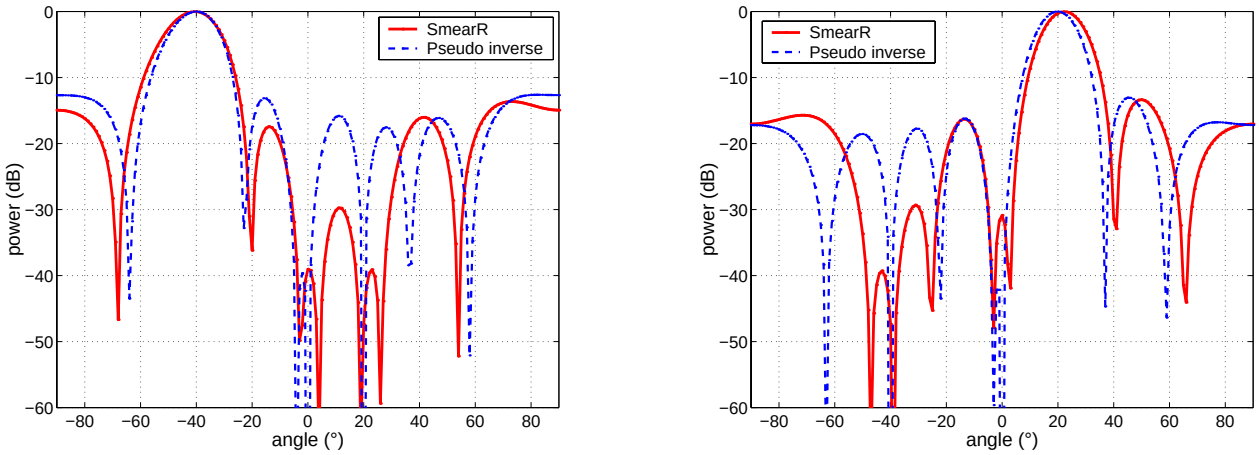

Figure 4.24. Sample pattern of **ULBF**, when three DOAs are present: $\phi_1 = -40°$,$\phi_2 = 0°$, and $\phi_3 = 20°$. Resulting spatial–prefilter for (a) ϕ_1 and (b) ϕ_3.

where

$$\hat{\mathbf{A}} = [\ \mathbf{a}(\hat{\phi}_1) \quad \mathbf{a}(\hat{\phi}_2) \quad \cdots \quad \mathbf{a}(\hat{\phi}_{\hat{L}})\ ]. \tag{4.4.5}$$

Thus each weight vector $\mathbf{w}_{ULBF,l}$ is constructed to get a main beam into $\hat{\phi}_l$ and *sharp* nulls into all other estimated DOAs.

4.4.2 Broad null beamforming

In a second approach I apply the **SmearR** algorithm (Sect. 4.7.1, p.73) that places *broad* nulls into the direction of all interferer. Figure 4.24 illustrates the different nulling approaches. While the conventional beamformer (Pseudo Inverse) places steep and narrow nulls, **SmearR** is forming broad nulls. The prize to be paid for such broad nulls is a slightly broader main beam and a slightly reduced gain. While the conventional beamformer reaches in this example an average gain of $G = 7.5dB$, the **SmearR** beamformer reaches only $G = 7.3dB$.

4.4.3 Run–time of uplink beamformer

I measured the average run–time in a typical, synthetic mobile radio channel. The run–time (Fig. 4.25) of the **ULBF** depends linearly on the number of DOAs, because the main effort is spent on Eq. (4.4.1). The conventional beamformer has about twice the run–time of **SmearR**.

4.4.4 Summary uplink beamformer

A conventional beamformer and the **SmearR** beamformer are implemented as spatial pre–filters. The run–time of **ULBF** presents a significant portion of **A**^{3}**P**'s overall run–time. Its main effort is spent in the actual beamforming (Eq. 4.4.1), resulting in a complexity that grows linearly with L, the number of the DOAs. Assessing a beamformer is not easy. The influence of various parameters (gain, null depth ...), on the overall system performance is not clear and thus will not be analyzed. Instead, the influence of placing broad nulls in the **ULBF** on the system performance will be discussed in Chapter 5.

In the next step the spatially resolved midambles are fed to the user identification.

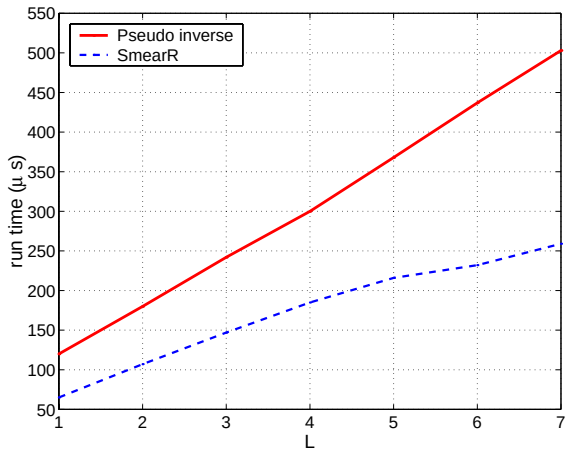

Figure 4.25. Average run–time of uplink beamformer (**ULBF**) in a typical scenario.

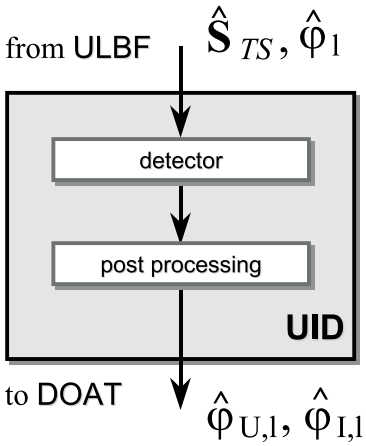

Figure 4.26. Schematic of the user identification (**UID**).

4.5 User identification

In GSM the signals are characterized by a user identifier, in our case the training sequence. The training sequence in the GSM standard is required for channel estimation and to distinguish signals from different base stations. The smart antenna can only suppress interference if the interferer signal applies a different training sequence. **A³P** thus distinguishes wanted signal information and interference by this user identifier. Actually, the **UID** decides which of the spatially resolved signals originate from the user.

The user identification **UID** [Rau98] is based on the detection of the spatially resolved midamble sequence, $\hat{\mathbf{S}}_{TS}$, at bit–level. By comparing the received midambles with the known user midamble, I calculate the number of bit errors within the training sequence. A spatially resolved signal, and thus the corresponding DOA, is attributed to a user when the number of bit errors is smaller than a threshold, θ_{BER}. I so identify not only a single, but *all* user paths that correspond to the intended user. The **UID** returns the classified DOAs (Fig. 4.26):

- $\hat{\phi}_{U,l}$, $l = 1 \ldots \hat{L}_U$, where $\hat{L}_U$ is the number of identified user DOAs (signals).
- $\hat{\phi}_{I,l}$, $l = 1 \ldots \hat{L}_I$, where $\hat{L}_I = \hat{L} - \hat{L}_U$ is the number of detected interferer DOAs (signals).

As detector I apply a proprietary GSM detector (Fig. 4.27, [Sch95]).

The **UID** is a key element in the present array processing scheme. Erroneous identifications, i.e. if an interferer signal is erroneously marked as a user signal, may significantly degrade the system performance. Then, of course, the chance that the main beam is directed towards such an erroneous user DOA would be high. The final decision in which direction the main beam points to is made after the tracking (Sect. 4.6). There I have the chance to remedy any wrong identifications by not selecting such a DOA.

4.5.1 Post–correlation

The post–correlation that follows the primary identification process improves the reliability of the classification. The detection results in soft decision bits, $\mathbf{b}_l$, for each of the $\hat{L}$ spatially resolved signals. From $\mathbf{b}_l$ the number of bit errors, $n_{BER,l}$, of the l–th spatially resolved signal

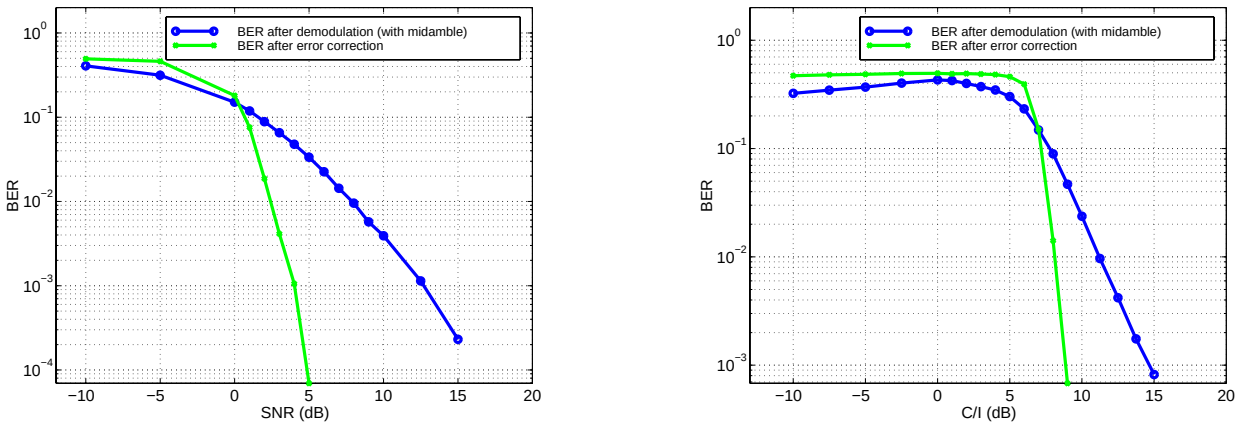

(a) (b)

Figure 4.27. Bit–error rate performance of stand-alone detector[Rau98]. (a) AWGN channel (no Rayleigh fading). (b) AWGN channel with interference (no Rayleigh fading). Note that the interference and noise level is sensed *after* the spatial pre–filter and not at the array input.

Apply the identification process to each spatially resolved signal $\mathbf{s}_{TS,l}$:

1. Detection: Use a standard sequence estimator to detect the bit sequence. As result we get soft decision bits, $\mathbf{b}_l$, and hard decision bits, $\tilde{\mathbf{b}}_l$.

$$\mathbf{b}_l = \text{detector}\{\mathbf{s}_{TS,l}\} \tag{4.5.1}$$

$$\tilde{\mathbf{b}}_l = \text{sign}\{\mathbf{b}_l\} \tag{4.5.2}$$

where

$$\text{sign}\{x\} = \begin{cases} +1 & \text{if } x > 0, \\ -1 & \text{otherwise.} \end{cases} \tag{4.5.3}$$

2. Calculate the number of bit errors, $n_{BER,l}$, within the midamble:

$$n_{BER,l} = \frac{26 - \tilde{\mathbf{b}}_l \mathbf{b}_{TS,K_u}^T}{2}, \tag{4.5.4}$$

where $\mathbf{b}_{TS,K_u}$ holds the 26 bits of the *known* user midamble.

3. Classification: The DOA, ϕ_l, corresponding to the signal $\mathbf{s}_{TS,l}$ is marked as user DOA, if the number of bit errors is smaller than the threshold θ_{BER}:

$$\phi_l = \begin{cases} \longrightarrow \hat{\phi}_{U,l} & \text{if } n_{BER,l} \leq \theta_{BER}, \\ \longrightarrow \hat{\phi}_{I,l} & \text{otherwise.} \end{cases} \tag{4.5.5}$$

4. Post-correlation (optional): If the DOA is marked as a user DOA, check whether the detected bit sequence resembles the known user training sequence best: Calculate the correlation of $\mathbf{b}_l$ with all possible training sequences, $\mathbf{b}_{TS,k}$

$$\nu_k = \mathbf{b}_l \mathbf{b}_{TS,K_u}^T. \tag{4.5.6}$$

If the maximum *does not* occur for the wanted user training sequence,

$$\arg\max_k \{\nu_k\} \neq K_u, \tag{4.5.7}$$

the current DOA is marked as interferer. Otherwise the decision of the detection process is verified and the DOA is attributed to the user.

Table 4.8. Summary of **UID**.

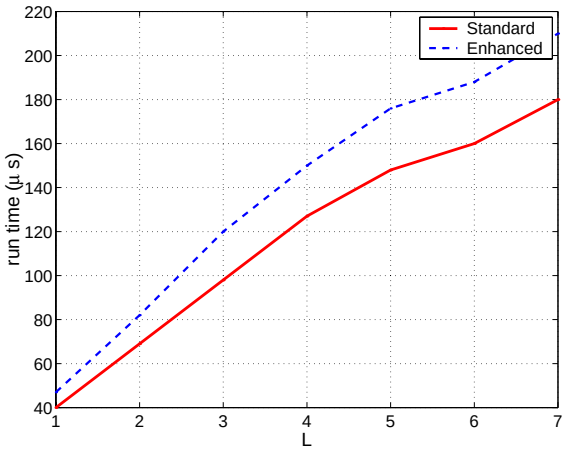

Figure 4.28. Average run–time of **UID** in a typical scenario. The enhanced configuration includes the post–correlation, the standard configuration is without the post–correlation.

is computed. When the **UID** decides that the l–th DOA corresponds to a user signal, i.e. when $n_{BER,l} \leq \theta_{BER}$, the post–correlation is applied to verify the decision. Then $\mathbf{b}_l$ is correlated with *each possible* training sequence[5]. If the maximum of these correlations occurs for the *user* training sequence, which is of course known to the BS, then the identification is verified, $\hat{\phi}_l \longrightarrow \hat{\phi}_{U,l}$. If, however, the correlation with any other training sequence is larger than the correlation with the user training sequence itself, the decision is canceled and the current signal (DOA) is classified as an *interferer* DOA, $\hat{\phi}_l \longrightarrow \hat{\phi}_{I,l}$.

Table 4.8 summarizes the user identification algorithm. How the post–correlation influences the overall system performance will be assessed in Chapter 5.

4.5.2 Run–time of user identification

I measured the average run–time of the user identification (**UID**) in a typical, synthetic mobile radio channel (Fig. 4.28). The run–time depends nearly linearly on the number of DOAs, because the main effort is spent in the detector. The post correlation increases the run–time only by about 18%.

4.6 Tracker

After the user identification, basically all information is at hand that allows directing the main beam into a user direction and nulling the interferer DOAs: estimated and classified DOAs and the corresponding power values. **A^{3}P** collects information from the current burst only, information from previous bursts is not yet used[6]. I will equip the tracker (**DOAT**) with a concept that exploits the knowledge collected from past bursts. This will significantly increase the robustness against severe interference and finite angular spread.

Interfering signals and the user signals often are incident from the same angular range. This does not necessarily mean that their LOS directions are close in angle. But if each signal, user and interferer, have many multipath components, the probability of an overlap in angle is large.

[5] In GSM 8 training sequences are used.

[6] An exception occurs when **PASTd** with burst–to–burst tracking is applied.

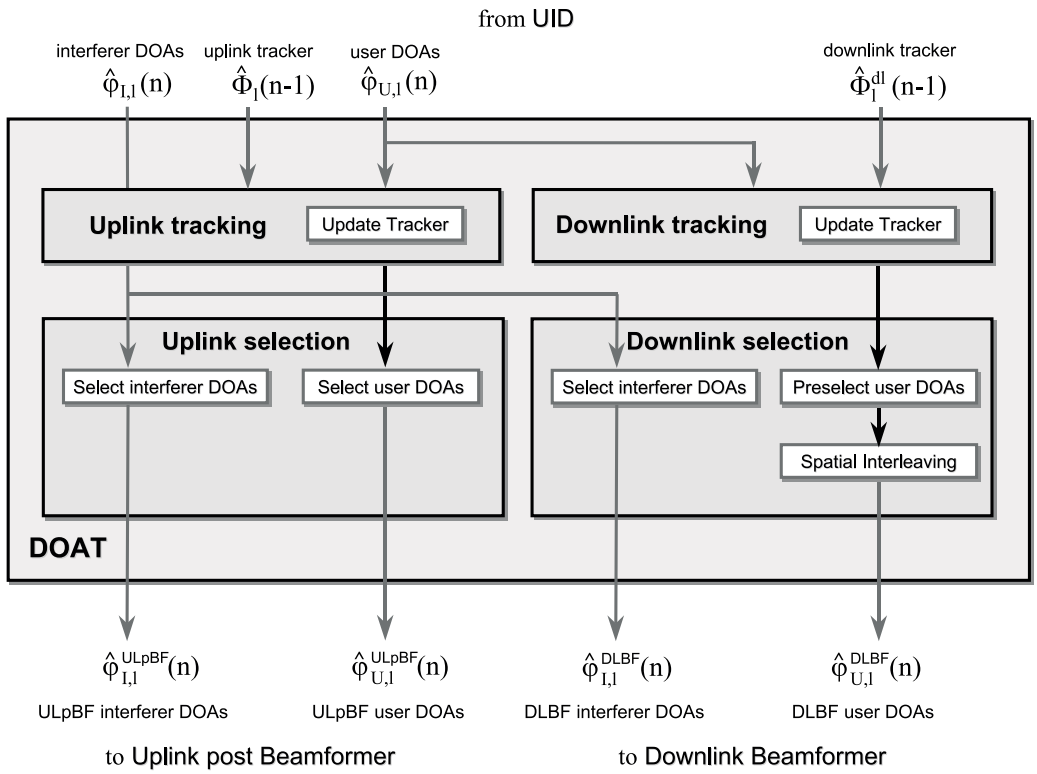

Figure 4.29. Schematic of the DOA tracker (**DOAT**).

In such situations, the probability of an erroneous identification by the **UID** will be increased. A main beam that is directed into an erroneously identified user direction is fatal: the burst will typically be lost. Here the tracker comes into play. It allows placing a main beam into a direction only, if the direction is proven to carry a user signal.

The finite angular spread in mobile radio cells can become quite large, even in macro–cells [PMF97]. This degrades the reliability of DOA estimators that rely on a planar wave model (Fig. 4.18). The larger the angular spread, the more far–off estimates are likely. I will present a tracking scheme that is based on a bank of independent filters. Although far–off estimates are also tracked, they will not influence the trackers of the user multipath components. Hence, far-off estimates cannot cause significant harm when the main beam is steered.

I only track *user* DOAs, because interferer DOAs may change from burst–to–burst with frequency hopping and dynamic channel assignment. For uplink and for downlink, I apply separate trackers because the averaging in downlink requires larger memory length. The **DOAT** mainly performs two tasks (Fig. 4.29): tracking of the DOAs, and selection of DOAs for final beamforming. Each of these tasks is done separately for uplink and downlink.

4.6.1 Tracking scheme

The present tracker does not only average the DOAs. It also collects information that allows quantification of the reliability of an identified user DOA. This will achieve a considerable increase in system robustness.

The tracking algorithm is based on a bank of independent Kalman filters [CC91]. A single tracker $\Phi_l(n)$ is updated with an estimate of a user DOA $\hat{\phi}_{U,l}$ if $|\hat{\phi}_{U,l} - \Phi_l(n)| < \theta_\phi$, i.e. when

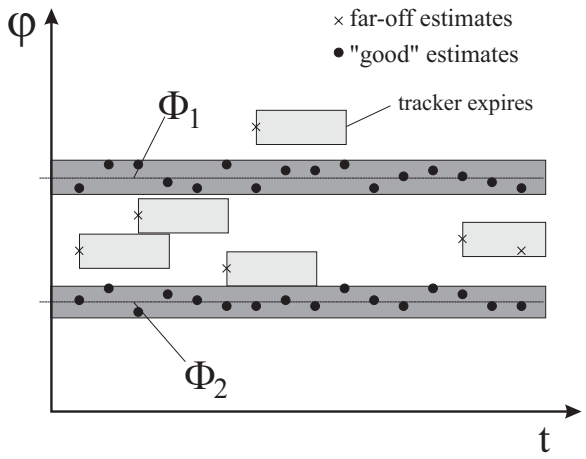

Figure 4.30. User DOAs and trackers in an environment with two mulitpaths. In each burst the current user DOAs are applied to update the existing trackers. A tracker is updated only, if a close-by user DOA is present in the current burst. If not, a new tracker is initialized.

the estimated DOA is close-by the tracker. The threshold θ_ϕ is typically some degrees. Thus I map each estimated DOAs on a single tracker. If there is no close–by tracker available, a new tracker is initialized. Figure 4.30 illustrates this effect. Here I assume that two multipath components are available (dark shaded regions). Correspondingly, two trackers, $\Phi_1(n)$ and $\Phi_2(n)$, are already initialized. When a far–off estimate (crosses) occurs, a new tracker will be initialized. If such a single tracker is not updated on a regular basis I assume it to be an artifact, caused by either an erroneous identification of a supposed user DOA or by far–off estimates. After 50 bursts of being not updated the tracker expires and is deleted. Thus trackers of far–off estimates will vanish after some time (light shaded regions). This principle allows suppressing the influence of the far–off estimates on the final beamforming process. Not only this, but the fact that the single trackers are *independent* guarantees that an artifact will not influence the other trackers at all.

A tracker may also expire because the signal becomes insignificant, i.e. its average power is 25dB smaller than the average power of all other trackers.

After the update, trackers that are too close in angle (angle difference $\leq 3°$) are combined.

The selection of the DOAs requires additional data that is collected for each tracker:

- Reliability
  To increase the system robustness, I have to make sure that the main beam does not look into *unreliable* directions, i.e. directions that have high probability not the carry user signals. I therefore define the reliability of a single tracker:

The *reliability* of a single tracker, $\Phi_l(n)$, is the total number of its updates.

  I will use the reliability to guarantee optimum robustness in the selection process.

- Instantaneous uplink power
  Although tracking implies *averaging* of the DOAs, I still allow instantaneous changes of the main beam direction by selecting the DOAs according to the instantaneous signal powers of the incident waves. The estimated user DOA $\phi_{U,l}$ corresponds to a spatially

resolved signal $\hat{\mathbf{s}}_{TS,l}$. The power of the spatially resolved signal

$$P_l = \hat{\mathbf{s}}_{TS,l}\hat{\mathbf{s}}_{TS,l}^H \tag{4.6.1}$$

is the estimate for the instantaneous uplink power of the signal incident from $\phi_{U,l}$. Since $\phi_{U,l}$ updates the tracker Φ_l, P_l is attributed to the l–th tracker.

- Average uplink power
  For the downlink I base the selection of user DOAs on average power values measured in uplink, i.e. I assume that the average power value (and therefore the mean path loss) is the same in uplink and downlink. The average uplink power is defined as,

$$\overline{P}_l(n) = \overline{P}_l(n-1)\beta_{T,max} + P_l(1-\beta_{T,max}) \tag{4.6.2}$$

  i.e. I apply an exponential averaging with the same time constant as for the tracker.

DOA tracking I will summarize the main results of the used Kalman tracker, for details I refer to [KTRS98], [KTRS97a]. The tracking is equivalent to an exponential weighted averaging, where the weight changes adaptively according to the estimation error (error covariance) [CC91].

$$\Phi_l(n) = \Phi_l(n-1)\,\beta_T(n) + \hat{\phi}_{U,l}\,(1-\beta_T(n)), \tag{4.6.3}$$

where $\Phi_l(n)$ is the tracked DOA after updating with the currently identified user DOA $\hat{\phi}_{U,l}$, $\Phi_l(n-1)$ is the tracker state of the previous burst, and $\beta_T(n)$ is the averaging weight.

$$\mu_T(n) = 1/(1-\beta_T(n)) \tag{4.6.4}$$

is the effective memory length (EML); a large EML means that the tracker averages over a large number of bursts. For the details of how to compute $\beta_T(n)$ please refer to [KTRS98]. Although $\beta_T(n)$ and thus $\mu_T(n)$ are implicitly given by the Kalman filter, I have the freedom to set the maximum memory length, $\mu_{T,max}$. Figure 4.31 illustrates the effect of $\mu_{T,max}$. I generated $N_{bursts} = 5000$ Gaussian distributed DOA estimates, $\phi_{u,l}$, with a standard deviation of 3° and a mean angle of $\phi_0 = 30°$. Then I applied Eq. 4.6.3 with two different settings of $\mu_{T,max}$. Finally I compute the root mean square error of the tracker

$$\varepsilon_T = \sqrt{\frac{1}{N_{bursts}}\sum_{l=1}^{N_{bursts}}(\Phi(n)-\phi_0)^2}. \tag{4.6.5}$$

Since the tracker is initialized with the first DOA, it may take more than 100 bursts (or 0.5s) until the tracker is close to the correct user DOA. In Fig. 4.31(b) the root mean square (RMS) tracking error after initialization is of course smaller, because the averaging is more pronounced. For maximum EML of $\mu_{T,max} = 100$ (1000), the RMS error is $\varepsilon_T = 0.5°$ ($\varepsilon_T = 0.28°$). If we also take the initialization phase into account, the errors are larger: 0.79° and 0.96°. The RMS tracking error is then larger when $\mu_{T,max} = 1000$, because the initialization takes longer.

I also tested the standard tracker in a non–stationary environment. Here I assumed a rather fast change of ϕ_0 over time (Fig. 4.32). To judge the angular change over time, the abscissa is scaled in seconds, corresponding to the number of bursts multiplied with the duration of a GSM frame. The mobile's angular velocity is roughly $0.08\,rad/s$, which gives a velocity of about $30km/h$ ($300km/h$) if the mobile is $100m$ ($1000m$) away from the BS. The comparison of

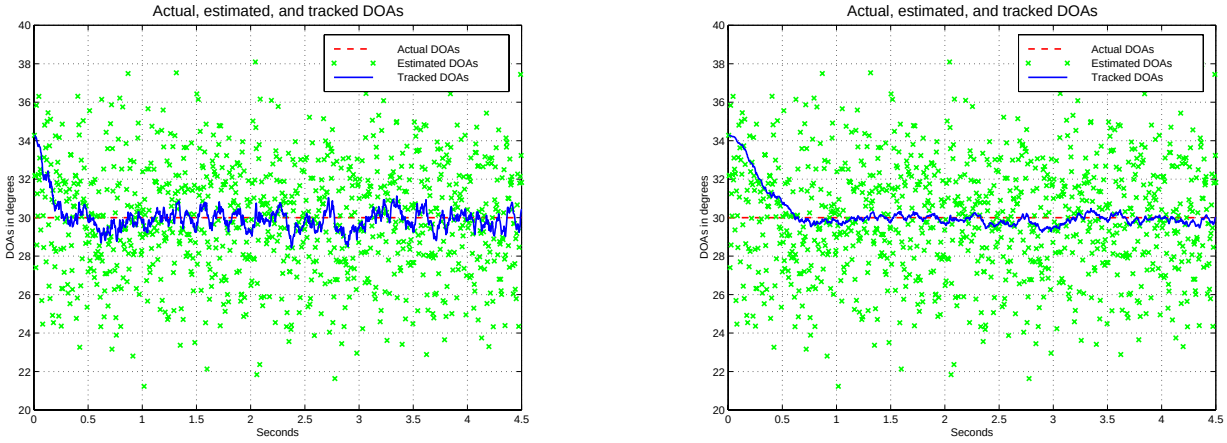

(a) (b)

Figure 4.31. Simulated tracking behaviour for a stationary scenario with an angular spread of 3°. (a) $\mu_{T,max} = 100$ bursts, (b) $\mu_{T,max} = 1000$ bursts.

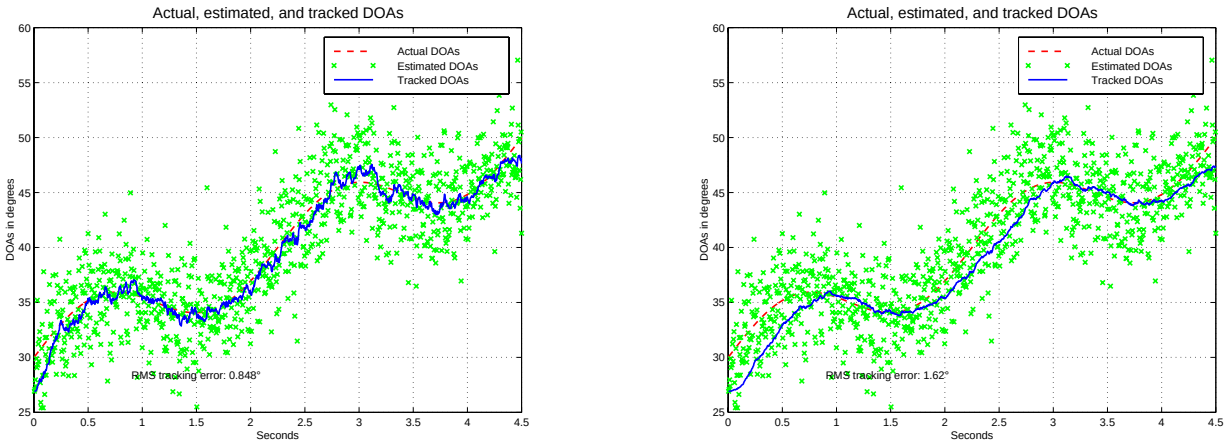

(a) (b)

Figure 4.32. Tracking behaviour of standard tracker for a non–stationary scenario with an angular spread of 3°. (a) $\mu_{T,max} = 100$ bursts, (b) $\mu_{T,max} = 1000$ bursts.

the different memory length settings reveals the typical behavior of a tracking algorithm. The larger the averaging effect (large $\mu_{T,max}$) the smoother the tracked DOAs. However, the RMS tracking error will increase when the tracker cannot follow the fast changes of the user DOA completely. This is the case for $\mu_{T,max} = 1000$, where $\varepsilon_T = 1.6°$. The error is then nearly twice as large as in the case of $\mu_{T,max} = 100$ ($\varepsilon_T = 0.8°$).

Optimum tracker setting I investigated the optimum tracker EML setting, i.e. the optimum $\mu_{T,max}$ to obtain minimum RMS tracking error, for the stationary and non–stationary sample scenario. To get statistically more reliable results I simulated 100 runs and averaged the RMS error over all runs. Each run consists of $N_{bursts} = 5000$ bursts for each $\mu_{T,max}$ setting. The angular spread of the scenarios was fixed to 3°. To remove the influence of the initialization phase, I plot ε_T for two different sets of data (see Fig. 4.33). The solid line shows the RMS error when *all* bursts have been included, while the other curve did not take the first 500 bursts, i.e. the initialization phase, into account.

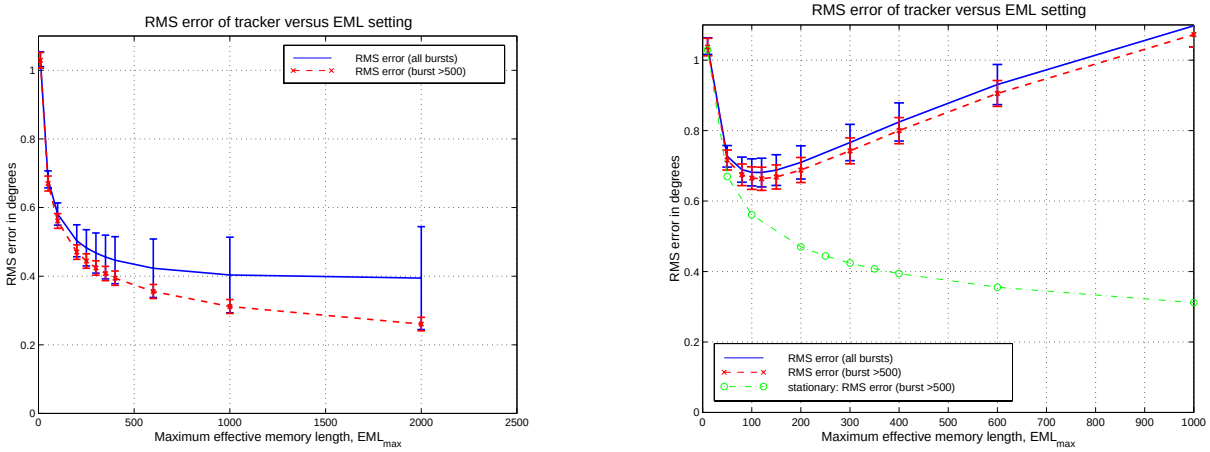

(a) (b)

Figure 4.33. RMS tracking error, ε_T, versus effective memory length setting, $\mu_{T,max}$. (a) Stationary scenario, (b) non–stationary scenario ($0.08 rad/s$ or $\approx 5^\circ/s$), including also a result of the stationary scenario for comparison. Error bars indicate one standard deviation of the test data. For each setting of $\mu_{T,max}$, 5000 bursts were simulated.

For the stationary scenario I find that the RMS tracking error decreases monotonically with increasing maximum effective memory length $\mu_{T,max}$. This is clear, because the nominal DOA was fixed to $\phi_0 = 30°$ and the more averaging the smaller the tracking error. However, I see that the tracking error decreases only slightly for larger $\mu_{T,max}$. A closer look at the results reveals that by increasing $\mu_{T,max}$ by a factor of 10, the RMS tracking error is approximately reduced by a factor of 1.8.

For the non–stationary scenario as shown in Fig. 4.32 the situation is different. Here I find a significant minimum in the tracking error for $\mu_{T,max} = 110$. The tracking error for the stationary scenario (dashed–dotted line in Fig. 4.33(b)) is a lower tracking error bound for scenarios with $AS = 3°$, i.e. the tracking error for any corresponding non–stationary scenario is larger. The RMS error for small $\mu_{T,max}$ ($mu_{T,max} < 110$) is nearly the same as in the stationary case, whereas it increases significantly for larger $\mu_{T,max}$ settings. If $\mu_{T,max} \gg 110$ the tracker cannot follow the fast changes of the DOAs and the tracking error increases. However, the optimum $\mu_{T,max}$ setting strongly depends on the angular velocity of the user.

4.6.2 Selection of DOAs for final beamforming

The tracker provides all information necessary for a reliable selection of the direction of the main beam. User DOAs for the final uplink post (downlink) beamforming are selected from the uplink (downlink) tracker. The directions of the nulls are selected from instantaneously estimated DOAs classified as interferers.

Uplink DOA selection The number of user DOAs that are selected for the uplink post beamforming is either $D = 1$ or $D = 2$. In the case of angular *selection* diversity the single strongest multipath, $\phi_{U,1}^{ULpBF,1}$, is selected ($D = 1$):

$$\phi_{U,1}^{ULpBF} = \Phi_l|_{l=\arg\max_l\{P_l\}} \tag{4.6.6}$$

Correspondingly, $\mathbf{A}^3\mathbf{P}$ can also extract $D = 2$ weight vectors to collect the energy from the two strongest multipaths; then angular *combining* diversity can be realized. In the following I assume $D = 1$.

The selection of the final user DOA is not only based on the signal power. Additionally I include a condition that assures that a reliable tracker is selected: A tracker has to be updated more than 10 times, before it can be selected. Although this sounds to be a severe restriction, it will actually help to avoid the selection of far–off estimates or of erroneously identified interferer DOAs.

To illustrate the angular selection diversity I set up a synthetic scenario with two user DOAs (a local scatterer and far scatterer contribution) and two interferer components (Fig. 4.34(a)). The scenario includes an angular spread of 3° of each multipath. In Fig. 4.34(b) I present the DOAs for 400 sample bursts. Each dot represents an estimated DOA (regardless of being a user or interferer DOA). In the first half (burst 1 to 200) the solid lines show the initialized trackers. We can clearly identify the two trackers for Path A and Path B of the user. Additionally there is a tracker artifact that resulted from an far–off DOA estimate ("far–off" tracker). However, this tracker expires after 50 bursts, because it was only updated once. Most important, this DOA will *never* be selected as main beam direction, because the tracker was not updated often enough. In the second half (burst 201 to 400) of the graph I plot the selected user DOAs, $\phi_{U,1}^{ULpBF}$, instead of the tracker. Here we can see the angular selection diversity at work. The main beam hops between the two trackers according to the instantaneous power.

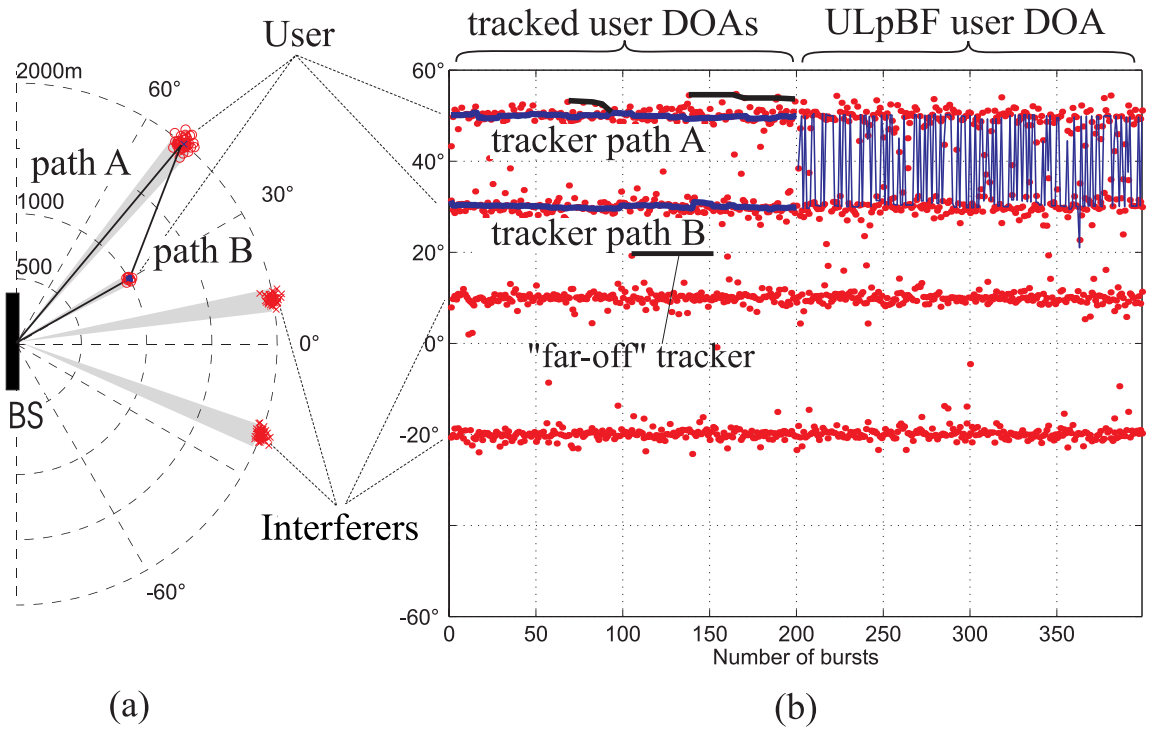

Figure 4.34. (a) Sample channel scenario for urban macro–cell environment. User signals are incident from 50° (local scatterers, path A) and 30° (far scatterers, path B), interferer DOAs from −20° and 10°. (b) DOAs of 400 sample bursts. I include the estimated DOAs (dots) and in the first 200 bursts all tracked DOAs (solid line). From burst 201 to 400 I illustrate the angular selection diversity, i.e. I plot the selected user DOA for final beamforming. However, tracking and angular selection diversity is operative over all 400 bursts.

In the next step the interferer DOAs are selected. For the beamforming an interferer means that a null is placed in the direction of the interferer. However, it is not necessary to force deep nulls in directions where only low power interferer are present. Other angular ranges — except the range of the main beam(s) — are suppressed according to the sidelobe level. I therefore place only nulls into the direction of interferers that have relative powers larger than −10dB. Here the relative power is the interferer power normalized to the *minimum* power of a selected tracker, i.e. I assure that an interferer may only be disregarded for beamforming if its power is small compared to the smallest user power.

Downlink DOA selection The selection of the DOAs for downlink beamforming follows the same principle as for the uplink post beamforming. Since the small–scale fading on the uplink and on the downlink is uncorrelated (frequency duplex), the current power at the downlink is unknown. Therefore the selection of user DOAs for downlink beamforming is based on average power values. I assume that the average power value (and therefore the mean path loss) is the same in uplink and downlink.

$$\phi_{U,1}^{DLBF} = \Phi_l^{dl}|_{l=\arg\max_l\{\overline{P}_l\}} \tag{4.6.7}$$

I suggest to use only one user DOA for downlink beamforming at a time.

Spatial Interleaving

Situations with changing shadowing might be critical. Therefore I apply *spatial interleaving*. Spatial interleaving is activated when more than one tracker has been *pre*selected for downlink beamforming. Since it does not make sense to transmit into a direction with large path loss (compared to the other directions), I preselect only those trackers that have similar average power (ratio between largest and smallest average power of the preselected trackers is smaller than 3dB). The concept of spatial interleaving means that I do not always select the same DOA (the one which fulfills Eq. 4.6.7), but switch the preselected DOAs from burst to burst. This means that the beam hops from one direction in one burst to another direction in the next burst (Fig. 4.35).

This concept shall improve the link quality especially in cases when one multipath component disappears and a new path appears. In the transition phase the average power of both directions will be on the same order, and therefore the spatial interleaving will be activated automatically.

For the selection of interferer DOAs in the downlink I apply the same strategy as in the uplink.

4.6.3 Summary tracker

The developed tracking concept has a single goal: improve the system's robustness, but do not degrade the SNR gain. The robustness can be improved by averaging, i.e. collecting knowledge over many bursts, before an actual decision where the main beam points to, is done. But this reduces the possibility to instantaneously react to the current channel situation and thus optimize the SNR gain. With the present tracking concept I found a compromise that allows instantaneous (burst–wise) hopping of the main beam, while simultaneously reaching very high reliability.

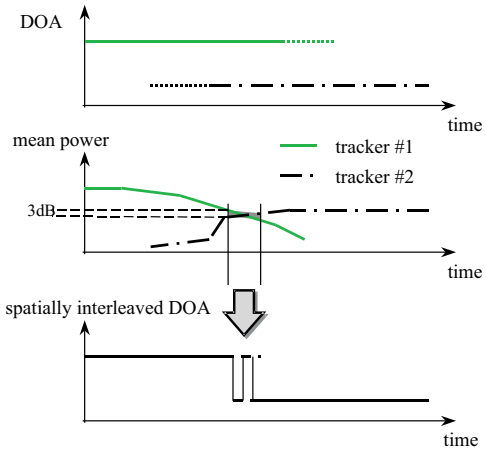

Figure 4.35. Principle of spatial interleaving at the downlink. The uppermost (lowest) figure sketches the tracked DOAs before (after) spatial interleaving. The mean power of the two paths (tracked DOAs) is plotted in the middle figure.

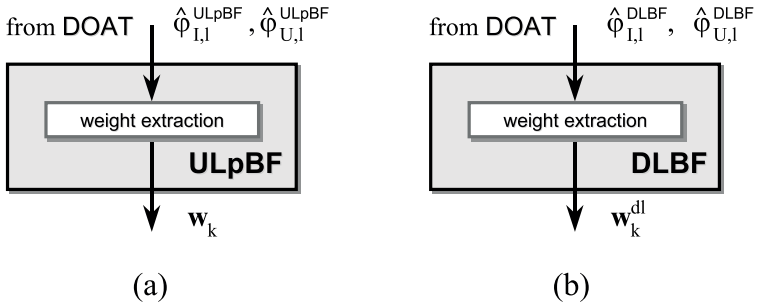

Figure 4.36. Schematic of the (a) uplink post beamformer (**ULpBF**) and (b) downlink beamformer (**DLBF**).

The concept consists of *independent* trackers. Each single tracker tracks (averages) the *user* DOA of a multipath component. Additionally, I measure the reliability of each tracker. A large reliability means that the tracked DOA *really* includes a signal originated from the user with good enough signal quality. I accomplish an *instantaneous* adaptation to the current channel situation by directing the main beam into the direction of the strongest tracker. The inherent angular selection diversity results in a beam hopping when more multipath components are present for the user. To guarantee the high robustness, only reliable enough tracker directions may be selected.

Finally I have a list of questions that I will answer in Chapter 5: How does the increased reliability affect the overall performance? Actually, what benefits do we gain? What is the optimum averaging constant of the tracker, i.e. the influence of the averaging? Does tracking significantly reduce the diversity gain?

4.7 Signal reconstruction – beamforming

The last task of **A**^{3}**P** is to compute the weight vectors for the uplink and downlink beamforming. To do so, I apply beamforming algorithms [TKL$^+$99] that place a main beam into the selected user DOA and *broad* nulls into the directions of the selected interferer DOAs. Note that the situation differs significantly to the pre–spatial filtering (**ULBF**). After the user identification I know whether a DOA belongs to a user or to an interferer. Also, the tracker has rendered the estimated DOAs more reliable.

The algorithms of the uplink post beamformer **ULpBF** and of the downlink beamformer **DLBF** are exactly the same, except that different input DOAs are applied (Fig. 4.36). Here I denote the user DOAs with $\hat{\phi}_U$ and the interferer DOAs with $\hat{\phi}_I$. In the case of the **ULpBF** $\hat{\phi}_U = \hat{\phi}_U^{UlpBF}$ and $\hat{\phi}_I = \hat{\phi}_I^{UlpBF}$, and similarly for the **DLBF**.

4.7.1 Broad null beamforming

Placing broad nulls (Fig. 4.37) to suppress interfering multipath components has several advantages compared to conventional sharp nulls:

- Imperfections in the hardware (mutual coupling, gain and phase imbalances) and non-ideal calibration cause the effective pattern to deviate from the theoretical one. Filled and shifted nulls will be the result. This may be disastrous in mobile communication

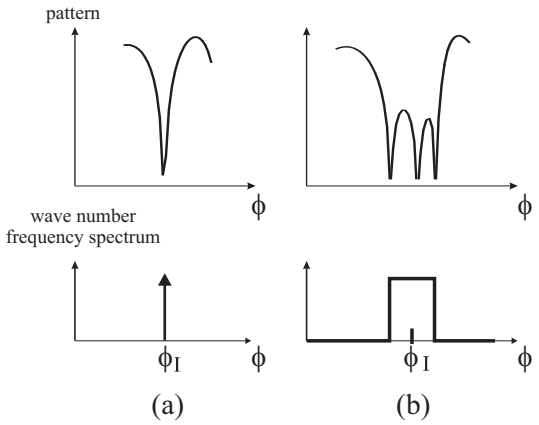

Figure 4.37. Concept of broad null beamforming. Portion of the antenna pattern (above) and wave number–frequency spectrum (below): (a) Dirac–shaped wave number–frequency spectrum; (b) smeared wave number–frequency spectrum.

systems, when the interferer suppression is based on sharp nulls. But broad nulls will guarantee a sufficient interferer suppression, because there will remain an effective null even if the nulls are shifted or filled up slightly.

- When the angular spread of the interfering components is large, a sharp null cannot provide sufficient suppression at all.
- When the angular spread is small, broad nulls relax the requirements on the DOA estimators, because the interferer DOA does not have to be known exactly.

The basic idea of the beamforming algorithm **SmearR** [TKL+99] is to *avoid* a Dirac–shaped wave number–frequency spectrum[7] for the interferers. Instead we use a wave number–frequency spectrum for each interferer that is broadened to achieve broad nulls in the antenna pattern (Fig. 4.37).

The covariance matrix is *not* computed from the steering vectors of the interfering signals, $\mathbf{a}(\hat{\phi}_{I,i})$, but from "smeared" versions of the interferer steering vectors,

$$\tilde{\mathbf{a}}(\hat{\phi}_{I,i}) = \mathbf{a}(\hat{\phi}_{I,i}) \odot \mathbf{v}(\hat{\phi}_{I,i}) \ , \quad 1 \leq i \leq \hat{L}_I \ . \tag{4.7.1}$$

where $\odot$ denotes element–wise multiplication. Here $\mathbf{a}(\hat{\phi}) = [1, e^{-jk\Delta \sin(\hat{\phi})}, \ldots, e^{-j(M-1)k\Delta \sin(\hat{\phi})}]^T$ denotes the steering vector of the DOA, $\hat{\phi}$, for a uniform linear array[8]. Δ is the distance between antenna elements and $k = 2\pi/\lambda$ the wave number. $\mathbf{v}(\hat{\phi}_{I,i})$ is the inverse Fourier transform of each interferer wave number–frequency spectrum sampled at the antenna elements, in our case

$$\mathbf{v}(\hat{\phi}_{I,i}) = ND_i \left[1, \frac{sin(\delta_i)}{\delta_i}, \ldots, \frac{sin((M-1)\delta_i)}{(M-1)\delta_i}\right] \ , \tag{4.7.2}$$

[7] The wave number–frequency spectrum is defined as the discrete Fourier transform of the array response [JD91]. In the special case of a plane wave incident on a uniform linear array the wave number–frequency spectrum consists of a Dirac impulse, and the corresponding array response is the steering vector.

[8] However, the algorithm is not limited to uniform linear arrays.

where $\delta_i = (NW/2) \cdot \pi \cos(\hat{\phi}_{I,i})$ denotes the half of the desired normalized null width, NW, and ND_i an interferer dependent weighting constant that determines the null depth. Equation 4.7.2 and Fig. 4.37(b) show an example for a rectangular shaped wave number–frequency spectrum in beam space, but any arbitrarily shaped wave number–frequency spectrum can be applied as well. This 'smeared' wave number–frequency spectrum guarantees the broad nulls in the pattern.

To obtain an adjustable sidelobe level we modify the steering vector of the user DOA, $\mathbf{a}(\hat{\phi}_U)$, with a noise term. In beam space the noise term has a constant wave number–frequency spectrum outside the main beam and is zero in the main beam region with a width of BW:

$$\tilde{\mathbf{a}}(\phi_U) = \mathbf{a}(\phi_U) \odot \mathbf{v}_N \ , \tag{4.7.3}$$

where the shaping vector,

$$\mathbf{v}_N = \left[1, \frac{2sin(BW'/2)}{2\pi - BW'}, \ldots , \frac{2sin((M-1)BW'/2)}{(M-1)(2\pi - BW')}\right] \ , \tag{4.7.4}$$

corresponds to the shape of the wave number–frequency noise spectrum. Thus a large nominal beam width, BW, gives a low sidelobe level and vice versa. The actual beam width, BW', is given by $BW' = BW \cdot \pi \cos(\phi_U)$.

Now a modified steering matrix,

$$\tilde{\mathbf{A}} = [\tilde{\mathbf{a}}(\phi_U), \tilde{\mathbf{a}}(\phi_{I,1}), \ldots , \tilde{\mathbf{a}}(\phi_{I,\hat{L}_I})], \tag{4.7.5}$$

and finally a modified spatial covariance matrix,

$$\tilde{\mathbf{R}}_{SmearR} = \tilde{\mathbf{A}}\tilde{\mathbf{A}}^H \ , \tag{4.7.6}$$

can be computed and inserted in

$$\mathbf{w} = \tilde{\mathbf{R}}^{-1}_{SmearR} \cdot \mathbf{a}(\hat{\phi}_{U,1}) \ , \tag{4.7.7}$$

to get the weight vector. Eq. 4.7.7 is a modification of Capon's beamformer [CGK67]. Here we use the "smeared" covariance matrix, instead of the sample covariance matrix. Because the modified angular covariance matrix, $\tilde{\mathbf{R}}_{SmearR}$, has Toeplitz structure, the complex–valued Levinson algorithm [Lev47] can be used for very efficient calculation of $\mathbf{w}$.

An advantage of the described algorithm is the simple adjustment of the required pattern constraints by directly setting the parameters null width, NW, beam width, BW, and null depth, ND. The parameters can be set independently within wide limits, but, of course, are subject to physical constraints.

4.7.2 Conventional beamforming

As reference I will compare **SmearR** with the Pseudo Inverse (Eq. 4.4.4, p.57) that places sharp nulls.

4.7.3 Run–time of uplink post beamformer

The run–time of the beamforming algorithms depends mainly on the number of interferer DOAs, i.e. the number of nulls (Fig. 4.9). The Pseudo Inverse depends more strongly on the number of interferer DOAs than **SmearR**.

Algorithm	$\hat{L_I} = 1$	$\hat{L_I} = 5$
SmearR	40 μs	55 μs
Pseudo Inverse	66 μs	192 μs

Table 4.9. Run–time measurements of uplink post beamformer (**ULpBF**). $\hat{L_I}$ is the number of interferer DOAs, i.e. the number of nulls.

4.7.4 Measured antenna pattern of SmearR

I measured the antenna pattern of **SmearR** on the roof top in a controlled environment (Fig. 4.8) to assess the capability to suppress interference. Figure 4.38 compares some measured antenna pattern with the theoretical pattern. Here I assumed that the user DOA is $\phi_U = 0°$ and a single interferer at $\phi_I = -19°$. The focus in this measurement lay on the broad null that was placed into the interferer direction. The optimum measured pattern showed a null depth of about $25dB$. I obtained this result for the configuration where $NW = 10°$ and $ND = 30dB$. However, this configuration resulted in a significant misalignment of the main beam, because the main beam is shifted by about 5° into the direction of the interferer. Selecting the same null width, but a reduced null depth parameter ND [9] results in a measured null depth of about $18dB$ at $\phi_I = -19°$. For this case the main beam fits very well with theory.

Finally I checked different settings of the null width, NW. $NW = 1°$ resulted in an interferer suppression of only $15dB$. Clearly the sharp null is filled up (Fig. 4.38(c)). A null width of 1° is already to small to be realizable with the present hardware. In contrast, selecting a larger null width, $NW = 20°$ (Fig. 4.38(d)), reduced the null depth even further to only $13dB$. Additionally the main beam is now shifted away from the user DOA. The other extreme, a very large null width, is also problematic. Severe pattern constraints (null depth more than $30dB$ over an angular range of 20°, see Fig. 4.38(d)) result in a poor measured antenna pattern.

From the sample pattern measured I conclude that a potential interferer suppression capability of $25dB$ is present with the implemented system. As a result of the pattern measurements, optimum parameters for **SmearR** are $NW = 10°$ and $ND = 30dB$. However, in the overall picture, best agreement between measurements and theory was obtained for the configuration: $NW = 10°$ and $ND = 10dB$. I have used this configuration in the measurements (see following chapters).

4.8 A³P run–time

I present the average run–time of the entire **A³P** in a typical synthetic channel scenario [KTT+99a]. I configure **A³P** with a typical standard parameter set: as DOA estimator **Unitary ESPRIT** is applied, **ULBF** = **SmearR**, the **UID** uses post–correlation and **ULpBF** = **DLBF** = **SmearR**. Additionally to **A³P** 's calculations the smart antenna processor has to perform some additional tasks. The so–called preprocessing includes interfacing and the calibration of the input data. This part has a constant run–time of about $560\,\mu s$.

I measured the dependence of the run–time on the number of estimated DOAs. Figure 4.39(a) shows the run–time of each subtask of **A³P** as well as the sum of all **A³P** subtasks

[9] ND is the null depth parameter; the parameter ND does not correspond to the null depth in the antenna pattern. Setting $ND = 10dB$ does not mean that the null is only $10dB$ deep, as can easily checked from the theoretical curve. The influence of ND on the null depth is only implicitly given by the algorithm.

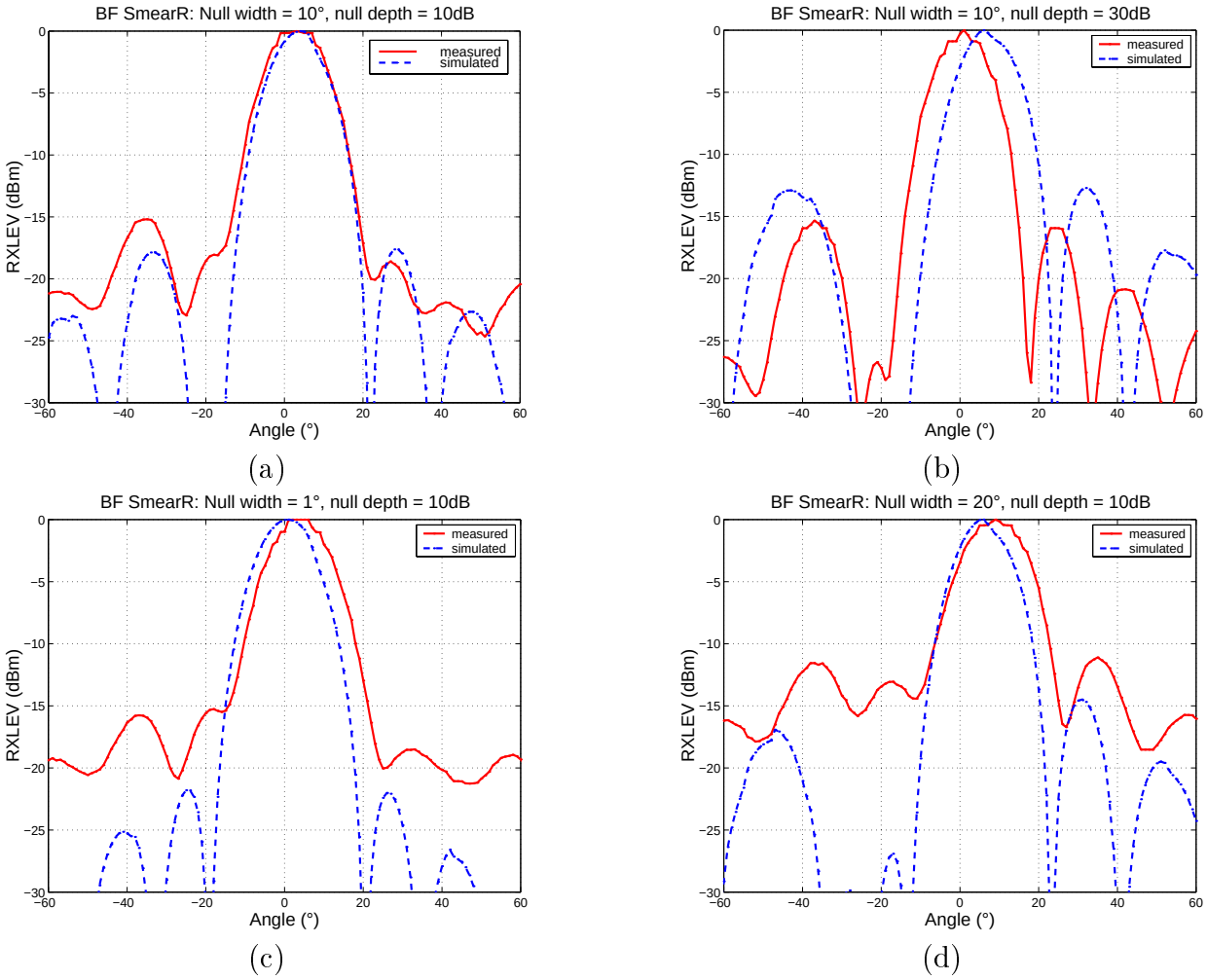

Figure 4.38. Measured and theoretical uplink antenna pattern of **SmearR**. The user DOA is $\phi_U = 0°$, the interferer DOA is $\phi_I = -19°$. **SmearR** with different parameter values of the null width parameter, NW, and null depth, ND. (a) $NW = 10°$ and $ND = 10dB$. (b) $NW = 10°$ and $ND = 30dB$. (c) $NW = 1°$ and $ND = 10dB$. (a) $NW = 20°$ and $ND = 10dB$.

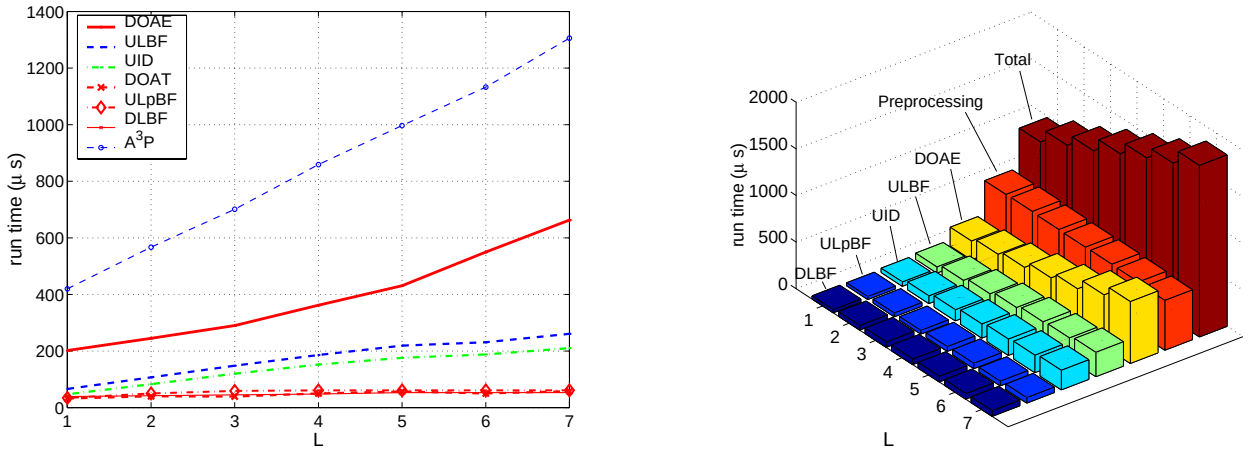

(a) (b)

Figure 4.39. Average run–time of the algorithms depending on the number of DOAs. (a) Run–time of each subtask and **A**^{3}**P**'s overall run–time. (b) Bar chart including the preprocessing and the total run–time.

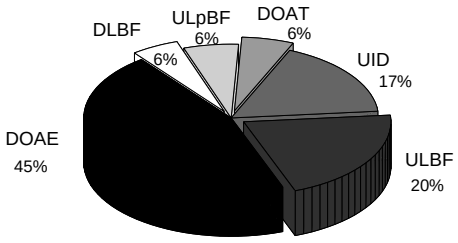

Figure 4.40. Relative run–time of **A**^{3}**P** in a typical scenario.

(**DOAE**, **ULBF**, **UID**, **DOAT**, **ULpBF**, and **DLBF**). For $L \leq 5$ the run–time of **A**^{3}**P** stays below $1ms$. A significant portion of the computational effort is spent in the **DOAE**. In a typical scenario this takes up 45% of **A**^{3}**P**'s processing (Fig. 4.40). The **DOAE**, **ULBF** and **UID** together make up 80%, the **DOAT** and the final beamforming need only 18%.

In Fig. 4.39(b) I also included the preprocessing. Then the total run–time of the smart antenna processor varies from about $1ms$ to $2ms$.

A^3**P** can spend about a frame duration of $4.6ms$[10] for the processing. After that period the input data of the next frame will be available. Because **A**^{3}**P**'s run–time is smaller than $2ms$, it is able to process *every* GSM burst. This allows adaptive beamforming *every* burst anew. As described in Chapter 2, **A**^{3}**P** in its current form, processes a single timeslot, out of eight. Thus we would require four processors of the kind of **A**^{3}**P** for a single carrier base station subsystem. However, **A**^{3}**P** is implemented on a general purpose processor, because this gave the most flexibility during development. This is not the optimum choice for a final implementation. The next step would be to check, which parts of the processing can be done in fixed point arithmetic and then select proper signal processors. This should reduce the hardware effort considerably.

[10] In practice, there is less time available, because the delay of any base band processing must be kept to a minimum.

Chapter 5

QUANTIFYING BENEFITS

The basic benefits of a smart antenna are increased *signal power* and reduced *interference*. This will result in a reduced bit error rate, hence an improved service quality. To fully exploit **A**^{3}**P**'s possibilities it is essential to understand how **A**^{3}**P** increases the system performance. Only this will allow to assess in which environments **A**^{3}**P** can be introduced with the largest possible gain. The bit error rate (raw or encoded) is a possible measure to assess a system, but it depends on the applied base band detector, the type of service (voice or data), ... Thus I will quantify **A**^{3}**P**'s benefits based on the *C/I gain* and *SNR gain*. This has an additional advantage: we will be able to better understand how the interference suppression depends on the power gain and vice versa, which in turn allows deeper insight into the mechanisms of a smart antenna system.

In this chapter I will investigate the influence of the various algorithms on the overall system performance based on measurement data. I will define the C/I (SNR) gain from the statistics of the C/I (SNR) values. For each subtask of **A**^{3}**P**, I will set up a scenario that illustrates the operation of the task. In the cases where it is not optimum, I will apply different configurations to find the optimum setting. Most importantly, these comparisons will result in answers to the list of questions that arose in the previous chapter:

- What is the influence of the DOA estimators on the SNR and C/I gain?
- Do we really need high–resolution DOA estimators to achieve optimum performance?
- How does the user identification affect the system?
- What is the effect of the tracker?
- Does interferer nulling work?
- Will broad nulls increase the system robustness?

To assess the performance of a smart antenna we have basically two possibilities — (i) simulations and (ii) field trial. Simulations are the proper choice when no measurements are possible. This is typically the case at the beginning of a development. They have the advantage that system parameters are easy to control, and that a system can be assessed with different algorithms on comparable data. Of course, the disadvantage is that simulations will never include all effects of a system in a real environment. In most cases the effect of imperfections of the system on the performance is not clear and thus the engineer does not know in advance which imperfections should be included in a model.

Field trials are a proper choice when the system has been verified and optimized. Then a field trial will allow to study the behavior of the smart antenna in different environments. Imperfections are now included in the data, but their effect cannot easily be studied, because

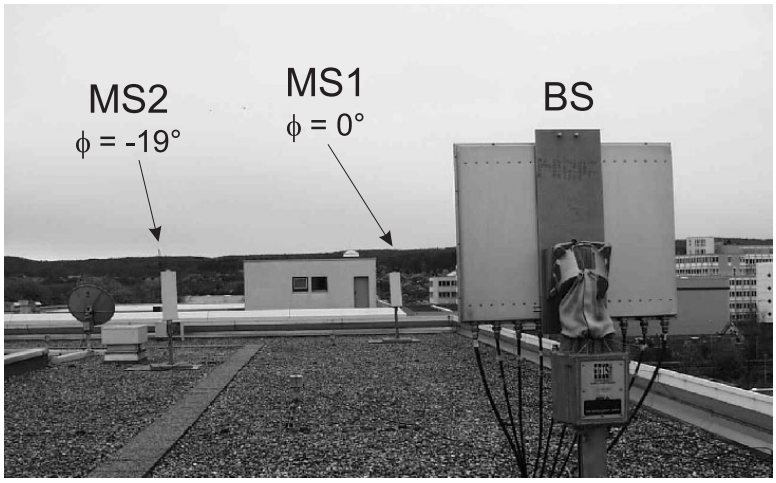

Figure 5.1. Controlled measurement environment on the roof top of the Alcatel building. There are two signal sources with LOS to the BS present: a GSM mobile station (MS1, user) and a continuos wave (MS2, interferer) signal generator. The two mobiles are angularly separated by 19° and have a LOS to the base station array.

field measurements do not allow a repeated evaluation of the smart antenna in *exactly* the same environment. At best, one can repeat the measurement along the same route. With **A**^{3}**P** two configurations can be compared simultaneously, but this still does not leave enough room for a thorough study of an algorithm.

In this work, I try to combine the advantages of both approaches: I assess **A**^{3}**P** with *simulations* based on *stored measurement* data. The data will include the typical imperfections of a "real world" system. But still it leaves the possibility of repeated processing of exactly the same data with different algorithms.

5.1 Measurements in a controlled environment

Before assessing **A**^{3}**P** with measurement data from the field, we confirmed the basic functionality of the system in a controlled environment [KTT+99b]. The array and two mobile stations (MS) antennas were placed on top of the roof of the Alcatel building (Fig. 5.1). The mobiles had line–of–sight (LOS) to the base station array and were angularly separated by 19°. The measurement scenario was static during the tests.

5.1.1 BER performance in an AWGN channel

I measured the raw BER in an additive white Gaussian noise (AWGN) channel. The MS and the BS are linked via a traffic channel with no interferer present. BER measurements were performed over a period of $10s$ or 2000 bursts for each SNR setting.

A^3**P**'s BER is compared to the BER of a single antenna with the same input data. From Fig. 5.2 the expected SNR gain of approximately $9dB$ over the single antenna is evident. Measurements and theory show excellent agreement.

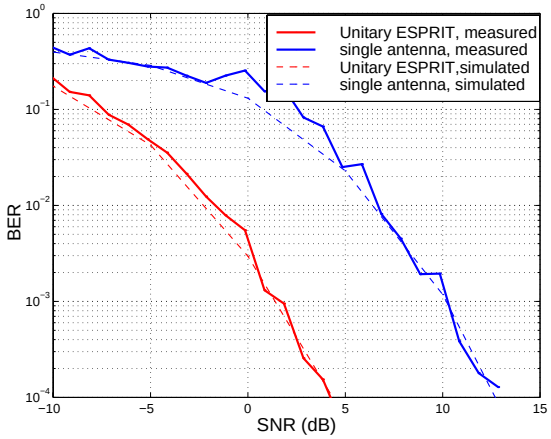

Figure 5.2. Raw BER of the **A**^{3}**P** in an AWGN channel.

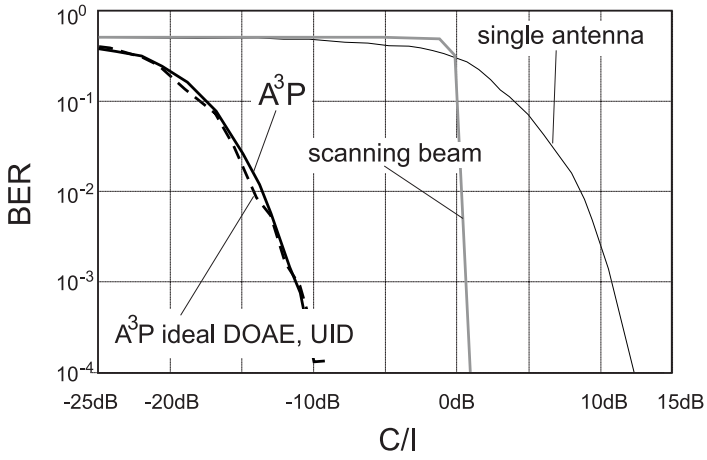

Figure 5.3. Raw BER of **A**^{3}**P** in a static channel with continuous wave interferer for an input SNR of $28dB$.

5.1.2 Interference suppression capabilities

To quantify the interference suppression capability, I measured the raw bit error ratio (BER) of the MS with an interfering continuous wave (CW) signal present. The user was positioned at $\phi = 0°$ and had constant power with an input SNR of $28dB$. The interferer, with varying power, was located at $\phi = -19°$. As references I used a scanning beam algorithm and a single antenna.

Scanning beam The scanning beam algorithm, as it is implemented in the BFCU, steers 128 regularly spaced, fixed beams and selects the signal corresponding to the beam that receives the most power. For later post–processing I also implemented the scanning beam algorithm with an angular resolution of 1°. First, I calculate the angular power spectrum (Eq. 4.3.27, p.54) at time index n, $P_{APS}(\phi_k, n)$, for all angles $\phi_k = -90 + (k-1)$, $k = 1 \ldots 181$. The scanning beam algorithm will return the DOA that gives maximum power

$$\phi_{SB}(n) = \arg\max_k P_{APS}(\phi_k, n), \tag{5.1.1}$$

and the corresponding output power

$$P_{SB}(n) = \max_k P_{APS}(\phi_k, n). \tag{5.1.2}$$

The scanning beam algorithm is a refined switched beam system, where the beamforming is realized in digital domain. Of course it is optimized for situations where no interference is present. Thus the scanning beam gives satisfactory BER only as long as the user signal is stronger than the interferer, i.e. for $C/I > 0dB$.

In contrast, **A³P** is much more robust against interference (Fig. 5.3). It gives a BER of 1% at an input C/I of $-14dB$. Another curve (**A³P** ideal **DOAE**, **UID**) quantifies the achievable interference robustness if the user and interferer DOAs would be known a priori. In this ideal situation, the interference suppression is only limited by the residual imperfections, e.g. receiver phase and amplitude imbalances *after* calibration. In the LOS scenario, **A³P** reaches the optimum performance, indeed.

5.2 Measures for performance evaluation

For the thorough assessment of **A³P**, we have stored uplink input data during field measurements, where a *single* mobile was active in each measurement. To model interference, I superpose several (typically two) of these measurements, each with a single transmitting signal source, and process the data off–line.

With this strategy I can evaluate the *same* data set with many different configurations of **A³P**. From a few data sets a large number of scenarios can be generated. Not only this, but also the fact that I know the part of the signal that is originated from the interference, is of advantage, because only then I can calculate the carrier–to–interference ratio. One disadvantage is that the noise contribution is unknown and therefore the noise power has to be measured separately to calculate the signal–to–noise ratio.

5.2.1 Measurement modeling — generating scenarios

A GSM signal is characterized by the training sequence. **A**^{3}**P** distinguishes the user signal from an interferer signal by this user identifier. Thus the interfering signal *must* use a training sequence different from that of the user. To generate the input data of **A**^{3}**P**, $\mathbf{X}$, for a certain scenario, I proceeded as follows:

- Measure the noise power
  To measure the noise power, P_N, the MS was deactivated. Then P_N can simple be measured from the input data on each antenna element $\tilde{\mathbf{x}}_{no\,user,m}$

$$P_N = \frac{1}{N_{bursts}\, M\, N_{symbols}} \sum_{n=1}^{N_{bursts}} \sum_{m=1}^{M} ||\tilde{\mathbf{x}}_{no\,user,m}(n)||_2. \tag{5.2.1}$$

  Here I calculate a mean noise power by averaging over all antenna elements and over many thousand bursts. Theoretically the noise power level should be the same for all antenna elements. In practice, the variation of the noise power over the antenna elements is on the order of $1dB$. The resulting average noise power was measured to be $P_N = -110.3dBm$.

- Measure the user signal
  In the next measurement, the mobile station (MS) transmitted with a certain training sequence, say training sequence number 0. The MS was placed in a van, with the mobile's antenna on the car's roof (Fig. 5.4). A voice traffic channel was built up between the MS and the BS. While the van drove along a measurement route, the input data at the array was logged and stored burst–by–burst in $\tilde{\mathbf{X}}_{user}(n) \in \mathbb{C}^{8\times 156}$, $n = 1 \ldots N_{bursts}$. Typically the number of bursts is $N_{bursts} = 5000$.

  The power of the received signal, including wanted signal and noise, at the m–th antenna element is

$$\tilde{P}_{S,m} = \frac{1}{N_{symbols}} ||\tilde{\mathbf{x}}_{user,m}||_2, \tag{5.2.2}$$

  where $N_{symbols} = 156$ is the number of samples in a GSM burst. $\tilde{\mathbf{x}}_{user,m}$ is the m–th row of the matrix $\tilde{\mathbf{X}}_{user}$. $||\mathbf{x}||_2$ is the $\mathcal{L}_2$–norm of the vector $\mathbf{x}$. Under the assumption of uncorrelated noise and user signal, the signal power at the m–th antenna element, $P_{S,m}$, can be obtained from

$$P_{S,m} \approx \tilde{P}_{S,m} - P_N. \tag{5.2.3}$$

  Of course this is only valid, if $\tilde{P}_{S,m} > P_N$, which was the case during the measurements.

- Measure the interfering signal
  To store an interferer signal, $\tilde{\mathbf{X}}_{intf,k}$, I repeat the procedure of the user measurement. The only difference is that the MS now transmits with a different training sequence.

  Of course it is possible to take more than a single interferer into account, thus the interference signal is labeled with index k.

- Generate a scenario
  Finally I sum up the different signal contributions to get the input signal

$$\mathbf{X} = \tilde{\mathbf{X}}_{user} + \tilde{\mathbf{X}}_{intf,\Sigma}, \tag{5.2.4}$$

$$\tilde{\mathbf{X}}_{intf,\Sigma} = \sum_{k=1}^{K_I} \tilde{\mathbf{X}}_{intf,k}, \tag{5.2.5}$$

  where K_I is the number of interferers taken into account. Thus I have generated a synthetic scenario with one user and K_I interferer signals. In Eq. 5.2.4 I assumed synchronous interference, i.e. that user and interferer signal are temporally aligned. This assumption will be relaxed in Chapter 6.

In practice, we have performed a large number of measurements on different routes with different training sequences. From these measurement signals, I selected the user and interferer signals to generate a certain measurement scenario.

Noise contributions The proposed approach differs from a field measurement *with* interference only by the fact that here more noise contributions are summed up. If I assume that these noise signals are uncorrelated, I can take their effect easily into account by summing up the noise *powers*. Then the SNR is modified corresponding to the sum of the noise powers. But if the noise would be correlated, the situation is worse. The total noise power would then be larger than the sum of the single power terms, i.e. the actual SNR is smaller than the calculated SNR. This would lead to an underestimation of $\mathbf{A}^3\mathbf{P}$'s performance.

Power control During the measurements the GSM power control was deactivated. However, before the logging of a measurement route took place, we chose the mobile's transmit power in a way to assure a received signal at the BS in the order of $-70dBm$. (Of course, in some measurements where the path loss was too high also smaller power levels occur.) The input data therefore include the small–scale fading and shadowing.

5.2.2 Definition of SNR and C/I

Before I start with the evaluation, let me define the various quantities, which I use to measure the performance of $\mathbf{A}^3\mathbf{P}$. I will assess the measurement data based on the *statistics of the signal–to–noise ratio (SNR)* and *the carrier–to–interference ratio (C/I)*. While the first is an important quantity in noise–limited environments, i.e. when we study the sensitivity enhancement, the C/I will tell how well $\mathbf{A}^3\mathbf{P}$ can suppress interference.

Signal–to–noise ratio The SNR describes, how the *signal* power is enhanced over the noise power. Because I have the separate *user* signal, $\tilde{\mathbf{X}}_{user}$, at hand, an SNR can easily be calculated. Even, if interference is present, the signal power, $P_{S,m}$, is available. But then there is an additional noise term as a consequence of the "interferer noise power terms", $\mathbf{N}_{intf,k}$, $k = 1 \ldots K_I$ that has to be taken into account for the SNR calculation. The total *interferer noise power* is

$$P_{N,I} = K_I P_N, \tag{5.2.6}$$

while the *user noise power* is

$$P_{N,U} = P_N, \tag{5.2.7}$$

Figure 5.4. Van with measurement equipment.

where the noise floor is $P_N = -110.3dBm$.

Definition: The input user SNR at the m–th antenna element in the n–th burst is defined as

$$SNR_{in,m}(n) = \frac{P_{S,m}(n)}{(P_{N,I} + P_{N,U})}. \tag{5.2.8}$$

$P_{S,m}$ is defined in Eq. (5.2.3). Note that also the interferer noise power has to be taken into account.

This definition assumes that the noise is uncorrelated with the information signal, and equal at all antenna elements and for all measurements. The input SNR is defined for each antenna element separately.

A^3**P**'s processing results in the n–th burst in a weight vector, $\mathbf{w}(n)$, for the uplink beamforming. Now we can calculate the user SNR *after* beamforming:

Definition: The *output user SNR*, $SNR_{out}(n)$, of the n–th burst is defined as

$$SNR_{out}(n) = \frac{||\mathbf{w}(n)^H \tilde{\mathbf{X}}_{user}(n)||_2 - P_N}{(P_{N,I} + P_{N,U})}, \tag{5.2.9}$$

where $\mathbf{w}(n)^H \tilde{\mathbf{X}}_{user}(n)$ is the estimated user signal after beamforming. The weight vector is normalized,

$$\mathbf{w}(n) = \frac{\mathbf{w}(n)}{\sqrt{M}\max_m\{w_m(n)\}}, \tag{5.2.10}$$

i.e. the maximum weight amplitude is $1/\sqrt{M}$.

A comment on the normalization: The normalization affects the SNR, because the SNR is calculated from an absolute noise power. Normalizing the weights to get a constant maximum weight amplitude assures that the SNR is correctly calculated. If I would normalize the weight vector to $||\mathbf{w}(n)||_2 = 1$, the effect of the tapering (see p. 89) would not be included in the SNR, leading to a seemingly larger SNR gain than actually achievable. To demonstrate this, let us assume that the most outward elements are not used. The not normalized weight vector looks e.g. $\mathbf{w} = [0\,1\,1\,1\,1\,1\,1\,0]$. The normalization would then result in $\mathbf{w}_{norm1} = 1/(\sqrt{8})\mathbf{w}$, if I apply Eq. (5.2.10), and $\mathbf{w}_{norm2} = 1/(\sqrt{6})\mathbf{w}$, if I force $||\mathbf{w}||_2 = 1$. Consequently the average SNR gain would be $10\log 6 = 7.8dB$ for $\mathbf{w}_{norm1}$, and in the other case $10\log 8 = 9dB$ for $\mathbf{w}_{norm2}$. Obviously, the first result is the correct one, because a 6–element array can only improve the SNR by 7.8. If the *norm* of the weight vector is kept constant, we simply would disregard the tapering loss (see Eq. (5.2.30), p.89).

Carrier–to–interference ratio With the same reasoning as for the user signal, I compute the interferer power

$$P_{I,m}(n) = \tilde{P}_{I,m}(n) - P_{N,I} \tag{5.2.11}$$

$$\tilde{P}_{I,m}(n) = \frac{1}{N_{symbols}}||\tilde{\mathbf{x}}_{intf,\Sigma,m}(n)||_2, \tag{5.2.12}$$

where $\tilde{\mathbf{x}}_{intf,\Sigma,m}$ is the m–th row of the matrix $\tilde{\mathbf{X}}_{intf,\Sigma}$. Here, of course, we have to consider the interferer power term. The C/I is only defined when interference is present.

Definition: The *input C/I*, $C/I_{in,m}(n)$, at the m–th antenna element of the n–th burst *prior* to beamforming is defined as

$$C/I_{in,m}(n) = \frac{P_{S,m}(n)}{P_{I,m}(n)}, \tag{5.2.13}$$

if $P_{I,m}(n) > 0$.

In this definition I again assume that any information bearing signal parts are uncorrelated to the noise. Consequently the output C/I *after* beamforming is:

Definition: The *output C/I*, $C/I_{out}(n)$, of the n–th burst *after* beamforming is defined as

$$C/I_{out}(n) = \frac{||\mathbf{w}(n)^H \tilde{\mathbf{X}}_{user}(n)||_2 - P_{N,U}}{||\mathbf{w}(n)^H (\tilde{\mathbf{X}}(n) - \tilde{\mathbf{X}}_{user}(n))||_2 - P_{N,I}}, \tag{5.2.14}$$

where $\mathbf{w}(n)$ is the normalized beamforming vector.

Again I have to distinguish between the noise power term of the user and the interferer signal.

Signal–to–interference and noise ratio A signal–to–interference and noise ratio (SNIR) can be calculated from the C/I and SNR, if interference is present, i.e. if $C/I(n) > 0$.

$$SNIR(n) = \frac{SNR(n)}{\left(1 + \frac{SNR(n)}{C/I(n)}\right)} \tag{5.2.15}$$

Here I assume that the wanted (signal) and unwanted signal components (interference) are uncorrelated. The SNIR is, of course, defined at the input and at the output.

In principle, I will focus on the C/I and SNR separately. Only in situations where it is not clear, whether the SNIR is dominated by interference or by noise, I will present SNIR values. For all other situations the SNIR is approximately

$$SNIR(n) \approx \begin{cases} SNR(n) & \text{if } C/I(n) \gg SNR(n), \\ C/I(n) & \text{if } SNR(n) \gg C/I(n). \end{cases} \tag{5.2.16}$$

5.2.3 Definition of C/I gain and SNR gain

I will assess the overall system performance based on the SNR gain and the C/I gain that I define from the cumulative distribution functions (CDF) of the SNR and C/I. When I assess a scenario, I generate the input data with the following procedure:

1. Apply $\mathbf{A}^3\mathbf{P}$ to N_{burst} bursts: To get a reliable statistic, I typically evaluate $N_{burst} = 5000$ bursts. From this evaluation I get 5000 SNR and C/I values.

2. Calculate the distributions of the various SNR and C/I values:

$$\mathcal{C}_{in,m}^{SNR} = \text{cdf}\{SNR_{in,m}\}, \tag{5.2.17}$$
$$\mathcal{C}_{out}^{SNR} = \text{cdf}\{SNR_{out}\}, \tag{5.2.18}$$
$$\mathcal{C}_{in,m}^{C/I} = \text{cdf}\{C/I_{in,m}\}, \tag{5.2.19}$$
$$\mathcal{C}_{out}^{C/I} = \text{cdf}\{C/I_{out}\}, \tag{5.2.20}$$

where $\text{cdf}\{\cdot\}$ estimates the CDF from the sample data. Basically, I calculate a histogram, i.e. a discrete PDF, and integrate the PDF to obtain the CDF.

3. Extract from these distributions the gain values:

Definition: The SNR gain and the C/I gain at the m–th antenna element at a certain probability level, γ, are

$$\Delta SNR_m^{\gamma} = SNR|_{\mathcal{C}_{out}^{SNR}=1-\gamma} - SNR|_{\mathcal{C}_{in,m}^{SNR}=1-\gamma}, \tag{5.2.21}$$
$$\Delta C/I_m^{\gamma} = SNR|_{\mathcal{C}_{out}^{C/I}=1-\gamma} - SNR|_{\mathcal{C}_{in,m}^{C/I}=1-\gamma}. \tag{5.2.22}$$

I define the *SNR gain*, ΔSNR^{γ}, and *C/I gain*, $\Delta C/I^{\gamma}$, as the average over all antenna elements

$$\Delta SNR^{\gamma} = \frac{1}{M}\sum_{m=1}^{M} \Delta SNR_m^{\gamma}, \tag{5.2.23}$$
$$\Delta C/I^{\gamma} = \frac{1}{M}\sum_{m=1}^{M} \Delta C/I_m^{\gamma}. \tag{5.2.24}$$

In this work I choose two values for the probability threshold: $\gamma = 99\%$ and $\gamma = 90\%$. A result is then interpreted as: The SNR gain, $\Delta SNR^{99\%}$ at the 1% probability, is the difference of the input and output SNR at the corresponding probability level. Note that I have not defined the gain values from statistics of the gain values. Although this would tell, e.g. that the C/I gain is in 99% of the time larger than e.g. $15dB$, this is *not essential*. Instead it is essential which output SNR (C/I) level is exceeded in 99% of the time.

SNR gain

Beamforming and diversity gain I want to distinguish between, basically, two effects that influence the statistics of the output SNR:

- The *beamforming gain* is that part of the SNR gain that is achieved by the combination of the M antenna elements. The beamforming principle relies on coherent waves incident at the array. If a single wave is incident, no fading is present, i.e. $SNR_{in,m} = SNR_{in}$, for $m = 1 \ldots M$, its theoretical maximum is $G_b = 10 \log M = 9dB$ (for $M = 8$). In a mobile radio environment, with fading present, I define the beamforming gain as the *average*

SNR gain.

Definition: The *beamforming gain*, G_b, is the average SNR gain, $\overline{\Delta SNR}$,

$$G_b = \overline{\Delta SNR} = \overline{SNR_{out}} - \overline{SNR_{in}}, \tag{5.2.25}$$

$$\overline{SNR_{in}} = \frac{1}{N_{bursts}\, M} \sum_{n=1}^{N_{bursts}} \sum_{m=1}^{M} SNR_{in,m}(n), \tag{5.2.26}$$

$$\overline{SNR_{out}} = \frac{1}{N_{bursts}} \sum_{n=1}^{N_{bursts}} SNR_{out}(n). \tag{5.2.27}$$

Three effects cause the degradation of the beamforming gain:

1. Tapering: The weight vector, $\mathbf{w}$, consists of M complex weights, w_m,

$$\mathbf{w} = [w_1 \ \ldots \ w_M]. \tag{5.2.28}$$

When *tapering* occurs,

$$||\mathbf{w}||_2 < 1, \tag{5.2.29}$$

i.e. some of the complex weights, w_m, have smaller amplitudes than others[1].Tapering results principally in a reduction of the output SNR. What causes the weight amplitudes to be smaller than others? The pattern shaping, i.e. the minimization of the sidelobe level and placing nulls in the antenna pattern.

Definition: The average *tapering loss*, L_{tap}, is defined as

$$L_{tap} = \frac{1}{N_{bursts}} \sum_{n=1}^{N_{bursts}} \frac{1}{||\mathbf{w}(n)||_2}. \tag{5.2.30}$$

With L_{tap} I am able to separate the effect of the tapering on the reduction of G_b, from the following two effects that also reduce G_b.

2. Angular spread: If the angular spread of the user signal is larger than the main beam width, $\mathbf{A}^3\mathbf{P}$ cannot collect all user energy. This results in a reduced output SNR. A remedy is to apply more than one main beams.
3. Wrong main beam directions: When the main beam looks into a wrong direction, the output SNR will be reduced significantly. However, this will only occur, if the interference situation is severe.

- *Diversity* is an averaging effect that combats fading.

Definition: I define the *diversity gain*, G_{div}^{γ}, at a probability level γ as

$$G_{div}^{\gamma} = \Delta SNR^{\gamma} - \overline{\Delta SNR}. \tag{5.2.31}$$

[1]Note that $\mathbf{w}$ is normalized so that the maximum absolute value of a complex weight is $1/\sqrt{M}$5.2.10.

The consequences of this definition becomes clearer when we look at the following cumulative distribution functions (CDF): The CDF of the average input SNR, $\mathcal{C}_{in}^{\overline{SNR}}$, and the CDF of the sum of the input SNRs, $\mathcal{C}_{in,\Sigma}^{SNR}$,

$$\mathcal{C}_{in}^{\overline{SNR}} = \mathrm{cdf}\{\frac{1}{M}\sum_{m=1}^{M} SNR_{in,m}\}, \tag{5.2.32}$$

$$\mathcal{C}_{in,\Sigma}^{SNR} = \mathrm{cdf}\{\sum_{m=1}^{M} SNR_{in,m}\}. \tag{5.2.33}$$

$$\tag{5.2.34}$$

In Fig. 5.5 I illustrate the averaging effect. It presents $\mathcal{C}_{in,m}^{SNR}$ (CDF of single input SNR), $\mathcal{C}_{in}^{\overline{SNR}}$ (CDF of average input SNR) as well as $\mathcal{C}_{in,\Sigma}^{SNR}$ (CDF of sum input SNR). In the NLOS case, the input SNRs are not correlated. Then the averaging process decreases the probability of small SNR values. Thus $\mathcal{C}_{in}^{\overline{SNR}}$ has a steeper slope than $\mathcal{C}_{in,m}^{SNR}$. The slope of the CDF gives the order of diversity offered by this particular channel with the current antenna configuration. When we read the gain at the 99% (90%) level, we find an diversity gain of $9.5dB$ ($4.4dB$). This is the maximum diversity gain that a smart antenna system with the current antenna configuration in this particular scenario can obtain.

The total gain consists of a diversity gain and a beamforming gain. The algorithm that achieves the theoretical optimum output SNR is maximum ratio combining (MRC) [Jak74]

$$SNR_{out,MRC} = \sum_{m=1}^{M} SNR_{in,m}. \tag{5.2.35}$$

Thus, $\mathcal{C}_{in,\Sigma}^{SNR}$ is also the CDF of the optimum output SNR, $\mathcal{C}_{out,opt}^{SNR}$, that can be achieved theoretically

$$\mathcal{C}_{out,opt}^{SNR} = \mathrm{cdf}\{SNR_{out,MRC}\} = \mathcal{C}_{in,\Sigma}^{SNR}. \tag{5.2.36}$$

In the LOS case $\mathcal{C}_{in}^{\overline{SNR}} \approx \mathcal{C}_{in,m}^{SNR}$, because nearly no fading is present (Fig. 5.5(b)). Then, of course, we find *no* diversity gain. Here the maximum total gain will only consist of the $9dB$ beamforming gain. Some CDFs of the SNR give the impression of an underlying two–hump, non–monotonous PDF. This is a property of the measurement scenario; evidently the path loss has changed. This can be seen from the input SNR of the single antenna elements.

An alternative definition would have involved the diversity gain relative to the theoretical maximum beamforming gain and not relative to the average SNR gain. This makes sense when a system (e.g. switched beams) has an average SNR gain of $9dB$. But otherwise it does not allow accounting for the effect of a reduced beamforming gain.

Having defined the quality measures for the smart antenna system, I will start with the evaluation of **A**^{3}**P**.

5.3 DOA estimation resolution and robustness

In the first evaluation I will investigate the influence of the DOA estimation on the overall performance. I will apply **A**^{3}**P** with different algorithms as DOA estimator (Sect. 4.3, p.32).

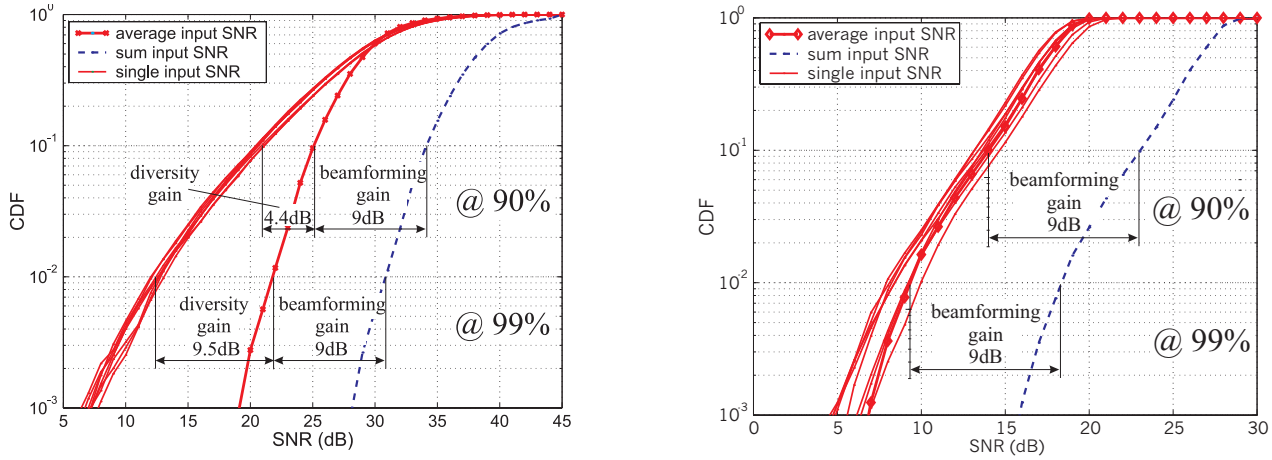

Figure 5.5. Measured exemplary statistic of the input SNR ($\mathcal{C}_{in,m}^{SNR}$ ... CDF of single input SNR, $\mathcal{C}_{in}^{\overline{SNR}}$ ... CDF of average input SNR, $\mathcal{C}_{in,\Sigma}^{SNR}$ ... CDF of sum input SNR). (a) NLOS scenario. (b) LOS scenario.

Here I want to find out whether **MVM**, which gave the best estimation quality (see Sect. 4.3.7, p.47), will give the highest gain values as well. I will then vary the resolution of **MVM** to get an idea about the required DOA estimation resolution. But first, I will define two scenarios with which I will assess the **DOAE**.

Scenarios A and A' The Scenarios A and A' consist both of two signals, Signal 1 and Signal 2, which were measured with LOS to the BS, but still have rather different properties (Fig. 5.6). To get an idea about the directional characteristic of the signals, I applied the scanning beam algorithm (see p.82). The result were the DOAs with largest power, $\phi_{SB}(n)$. From these I calculated the *variation of the strongest DOAs over 100 bursts*,

$$\sigma_{SB}(n) = \sqrt{\frac{1}{100}\sum_{k=n}^{n+99}\left(\phi_{SB}(k) - \overline{\phi}_{SB}(k)\right)}, \tag{5.3.1}$$

where the average DOA is

$$\overline{\phi}_{SB}(k) = \frac{1}{100}\sum_{k=n}^{n+99}\phi_{SB}(k). \tag{5.3.2}$$

$\sigma_{SB}(n)$ is the second central moment of the strongest DOAs in a time window of 100 bursts (not to be confused with the angular spread). This is a measure for the angular range in which the strongest waves are incident. The variation of the strongest DOAs better describes a scenario than the angular spread[2].

In the following I will use the word "angular spread" not as the definition for the quantity *angular spread*, but for the qualitative observation whether signals are incident from a small or large angular range. Sometimes I will use it as synonym for $\sigma_{SB}(n)$, typically when I point out the difference between two scenarios.

Signal 1 has a clear LOS to the BS, which results in a small angular spread, $\sigma_{SB} \approx 0.5°$. The signal power varies only by a few dB. The situation is different for Signal 2. Here, the angular spread is significantly larger ($\sigma_{SB} \approx 5°$), and correspondingly the fading is more pronounced. Actually, the MS had a quasi–LOS to the BS that was obstructed by trees and cars. For Signal 2 the MS was standing close to buildings, leading to significant local scattering.

From Signal 1 and Signal 2 I generate the Scenarios A and A' by letting either Signal 1 (for Scenario A) or Signal 2 (for Scenario A') to be the user signal, while the other signal acts as an interferer. Because of the simplicity of the scenarios, it will be easier to understand the influence of the **DOAE**. Obviously these scenarios are favorable for a DOA based smart antenna system. We do not only have either a user or an interferer signal with small angular spread (Signal 1), but the user and interferer DOAs are far apart in angle. With Scenario A I will be able to find the optimum C/I gain.
In the following, I will apply the **DOAE** in various configurations. I start with a standard

[2]The angular spread is defined as the second central moment of the angular power spectrum. Typically the angular power spectrum is measured with a rotating beam. This results in an angular spread that is significantly increased because of the large width of the main beam. A correction of this angular spread by the main beam width is not trivial, because the main beam width itself depends on the nominal DOA (for endfire direction the main beam is broader than for broadside direction). If the angular spread is not corrected, we get an average angular spread of 31° for Signal 1 (LOS) and 26° for Signal 2 (NLOS). Evidently those numbers are not helpful in understanding the environment. The reason for the larger angular spread in the case of the LOS signal lies in the broader main beam width at around $\phi = 40°$ than at $\phi = -20°$ (Signal 2).

A³P standard configuration		
Subtask	Algorithm	Configuration
DOAE	**MVM**	$R_f = 0.1°$, $R_c = 1°$
ULBF	Pseudo Inverse	—
DOAT	—	$\mu_{T,max} = 100$
UID	enhanced	$\theta_{BER} = 1$, with post–correlation
ULpBF	**SmearR**	$NW = 10°$, $ND = 10dB$

Table 5.1. Initial standard configuration of **A³P**.

configuration (Tab. 5.1) and when I apply a different configuration I will always specify only the difference to the standard setting.

Absolute SNR and C/I gain Here I discuss the absolute gain obtained for the standard configuration. The C/I gain is very high for both scenarios (Fig. 5.7, Tab. 5.2). The interference can be suppressed by as much as $25dB$! Of course, $\Delta C/I^{\gamma}$ is higher when the angular spread of the interferer is smaller. Thus Scenario A' yields a by 2dB higher C/I gain than Scenario A. This proves that the C/I suppression originates, at least partly, from interferer nulling and not *only* from low side lobes.

The beamforming gain is slightly larger for Scenario A than for Scenario A'. For Scenario A, $G_b = 7dB$, while it is $1.2dB$ smaller for Scenario A'. That **A³P** does not reach the optimum beamforming gain in Scenario A is mainly a consequence of the tapering. Without the tapering loss the optimum gain would nearly be reached, $G_b + L_{tap} = 8.7dB$. For Scenario A' the tapering loss is slightly larger. Let's take a look on the differences in the selected user and interferer DOAs for the two scenarios (Fig. 5.8(b) and (d)). In Scenario A' we sometimes find bursts where an interferer DOA (cross) is close to a user DOA (circle). This puts severe requirements on the beamforming algorithms, because it must place a broad null close to the main beam. Hence, the tapering is more pronounced. The nulls close to a user DOA also will cause an unwanted shift of the main beam, and thus a reduction in G_b.

The diversity gain is, in contrast to the beamforming gain, larger for Scenario A'. At the 1% level it is $G_{div}^{99\%} = 2.6dB$ for Scenario A' and $G_{div}^{99\%} = 0.6dB$ for Scenario A. Of course, this is a consequence of the different angular spread for the user signal. Practically, there is no diversity gain to obtain in Scenario A, because almost no fading of the user signal is present. This can also be seen from the CDF of the theoretical optimum output SNR (Fig. 5.7(a)); it has the same slope as the input SNR statistic. In Scenario A', the theoretical diversity gain is much larger. **A³P** cannot fully exploit this, because interference is present. Note that the theoretical optimum output SNR does not take the current interference situation into account. It just defines the upper bound for the SNR, under the assumption of *no* interference[3]. For every interferer DOA that has to be nulled, the system looses at least one degree of freedom (for sharp nulling) that otherwise could be used to exploit diversity.

To summarize, **A³P** achieves excellent interferer suppression, but non–optimal SNR improvement. This is what we would expect in a interference limited scenario, where the input SNR is about 30dB.

[3]Also the optimum combining algorithm that reaches the optimum SNIR would not exploit the diversity, but instead suppress interference, because this environment is strictly interference limited.

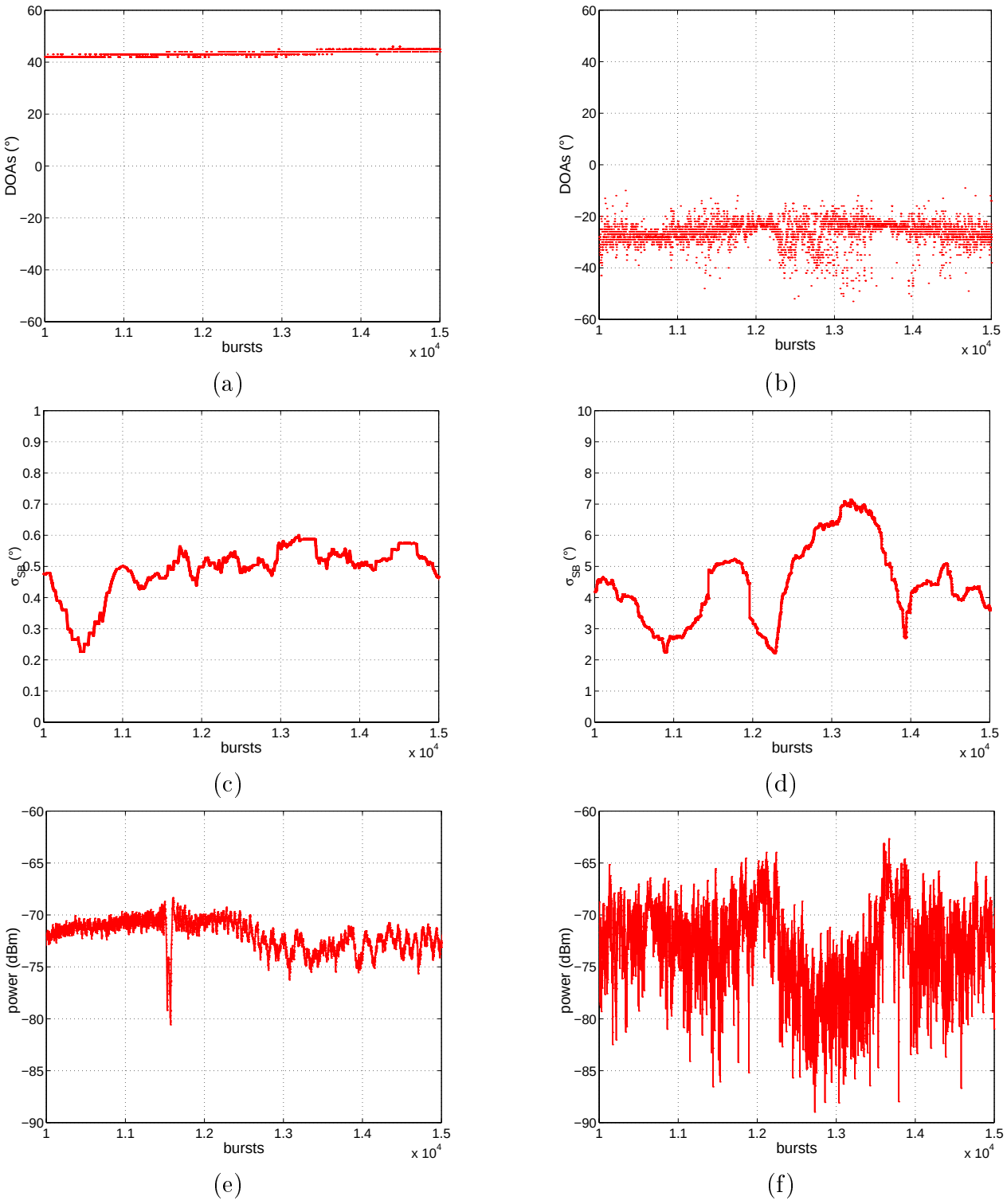

Figure 5.6. Signals of Scenario A and A'. Both scenarios include the same two signals, Signal 1 and Signal 2. In Scenario A the user signal (Signal 1) has a large angular spread and the interferer signal (Signal 2) has a small angular spread. The situation is vice versa in Scenario A', where the user signal and interferer signal are exchanged. (a), (b) DOAs, $\phi_{SB}(n)$, resulting from the scanning beam algorithm. (c), (d) Angular spread. (e), (f) Average input power. (a), (c), and (e) are for Signal 1. (b), (d), and (f) are for Signal 2.

Configuration	Scenario A					
All values in dB	$\Delta C/I^{90\%}$	$\Delta C/I^{99\%}$	$\Delta SNR^{90\%}$	$\Delta SNR^{99\%}$	G_b	L_{tap}
Unitary ESPRIT	22.1	21.2	6.8	3.9	6.7	1.4
PASTd	22.1	22.1	7.0	6.7	6.8	1.7
PASTd, w/o burst–to–burst track.	22.0	21.8	7.0	6.0	6.8	1.7
standard, **MVM**	21.9	21.7	7.2	7.6	7.0	1.7
theoretical optimum	—	—	9.3	9.8	9.0	0
Configuration	Scenario A'					
Unitary ESPRIT	23.9	24.6	5.5	5.1	5.4	2.2
PASTd	24.1	24.6	5.6	7.1	5.4	2.1
PASTd, w/o burst–to–burst track.	24.2	24.6	5.8	5.4	5.5	2.2
standard, **MVM**	24.7	26.4	6.5	8.4	5.8	2.3
theoretical optimum	—	—	11.7	16.2	9.0	0

Table 5.2. Influence of different DOA estimators on the SNR and C/I gain of Scenario A and A'.

Different DOA estimators From the comparison of the various **DOAE** estimators, I conclude that **MVM** gives the best results. The C/I gain in Scenario A is nearly independent of the algorithm's choice (Tab. 5.2). In Scenario A' $\Delta C/I^{99\%}$ for **MVM** is by $1.8dB$ larger than for the other DOA estimators. Larger differences in the SNR gain values are present in both scenarios. Especially in Scenario A' **MVM** outperforms the other configurations by up to $3dB$. Again I can explain this with the selected DOAs (Fig. 5.8). Compare the different results for **MVM** (b) and **Unitary ESPRIT** (a). **Unitary ESPRIT** results in much more estimated DOAs and finally in more interferer DOAs. More nulls and nulls close to the main beam, result in reduced beamforming and diversity gain for **Unitary ESPRIT**. **PASTd** is more robust, especially when burst–to–burst tracking is applied.

I conclude that **MVM** is most robust and achieves the best results. This is in agreement with the conclusions drawn from the evaluation of the estimation quality (Ch. 4, p.52). The robustness of **MVM** becomes even clearer when we compare the DOAs with the ones of **Unitary ESPRIT** (Fig. 5.8).

5.3.1 Resolution of DOA estimator

To answer the question which DOA estimation *resolution* is necessary, I apply **MVM** with different fine resolution settings. The results are illustrated in Fig. 5.10 and summarized in Tab. 5.3. The degradation of the performance is only noticeable, when the fine resolution, R_f, is 10°. This is no surprise, because **A**^{3}**P** is designed to cope with a deficient estimation quality. Here, the tracker and the broad nulls in the beamforming are responsible for the excellent robustness: First, the tracker renders the DOA estimates more reliable, by smoothing the estimated DOAs. Second, the broad nulls make sure that certain DOA errors will not cause the C/I to drop, because interference is still suppressed sufficiently.

The SNR gain is reduced significantly in Scenario A when $R_f = 10°$. The narrow main beam and a small angular spread of the user signal in Scenario A cause a significant power (SNR) loss, when the user DOA is shifted by some degrees. The question that remains unanswered is why the main beam is sometimes not directed towards the user, although the tracker is

MVM configuration	Scenario A					
All values in dB	$\Delta C/I^{90\%}$	$\Delta C/I^{99\%}$	$\Delta SNR^{90\%}$	$\Delta SNR^{99\%}$	G_b	L_{tap}
standard, $R_c = 1°$,$R_f = 0.1°$	21.9	21.7	7.2	7.6	7.0	1.7
$R_c = 2°$,$R_f = 1°$	21.9	21.7	7.2	7.6	7.0	1.7
$R_c = R_f = 5°$	21.9	21.9	7.2	7.7	7.0	1.6
$R_c = R_f = 10°$	21.2	20.2	6.5	5.1	6.4	1.9
theoretical optimum	—	—	9.3	9.8	9.0	0
Configuration	Scenario A'					
standard, $R_c = 1°$,$R_f = 0.1°$	24.7	26.4	6.5	8.4	5.8	2.3
$R_c = 2°$,$R_f = 1°$	24.7	26.4	6.5	8.6	5.8	2.3
$R_c = R_f = 5°$	24.7	26.4	6.6	8.4	5.8	2.3
$R_c = R_f = 10°$	24.2	24.7	6.4	8.1	5.6	2.2
theoretical optimum	—	—	11.7	16.2	9.0	0

Table 5.3. Influence of **MVM**'s fine resolution, R_f, on the SNR and C/I gain of Scenario A and A'.R_c is the coarse resolution.

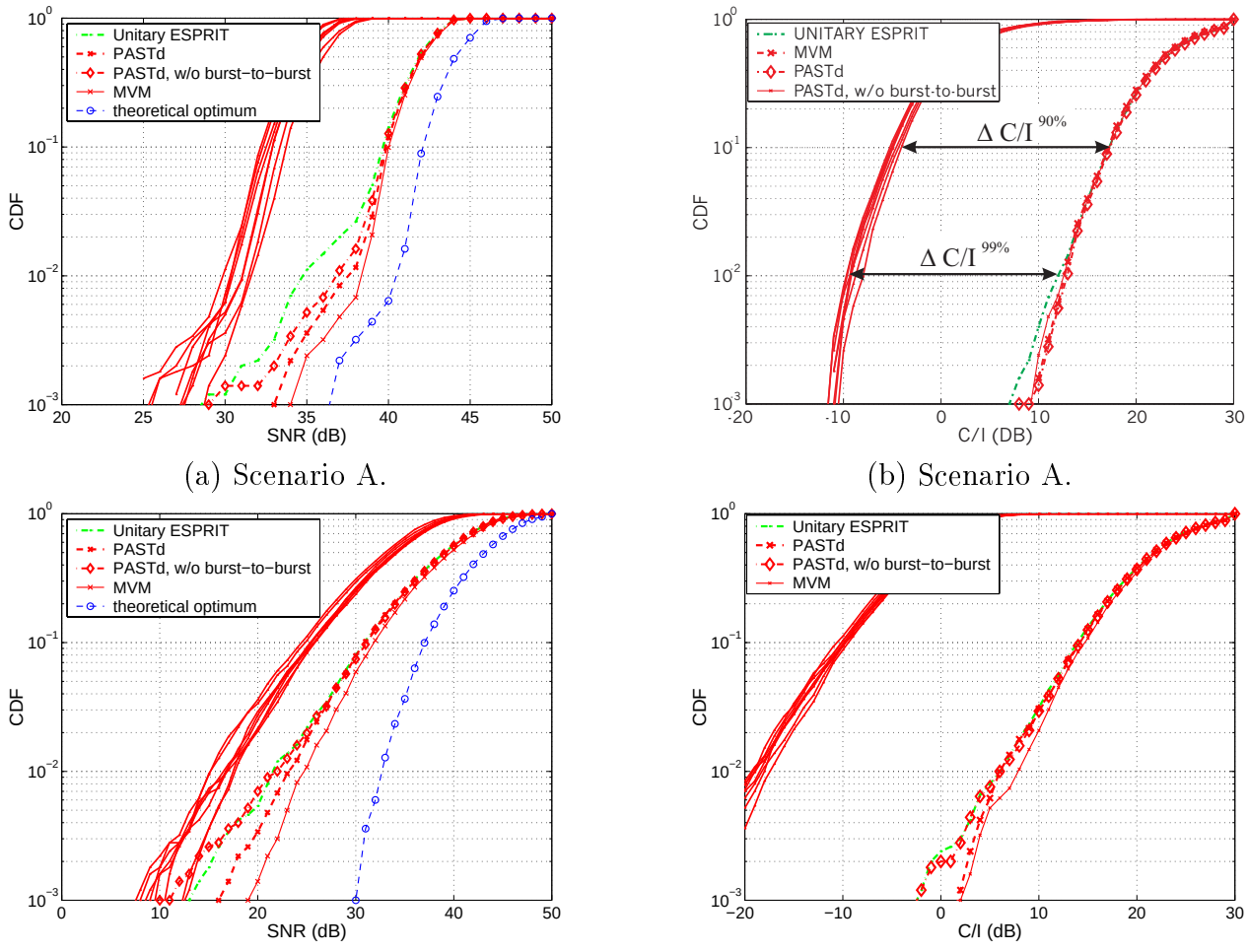

(a) Scenario A.

(b) Scenario A.

(c) Scenario A'.

(d) Scenario A'.

Figure 5.7. Influence of DOA estimators on the SNR statistics (a,c) and C/I statistics (b,d).

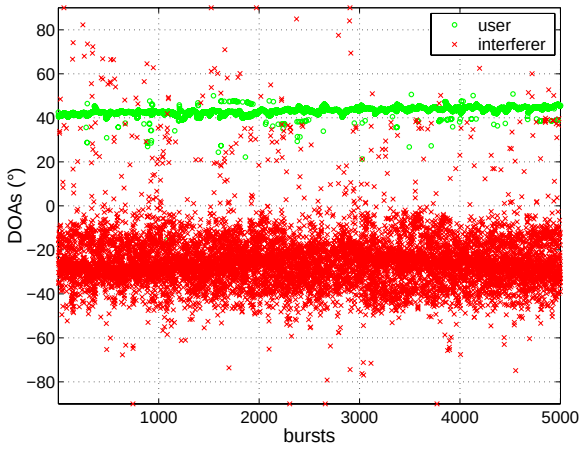

(a) Scenario A.

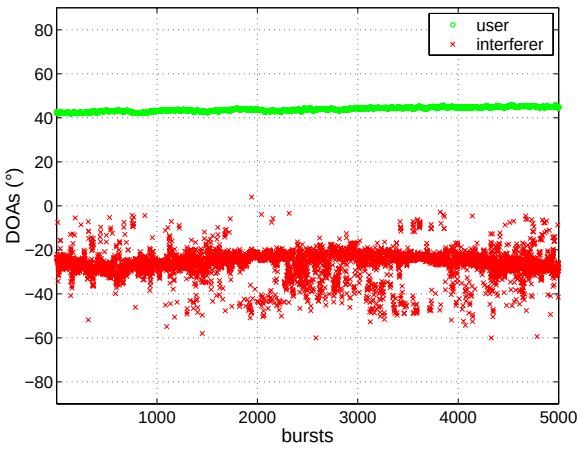

(b) Scenario A.

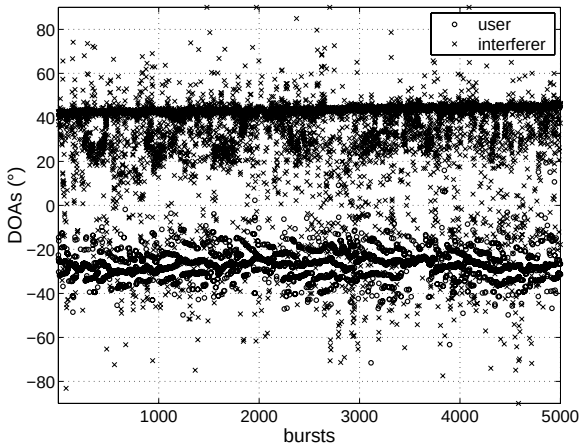

(c) Scenario A'.

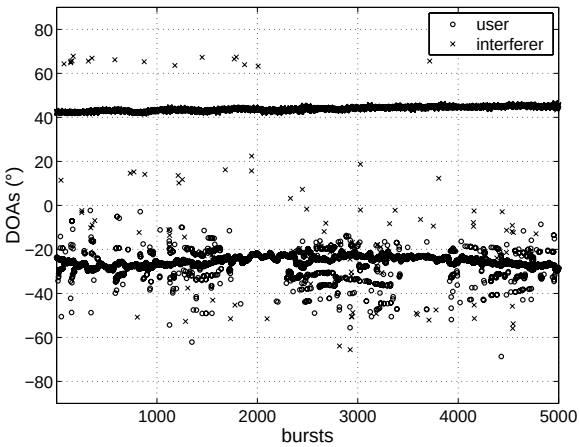

(d) Scenario A'.

Figure 5.8. Selected user and interferer DOAs for Scenario A (a) and (b), and A' (c) and (d). (a) and (c) **Unitary ESPRIT**. (b) and (d) **MVM**.

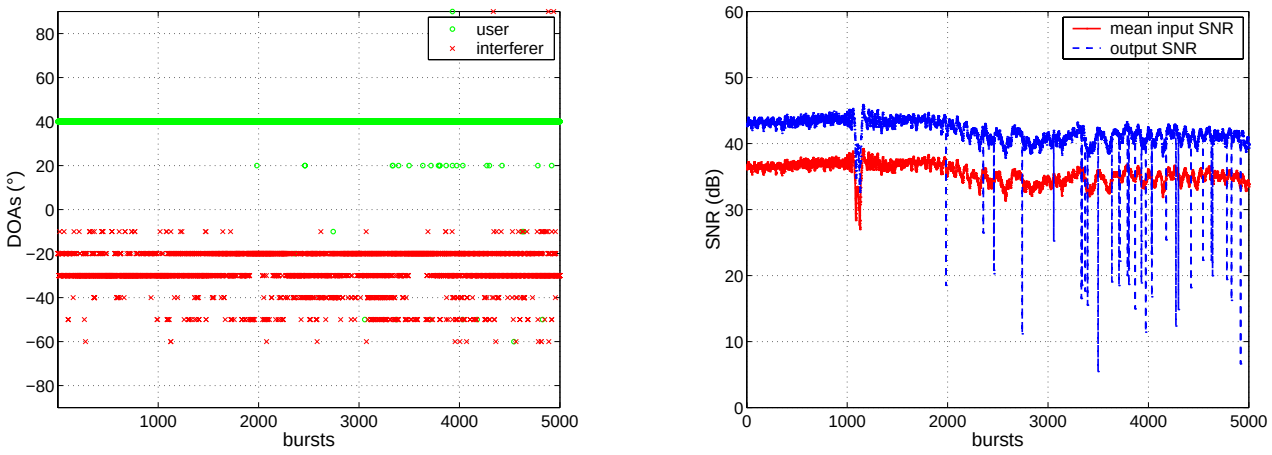

(a) (b)

Figure 5.9. MVM with very low angular resolution, $R_f = 10°$. Selected user and interferer DOAs (a) and resulting average input SNR and output SNR (b) for Scenario A. The drops in output SNR occur, when the user DOA is at $\phi = 20°$.

activated. Actually, the tracker can remedy the coarse DOA resolution up to a certain amount, but not anymore in the case of $R_f = 10°$. In the current configuration the **UID** will return user DOAs mainly at $\phi_U = 40°$. But in some bursts $\phi_U = 20°$, which will result in a tracker that is initialized at this angle. Obviously the tracker is updated often enough that the **DOAT** selects the tracker as a final user DOA (e.g. burst number 1990 in Fig. 5.8(a)). The tracker at $\phi_U = 20°$ will not change its DOA, because every new update will only happen when ϕ_U is again 20°. Also the tracker will not merge with the tracker at 40°, because this one is too far apart. The main beam then points into $\phi = 20°$, if the current power at this direction is larger than at $\phi = 40°$. In those bursts we will get an SNR degradation (Fig. 5.9). This behavior is not so significant for Scenario A', because there the angular spread of the user signal is much larger.

5.3.2 Conclusions

From the assessment of the **DOAE** in Scenario A and A' I conclude:

- **MVM** is the most robust estimator, closely followed by **PASTd**. If **Unitary ESPRIT** is applied, the performance is significantly degraded. This agrees with the findings in Sect. 4.3.7 and supports the conclusion that the estimation quality is a suitable quantity for the assessment of smart antenna systems.
- **A^{3}P** does not require DOA estimates with very high resolution. Instead it is more important that the estimators have superior estimation quality. The degradation of the C/I and SNR gain is larger when we apply another DOA estimator, than when **MVM** is applied with smaller angular resolution.
- **A^{3}P** is optimized to cope with interference. In Scenario A' **A^{3}P** achieves C/I gains up to 26dB, when measured at the 99% probability. Because the beamforming uses most degrees of freedom to suppress interference, the SNR gain cannot be optimum.
- The beamforming gain is larger when the angular spread of the user signal is smaller.

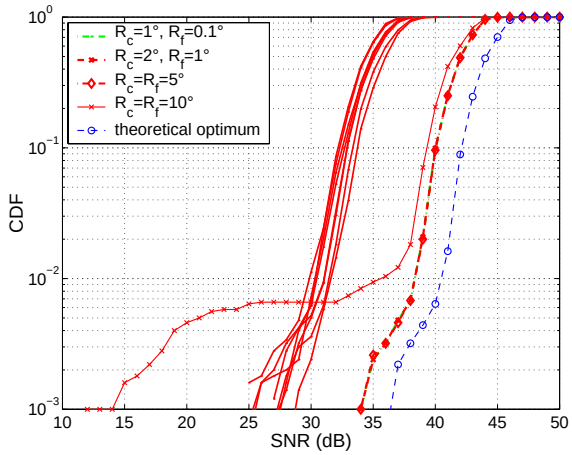

(a) Scenario A.

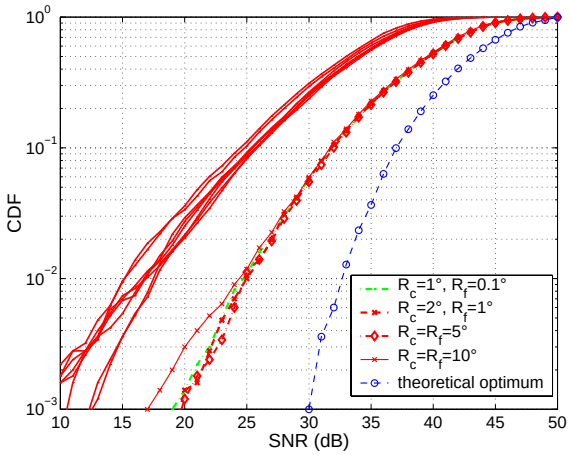

(b) Scenario A'.

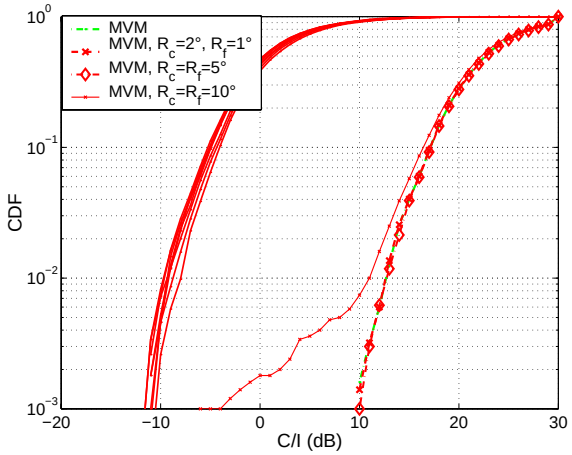

(c) Scenario A.

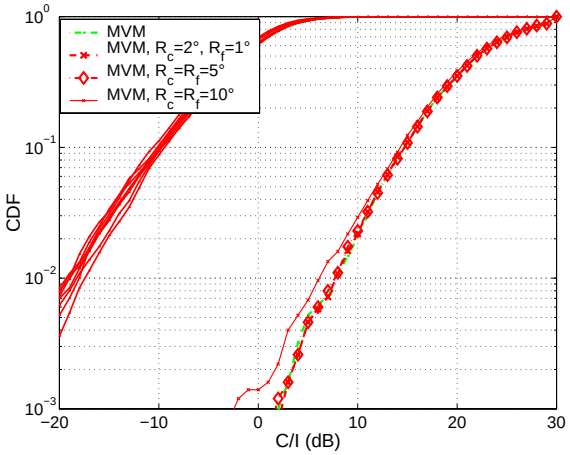

(d) Scenario A'.

Figure 5.10. Influence of **MVM**'s fine resolution, R_f, on the statistic of SNR (a,b) and C/I (c,d).

This is not a result of the narrow beam width, because the beam width is larger than the angular spread (even in Scenario A'). Instead, the tapering loss is smaller.

- **A^{3}P** 's diversity gain is larger when the angular spread of the user signal is larger. It is not surprising that a channel with larger angular spread offers higher diversity gain. But it is noteworthy that **A^{3}P** is able to exploit a certain amount of it. In the case of **MVM** it is $G_{div}^{99\%} = 2.6dB$ in Scenario A'.

- The interference suppression is higher when the angular spread of the interferer DOAs is smaller. However, the difference is only in the order of $3 - 4dB$ for the standard configuration (broad nulls), although the angular spread is 0.5° in the favorable scenario and 5° in the other. This is a first indicator that the interferer nulling does not work reliably.

5.4 Effect of nulling strategy in spatial pre–filter

Here I will answer the question whether broad nulling in the spatial pre–filter (**ULBF**, see Sect. 4.4, p.57) is of advantage, or whether we can use the conventional beamformer.

The nulling strategy that is applied in the **ULBF**, i.e. placing a broad null with **SmearR** or a sharp null with the Pseudo Inverse, does not affect the system performance in Scenario A and A' (Tab. 5.4). I therefore set up another scenario that is much more challenging.

Scenario B I selected both the user and interferer signal from a measurement set where large angular spreads are present (Fig. 5.11). Additionally, I chose a situation where the wanted and interfering signals arrive from the *same* angular ranges. The user signal has two multipaths around $\phi_1 = 20°$ and $\phi_2 = 40°$. The interferer signal has in most bursts an overlap around ϕ_2. Of course, this is a challenging situation for a smart antenna system that is based on DOA estimation. Note that in Scenario B, the input C/I is smaller than $0dB$ ($-13dB$) in about 50% (10%) of the cases (Fig. 5.12(a)).

Absolute SNR and C/I gain For the standard configuration, the C/I gain in Scenario B is still very high, $\Delta C/I^{99\%} = 18.5dB$! This is an excellent result, when we consider how severe the interference situation is. The SNR gain is low, because all degrees of freedom are used up to suppress the interference significantly. The beamforming gain is slightly smaller in Scenario B than in Scenario A' while the tapering loss is the same. We still achieve a beamforming gain of $4dB$, but now there is nearly no diversity gain.

Broad nulls or sharp nulls for the ULBF In Scenario B, the two nulling strategies lead to the same results (Tab. 5.4). This is in agreement with simulation results, and indicates, that the **DOAT** makes the processing more robust and thus it suppresses the influence of the spatial pre–filter qualities. The **ULBF** has to separate the incident signals; it outputs a spatially resolved signal for each estimated DOA (see Sect. 4.4, p.57). Ideally each spatially resolved signal consists *only* of contributions from the estimated DOA. In practice, the spatially resolved signal also includes contributions from other directions, thus the "carrier–to–interference ratio"[4] for the estimated DOA is finite. The better the spatial pre–filter, the higher will be the "carrier–to–interference ratio" of each spatially resolved signal. This will allow more reliable decisions in the **UID**. But

[4]Here the wanted signal information is the signal coming from the estimated DOA, *all* other signal contributions are understood as interferer. Note that at the stage of the **ULBF** we do not yet know, where the user and interferer signals are coming from.

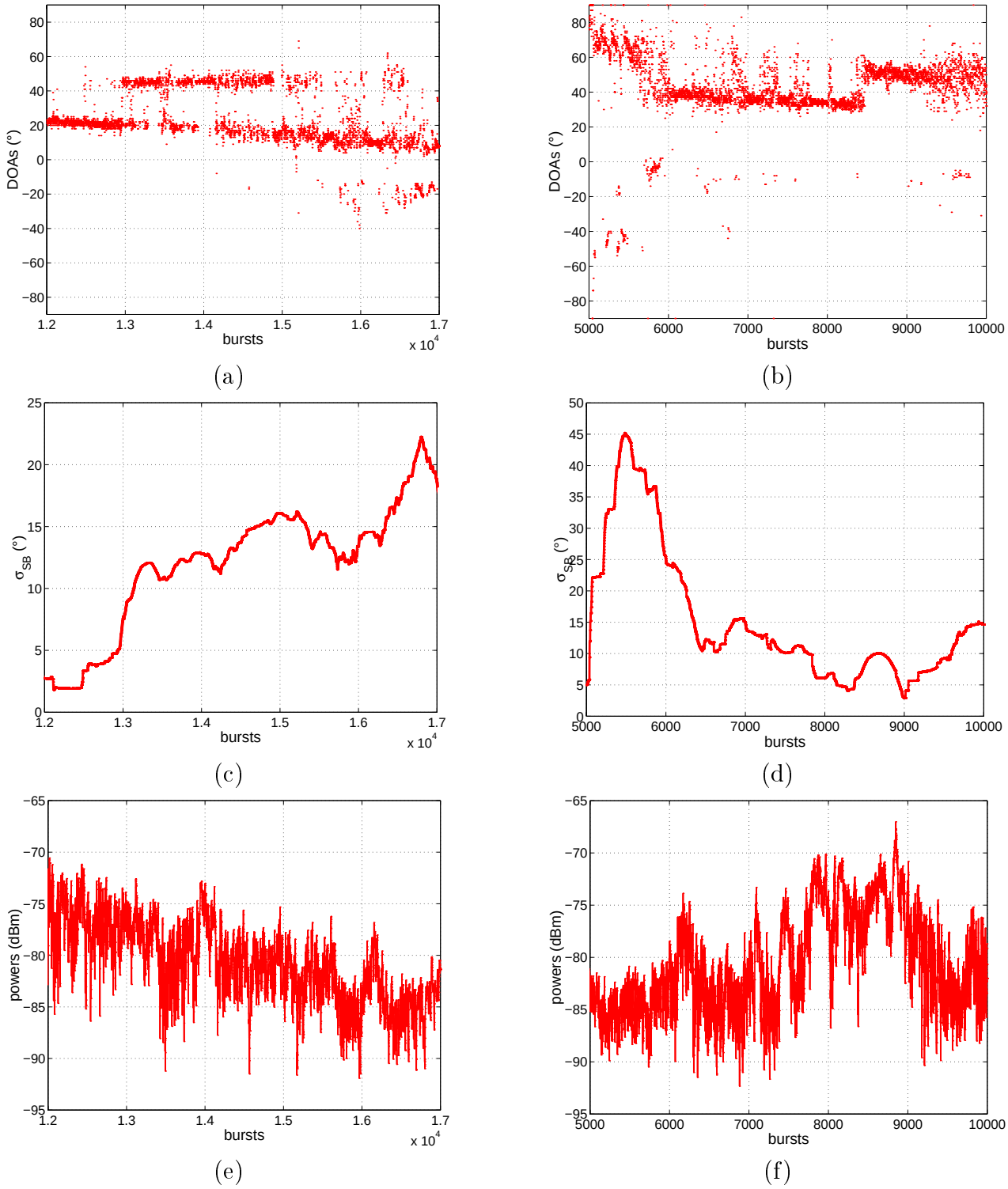

Figure 5.11. Signals of Scenario B: In Scenario B the user and interferer signal partly overlap in angle, thus leading to a challenging scenario. (a), (b) present the DOAs resulting from the scanning beam algorithm, $\phi_{SB}(n)$. (c), (d) Angular spread, $AS(n)$. (e), (f) Average input power. (a), (c), and (e) present the user signal. (b), (d), and (f) present the interferer signal.

ULBF configuration	Scenario A					
All values in dB	$\Delta C/I^{90\%}$	$\Delta C/I^{99\%}$	$\Delta SNR^{90\%}$	$\Delta SNR^{99\%}$	G_b	L_{tap}
sharp nulls, standard	21.9	21.7	7.2	7.6	7.0	1.7
broad nulls	21.9	21.8	7.2	7.6	7.0	1.7
theoretical optimum	—	—	9.3	9.8	9.0	0
ULBF configuration	Scenario A'					
sharp nulls, standard	24.7	26.4	6.5	8.4	5.8	2.3
broad nulls	24.5	26.5	6.5	8.0	5.8	2.3
theoretical optimum	—	—	11.7	16.2	9.0	0
ULBF configuration	Scenario B					
sharp nulls, standard	18.5	18.5	4.5	3.9	4.3	2.3
broad nulls	18.3	19.4	4.6	4.1	4.3	2.1
theoretical optimum	—	—	13.5	18.3	9.0	0

Table 5.4. Effect of nulling strategy in the spatial pre–filter on the C/I and SNR gain for Scenarios A, A' and B. The Pseudo Inverse is applied to get sharp nulls, **SmearR** to get broad nulls.

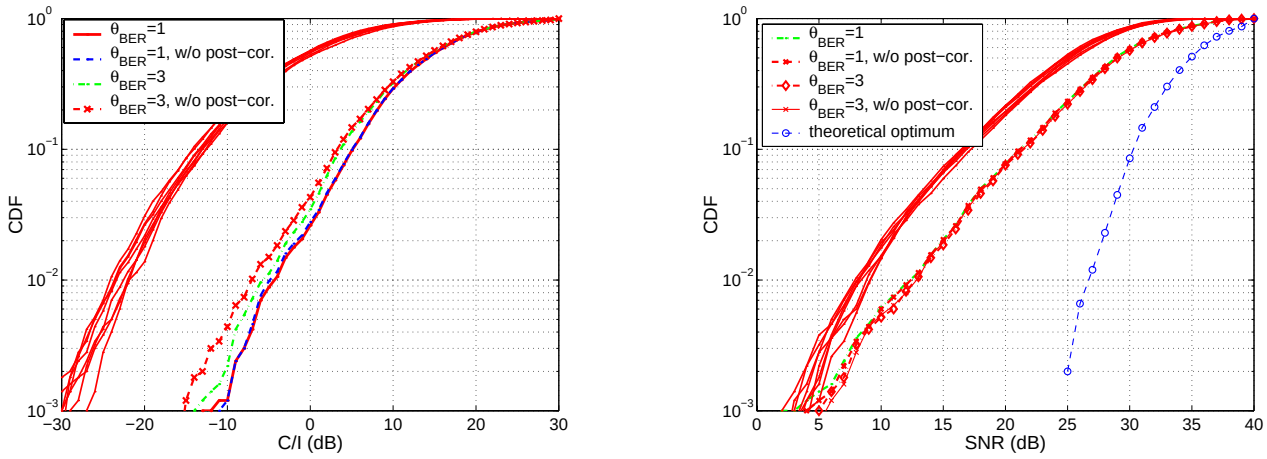

Figure 5.12. Effect of different **UID** configurations on the C/I and SNR statistics of Scenario B. (a) C/I. (b) SNR.

if the **ULBF** does not separate the spatially resolved signals properly, it does not necessarily mean an degradation of the overall system performance. The **DOAT** takes the final decision where the main beam is put, and it has the chance to remedy any erroneous identifications of the **UID** (that are caused by insufficient separation in the **ULBF**).

The conclusion is that we can select for the **ULBF** the beamformer that gives needs the least computational effort, because the SNR or C/I performance is not affected by the choice.

5.5 Influence of user identification

In this section I will answer the question whether the post–correlation affects the overall system performance (Sect. 4.5, p.60). Up to now, I have configured the **UID** to use an threshold for the

UID configuration	Scenario B					
All values in dB	$\Delta C/I^{90\%}$	$\Delta C/I^{99\%}$	$\Delta SNR^{90\%}$	$\Delta SNR^{99\%}$	G_b	L_{t}
standard, $\theta_{BER} = 1$, with post–correlation	18.5	18.5	4.5	3.9	4.3	2.
$\theta_{BER} = 1$, without post–correlation	18.4	18.0	4.5	3.9	4.3	2.
$\theta_{BER} = 3$, with post–correlation	17.0	17.1	4.7	4.4	4.4	2.
$\theta_{BER} = 3$, without post–correlation	16.6	15.9	4.7	4.4	4.4	2.
theoretical optimum	—	—	13.5	18.3	9.0	0

Table 5.5. Effect of different **UID** configurations on the C/I and SNR gain in Scenario B.

number of bit errors of $\theta_{BER} = 1$. This is a very robust configuration, because then the **UID** will acknowledge a signal to be originated from a user only, when the number of bit errors is 0 or 1. I now check the influence of θ_{BER} on the C/I and SNR gain. I apply various configurations of the **UID** (Fig. 5.12 and Tab. 5.5) to Scenario B. Surprisingly, the post–correlation has not the significant effect on the C/I and SNR gain that simulations have shown. In the case of $\theta_{BER} = 1$, the system performs equally well, regardless of the activation of the post–correlation. The **UID** is then already in a very robust configuration, and thus the post–correlation cannot improve any further. To be more precise, the primary identification process (Sect. 4.5, p.60ff) already returns only the most reliable user signals and thus the post–correlation can only verify these decisions.

The outcome is slightly different when $\theta_{BER} = 3$. Then the primary identification is not so reliable and the post–correlation has the chance to render the decisions more reliable. This results in an improvement of the C/I gain of up to $1dB$, when we compare the system with and without post–correlation.

Interesting is another behavior: **A**^{3}**P** is less robust against interference, i.e. the C/I gain is reduced, when we change θ_{BER} from 1 to 3, because then more DOAs will be identified as originated from the user (all DOAs with the number of bit errors, $n_{BER} < 3$ and not only those with $n_{BER} < 1$). The final decision, where the main beam points to, is then based on a larger set of user DOAs. Thus the probability that the main beam points into an interferer DOA is increased. But at the same time, the diversity gain increases slightly (the beamforming gain stays constant), because the probability that the beam with the largest power is selected is increased. Although this effect here is minor, it is worth mentioning, because it shows that a system can *either* exploit diversity *or* suppress interference.

Conclusion The different **UID** configurations do not alter **A**^{3}**P**'s C/I and SNR gain significantly. The post–correlation presents a minor improvement on the overall performance. Instead the bit error threshold has a stronger influence on the system. The difference in C/I gain caused by the different settings for θ_{BER} is up to $2dB$. However, $\theta_{BER} = 1$, in general, will reduce the SNR gain, because the number of user DOAs is reduced.

5.6 Effect of tracking

The tracker is the key element in the **A**^{3}**P** that guarantees system robustness (Sect. 4.6, p.63). I will prove this by assessing Scenario B with and without a tracker.

A^3**P without tracking** When the tracker is deactivated, the difference to the standard configuration is twofold: **A**^{3}**P** cannot cope with far–off estimates and most importantly, it cannot

DOAT configuration	Scenario B					
All values in dB	$\Delta C/I^{90\%}$	$\Delta C/I^{99\%}$	$\Delta SNR^{90\%}$	$\Delta SNR^{99\%}$	G_b	L_{tap}
standard	18.5	18.5	4.5	3.9	4.3	2.1
no tracking	12.9	0.9	4.8	3.6	4.5	2.0
theoretical optimum	—	—	13.5	18.3	9.0	0

Table 5.6. Effect of tracking on the C/I and SNR gain in Scenario B.

remedy erroneous identifications of the **UID**. Second, **A**^{3}**P** will put the main beam into the direction of the strongest user DOA and does not include any additional measures to increase the reliability of the decision where the main beam aims at. The interferer selection is the same, because the **DOAT** tracks only the *user* DOAs (see Sect. 4.6, p.63).

5.6.1 Is tracking just averaging?

The tracking concept consists of the bank of independent DOA trackers (DOA averaging), but additionally measures the reliability of a tracker (Sect. 4.6). The main beam will only be pointed into a direction that has high enough reliability. This will increase system robustness.

It is of interest to see whether *averaging of the DOAs* or increasing the robustness by *selecting only DOAs with high enough reliability* has larger influence on the performance.

An astonishing effect of the tracker is illustrated in Fig. 5.16. Deactivating the tracker (no averaging and no measurement of the reliability) reduces the C/I gain by a tremendous $17.6dB$ ($5.6dB$) at the 99% (90%) probability level in Scenario B[5]! To identify the reason for this improvement, I vary the averaging constant of the tracker. Therefore I apply the tracker with different settings of the memory length, $\mu_{T,max}$. The larger $\mu_{T,max}$, the stronger is the averaging. By setting $\mu_{T,max} = 1$, the DOA tracker does not average anymore. But still all other information, like the reliability is calculated and used. Thus I say that I can deactivate the averaging of the DOAs, while still having the tracking concept (reliability, etc.) activated.

The memory length, $\mu_{T,max}$, has much less influence on the SNR and C/I statistics, than whether the reliability concept is applied or not (Fig. 5.15 and Tab. 5.7). Even, if I do *not* apply any averaging at all ($\mu_{T,max} = 1$), but still measure the reliability, the C/I gain is only slightly reduced by $0.5dB$. Thus the reliability concept increases the robustness considerably and is much more important for the C/I gain than averaging the DOAs.

The optimum C/I gain occurs for $\mu_{T,max} = 100$, although the dependence on $\mu_{T,max}$ is not strong (Fig. 5.14). Too much averaging ($\mu_{T,max} = 1000$) will also reduce the C/I gain. The SNR gain is more or less independent of $\mu_{T,max}$. Fig. 5.13 illustrates the effect of the tracking concept. I have plotted the C/I values and the selected user and interferer DOAs for 500 sample bursts. When the tracker is applied, the output C/I is larger in almost all bursts. In contrast there are many bursts where the output C/I is smaller than the input C/I when the tracker is not activated (Fig. 5.13(c)). When we look at the selected DOAs for these bursts, we find that without the tracker **A**^{3}**P** places the main beam into the direction of the interferer. Obviously the **UID** identified those interferer DOAs as user DOAs erroneously. If the tracker is activated, it will remedy these wrong decision, because such a DOA is never selected. Note that the **UID** will give erroneous identifications especially when spatially resolved signals have bad C/I, i.e.

[5]The effect is, of course, much less pronounced for the Scenarios A and A'. There the C/I gain differs by about $0.3dB$.

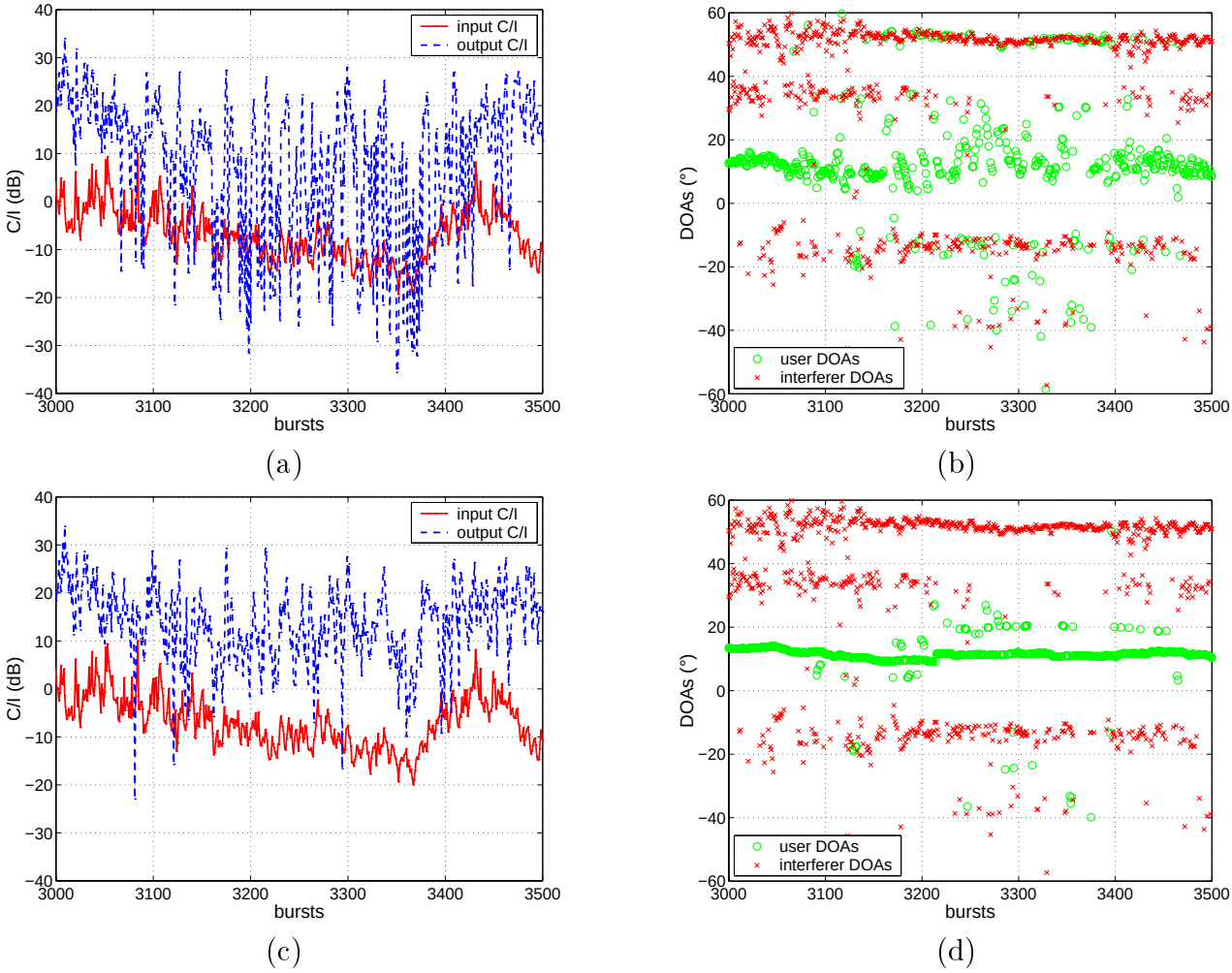

Figure 5.13. Effect of the tracking concept on the selected C/I and the DOAs for sample bursts 3000 ... 3500 of Scenario B. (a,b) Without tracking. (c,d) With tracking.

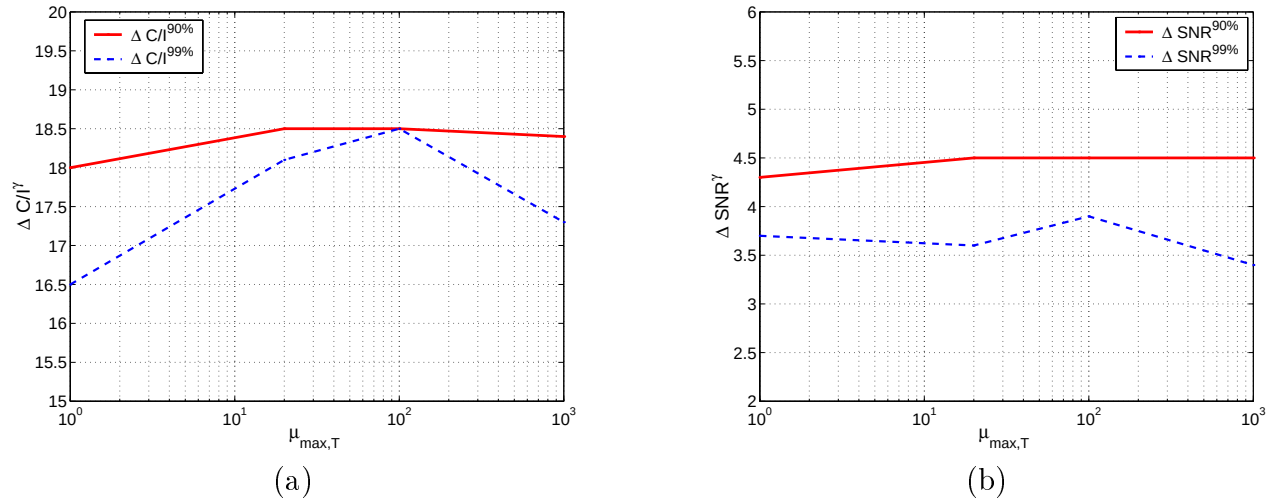

Figure 5.14. Effect of the tracker memory length, $\mu_{T,max}$, on the C/I gain (a) and SNR gain (b).

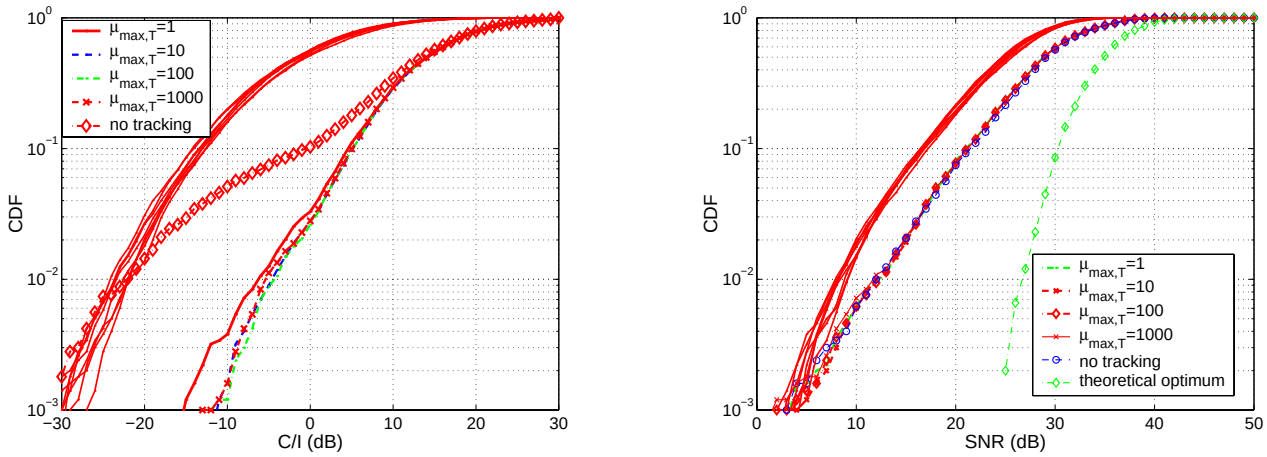

Figure 5.15. Effect of tracker memory length, $\mu_{T,max}$ on the C/I and SNR statistics. (a) C/I. (b) SNR.

when the input C/I is low.

5.6.2 Summary

I have assessed the **DOAT** in a challenging scenario, i.e. the scenario with strong interference from large angular ranges. The expected improvement of the tracker over the system without any tracking concept will be optimum in such a scenario. I conclude:

- Tracking increases **A^{3}P**'s robustness against interference by up to $17dB$. The **DOAT** is this the key element to remedy erroneous decisions of the **UID**.
- Not the averaging effect of the tracker, but the tracking concept itself guarantees the high C/I gain in low C/I situations. Among those features are:
  - A main beam will only be placed in "reliable" directions.
  - The influence of far–off estimates is reduced.
  - Although the tracked DOAs are averaged, the system hops instantaneously from one tracked DOA to another.
- The averaging constant has little influence on the gain. However, optimum performance is achieved for $\mu_{T,max} = 100$. Note that the assessment of the stand–alone **DOAT** (Sect. 4.6, p.63) with simulations resulted in an optimum memory length of $\mu_{T,max} = 110$.

5.7 Effect of the nulling strategy

The last subtask to assess is the **ULpBF**(Sect. 4.7, p.73). I will quantify the influence of placing broad nulls on the C/I and SNR. I will also investigate the influence of the null width and the null depth parameters on the gain. And I will demonstrate that broad nulls increase the system's robustness against angular spread and against DOA estimates with less resolution. To get sharp nulls, I apply the Pseudo Inverse, and to get broad nulls, the following standard

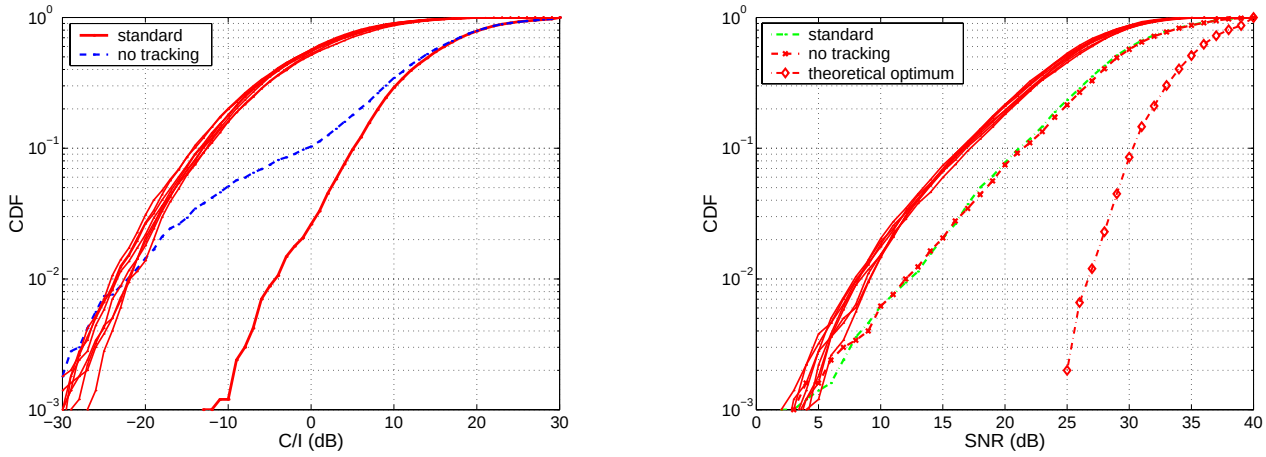

(a) (b)

Figure 5.16. Effect of the tracking concept on the C/I and SNR statistics. (a) C/I. (b) SNR.

DOAT configuration	Scenario B					
All values in dB	$\Delta C/I^{90\%}$	$\Delta C/I^{99\%}$	$\Delta SNR^{90\%}$	$\Delta SNR^{99\%}$	G_b	L_{tap}
$\mu_{T,max} = 1$	18.0	16.5	4.3	3.7	4.3	2.1
$\mu_{T,max} = 10$	18.5	18.1	4.5	3.6	4.3	2.1
$\mu_{T,max} = 100$, standard	18.5	18.5	4.5	3.9	4.3	2.1
$\mu_{T,max} = 1000$	18.4	17.3	4.5	3.4	4.3	2.1
no tracking	12.9	0.9	4.8	3.8	4.5	2.0
theoretical optimum	—	—	13.5	18.3	9.0	0

Table 5.7. Effect of tracker memory length, $\mu_{T,max}$ on the C/I and SNR gain in Scenario B.

configuration is applied: The **ULpBF** is **SmearR** with a null depth of $ND = 10dB$ and a null width of $NW = 10°$.

The effective interference suppression that can be achieved with beamforming scheme depends strongly on the quality of the calibration. Hardware imperfections will cause the effective antenna pattern to deviate from the theoretical ones and in turn degrade the system performance. In the operation it is not known, whether a null is effectively present or not. Thus I can study only the indirect effects of the imperfections, i.e. quantify the C/I gain. When the selected directions for the final beamforming are correct, the C/I gain will be *only* limited by the imperfections. Note that the angular spread is taken into account by trying to place broad nulls. In a GSM base station we cannot expect a highly calibrated system, because this will blow up the hardware costs considerably. In the present base station a economically justifiable calibration is included. In this section I discuss how the overall performance is limited by the calibration.

5.7.1 Interferer nulling — does it work?

Before I compare the two nulling strategies, let us take a look on the absolute improvement of the C/I gain caused by placing nulls into the directions of interferers.

I applied **A**^{3}**P** with and without placing nulls, either broad or sharp, to the Scenarios A, A', and B. The results are summarized in Tab. 5.8. Most importantly, the C/I gain is larger, if nulls are present. However, the improvement is not very large, and differs for the scenarios. In general, we gain more with nulling, when the angular spread of the interference is larger (Scenario A and B), regardless of the nulling strategy.

These measurements do not allow decisive conclusions about the pattern parameter, like the effective null depth. However, some conclusions can be drawn by studying the C/I gain in the different scenarios.

- First, the C/I gain is at most only $4dB$ higher with nulling than without nulling. Second, when the angular spread is small, the C/I gain increases less than if interference has large angular spread. Thus the effective null depth is not high. In the antenna pattern this corresponds to either shifted or filled nulls.

- $\Delta C/I^{\gamma}$ increases stronger, if the angular spread is larger. Thus I conclude that the effective null depth does not cause the increase in C/I gain alone, i.e. there are not always deep nulls present at the direction of the interferer. If nulls are placed, the sidelobe level near nulls is smaller, than without nulling. This causes the larger gain, if the angular spread is large.

  To support these conclusions, I have plotted *theoretical*[6] sample antenna patterns for the various configurations (Fig. 5.17). When we compare the pattern for Scenario A with nulling (a) and without nulling (b), we find, especially for **SmearR** *with* nulling not only a much deeper broad null, but also a reduced sidelobe level ($\phi \approx -10°$). Although in theory the interference suppression would be improved by $10dB$ to $15dB$, this effect is in practice less pronounced. But still the interference suppression improves by about $4dB$.

[6]The antenna pattern that is effectively caused during operation cannot be measured. However, we have measured sample uplink pattern that demonstrate how good the theoretical pattern agree with the measured ones (see Fig. 4.38, p.77).

ULpBF configuration	Scenario A					
All values in dB	$\Delta C/I^{90\%}$	$\Delta C/I^{99\%}$	$\Delta SNR^{90\%}$	$\Delta SNR^{99\%}$	G_b	L_{tap}
SmearR, broad nulls	21.9	21.7	7.2	7.7	6.9	1.7
SmearR, no nulls	18.7	19.2	7.5	8.0	7.2	1.6
Pseudo Inverse, sharp nulls	21.2	21.6	8.6	9.0	8.5	0.2
Pseudo Inverse, no nulls	16.6	17.5	9.2	9.7	9.0	0
theoretical optimum	—	—	9.3	9.8	9.0	0
ULpBF configuration	Scenario A'					
SmearR, broad nulls	24.7	26.4	6.5	8.4	5.8	2.3
SmearR, no nulls	24.3	25.7	6.8	8.8	6.0	2.1
Pseudo Inverse, sharp nulls	25.0	26.5	8.8	10.6	7.9	0.5
Pseudo Inverse, no nulls	22.4	25.3	9.0	11.0	8.3	0
theoretical optimum	—	—	11.7	16.2	9.0	0
ULpBF =**SmearR** configuration	Scenario B					
SmearR, broad nulls	18.5	18.5	4.5	3.9	4.3	2.1
SmearR, no nulls	17.0	17.4	5.0	4.4	4.7	1.9
Pseudo Inverse, sharp nulls	17.9	18.3	6.5	5.4	6.3	1.0
Pseudo Inverse, no nulls	14.1	14.0	7.6	7.1	7.0	0
theoretical optimum	—	—	13.5	18.3	9.0	0

Table 5.8. ULpBF with and without interferer nulling.

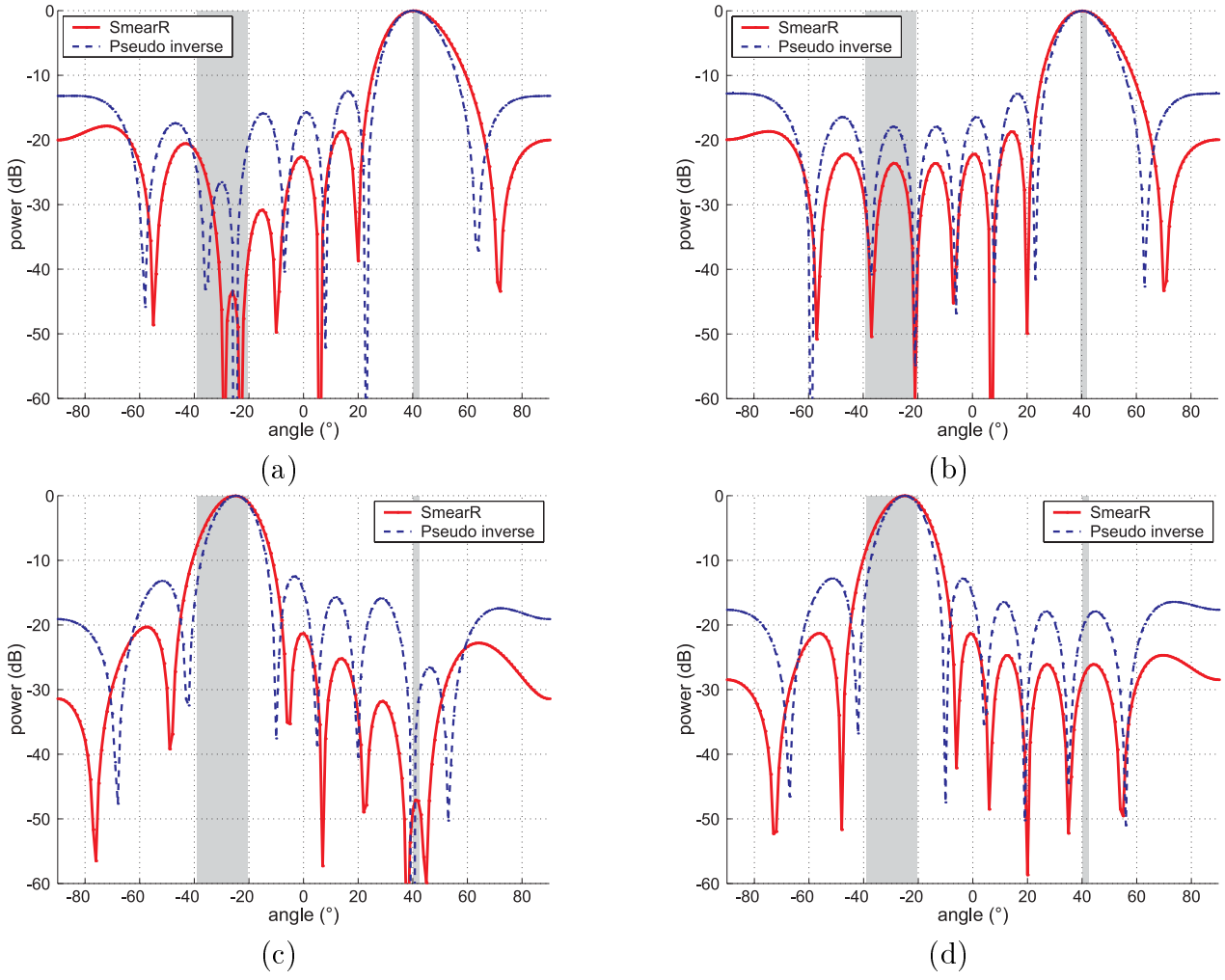

Figure 5.17. Effect of nulling on the theoretical antenna pattern. Sample pattern are plotted with (a, c) and without nulling (b, d). Scenario A (a, b). Scenario A' (c, d). .

ULpBF configuration	Scenario A					
All values in dB	$\Delta C/I^{90\%}$	$\Delta C/I^{99\%}$	$\Delta SNR^{90\%}$	$\Delta SNR^{99\%}$	G_b	L_{tap}
broad nulls	21.9	21.7	7.2	7.7	6.9	1.7
sharp nulls	21.2	21.5	8.6	9.0	8.5	0.2
theoretical optimum	—	—	9.3	9.8	9.0	0
ULpBF configuration	Scenario A'					
broad nulls	24.7	26.4	6.5	8.4	5.8	2.3
sharp nulls	25.0	26.5	8.8	10.6	7.9	0.5
theoretical optimum	—	—	11.7	16.2	9.0	0
ULpBF =**SmearR** configuration	Scenario B					
sharp nulls	17.9	18.3	6.5	5.4	6.3	1.0
broad nulls, $NW = 10°$, $ND = 10dB$	18.5	18.5	4.5	3.9	4.3	2.1
$NW = 10°$, $ND = 30dB$	17.1	16.6	2.9	1.9	3.7	2.1
$NW = 1°$, $ND = 10dB$	18.5	18.6	4.8	4.2	4.6	2.0
$NW = 20°$, $ND = 10dB$	17.6	18.2	4.3	4.0	4.2	1.9
theoretical optimum	—	—	13.5	18.3	9.0	0

Table 5.9. ULpBF with broad nulls (**SmearR**) and with conventional nulls (Pseudo Inverse).

5.7.2 Broad nulling versus sharp nulling

Figure 5.18 illustrates that there is nearly *no* improvement in the C/I gain by broad nulling over the conventional nulling in the Scenarios A, A', and B. But, the conventional beamformer has a tapering loss that is about $1.5dB$ lower than that of **SmearR**. This is a surprising result, because we expected a more significant gain of the broad nulling scheme compared to the sharp nulling (compare simulation results on p.115 and [KTT+99c]). But let's take a closer look on the C/I gain in Tab. 5.9.

In Scenario A', where the interference is incident from a small angular range, a similar C/I gain would be expected for both beamformers. Actually there, the Pseudo Inverse should give slightly better C/I gain, because the nulls are deeper. The measurements agree to the expectations: we find a C/I gain that is $0.2dB$ larger for the Pseudo Inverse.

In Scenario A, where the interference has a larger angular spread than in Scenario A', beamformer **SmearR** should improve the C/I gain significantly. However, from the measurements I find a C/I gain that is only $0.5dB$ better for **SmearR** than for the Pseudo Inverse.

And finally, in Scenario B, the angular spread is even larger than in Scenario A. Here, also, the C/I gain is only about $0.5dB$ larger for **SmearR**.

From these results I conclude that it is not worth placing broad nulls instead of sharp nulls, because the improvement of the C/I gain is only marginal. Instead **SmearR** looses about $1.5dB$ in SNR, because of tapering. But this is not the whole story. As I will show with the following results, broad nulling does make sense after all.

5.7.3 Broad nulls and the DOA estimation

Intuition tells us that a broad null will reduce demands on the DOA estimation resolution. The idea is that if I can place a broad null into the direction of an interferer, the interferer DOA does not have to be known so exactly, as long as the angular spread of the interferer is smaller

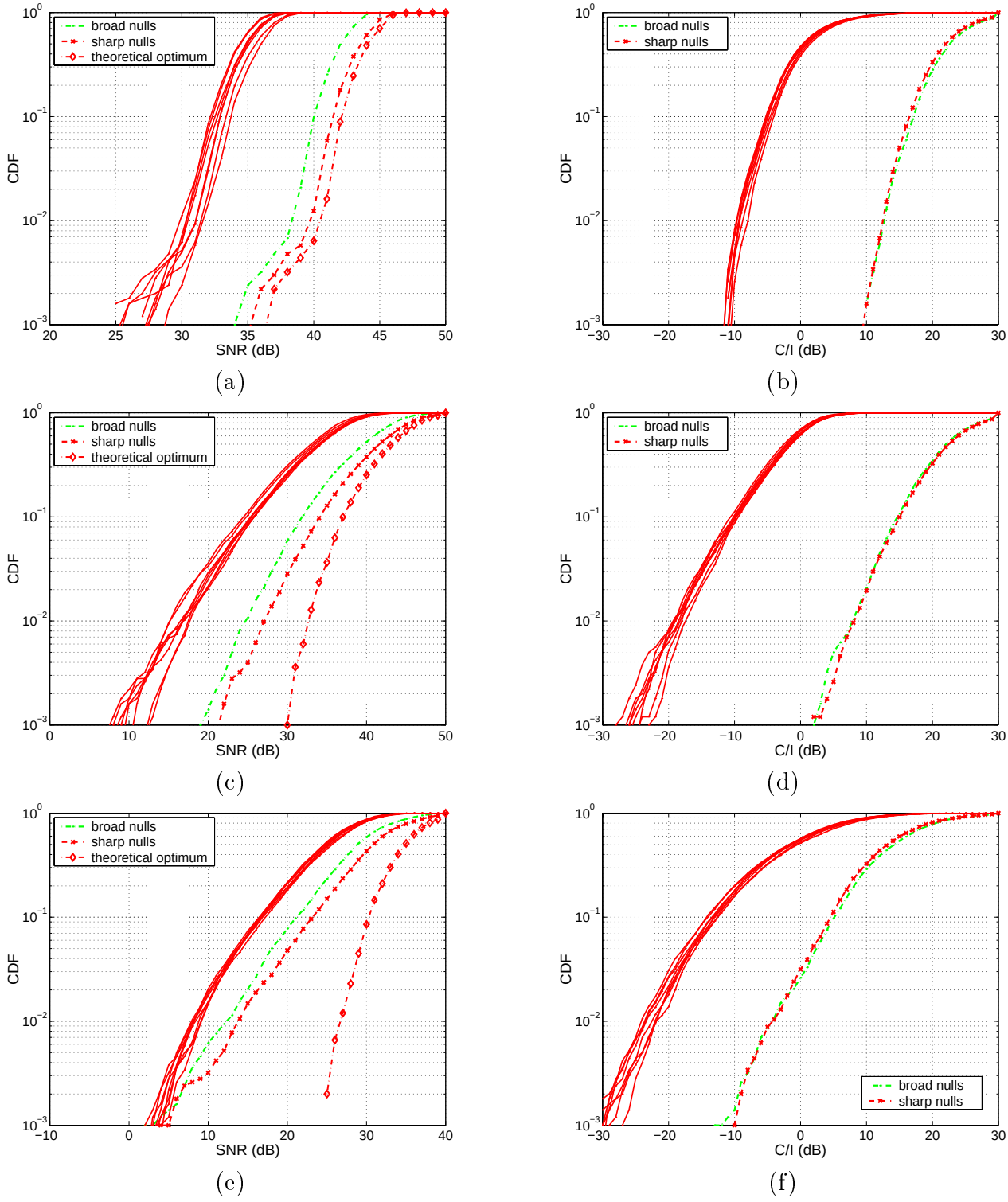

Figure 5.18. Effect of broad nulls in the final beamformer (**ULpBF**) on the SNR gain (a,c,e) and C/I gain (b,d,f). To get sharp nulls the conventional beamformer **ULpBF** =Pseudo Inverse is applied. The broad nulls are generated with **SmearR**. (a, b) Scenario A. (c, d) Scenario A'. (e, f) Scenario B.

than the null width.

Thus I applied the **MVM** with different fine resolution settings and present the C/I gain in Fig. 5.19. Increasing the angular resolution of the DOA estimation has a similar effect as an "artificial" shift of the nulls. The C/I gain decreases less for the broad nulling strategy! In Scenario A the C/I gain drops significantly for the Pseudo Inverse, when the fine resolution is larger than $R_f = 1°$, while for the beamformer with broad nulls the gain stays constant until $R_f = 5°$. This is the scenario, where the angular spread of the interference is large. In Scenario A', the C/I gain stays more constant for both beamformers, although it drops more for the Pseudo Inverse than for **SmearR**.

From the measurement results I conclude:

- **SmearR** is robust against poorly estimated interferer DOAs: When the angular resolution of the DOA estimation, R_f, is increased, the degradation of $\Delta C/I^{\gamma}$ for **SmearR**, is nearly independent of the angular spread. In both scenarios, Scenarios A and A', $\Delta C/I^{\gamma}$ decreases not more than $1.5dB$ (Fig. 5.19). ad. When the null is shifted, because the interferer DOAs are not correct anymore (R_f increases), the C/I gain will stay constant until the shift (R_f) is larger than the effective null width. The degradation of C/I gain starts when $R_f > 5°$, thus I conclude that the effective null width is in the order of 5°. Note that **SmearR** is configured to have a null width of 10°.

- The effective null width is larger for **SmearR** than for the Pseudo Inverse.
  The degradation of the C/I gain starts for the Pseudo Inverse already at $R_f = 1°$. Thus, I conclude that the null width is smaller than for **SmearR**. This agrees with conclusions from the theoretical antenna pattern.

- The effective null depth is larger for the Pseudo Inverse than for **SmearR**.
  The Pseudo Inverse effectively places sharper nulls than **SmearR**. Compare the C/I gain degradation that is caused by *not* placing any nulls with the case of interferer nulling (Tab. 5.8). Here, $\Delta C/I^{\gamma}$ drops stronger for the Pseudo Inverse than for **SmearR**. I therefore assume that the null depth is in reality larger for the Pseudo Inverse. Additionally the C/I gain is in the case of small angular spread of interference (Scenario A') slightly larger for the Pseudo Inverse than for **SmearR**.

- Null shifting is the limiting effect for the sharp nulling strategy.
  Because nulling with the Pseudo Inverse does not give a large improvement of $\Delta C/I^{\gamma}$ in Scenario A' (when the interference is incident with small angular spread), I conclude that the nulls are not effectively in the wanted interferer direction, but shifted (Tab. 5.8).

  This is supported by another result: When R_f is increased and the angular spread is small (Fig. 5.19(b)), the degradation of the C/I gain is not significantly larger for the Pseudo Inverse than for **SmearR**.

- Sidelobes near nulls are higher for the sharp nulling strategy than for **SmearR**.
  Up to now it is not clear, why $\Delta C/I^{\gamma}$ degrades stronger for the Pseudo Inverse (by $4dB$) than for **SmearR** (by $1.5dB$) in Scenario A (Fig. 5.19(a)). A reasonable explanation for that result is that for the case of the Pseudo Inverse higher sidelobes near the null exist.

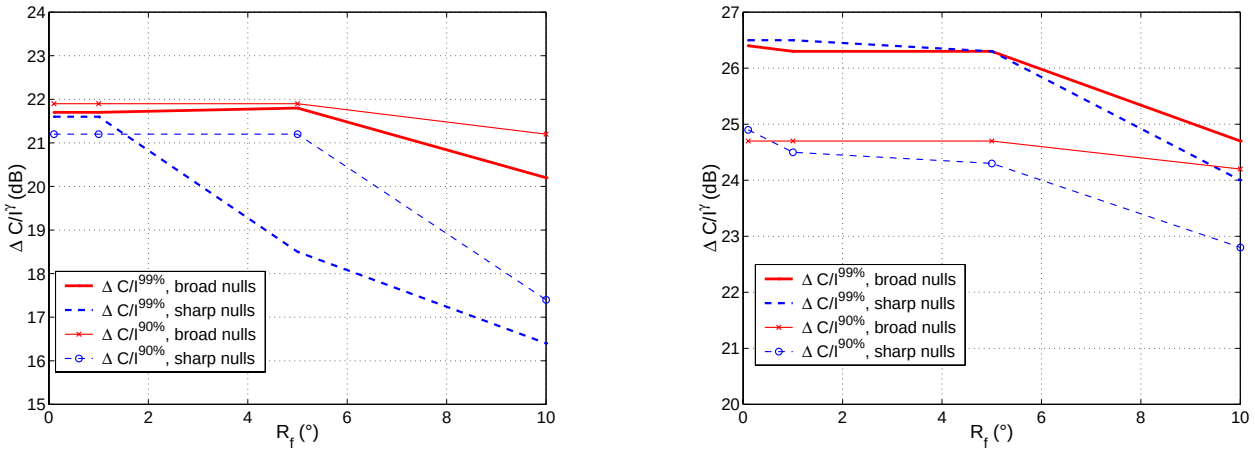

(a) (b)

Figure 5.19. Effect of broad null beamforming on the robustness of the C/I gain against less accurate DOA estimates. R_f is the angular resolution of **MVM**. To get sharp nulls the conventional beamformer (**ULpBF** =Pseudo Inverse) is applied. The broad nulls are generated with **SmearR**. (a) Scenario A, $\sigma_{SB}(n) \approx 5°$ for the interferer. (b) Scenario A', $\sigma_{SB}(n) \approx 0.5°$ for the interferer.

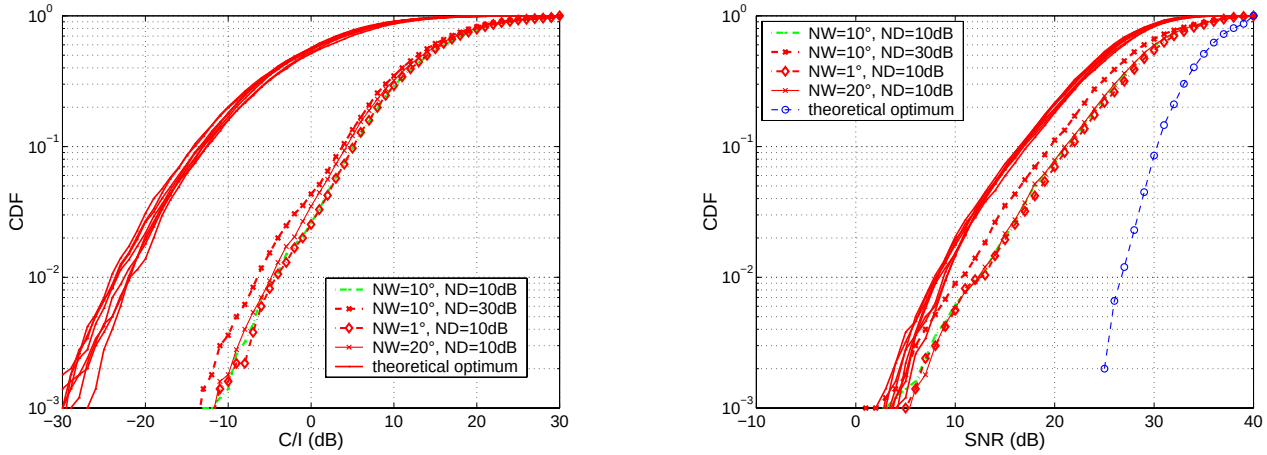

(a) (b)

Figure 5.20. Effect of null depth, ND, and null width, NW, of **SmearR** in the **ULpBF** on the C/I (a) and SNR (b) in Scenario B.

5.7.4 Null width and null depth

Of course it is of interest to know, whether other null width, NW, or null depth, ND, settings for **SmearR** would result in a better interferer suppression. I therefore applied **SmearR** with different configurations in Scenario B. Here, I chose the same configurations for which I have measured the sample pattern (see Fig.4.38, p.4.38). The optimum result is obtained for configuration $NW = 10°$ and $ND = 10dB$. Forcing deeper nulls ($ND = 30dB$) reduces the C/I gain as well as the SNR gain (Tab. 5.9). Although the optimum null depth for the measured antenna pattern occurred for $NW = 10°$ and $ND = 30dB$, the measured pattern also showed a shift of the main beam. This degrades the output user power and thus the C/I and SNR for this setting.

5.7.5 Broad nulls and angular spread

It is evident that the angular spread affects the system performance. Finally I will quantify how the broad nulling improves the robustness against angular spread under the assumption of perfect calibration. Because situations with a specific angular spread cannot be easily measured, I here rely on simulation results.

I assess the beamforming algorithms by investigating their influence on the mean SNIR improvement and on the raw bit error rate (BER). Here I use synthetic test data from the Geometry–based Stochastic Channel Model (Chapter 3). A realization of the used channel configuration is shown in Fig. 5.21. The user is located at $+10°$ and a single interferer at $-20°$. The user transmits with a mean power that is 5 dB lower than the interferer. The number of antenna elements is $M = 8$. I simulated 5000 GSM bursts with independent small–scale fading for various settings of the angular spread. In the GSCM the angular spread is defined as the second order moment of the angular power spectrum [LMB98].

The mean input SNIR varies with the angular spread as a consequence of the channel model (Fig. 5.22(a)). **SmearR** has the highest output SNIR regardless of the angular spread except for the Pseudo Inverse at the very small angular spread of 0.1°. Interference suppression of the algorithm that places sharp nulls is in principle unlimited, because, in the simulations, array imperfections are not accounted for. In this simulation the mean output SNIR is limited to

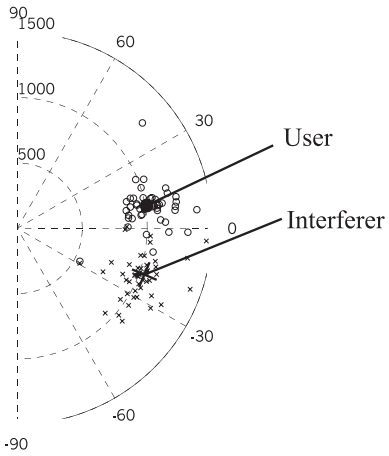

Figure 5.21. Realization of a GSCM scatterer distribution for an angular spread of 30°. The user mobile station is located at +10° and a single interferer at −20°. The small circles (crosses) symbolize the local scatterers for user (interferer). The distance between local scatterers and mobile stations has Gaussian distribution with a variance depending on the angular spread [LMB98].

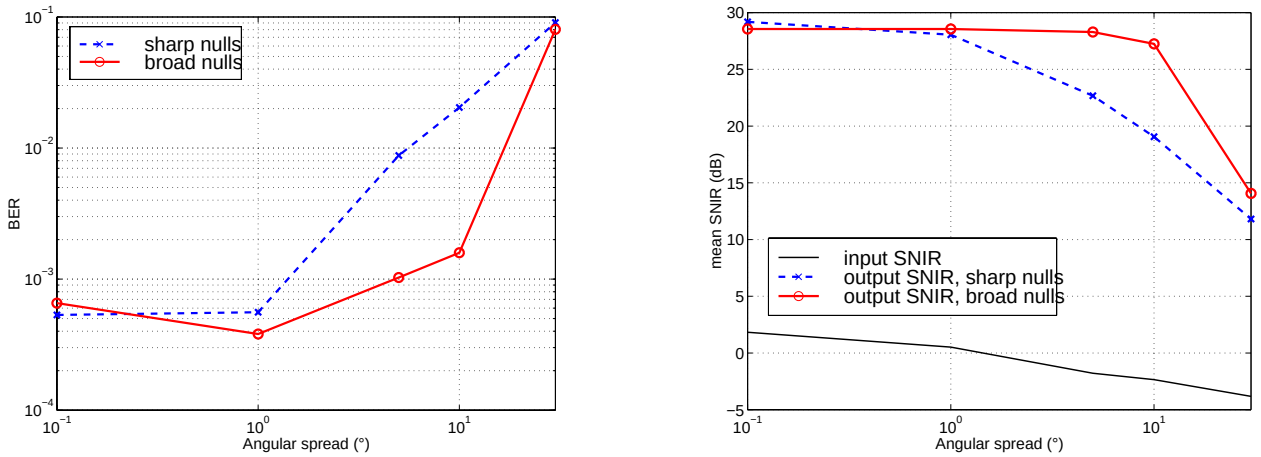

Figure 5.22. Effect of broad null beamforming on the (a) raw BER and (b) mean output SNIR. Because the mean input SNIR decreases with increasing AS the BER curves should only be compared with each other at a given AS value.

$29dB$, which is the consequence of a finite mean input SNR of $20dB$ and the maximum average SNR gain of $10 \log M = 9dB$ for the 8–element array. While for **SmearR** the SNIR reaches up to the maximum (noise–limited case, SNR=SNIR) nearly independently of the angular spread, the Pseudo Inverse is still interference limited for an angular spread larger than 1°.

The performance of **SmearR** starts to degrade only when the angular spread is larger than the null width (in this case $NW = 10°$). **SmearR** has a BER that is up to an order of magnitude smaller (Fig. 5.22(b)) compared to the Pseudo Inverse. Because the mean input SNIR decreases with increasing angular spread, the BER curves can only be compared for each angular spread setting individually.

5.7.6 Conclusions

From the results presented in this section I conclude:

- Forcing nulls into the direction of interferers increases the C/I gain by up to $4dB$.
- Placing broad nulls, instead of sharp nulls, increases the system's robustness against:
  - Estimated DOAs with reduced angular resolution.
  - Large angular spread of the interference.
- The measurements have verified the concept of broad null beamforming. Still, the nulling strategy does not affect the C/I gain as much as simulations have shown. Thus it is of importance to include hardware imperfections in the simulations, to increase the reliability of the results.
- Array imperfections limit the C/I gain. They cause shifted and filled nulls. The effect of the imperfections depends on the beamforming strategy.

5.8 Summary and conclusions

Finally I summarize the most important results of this chapter:

- **A^{3}P** achieves excellent C/I gain values up to $25dB$. The interferer suppression is not significantly depending on the environment. Even in an environment with large angular spread and interference from the same directions, the interferer suppression is as high as $18dB$.
- In interference limited environments, the optimum SNR gain cannot be reached. Only in the case, when the user signal has small angular spread, and thus no fading, the beamforming gain is only reduced by the tapering loss and reaches $7dB$.
- A DOA estimator with superior estimation quality, results in superior C/I gain and SNR gain. I thus conclude that the estimation quality is a suitable measure to assess the applicability of a DOA estimator to a smart antenna.
- The tracker is the key element that assures robustness of the system. Because it can remedy inferior performance of algorithms that are executed *before* the **DOAT**, the requirements on these algorithms are relaxed:
  - The influence of the **DOAE** on the overall performance is strongly suppressed. The C/I gain and SNR gain are independent of the angular resolution, as long as it is smaller than $10°$.
  - The choice of the specific configuration for the **UID** and **ULBF** does not affect the overall performance.
- We do not need a DOA estimator with high–resolution. Following this argumentation could lead to the conclusion that a switched beam system that includes a user identification would already suffice. This is not the case. The advantage of a switched beam system is that only a single transceiver train is required [NNK98]. But this would also

mean that for the final beamforming only the very limited choice of beams is available. Especially null steering is not possible with a switched beam system.

Thus we still need a DOA estimators, but only with angular resolutions in the order of some degrees. For **A**^{3}**P** this results in a run–time reduction, because **MVM** can be applied with larger resolution, R_f.

- Not the DOA averaging, but the tracking concept itself guarantees the excellent C/I gain.
- Interferer nulling increases the C/I gain by up to $4dB$.
- Beamforming with broad nulls does not enhance the C/I gain significantly compared to the sharp nulling. However, it increases the robustness against angular spread and against DOA estimates with low angular resolution.
- Calibration is the limiting factor in a DOA–based smart antenna system. It is the final beamforming, where the calibration limits the C/I gain. The SNR gain is, however, not influenced by the array imperfections. The DOA estimators are robust enough to cope with the imperfections.
- The key elements of a DOA–based smart antenna are: user identification and tracking. Together they provide very reliable decisions, where the main beam should aim at, resulting in an excellent interferer suppression, even in low C/I environments.

Chapter 6

APPLICATIONS

We are now familiar with **A**^{3}**P**, have studied the behavior of each subtask and quantified the achievable benefits. In this chapter I will present applications of **A**^{3}**P** in different environments. The first sections deals with sensitivity enhancement. I will show the benefits of **A**^{3}**P** in noise limited environments, i.e. when no interference is present. Here, I will illustrate an application with dual beams to maximize the diversity gain, and I will discuss in which environments the gain is largest.

In the second part I will discuss **A**^{3}**P**'s applicability to environments that are either noise or interference limited. I will show in an exemplary environment how **A**^{3}**P** can be either optimized for interferer suppression or SNR improvement.

The third part of this chapter will deal with network asynchronity. In an SFIR system interference is generated in co–channel cells. Today, the base stations of a GSM system are not synchronized. Thus I will study the influence of asynchronous interference on **A**^{3}**P**'s performance in different sample environments.

Finally I will show that **A**^{3}**P** is fully compatible with frequency hopping.

6.1 Sensitivity enhancement

The previous chapter has dealt with interference limited environments only. In such environments the SNIR is dominated by the interferer term, $C/I \ll SNR$. **A**^{3}**P** is designed and optimized to suppress interference, especially in low C/I situations. Still I am also interested in the sensitivity enhancement of **A**^{3}**P** in an environment where *no* interference is present. This sensitivity enhancement is of importance, when the smart antenna is applied to extend the range of a base station. In this context the SNR gain, the beamforming gain, and the diversity gain are of interest. Here, I will quantify the diversity gain that **A**^{3}**P** can achieve by its inherent *angular diversity* (see Sect. 4.6, p.63).

Angular diversity and angular spread In general, a DOA–based smart antenna will give optimum performance when the angular spread is low. I will discuss this in more detail.

In Chapter 5 we have seen that the interference suppression is largest, when the interference is incident from a small angular range (see Sect. 5.7, p.106).

In the following we will see that a large angular spread of the *user* signals does not necessarily

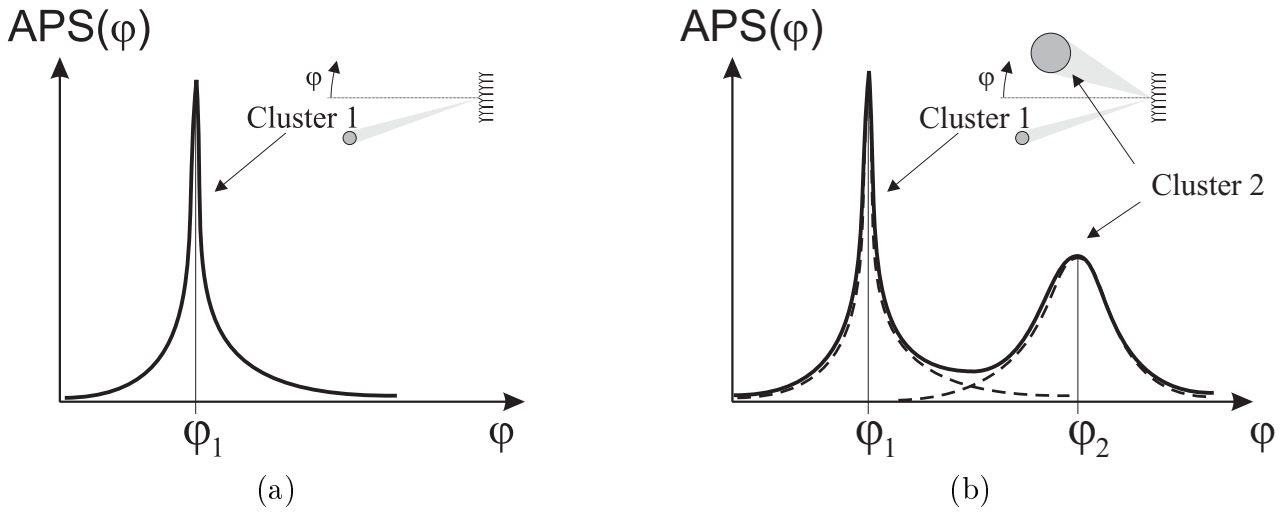

Figure 6.1. Angular power spectrum, $APS(\phi)$ of the user signal and corresponding channel model. (a) Single cluster. (b) Two clusters, the dashed line shows the APS of the individual clusters.

reduce the performance. The angular spread is defined as [Egg95]

$$AS = \sqrt{\frac{\int_{-\frac{\pi}{2}}^{\frac{\pi}{2}} \left(\phi - \overline{\phi}\right)^2 APS(\phi) d\phi}{\int_{-\frac{\pi}{2}}^{\frac{\pi}{2}} APS(\phi) d\phi}}, \tag{6.1.1}$$

where

$$\overline{\phi} = \frac{\int_{-\frac{\pi}{2}}^{\frac{\pi}{2}} \phi APS(\phi) d\phi}{\int_{-\frac{\pi}{2}}^{\frac{\pi}{2}} APS(\phi) d\phi}. \tag{6.1.2}$$

$APS(\phi)$ is the angular power spectrum (APS) that describes the power distribution over the angle ϕ. However, with this definition the angular spread cannot be directly related to the performance of a DOA–based smart antenna.

Here I apply a different definition. The angular spread is defined as an integral over the APS that includes *all* signal components. Assume that we can separate the signal components of the clusters, for example in a channel model by deactivating all clusters but one. This will result in an angular power spectrum for each cluster (Fig 6.1(b), dashed line), APS_l. Thus we can calculate an "angular spread" for each cluster by applying Eq. 6.1.1 to the individual angular power spectra. I call APS_l the *angular spread of a multipath component* or in short the *component angular spread* (CAS). In the following I will discuss the influence of the angular spread of the *user* signals on the performance.

If a single cluster[1] is present — or if the APS has a single peak — the angular spread and the CAS are equivalent. A large angular spread means a reduced performance of $\mathbf{A}^3\mathbf{P}$. Actually,

[1]The term *cluster* is borrowed from channel modeling. In the GSCM, finite angular spread is modeled by

the beamforming gain will be reduced when the CAS is larger than the main beam width, i.e. if the main beam cannot collect all offered energy. This is also true in the case of more nominal DOAs. If the CAS is larger than the main beam width, the angular diversity gain will be increased.

When more clusters (multipath components) are present (Fig. 6.1(b)), the angular spread is not a good measure, but the CAS will be of importance. Just assume a situation will two well separated multipath components, each having a CAS of smaller than the main beam width. This results in a large angular spread, depending mainly by the angular separation of the multipath components. In that case **A³P** can *better* exploit the offered diversity by its angular selection diversity than in the case of a single multipath component with larger angular spread. How large the *angular* diversity gain of **A³P** will be, depends on the channel conditions. It will be optimum if more clusters are available, *each* with a CAS smaller than the beam width and with similar average powers. A larger CAS will again degrade the beamforming gain, but not the diversity gain.

Summary From the angular spread we cannot draw general conclusions on the performance of a DOA–based smart antenna system. Instead the CAS is a proper measure. **A³P** can exploit independently fading multipath components with a CAS smaller than the main beam width by angular diversity. The beamforming gain is reduced, if the CAS is larger than the main beam width. However, the CAS cannot be measured easily in a system and is more a concept to explain the behavior of a DOA–based smart antenna.

The large angular spread results in a small correlation of the signal envelopes [Egg95]. Spatial diversity would then yield a high diversity gain. In such an environment **A³P** can exploit only small parts of the offered diversity gain.

Under the assumption of uncorrelated Rayleigh fading of the multipath components, **A³P** can exploit an angular diversity gain. The diversity order achieved is then the number of the clusters. Unequal average power and correlated fading will, of course, degrade the diversity gain.

In the following I will study the diversity gain that **A³P** can achieve in three different environments.

6.1.1 A³P dual beam

A³P is able to steer two independent main beams to increase the SNR gain [KTTH99]. When **A³P** is in *dual beam* mode, the processing may result in two weight vectors for appropriate channel configurations. Each weight vector has a main beam independent from the other. For single–cluster channels, only a single main beam if formed. Then a single weight vector is used. If two weight vectors are available, they will be both used in the frame unit to compute two base band signals that are fed to a post–detection combining diversity receiver[2] [Ada93]. Thus, the dual beam configuration implements angular *combining* diversity, rather than angular *selection* diversity in the single beam mode. Because combining takes place in the frame unit, I cannot

local scatterers around the MS. These scatterers form a so–called *cluster*, i.e. a concentration of energy around a certain coordinate in the angle/delay domain. In GSCM we typically apply one or two clusters are present. The second cluster is modeled by far scatterers (Fig. 3.4, p.26).

[2]The combination of the signals is not done prior to detection. Instead, the soft decision bit sequences that result from the detection are combined. A combination prior to detection would, of course, mean that only a single weight vector has to be calculated, i.e. a weight vector that includes already two main beams. During the development of **A³P**, this option turned out to be less successful.

calculate the output signal in the data evaluation[3]. To assess the dual beam mode, I instead calculate the SNRs for each weight vector and sum them up to get the output SNR for the dual mode

$$SNR_{out,beam1}(n) = \frac{||\mathbf{w}_1(n)^H \tilde{\mathbf{X}}_{user}(n)||_2 - P_N}{(P_{N,I} + P_{N,U})}, \tag{6.1.3}$$

$$SNR_{out,beam2}(n) = \frac{||\mathbf{w}_2(n)^H \tilde{\mathbf{X}}_{user}(n)||_2 - P_N}{(P_{N,I} + P_{N,U})}, \tag{6.1.4}$$

$$SNR_{out}(n) = SNR_{out,beam1}(n) + SNR_{out,beam2}(n). \tag{6.1.5}$$

The resulting output SNR will present an upper bound for the actual SNR that is achievable by combining the signals. It assumes that the noise contributions in the two resulting output signals are decorrelated. This is a realistic assumption, when the main beams do not look into the same direction[4] which of course is guaranteed by $\mathbf{A}^3\mathbf{P}$.

6.1.2 Scenario Urban 1

The first scenario where I assess the diversity gain is in an urban environment (Fig. 6.2[5]). The array was standing on top of the four storey high Alcatel building in Stuttgart and was oriented to the west. The neighboring building is one floor higher than the Alcatel building. Thus a part of the area served by the base station is strongly shadowed. This base station arrangement was used in *all* measurements. There are other office buildings and factory buildings in the surroundings.

During the measurement, the MS had for most of the bursts a NLOS to the BS; the LOS was obstructed by the neighboring building. The van drove with a speed of about $10km/h$. There are two multipath components evident from the DOAs of the scanning beam algorithm (Fig. 6.2(b)). The direct LOS component changes from $\phi_1 \approx 20°$ to $\phi_1 \approx 10°$. Because the neighboring building that causes the shadowing is only one floor higher, still most of the power reaches the array by diffraction over the roof. The second multipath component is incident from $\phi_2 \approx 45°$. Probably, these waves are reflected at a building to the north–west of the BS (dashed line in Fig. 6.2(a)). Because of the two multipath components I expect $\mathbf{A}^3\mathbf{P}$ to reach a high diversity gain.

Diversity gain First I investigate the influence of the tracker on the overall performance. I thus applied $\mathbf{A}^3\mathbf{P}$ in a standard configuration and with deactivated tracker in Scenario *Urban 1* (Fig. 6.3(a)). Deactivating the tracker results in the same beamforming gain, but in an increased diversity gain, G_{div}^{γ} (Tab. 6.1). $G_{div}^{99\%}$ is by $2.5dB$ larger when the tracker is deactivated than in the standard configuration, which is a consequence of the larger slope of the CDF of the output SNR. $\mathbf{A}^3\mathbf{P}$ *without tracking* achieves nearly the same diversity order as the scanning beam, as evident from the rather constant distance of the CDF of $\mathbf{A}^3\mathbf{P}$ to the CDF of the scanning beam. The diversity gains of $\mathbf{A}^3\mathbf{P}$ *without tracking* and scanning beam differ only by $0.4dB$ to $0.9dB$ (Tab. 6.1). As a consequence of the similar performance, I conclude that $\mathbf{A}^3\mathbf{P}$ without

[3] In this work, I do not apply a detector, but only compute the output signal after beamforming and from that the C/I and SNR.

[4] When we assume that the noise is spatially white, the two weight vectors must be orthogonal to achieve full decorrelation. I have checked typical values for the correlation of the two weight vectors, and it was in the range of $0.1 \ldots 0.2$.

[5] This is the same as Scenario B, but without interference (Fig. 5.11, p.101).

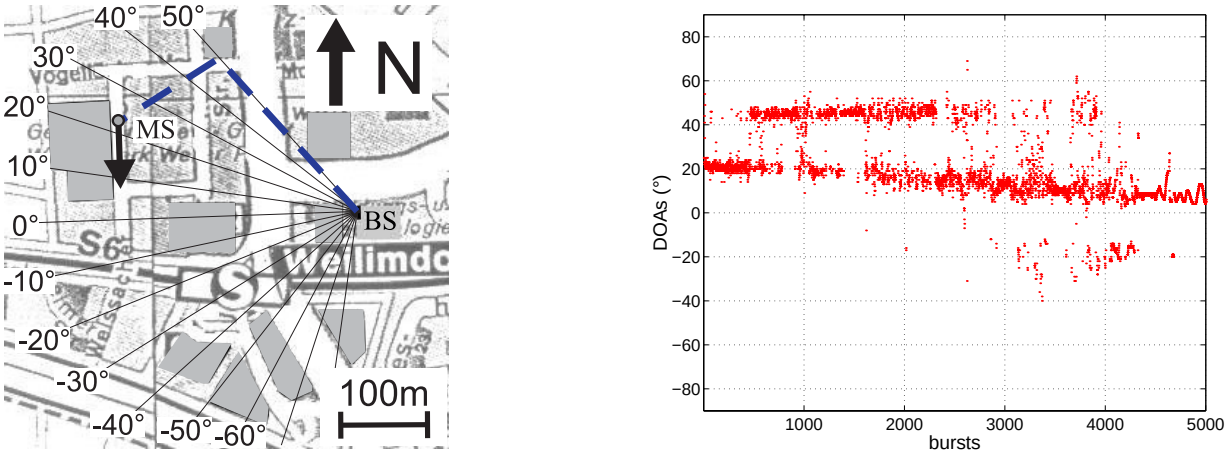

Figure 6.2. Scenario *Urban 1*. (a) Map of measurement route. The van (MS) drove with a velocity of about $10km/h$ along the route (arrow). (b) DOAs, $\phi_{SB}(n)$, of scanning beam.

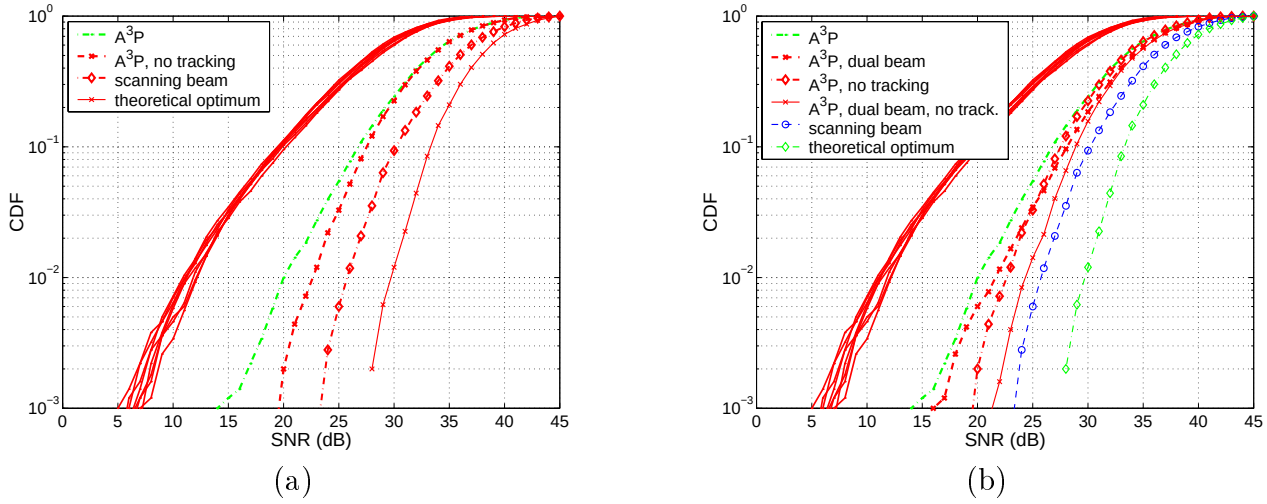

Figure 6.3. Statistic of the SNR values in Scenario *Urban 1*.

A^3**P** configuration	Scenario *Urban 1*				
All values in dB	$\Delta SNR^{90\%}$	$\Delta SNR^{99\%}$	G_b	$G_{div}^{90\%}$	$G_{div}^{99\%}$
A^3**P**	7.1	8.6	5.2	2.0	3.5
A^3**P**, dual beam	8.4	10.2	5.7	2.7	4.5
A^3**P**, no tracking	7.8	11.3	5.3	2.5	6.0
A^3**P**, dual beam, no tracking	9.1	12.9	5.8	3.3	7.1
Scanning beam	10.4	14.4	7.5	2.9	6.9
Theoretical optimum	13.5	18.3	9.0	4.5	9.3

Table 6.1. SNR gain and diversity gain in Scenario *Urban 1*.

tracking results practically in the same beam steering as the scanning beam, i.e. **A**^{3}**P** puts the main beam in the same direction as the scanning beam. But, the beamforming gain is for **A**^{3}**P** by $1.3dB$ smaller than for the scanning beam, because of the tapering loss of the beamformer **SmearR** (see Sect. 5.7, p.106).

In Section 4.6 I have discussed the tracking concept. The tracker's main task is to assure possibly high interference suppression, even at low input C/I. This is accomplished by taking additional reliability measures into account. As a result, the main beam is not pointed into the direction of the largest power, but in the direction of the *most reliable* trackers with largest power. This practically results in a degradation of the output SNR compared to the scanning beam, because not necessarily the direction with the *largest signal power* is in the list of the most reliable trackers and thus cannot always be selected. As an example consider a multipath that just arises, i.e. a new direction for the user signals. For the first few bursts the tracker will not allow putting the main beam into that direction, because the reliability of this new DOA is too low (it could be a far–off estimate or even an interferer DOA). Regardless of its power, only after 10 bursts, the new DOA can be selected. Thus **A**^{3}**P** results in an output power smaller than the output power of scanning beam.

To maximize the output power, it is not necessary to take additional signal quality measures, like the reliability, into account. When no interference is present, interferer suppression is not an issue and it is therefore not required to apply the tracking concept. Steering the main beam into the direction of the largest power is enough. In this sense, the scanning beam algorithm reaches the optimum SNR under the assumption that a single beam with constant beam width is steered. Still **A**^{3}**P** *without tracking* does not reach the performance of the scanning beam. The explanation is similar as the one before: Even if the tracker is deactivated, **A**^{3}**P** selects the DOAs only from the identified *user* DOAs. In contrast, the scanning beam may select any DOA. But here, **A**^{3}**P**'s limitation results in only little degradation of the output power.

There are two conclusions from this discussion:

- We can trade interference robustness against diversity gain. This will become even clearer in the next section, where I discuss the transition from noise limited to interference limited cases. In the current result, higher SNR gain is achieved, when the tracker is deactivated. But in Sect. 5.6 on page 103 we have seen that this causes a fatal degradation of the C/I gain, when interference is present.

- There are two configurations of **A**^{3}**P** available, where **A**^{3}**P** either is most robust against interference, or optimizes the diversity gain. This gives room for improvement: we just have to estimate the interference situation and correspondingly adapt the configuration of **A**^{3}**P** (see Chapter 7).

The scanning beam does not reach the theoretical optimum output SNR, because of two reasons. First, the energy arrives in some bursts from a larger angular range than the main beam width of the scanning beam (e.g. around burst number 4000 in Fig. 6.3(b)). This reduces the beamforming gain by $1.5dB$ from the theoretical optimum. Even if we would add $1.5dB$ to ΔSNR^{γ}, i.e. disregard the effect of large angular spread, the SNR gain does not reach the theoretical limit. Thus, secondly, the *diversity* gain of the scanning beam is smaller than it is optimally. The theoretical limit can be achieved with maximum ratio combining. The scanning beam, however, realizes an angular *selection* diversity. Of course this is inferior to a combining diversity strategy. This result shows basic limitations of an angular diversity scheme.

To increase the SNR gain I apply the dual beam configuration of **A**^{3}**P** (Fig. 6.3(b)). As expected, the dual beam mode outperforms the single beam mode, regardless of the activation

of the tracker (Tab. 6.1). Because **A**^{3}**P** collects energy with two beams from a larger angular range, the beamforming gain is increased. But, the improvement of G_b is only $0.5dB$, because the "first" beam (the beam with the largest signal power) covers already most of the energy. Not surprising, applying an angular *combining* diversity does not increase the average SNR gain (beamforming gain) significantly, compared to the angular *selection* diversity. Still, the increase of the diversity gain is larger than the increase in beamforming gain. Here, the dual beam configuration reaches an up to $1dB$ larger diversity gain than in the case of a single beam.

When the tracker is deactivated in the dual beam mode, **A**^{3}**P** results in a slightly larger diversity gain than the scanning beam. This is of no surprise in the current environment. The scanning beam is in single beam operation and thus a *selection* diversity scheme, while **A**^{3}**P** *combines* the signals of the two beams. But, speaking in absolute numbers, the SNR gain, ΔSNR^{γ}, of **A**^{3}**P** *dual beam* is still smaller than the one of scanning beam. Again the explanation lies in the beamforming gain that is $1.8dB$ larger for the scanning beam, because it has no tapering loss.

In summary, **A**^{3}**P** in *dual beam* mode and *no tracker* results in the largest diversity gain and nearly reaches the performance of the scanning beam algorithm. The diversity gain is as high as $7dB$ when measured at the 1% probability. The SNR gain is still up to $4dB$ lower than the theoretical optimum; a consequence of the tapering loss, a larger angular range than the beam width, and the user identification. Deactivating the tracker increases the performance more strongly than applying a second beam. This is also evident from the statistics of the output SNRs (Fig. 6.3(b)). The configurations *without tracking* have the same, larger, slope than the configurations *with tracker*.

The presented results were obtained in a scenario that favors angular diversity. **A**^{3}**P** achieves a large diversity gain because the CASs are small, and *although* the *angular spread* is large. In the following subsections I study two other environments.

6.1.3 Scenario Highway

In the Scenario *Highway* the van drove with high speed on the Autobahn (Fig. 6.4(a)). Most of the measurement time, the MS had quasi–LOS to the BS. Passing cars and vegetation along the Autobahn caused temporarily obstructed LOS. During these periods we observed a small angular spread (Fig. 6.4(b)). Only during the bursts 3000 to 5800, we had NLOS caused by an office building. During that time most of the signal energy arrived from angles around $\phi = -40°$. A possible explanation is that the signals were reflected at the office buildings south to the railway (S–Bahn) station, depicted by the dashed line in Fig. 6.4(a).

Results Regardless of the configuration, **A**^{3}**P** achieves a high beamforming gain of $G_b = 6.9dB$ (Tab. 6.2). The degradation from the theoretical optimum is caused by the tapering loss. This scenario offers only little diversity gain (Fig. 6.5). Only in the *dual beam* configuration *without tracking*, a small diversity gain is achieved. This configuration performs as well as the scanning beam, except for the difference in beamforming gain caused by the tapering loss. In contrast to Scenario *Urban 1*, the dual beam cannot outperform the scanning beam. This and the low diversity gain occur because most of the time quasi–LOS exists that causes only a single multipath. Futhermore even during the short NLOS period, only a single multipath is present because of the strong shadowing in the LOS direction.

Summary: Scenario *Highway* does not offer a diversity gain that **A**^{3}**P** can utilize with angular diversity. **A**^{3}**P** can achieve a significant diversity gain only in scenarios that have more than one multipath with similar power. This is in agreement with the expected behavior. Instead,

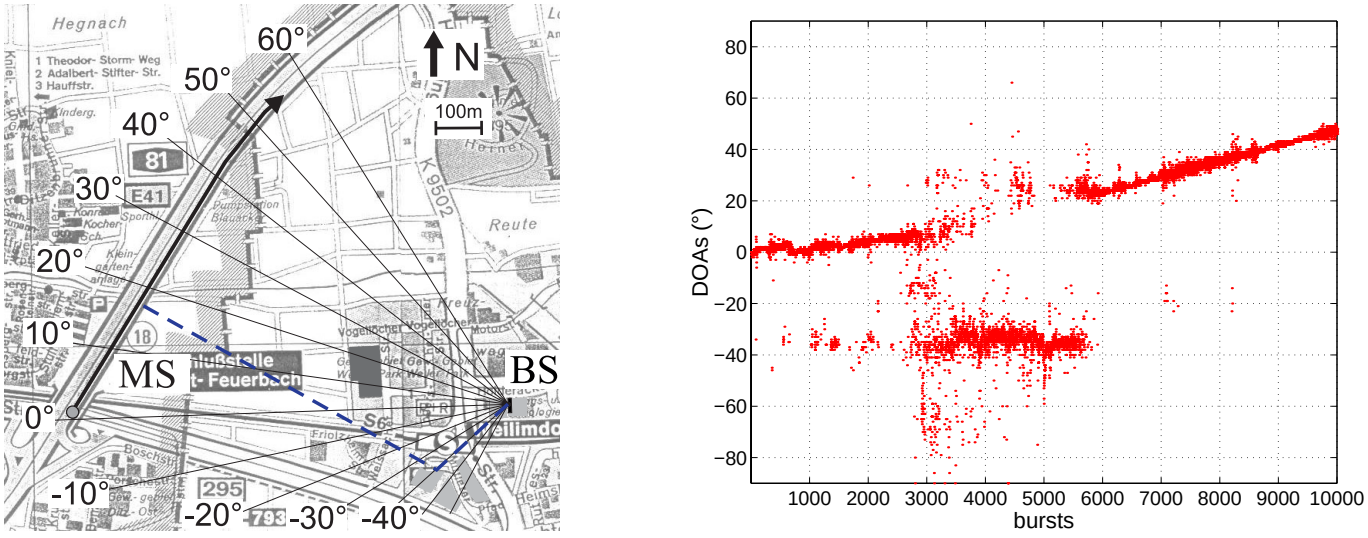

(a) (b)

Figure 6.4. Scenario *Highway*. (a) Map of measurement route. The van (MS) drove with a velocity of up to $100km/h$ along the highway (arrow). (b) DOAs, $\phi_{SB}(n)$, of scanning beam.

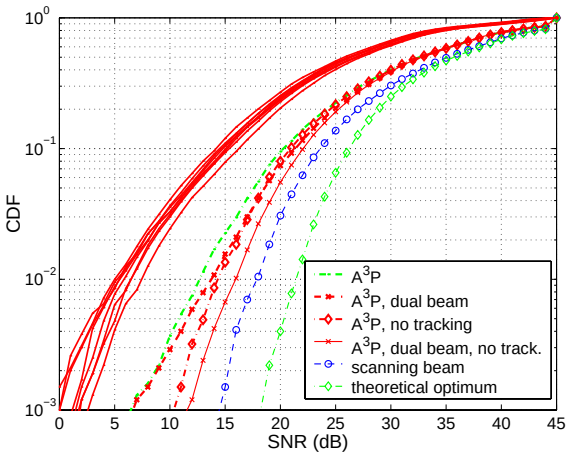

Figure 6.5. Statistic of the SNR values in Scenario *Highway*.

A^3**P** configuration	Scenario *Highway*				
All values in dB	$\Delta SNR^{90\%}$	$\Delta SNR^{99\%}$	G_b	$G^{90\%}$	$G^{99\%}$
A^3**P**	5.3	6.7	6.9	-1.6	0.2
A^3**P**, dual beam	6.4	7.8	6.9	-0.5	0.9
A^3**P**, no tracking	6.0	8.3	6.9	-0.9	1.4
A^3**P**, dual beam, no tracking	7.0	10.0	6.9	0.1	3.1
Scanning beam	8.7	12.0	8.9	0.2	3.1
Theoretical optimum	11.3	15.5	9.0	2.3	6.5

Table 6.2. SNR gain and diversity gain in Scenario *Highway*.

A^3**P** achieves a high beamforming gain of nearly $7dB$.

6.1.4 Scenario Urban 2

In Scenario *Urban 2* the MS moved with little speed between high office buildings (Fig. 6.6(a)). During the entire measurement the MS had *no* LOS to the BS, resulting in a large angular spread (Fig. 6.6(b)). This is a challenging situation for a DOA–based smart antenna.

Results The theoretically achievable diversity gain in Scenario *Urban 2* is larger than in Scenario *Highway*, but smaller than in Scenario *Urban 1*.

Here, the **A**^{3}**P** configurations *with tracking* suffer in performance. The CDF of the output SNR has a *smaller* slope than the one of the input SNR (Fig. 6.7(a)). To better understand why the tracker degrades the performance in this environment, I plot the selected DOAs (Fig. 6.8). The selected user DOAs of **A**^{3}**P** *without tracking* look similar to the DOAs of the scanning beam (Fig. 6.6(b)), thus the similar output SNR of **A**^{3}**P** *without tracking* and the scanning beam. But when the tracker is activated, the main beam cannot hop freely. Instead **A**^{3}**P** selects the direction of the main beam (=selected user DOA) from a list of tracked DOAs. Figure 6.8(a) demonstrates that several trackers exist simultaneously (arrows). Although this plot shows for each burst only a single user DOA, i.e. the selected user DOA, where the main beam points to, we can clearly identify the progress of the trackers over the bursts. Of course, there is only a limited number of trackers initialized and therefore not every DOA can be selected as main

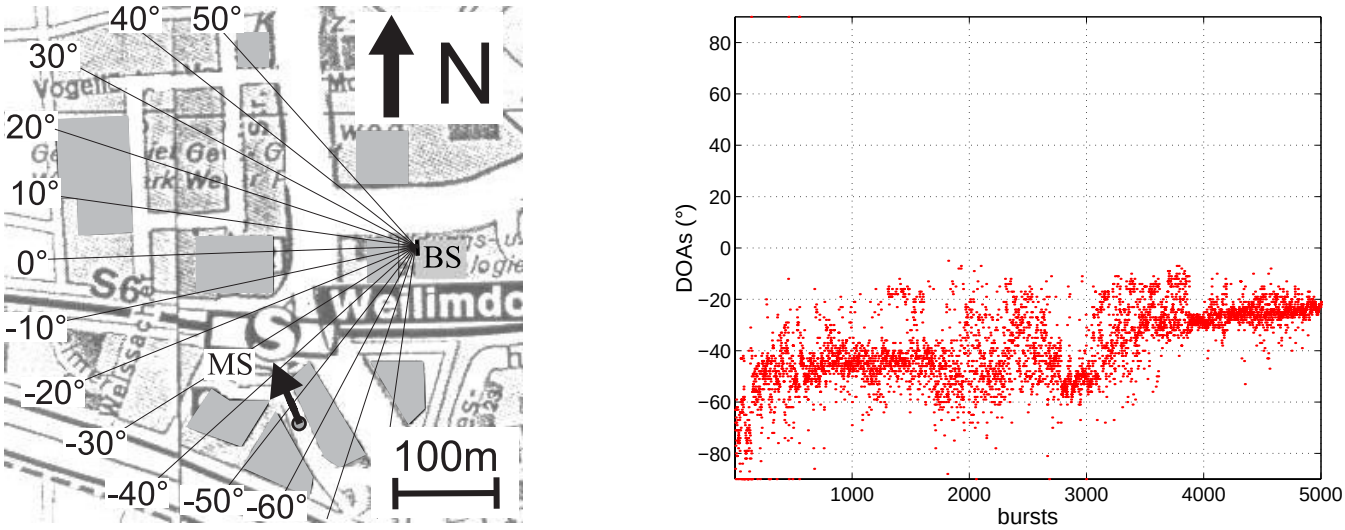

(a) (b)

Figure 6.6. Scenario *Urban 2*. (a) Map of measurement route. The van (MS) drove with a velocity of about $30km/h$ between office buildings with up to eight floors (arrow). (b) DOAs, $\phi_{SB}(n)$, of scanning beam.

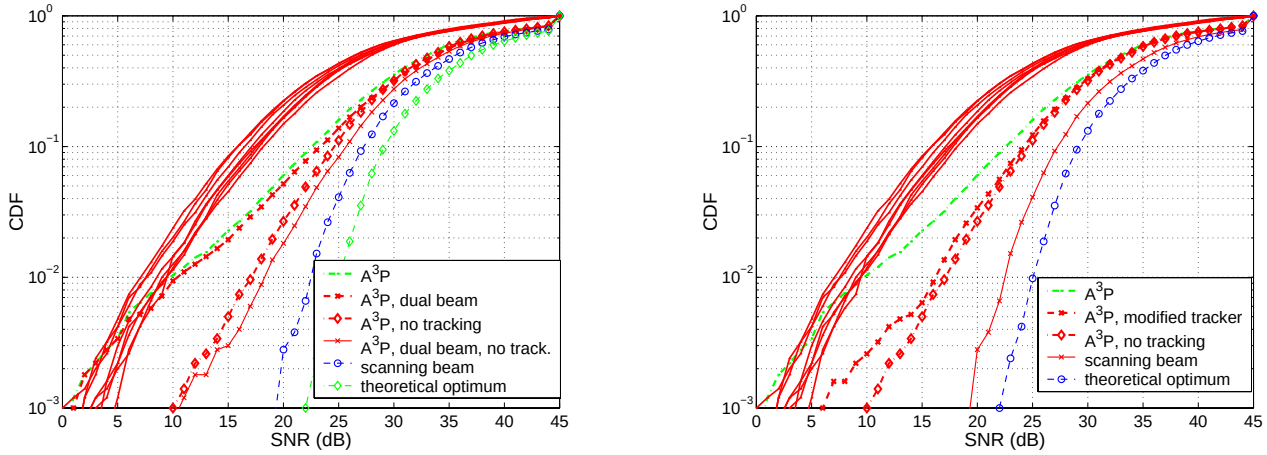

Figure 6.7. Statistic of the SNR values in Scenario *Urban 2*.

beam direction. Additionally, **A^{3}P** selects a tracked direction only when the tracker has been updates at least 10 times.

In the current scenario many new trackers are initialized. The overall directional characterization of the channel changes so rapidly that as soon as a tracker is verified often enough to be a candidate for the main beam direction, it is already obsolete. Thus the tracker has to stick to directions that are more reliable, but result in a reduced output SNR.

I have applied the tracker with a modified, less robust configuration, to support the explanation of the performance degradation. The modification is that a tracker now only has to be updated two times (instead of 10 times) before it can be selected. **A^{3}P** with *modified tracker* reaches nearly the performance of the system without tracker (Fig. 6.7(b)), thus verifying my explanation.

The current example reveals another peculiarity of **A^{3}P**. Although there is *no* interference active during the measurement, **A^{3}P** classifies some DOAs as interferers, because they have more than three bit errors in the training sequence. This may have three reasons: Either the **DOAE** has detected a very weak signal component (low SNR) or the DOA is a far–off estimate and thus no signal is incident from that particular direction. Third, delay spread causes a large number of bit errors.

In summary: **A^{3}P** can utilize parts of the offered diversity gain only when the tracker is deactivated, but this will decrease the robustness against interference. The improvement of the dual beam mode compared to the single beam mode, is similar to that in Scenario *Urban 1*. The largest diversity gain is $3.5dB$. Because no separate multipaths with smaller angular spread are available, **A^{3}P** will not achieve such a high diversity gain as in Scenario *Urban 1*. Obviously the angular spread is not large enough to cause a significant degradation of the beamforming gain, because **A^{3}P** achieves a beamforming gain larger than $6dB$.

6.1.5 Summary

From the evaluation of the three scenarios I conclude:

- **A^{3}P** realizes a diversity gain of $7dB$ in an environment with two multipaths present. To get a large angular diversity gain the environment has to offer more than one multipath component with similar average power.

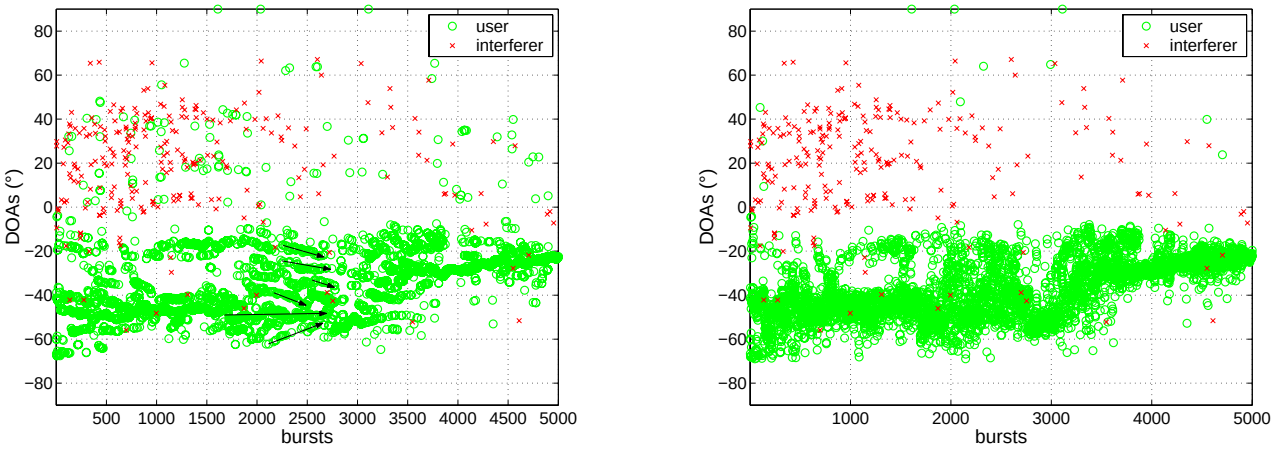

Figure 6.8. Selected user and interferer DOAs for final beamforming in Scenario *Urban 2*. (a) **A**^{3}**P**. (b) **A**^{3}**P** without tracking.

A^3**P** configuration	Scenario *Urban 2*				
All values in dB	$\Delta SNR^{90\%}$	$\Delta SNR^{99\%}$	G_b	$G^{90\%}$	$G^{99\%}$
A^3**P**	5.7	1.4	6.1	-0.4	-4.7
A^3**P**, dual beam	6.4	1.9	6.4	0.0	-4.5
A^3**P**, no tracking	7.6	8.8	6.2	1.4	2.6
A^3**P**, dual beam, no tracking	8.8	10.1	6.6	2.2	3.5
A^3**P** , modified tracker	7.3	7.7	6.2	1.1	1.5
Scanning beam	10.3	14.0	8.5	1.8	5.5
Theoretical optimum	12.2	16.6	9.0	3.2	7.6

Table 6.3. SNR gain and diversity gain in Scenario *Urban 2*.

- The angular spread is not the proper choice to describe the angular diversity gain, but the CAS (component angular spread) and the number of simultaneously existing nominal DOAs (clusters). In Scenario *Urban 1* two nominal DOAs exist simultaneously, resulting in the largest diversity gain of the studied scenarios.

- The beamforming gain is always larger than $5dB$ and increases in environments with small angular spread up to $7dB$.

- If the diversity gain is small, the beamforming gain is larger, resulting in a total SNR gain that is in all scenarios in the order of $8dB$ (**A**^{3}**P** *without tracking*).

- The scanning beam algorithm outperforms **A**^{3}**P** in noise limited environments. When we consider smart antenna systems that apply a single main beam with constant beam width (as **A**^{3}**P** and the scanning beam), the scanning beam achieves optimum SNR gain, because it always will select the DOA with largest output power.

- SNR enhancement can be traded against interference robustness. **A**^{3}**P** can be configured to either optimize the SNR gain (no tracking, modified tracker) or to be most robust against interference (with tracking). This leaves room for improvement: A hybrid **A**^{3}**P** can adapt its configuration automatically to the current channel situation (see Chapter 7).

- The *dual beam* configuration increases the SNR gain by up to $2dB$. The improvement is basically caused by an increased diversity gain.

6.2 Interference to noise limited environments

In the previous chapter we have seen results in interference limited environments. In the previous section I discussed the case of noise limited environments. Here, I will show how **A**^{3}**P** behaves when we start with a strongly interference limited situation and gradually transform the environment to the noise limited case.

6.2.1 Environment I⟼N

The Environment $I{\longmapsto}N$ includes a user signal and an interferer (Fig. 6.9). The mobile station of the user (MS2) moved along a road from north to south with an average speed of $35km/h$. It never had a LOS to the BS, resulting in a large angular spread of the user signal.

The interferer (MS1) drove in a circle near the railway station (Fig. 6.9(a)). There the van had a quasi–LOS to the BS. The LOS was only obstructed by structures of the railway station, trees and cars. Near the van, to the south and to the east, large office buildings cause local scattering. This results in a significant angular spread of the interferer signal. The interferer power is high compared to the user power. From the system point of view, it would be rather unlikely that MS1, which has a lower path loss to the BS and is closer than MS2, is served at another BS, while MS2 is the user. However, I selected this environment because of the low input C/I and the angularly well separated user and interferer signals. This is an SDMA scenario, or SFIR during hysteresis of handover.

This setup results in an interference–limited scenario, when I superpose the user and the interferer signal as in Eq.5.2.4 on page 84. To gradually change the scenario from the interference limitation to a noise limited scenario, I attenuate the interferer signal

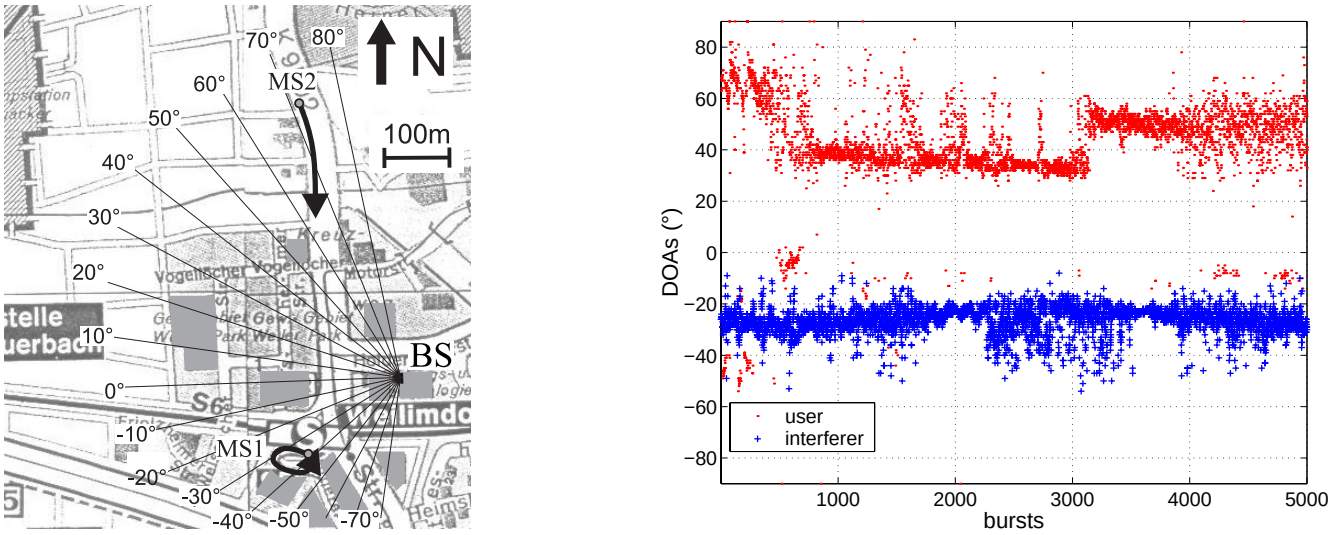

(a) (b)

Figure 6.9. Environment $I \rightarrowtail N$. (a) Map of measurement route. MS1 drove in a circle near the railway station with a velocity of about $20km/h$. MS2 drove along a road from north to south with a maximum speed of $60km/h$. (b) DOAs, $\phi_{SB}(n)$, of scanning beam. I include in this diagram the DOAs that scanning beam calculated separately from the user signals (dots) as well as from the interferer signals (crosses).

$$\mathbf{X}(n) = \tilde{\mathbf{X}}_{user}(n) + \sqrt{\alpha}\tilde{\mathbf{X}}_{intf,\Sigma}(n), \tag{6.2.1}$$

where α is a constant interferer attenuation factor. Consequently the interferer noise power (Eq. 5.2.6) is attenuated

$$P_{N,I} = \alpha K_I P_N. \tag{6.2.2}$$

In the following I varied α from $0dB$ down to $-60dB$ in Environment $I \rightarrowtail N$ to generate several scenarios (Scenario $I \rightarrowtail N_\alpha^{0dB}$, Scenario $I \rightarrowtail N_\alpha^{-20dB}$, ...). In these scenarios I study the behavior of **A**^{3}**P**.

6.2.2 Interference or noise — what is the limiting factor?

I first demonstrate how α affects the C/I, SNR and SNIR. Here I applied **A**^{3}**P** *without tracking* to the scenarios $I \rightarrowtail N_\alpha$ and present the statistics for the case of $\alpha = \{0dB, -20dB, -40dB, -60dB\}$ (Fig. 6.10).

Starting with the left column, the C/I shows the strongest variation over the different scenarios. When we go through the scenarios from top to bottom, i.e. from strong interference to weak interference, we find the expected shift of the input C/I. The output C/I, of course, also increases, when α decreases. But here, the CDF are not only shifted. Instead the behavior of **A**^{3}**P** changes. I will discuss this in the next subsection.

In the middle column I show the statistic of the SNR. The CDFs of the input SNR stay constant for all values of α. The only exception is a slight shift of approximately $3dB$ when we compare Scenario $I \rightarrowtail N_\alpha^{0dB}$ with the other scenarios. This is caused by the interferer noise term, $P_{N,I}$ (Eq. 6.2.2). In the current scenario, where $K_I = 1$ the total noise power is

$$\begin{aligned} P_{N,total} &= P_{N,U} + P_{N,I} && (6.2.3)\\ &= P_N + \alpha P_N && (6.2.4)\\ &= P_N(1+\alpha). && (6.2.5) \end{aligned}$$

If $\alpha = 0dB$, the total noise power will be almost double the noise power of the case $\alpha = -20dB$, hence the change in input SNR.

A^3**P**'s output SNR changes significantly when the input C/I varies. The input SNR stays constant and therefore the SNR gain improves dramatically when interference becomes small (see also Fig. 6.11(b)). This clearly demonstrates a typical behavior of a smart antenna system: When interference is high, all degrees of freedom are used to optimize the interferer suppression. On the other hand, when interference is of no concern, the system can optimize the output SNR.

Finally I discuss the SNIR. For $\alpha = 0dB$ and $\alpha = -20dB$ the SNIR at the input and at the output is dominated by the C/I. Consequently

$$\begin{aligned} \mathcal{C}_{in,m}^{SNIR} &\approx \mathcal{C}_{in,m}^{C/I}, \text{for all } m, \text{ and} && (6.2.6)\\ \mathcal{C}_{out}^{SNIR} &\approx \mathcal{C}_{out}^{C/I}. && (6.2.7) \end{aligned}$$

We say that the system is *interference limited* both at the input and at the output. When $\alpha = -40dB$ the situation changes (Fig. 6.10, third row). At the input, both the interference

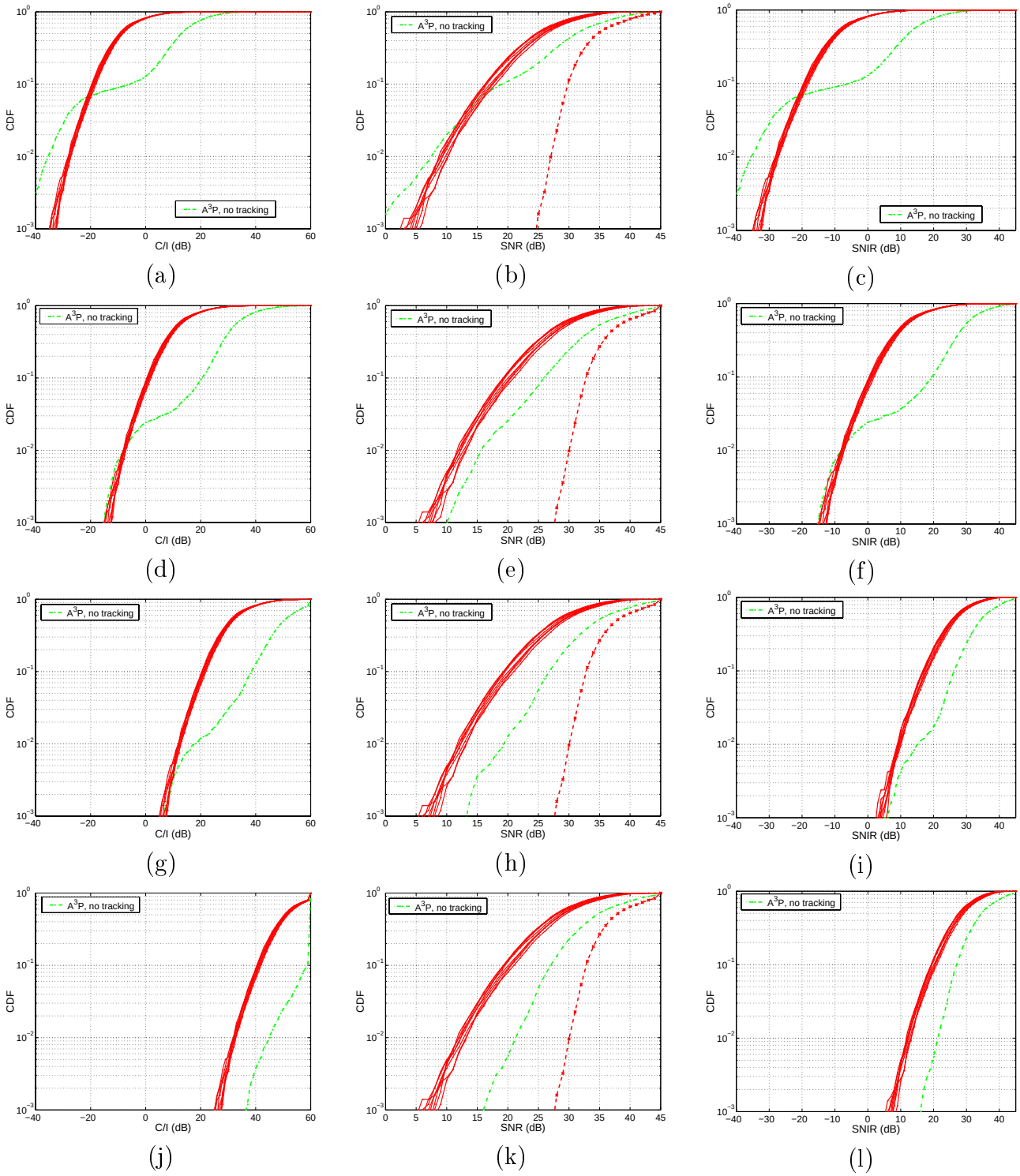

Figure 6.10. From interference limited to noise limited applications: Cumulative distribution function (CDF) of the C/I, SNR and SNIR. Left column (a,d,g,j): C/I, middle column (b,e,h,k): SNR, right column (c,f,i,l): SNIR. First row (a,b,c): Scenario $I \rightarrowtail N_\alpha^{0dB}$, $\overline{C/I}_{in} = 3dB$, second row (d,e,f): Scenario $I \rightarrowtail N_\alpha^{-20dB}$, $\overline{C/I}_{in} = 23dB$, third row (g,h,i): Scenario $I \rightarrowtail N_\alpha^{-40dB}$, $\overline{C/I}_{in} = 43dB$, fourth row (j,k,l): Scenario $I \rightarrowtail N_\alpha^{-60dB}$, $\overline{C/I}_{in} = 63dB$.

and the noise term influence the SNIR. In this situation the noise power and the interferer power are approximately equal, thus $\mathcal{C}_{in,m}^{SNR} \approx \mathcal{C}_{in,m}^{C/I}$ (Fig. 6.10(g) and (h)). This results in an input SNIR that is about $3dB$ lower than the SNR (C/I). When the C/I gain is larger than the SNR gain, the output SNIR will be dominated by the noise term only. Consider the gain values at the 10% probability level: $\Delta C/I^{90\%} \approx 20dB$ and $\Delta SNR^{90\%} \approx 7dB$. At this probability level the output SNIR is limited by noise only, i.e. the SNIR gain is in the order of the SNR gain. We say: the system is *noise limited* at the *output*, although this is not the case at the input. As said before, both interference and noise dominate the input. At the lower probability level, $\gamma = 1\%$ the situation is different. Here $\Delta C/I^{99\%} \approx 8dB$ and $\Delta SNR^{99\%} \approx 7dB$, for smaller γ, $\Delta C/I^{99\%}$ vanishes and $\Delta SNR^{99\%}$ stays constant. Therefore the output SNIR is then still limited by interference.

In the last scenario, when $\alpha = -60dB$ (Fig. 6.10, fourth row), the system is clearly *noise limited* at the input and at the output

$$\mathcal{C}_{in,m}^{SNIR} \approx \mathcal{C}_{in,m}^{SNR}, \text{for all } m, \text{ and} \tag{6.2.8}$$

$$\mathcal{C}_{out}^{SNIR} \approx \mathcal{C}_{out}^{SNR}. \tag{6.2.9}$$

With this discussion I tried to clarify the difference between interference and noise limited systems. When interference power is much larger than the noise power, the system will be interference limited at both input and output. From the results we saw that a smart antenna can be interference limited at the input, but already noise limited at the output when the C/I gain is larger than the SNR gain. Thus we have to assess the input and the output of a system separately.

6.2.3 Tracking — or not?

First, I will study the behavior of **A³P** *with tracker* (standard configuration) when interference becomes weaker. The output SNR is rather independent of the input C/I (Fig. 6.11(a)) but the SNR gain is low (Fig. 6.13(a)). When the tracker is activated the SNR gain, $\Delta SNR^{99\%}$, decreases when interference becomes weaker ($\overline{C/I}_{in} \approx 33dB$) and only increases when the interference vanishes ($\overline{C/I}_{in} \approx 63dB$).

Of course we would have expected the same behavior as in the case of no tracking: The SNR gain should increase, when the interference power decreases. But this is not the case. The SNR gain decreases with decreasing interference and increases only, when the interference is already very weak.

To demonstrate, why the SNR gain has a minimum for weak interference, I plot the selected user DOAs for $\alpha = -40dB$ ($\overline{C/I}_{in} \approx 43dB$) and compare the DOAs with the "ideal" DOAs of the scanning beam (Fig. 6.14). In Fig. 6.14(b) we often find user DOAs in the angular range of the interferer. When we take a careful look on the actual channel situation, we find user components that are incident from the same angular range as the interference (Fig. 6.14). As long as the interference is large, the **UID** will not identify those directions as user DOAs and **A³P** main beam will stick to directions at positive azimuth angles.

In the current situation, the interference is already so weak that the **UID** identifies user DOAs at $\phi < 0°$. The **UID** decides correctly, as we can deduce from the excellent SNR of **A³P** *without tracking*, because then the **UID** identifies exactly the same user DOAs.

But the tracker selects the user DOAs differently and causes the degradation of ΔSNR. The arguments are here the same as in scenario urban 2 and can be looked up at page 127. The user DOAs at $\phi < 0°$ also explain the small C/I gain, $\Delta C/I^{99\%} < 0dB$ for $\overline{C/I}_{in} \approx 43dB$. In terms

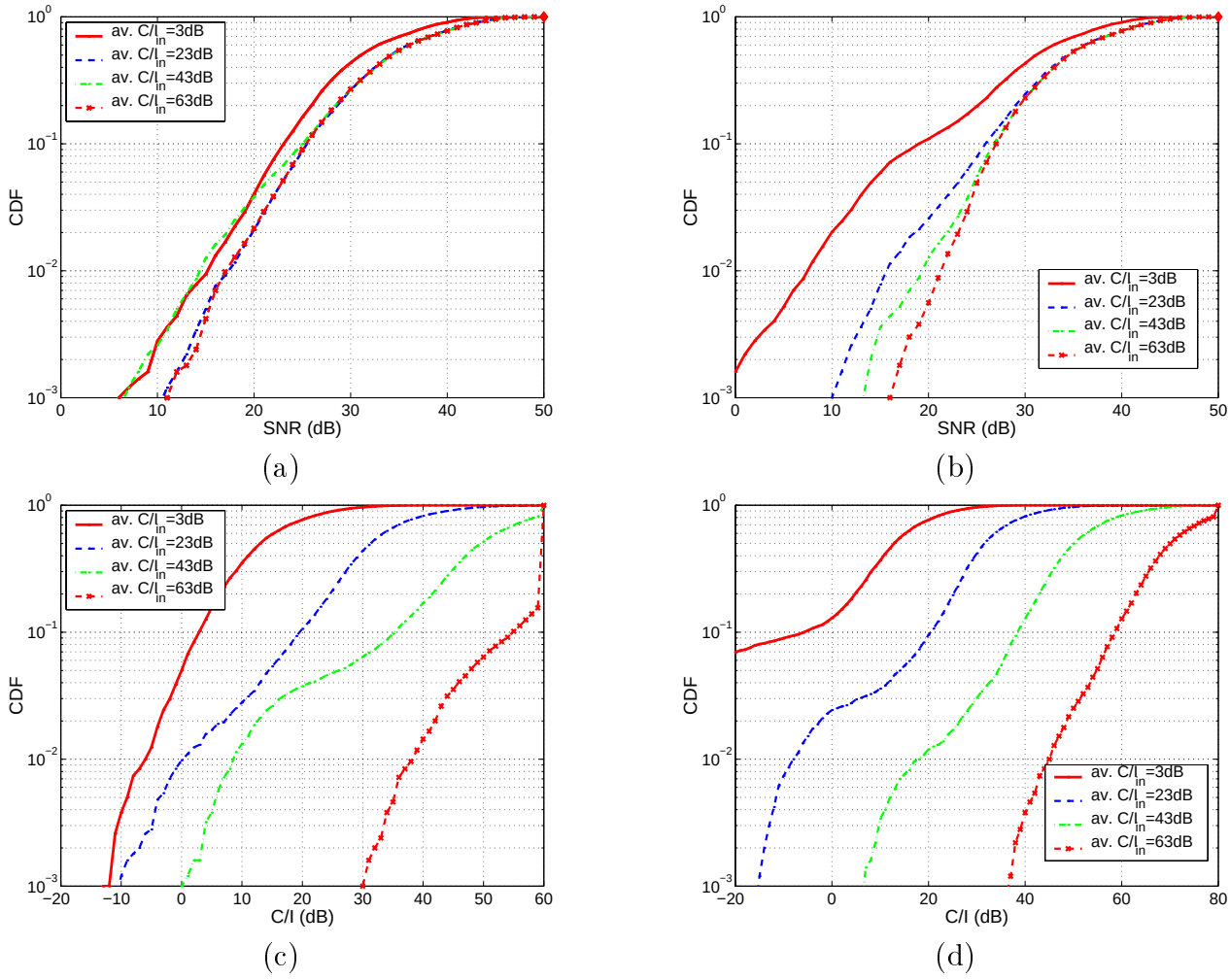

Figure 6.11. From interference limited to noise limited applications for a standard configuration (left column: a,c) and deactivated tracker (right column: b,d). (a,b) Statistic of the output SNR. (c,d) Statistic of the output C/I.

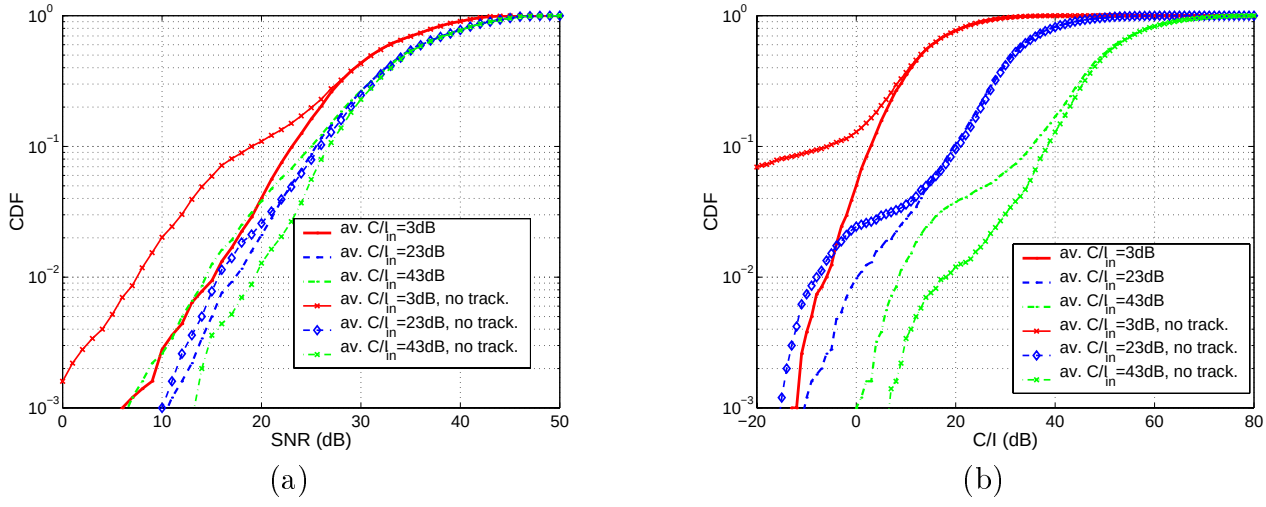

Figure 6.12. Comparison of **A**^{3}**P** *with* and *without* tracking. (a) Statistic of the output SNR. (b) Statistic of the output C/I.

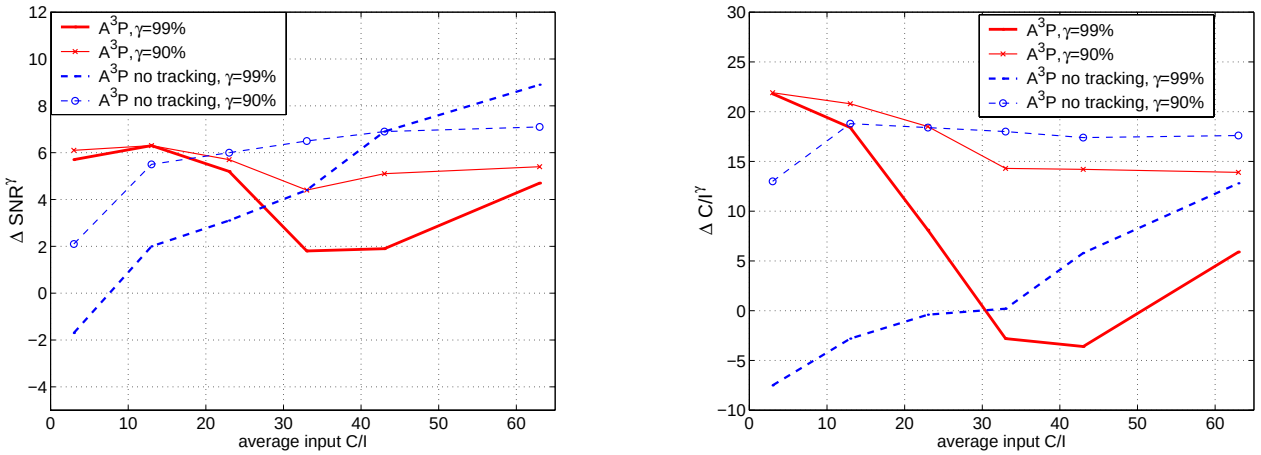

(a) (b)

Figure 6.13. From interference limited to noise limited applications for a standard configuration (solid line) and deactivated tracker (dashed line). (a) SNR gain. (b) C/I gain.

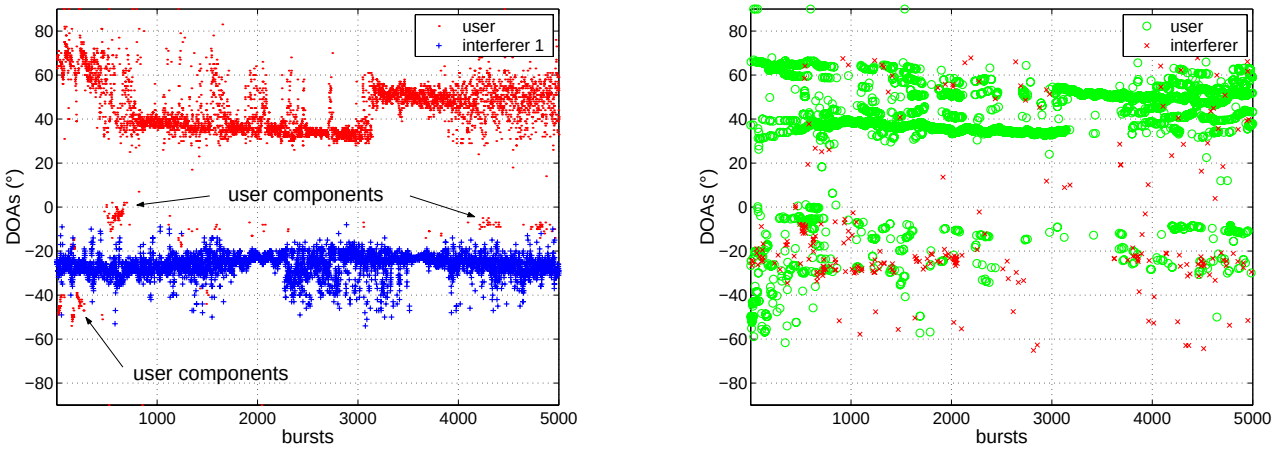

(a) (b)

Figure 6.14. DOAs in Environment $I \rightarrowtail N$. (a) Actual user and interferer DOAs (from scanning beam). (b) Selected user DOAs (main beam direction) and interferer DOAs (nulls) in the case of $\alpha = -40dB$.

of interference reduction, placing a main beam into these directions is of course suboptimum. But at such large input C/I, the C/I gain is not of importance, what counts is the absolute output C/I (Fig. 6.11(c)).

When we compare the output C/I to the output SNR at $\overline{C/I}_{in} \approx 43dB$, we find that the system is neither clearly dominated by noise nor by interference.

When we compare the performance of **A**^{3}**P** with and without tracker we find:

- **A**^{3}**P** *with tracking* reaches higher output SNR and C/I as long as **A**^{3}**P** is interference limited at the output. In the CDFs of the output SNR and C/I (Fig. 6.11 and Fig. 6.12), we see that

- **A**^{3}**P** *without tracking* performs better, when $\overline{C/I}_{in} \geq 43dB$, i.e. when the output is noise limited.

These conclusions are supported by the results for the gain (Fig. 6.13). The deactivation of the tracker results in larger gain values when the average input C/I is between $20 - 30dB$, which is the region where noise becomes the limiting factor (The average input SNR is $33dB$).

6.2.4 Summary

A^3**P** in its standard configuration (with tracking) is optimized for low C/I situations. Then the tracker guarantees a large C/I gain that is independent of the interference power level. The C/I gain degrades gradually when interference becomes less important. When the system is at the output noise limited, it is of advantage to deactivate the tracker. This will result in large output SNR and output C/I. Thus the best results will be achieved with **A**^{3}**P** when the configuration is adapted to the current interference situation.

6.3 Asynchronous networks

In a GSM system, base stations are not necessarily synchronized. In an asynchronous network, the time structure of the GSM signals of the different BSs may be arbitrarily shifted. Figure 6.15 illustrates the effect of synchronity. Consider an SFIR system where the user is served by BS1 in the fourth timeslot (TS4). Furthermore, BS2 operates at the same frequency and is the nearest co–channel BS to BS1. Thus the user of BS2 causes the dominant co–channel interference (CCI) for the user signals of BS1. In the synchronous case (Fig. 6.15(a)), the CCI is aligned in time. If the network is asynchronous, the interfering signal may be delayed ($N_{sync} > 0$) or advanced ($N_{sync} < 0$). N_{sync} is the network *asynchronity*, measured in symbols. For example, $N_{sync} = 50$ means that the signals of the mobiles served by BS1 and BS2 arrive at the BS1 in uplink with a relative delay of 50 symbols, with the user signal being the first to arrive. This misalignment means that during the timeslot of the user, *two* different interferer mobiles transmit. In the example (Fig. 6.15) the BS1 receives during TS4 parts of the TS4 *and* TS3 of BS2. Thus the interferer situation changes within the timeslot!

6.3.1 **A**^{3}**P** and the GSM timeslot structure

Before I present any results, I want to repeat which data **A**^{3}**P** needs for its calculations (Fig. 6.16):

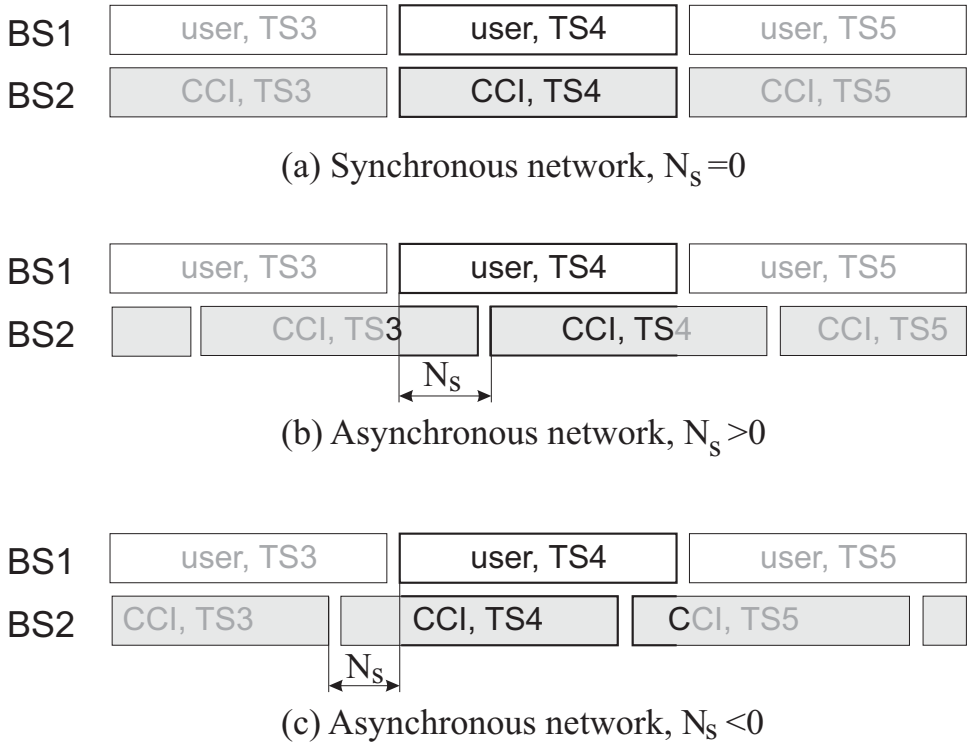

Figure 6.15. Synchronous and non–synchronous network.

- **A^{3}P** estimates the DOAs from the data of the *entire burst*[6] when **MVM** or **Unitary ESPRIT** is used, but not necessarily for **PASTd**. Here, I will focus on **MVM**.

- The classification of the estimated DOAs (**UID**) is based on the midamble. The **UID** exploits the a priori knowledge of the training sequence of the user signal. Based on this information, the user DOAs are identified.

Influence of asynchronity on A^{3}P Because the DOAs are estimated from the sample covariance matrix (Eq. 4.3.17), the DOA estimation will principally not suffer from any misalignment of the interference. The DOA estimation will be able to estimate all DOAs, including the DOAs of *both* interferers as long as they have large enough power. Because the data of the entire burst is cumulated in the covariance matrix, only the energy of the interferer signals will vary with N_{sync}. Assume, for example, that 10% of the burst interference is present. For the DOA estimation an interferer that is present only 10% of the time is equivalent to an interferer that is present 100% of the burst, but with $10dB$ less power [Str98].

The situation is different for the user identification. Because the **UID** evaluates only samples 66 to 91 (Fig. 6.16(a)) the synchronity will certainly influence the result. In Fig. 6.17 I demonstrate the different cases:

$0 < N_{sync} < 66$ The data of the midamble only includes Interferer 1. The **DOAE** has estimated also the DOAs of Interferer 2. The **ULBF** thus extracts also spatially resolved signals for the DOAs of Interferer 2. But from those directions no signal is arriving during the

[6]Note that burst and timeslot here means the same.

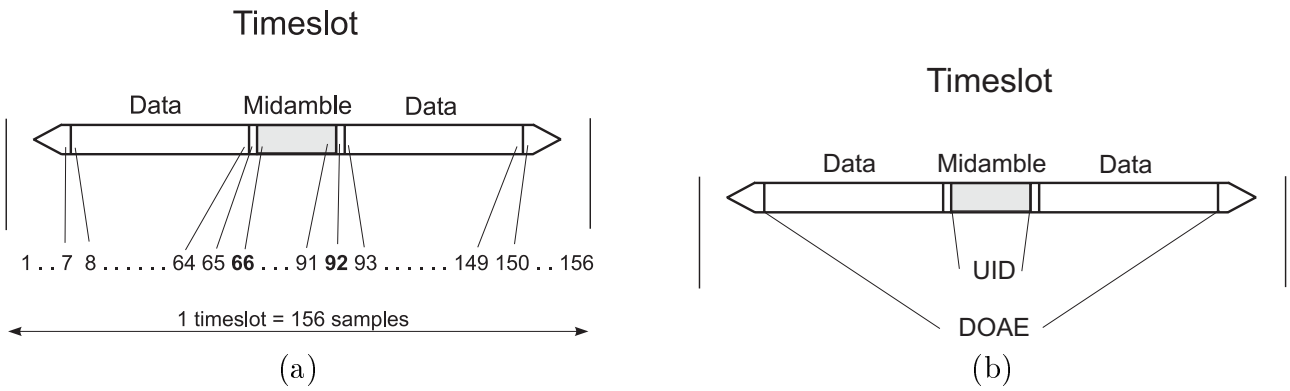

Figure 6.16. GSM timeslot (burst) structure and how **A**^{3}**P** uses the data. (a) Content of timeslot and sample numbering. (b) The **DOAE** uses the data of the entire burst, the **UID** only data of the midamble.

midamble and therefore the spatially resolved signals will only include a mixture of the user signals and the signals of Interferer 1, but not what is expected: a signal of Interferer 2. It will strongly depend on the directional characteristic of the situation whether this spatially resolved signal is includes more user or more interferer signal power (The sidelobe level and the null shape at the user directions and the other interferer directions will determine the output signal). Thus it is unclear whether these (interferer) DOAs are identified as a user or as an interferer DOA. Of course, this is a problem and will cause significant degradation of the performance.

$66 \leq N_{sync} < 92$ Only in this range of N_{sync}, the **UID** has a chance to sense both interferers. This is the range of asynchronity, where the performance will be optimum. Because the **UID** detects the spatially resolved signals, it will strongly depend on N_{sync} how many bit errors can be caused by an interferer. If, for example $N_{sync} = 68$, only the first three symbols of the midamble are disturbed by Interferer 2. This might already be too less to classify a signal originally coming from Interferer 2 as interferer DOA. Note that a signal has to have more than three bit errors to be classified as an interferer signal.

$92 \leq N_{sync} \leq 156$ This is the equivalent to the first range of N_{sync}, only that now the **UID** only gets signals from Interferer 1, but not from Interferer 2.

In the current assessment I assume a symmetry: The interference in the timeslot *before* and *after* the timeslot of Interferer 1 is the same ((Fig. 6.17).

6.3.2 Environment SFIR

In the following I will demonstrate the influence of the asynchronity on the C/I and SNR gain. The Environment *SFIR* includes data from three measurements (Fig. 6.18). MS1 was driving in a circle near the railway station[7]. MS2 and MS3 were both measurements where the van drove through a field. Because this area is slightly elevated, MS2[8] and MS3 had LOS to the BS. With these measurement signals I set up three scenarios:

Scenario *SFIR 1* MS2 is the user signal and MS1 the only interferer (Fig. 6.19). Data from MS3 is not used in this scenario. This is the same configuration as Scenario A (see p.5.3). When N_{sync} is varied, I can study how a single non–synchronous interfere influences the performance.

Scenario *SFIR 2* This scenario is the same as Scenario *SFIR 1*, except that I now apply *two* interferers (Fig. 6.21). MS1 acts as Interferer 1 that is served in timeslot 4 in BS2. MS3 is Interferer 2 that is served in timeslot 3 at BS2.

Scenario *SFIR 3* For the third configuration I exchange the role of user and Interferer 1 (Fig. 6.25). MS1 is now the user signal and MS2 the Interferer 1.

6.3.3 A^3P in Scenario SFIR 1

I investigate the influence of the asynchronity on $\mathbf{A^3P}$'s performance by varying N_{sync}. When N_{sync} changes, the interferer situation changes and thus the input C/I. The variation is stronger

[7] The signal of MS1 is *Signal 1* from Scenario A (Chapt. 5) and also used in Environment $I \rightarrowtail N$.
[8] The signal of MS2 is *Signal 2* from Scenario A (Chapt. 5).

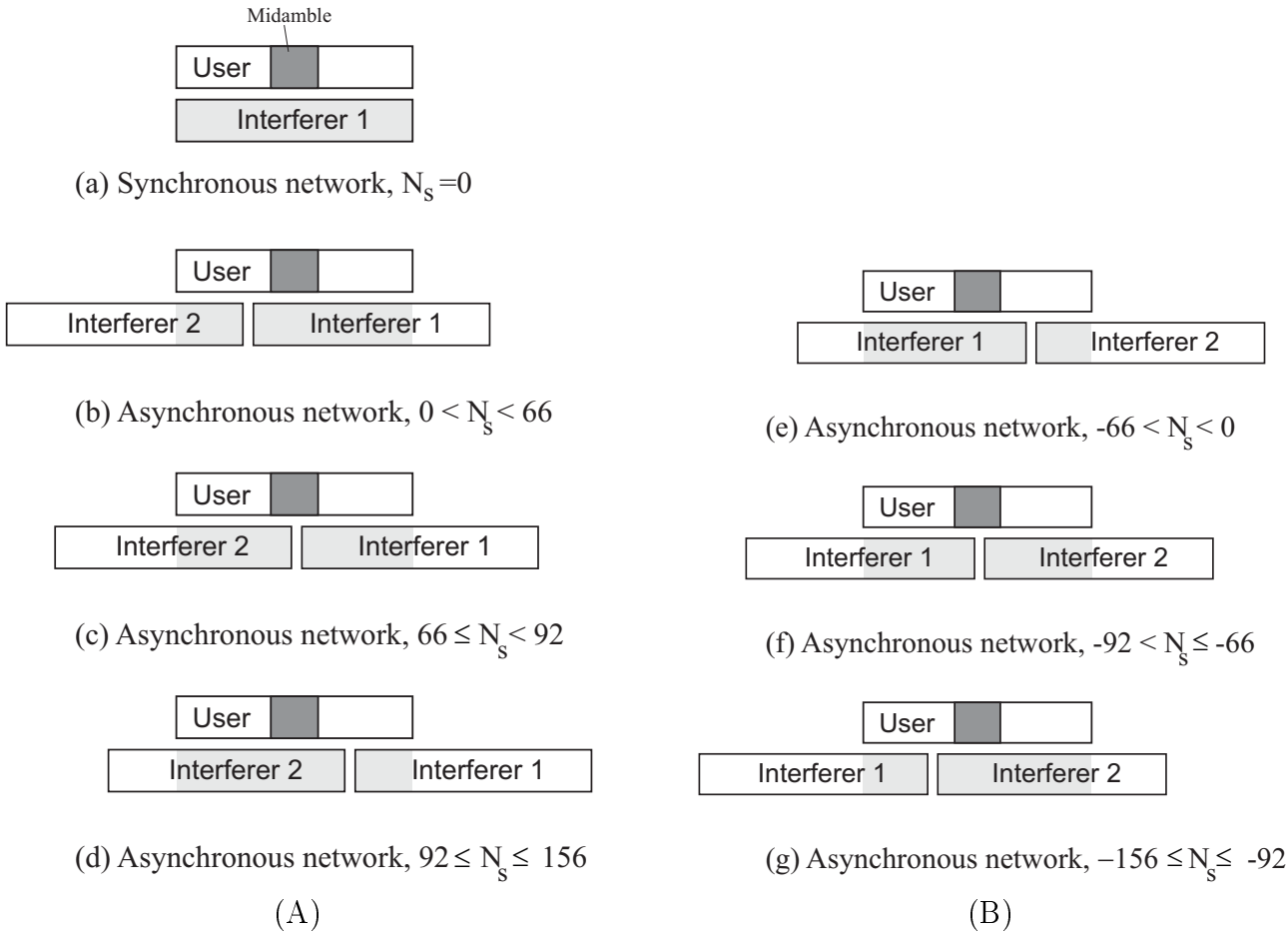

Figure 6.17. Different asynchronous situations. (A) Positive synchronity, $N_{sync} \geq 0$. (B) Negative asynchronity, $N_{sync} < 0$.

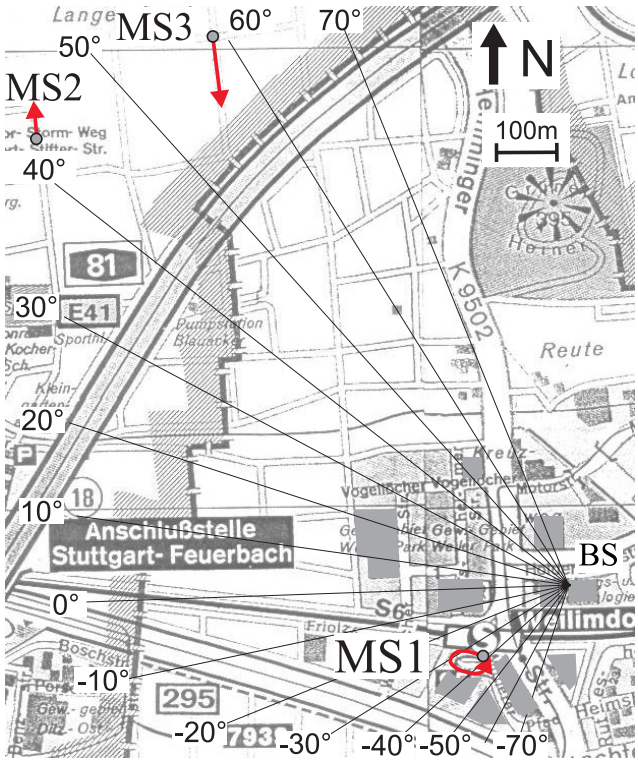

Figure 6.18. Environment *SFIR*. (a) Map of measurement route. MS1 drove with a velocity of about $20km/h$ along the highway (arrow), MS2 with about $20km/h$, and MS3 with about $60km/h$. MS1 had no LOS to the BS, MS1 and MS2 had LOS.

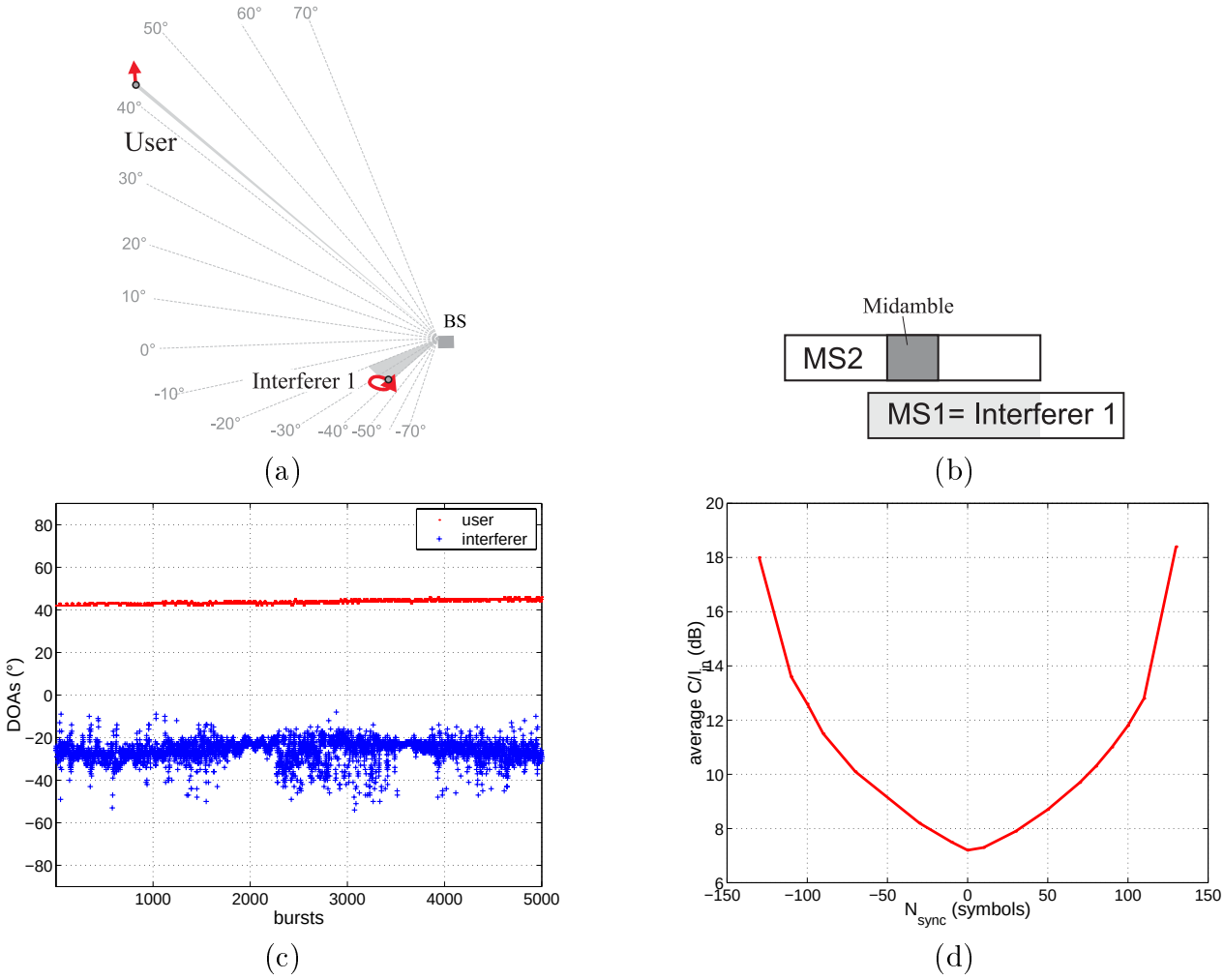

Figure 6.19. Scenario *SFIR 1*: (a) Spatial configuration. (b) Temporal structure. (c) Angular characterization. (d) Average input C/I when asynchronity, N_{sync}, varies.

when only one interferer is present. When $N_{sync} = 0$ the average input C/I, $\overline{C/I}_{in}$, will reach its minimum (Fig, 6.19(d)). Larger values of N_{sync} mean an interferer that is shifted outside the timeslot of the user and correspondingly $\overline{C/I}_{in}$ increases. A negative shift, $N_{sync} < 0$, causes the same effect, because the power within a burst stays constant and it makes no difference whether the first part of the interferer timeslot is seen by the user or the last part.

Results The SNR gain is hardly influenced by N_{sync} (Fig. 6.20(a)), except for $N_{sync} > 80$, where we find a slight increase in ΔSNR^{γ}. As long as the interferer is present during the midamble of the user signal ($66 \leq N_{sync} < 92$), **A³P** can place nulls to suppress the interference. Consequently $\Delta C/I^{\gamma}$ stays constant for $N_{sync} < 90$ (Fig. 6.20(b)). The resulting C/I gain is exactly the same as for **A³P**'s standard configuration in Scenario A (compare Tab. 5.8 on p.109, **SmearR**, broad nulls). When the interference moves out of the midamble, **A³P** will not place nulls and the C/I gain decreases by about $4dB$ (Tab. 5.8, **SmearR**, no nulls).

In summary: Asynchronity does not change the performance as long as the **UID** can detect the interference. If this is not the case, because the interferer is shifted out of the range of the midamble, the C/I gain will drop to the performance of **A³P** without nulling. In the case of

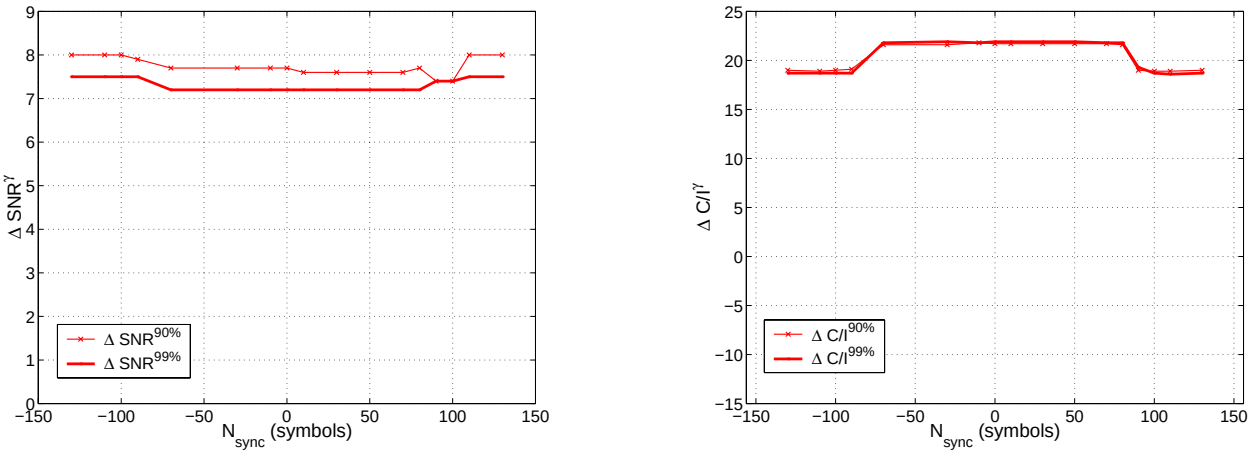

(a) (b)

Figure 6.20. Asynchronity and its effect on the input C/I in Scenario *SFIR 1*: (a) SNR gain. (b) C/I gain.

a single interferer the performance does not suffer significantly, because of two reasons: First $\Delta C/I^{\gamma}$ does not decrease strongly without nulling. Secondly, there is no second interference present that could cause erroneous identified DOAs. The SNR gain is hardly affected by the degree of asynchronity in the current scenario. If no nulls are placed, the SNR gain increases slightly. Because of a constant user and interferer power within the burst, the performance is symmetrical, i.e. the gain values are the same for the cases $N_{sync} = -N_{sync}$.

6.3.4 A^{3}P in Scenario SFIR 2

In this scenario the *directional* characterization of the interference will change significantly within the burst (Fig. 6.21). The variation of the average input C/I is smaller than in the previous scenario. If $N_{sync} = 0$, only Interferer 1 will be present. The other extreme is, if $N_{sync} = 156$; then only Interferer 2 is present. The average powers of Interferer 1 and Interferer 2 are nearly the same, $\overline{C/I}_{in} = 7dB$. But then, why does the average input C/I vary for other values of N_{sync}?

Let us consider the case $N_{sync} = 80$, where the interference situation switches in the middle of a burst. The interference power (Fig. 6.22(a)) consists of two parts, each independently fading. Note that the power plotted in the diagram is the *instantaneous* interference power *within* a sample burst. This is qualitatively different form the power values that I computed for an entire burst. When I said "independent fading" I meant that the total power contribution of the interferer in a burst varies from one burst to the next, caused by the Rayleigh fading. This results in much stronger variation of the power than the small variations[9] of the instantaneous power at symbol level that are recognizeable in Fig. 6.22(a). The total interference power (calculated over the entire burst) thus consists of a sum of two independently fading power terms. This averaging (summation) changes the statistic of the interference power. Let's assume that in case of a single interferer the interferer power is Rayleigh distributed with a certain average energy. In the other case ($N_{sync} = 80$), we add two independently Rayleigh

[9]The small variations of the power (on the order of 5dB) take place at symbol rate. The Gaussian filter of the GMSK modulator causes intersymbol interference over three symbols. Therefore the amplitude of the output signal is not constant anymore.

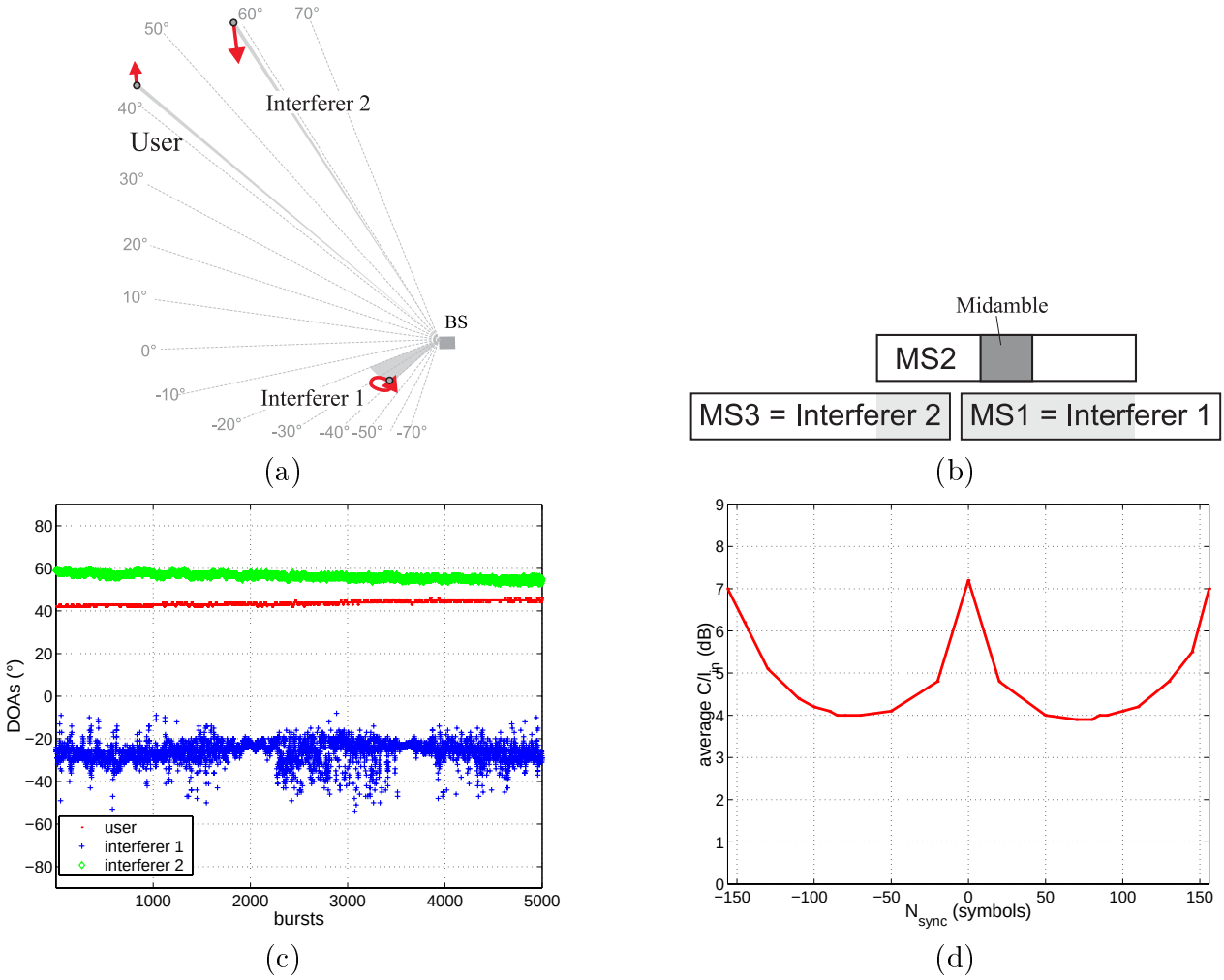

Figure 6.21. Scenario *SFIR 2*: (a) Spatial configuration. (b) Temporal structure. (c) Angular characterization. (d) Average input C/I when asynchronity, N_{sync}, varies.

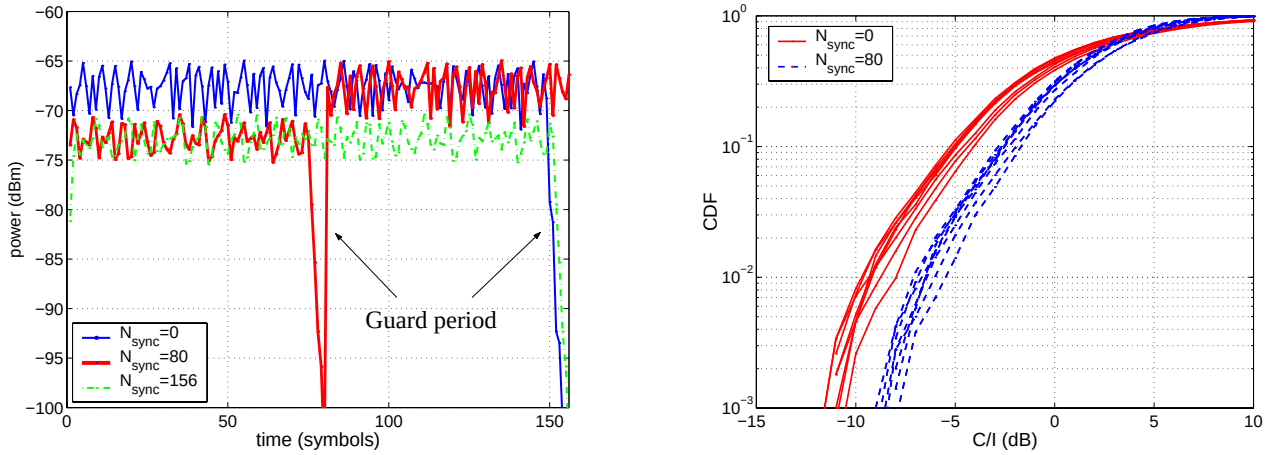

(a) (b)

Figure 6.22. Synchronization and its effect on the input C/I. (a) Instantaneous interference power variation within a sample burst. In the synchronous network ($N_{sync} = 0$) only a single interferer is present. For the asynchronous case ($N_{sync} = 80$) two signals contribute to the interference. (b) Statistics of the input C/I.

fading variables, but each with *half* of the average energy as before (because each interfering signal is only available half of the time). Thus it becomes less likely that the sum of the two independent fading contributions is large, i.e. small C/I values are less likely. Correspondingly the slope of the CDF of the input C/I becomes steeper than in the case of a single interferer ($N_{sync} = 0$) and is for small probability levels by about $3dB$ shifted to the right ((Fig. 6.22(b)). This is of course better, because it is less likely that the C/I is very low. But still, the average input C/I is smaller for $N_{sync} = 80$.

Results In Scenario *SFIR 2* the SNR gain and C/I gain are stronger influenced by the degree of asynchronity (Fig. 6.23). When $N_{sync} = 0$ we again achieve the same results as in the previous scenario. If only the second interferer, Interferer 2, is present, $N_{sync} = 156$, $\Delta C/I^{\gamma}$ is only $5dB$, because user and interferer are very close in angle. At the beginning of the measurement, user and interferer are separated by 18°, but after 5000 burst they are as close as 12° (Fig. 6.21(c)). This is too close to achieve sufficient interferer suppression. Note that in the previous chapter I have studied a scenario where a stronger overlap of user and interferer occurred (Scenario B, p.100). Then **A**^{3}**P** could still achieve an excellent C/I gain of $18dB$. This was only possible because in Scenario B the user signal included additional signal components available at other angular ranges, where interferer and user signals were not close. In this sense the large angular spread of the signals was of advantage. However, in the current scenario, no other multipath exists for the user (LOS).

For the asynchronity this means that the interference situation changes between two extremes: **A**^{3}**P** can suppress Interfere 1 very well, but not Interferer 2. This is reflected by a gradual degradation of $\Delta C/I^{90\%}$ correspondingly to the ratio of the interference terms, when the asynchronity increases from $N_{sync} = 0$ to $N_{sync} = 156$. But the situation is not that simple.

$\Delta C/I^{99\%}$ shows a different behavior. If $N_{sync} > 85$, $\Delta C/I^{99\%}$ drops dramatically, which means that in a certain percentage (in the case of $N_{sync} = 90$ about 2.5% of the bursts) **A**^{3}**P** fails (Fig. 6.24(f)). Again the selected user and interferer DOAs help to understand **A**^{3}**P** 's

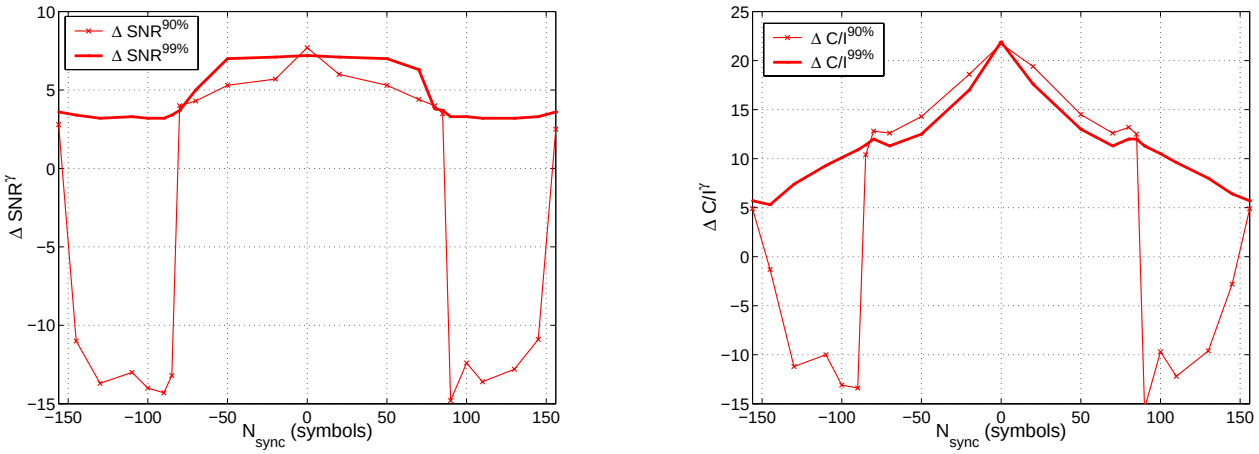

(a) (b)

Figure 6.23. Asynchronity and its effect on the input C/I in Scenario *SFIR 2*: (a) SNR gain (b) C/I gain.

behavior. If $N_{sync} = 0$, **A^{3}P** works without failure and detects Interferer 1. If $N_{sync} = 50$, **A^{3}P** is only in rare cases able to detect Interferer 2, because it is not yet present during the midamble. There is, of course, a degradation of the C/I gain because of the undetected, but still rather weak, interference.

When the second interferer is also present during the midamble, $N_{sync} = 80$, **A^{3}P** recognizes both interferers. If the second interferer would not be so close in angle, the C/I gain could still be high.

The situation changes abruptly when Interferer 1 moves out of the window of the midamble and is not sensed anymore by the **UID** ($N_{sync} > 90$). Then **A^{3}P** will often put the main beam into the direction of the first interferer (misdirected user DOAs in Fig. 6.24(c)), because the **UID** does not sense the strong interferer at those directions. The situation is here especially dramatic, because **A^{3}P** is tempted to look for another multipath of the user, because Interferer 2 is so close in angle. And here the **DOAT** is supported by the **UID** to select those wrong DOAs. The **UID** returns in some bursts a *user* DOA in the angular range of $-20°$ to $-40°$, i.e. the direction of Interferer 1. The situation does not relax as long as N_{sync} gets close to 156. The same reasoning applies for the behavior of the SNR gain.

In Summary: The current situation is severe in many respects (strong interference, angularly *not* well separated signals), it demonstrates the issues of non–synchronous interference. **A^{3}P** can cope under these circumstances with asynchronity in certain ranges. When the asynchronity causes both interferers to be sensed by the **UID**, **A^{3}P**'s performance degradation from the synchronous performance is only marginal.

6.3.5 A^{3}P in Scenario SFIR 3

In the last scenario, I exchange the role of the user and interferer to get a situation where the interference is angularly well separated form the user (Fig. 6.25). Here, Interferer 1 is on average by $7dB$ stronger than Interferer 2. Thus the average C/I at the input increases monotonically with N_{sync}. I include only results for $N_{sync} > 0$, because of the symmetry.

Results Both interferers are well angularly separated, thus we find less variation of the C/I gain with changing asynchronity. For the limits, $N_{sync} = 0$ and $N_{sync} = 156$, the C/I gain differs only by $2dB$. In both cases it is higher than $23dB$.

In between we find a degradation of the gain similar to the previous scenario, but less pronounced. Especially at $N_{sync} = 85$ **A^{3}P** often steers the main beam into the wrong direction. At this asynchronity, Interferer 1 is nearly invisible to the **UID**. Then the **UID** often *erroneously* identifies the direction $\phi = 40°$ as a user DOA, because the spatially resolved signal includes a (arbitrary) mixture of the user signal and the signal of Interferer 2 (see explanation at page 139). Additionally, Interferer 1 often has larger power than the user and in those cases the main beam will be pointed to $\phi = 40°$. The situation relaxes, when N_{sync} increases,. Interferer 1 has then less influence and the interferer power decreases correspondingly. Hence, it becomes less probable that $\phi = 40°$ will be the direction of the largest power and the main beam is not misdirected often.

The same line of arguments can be followed to explain the performance degradation when Interferer 2 is not seen by the **UID** ($N_{sync} < 66$). The C/I gain shows basically the same drop ($N_{sync} = 70$[10]), but it is less deep, because Interferer 2 has lower power. Therefore the

[10]Note that the drop occurs when Interferer 2 nominally is still visible during the midamble. The numbering

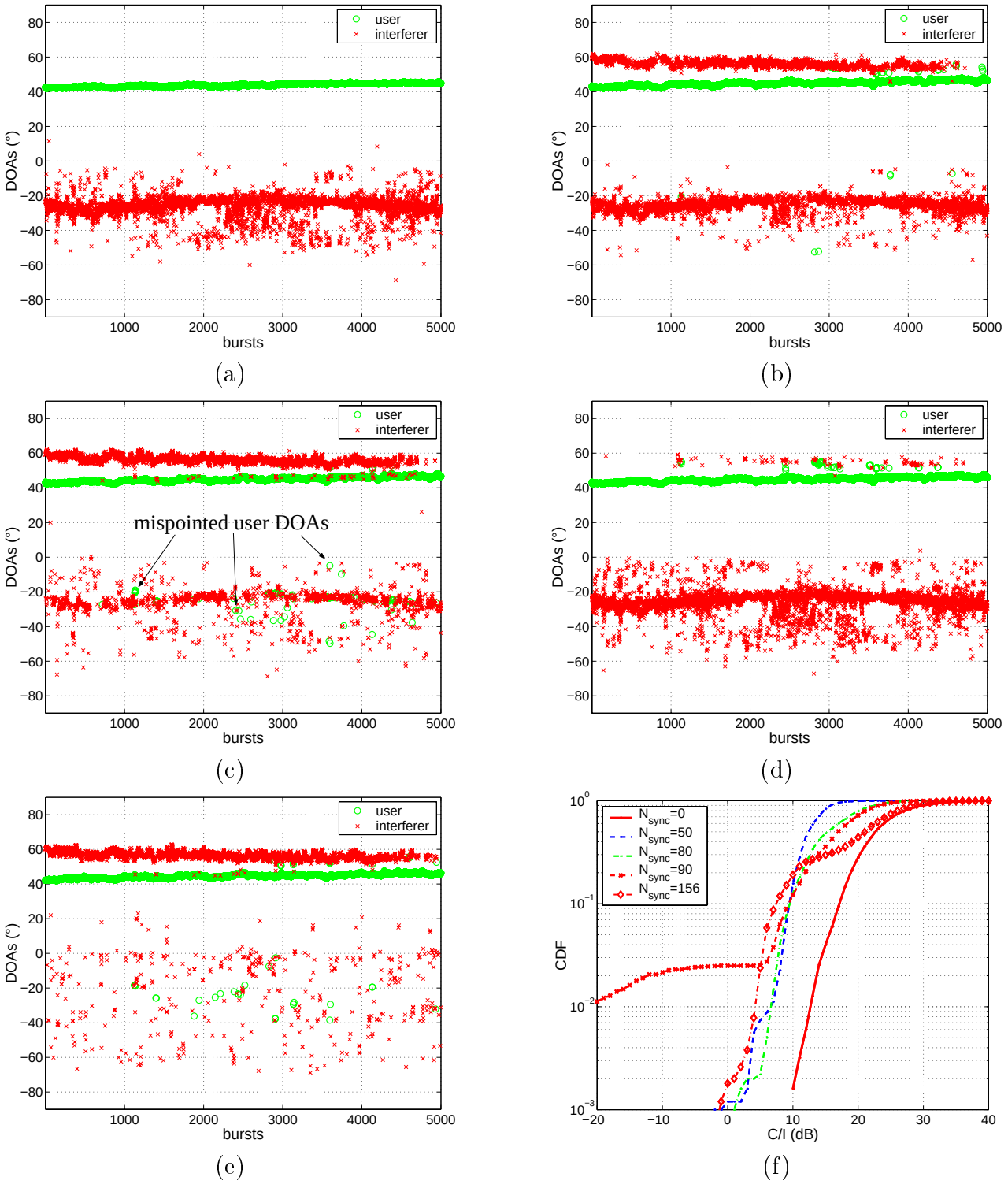

Figure 6.24. Synchronization and its effect on the selected user and interferer DOAs. (a) Synchronous interference, $N_{sync} = 0$, interferer is MS1. (b) Asynchronous interference, $N_{sync} = 80$. Both interferers are still "visible" during the midamble. (c) Asynchronous interference, $N_{sync} = 90$. Only Interferer 2 is "visible" during the midamble. (d) Asynchronous interference, $N_{sync} = 50$. Only Interferer 1 is "visible" during the midamble. (e) Synchronous interference, $N_{sync} = 156$, interferer is MS3. (f) CDF of output C/I.

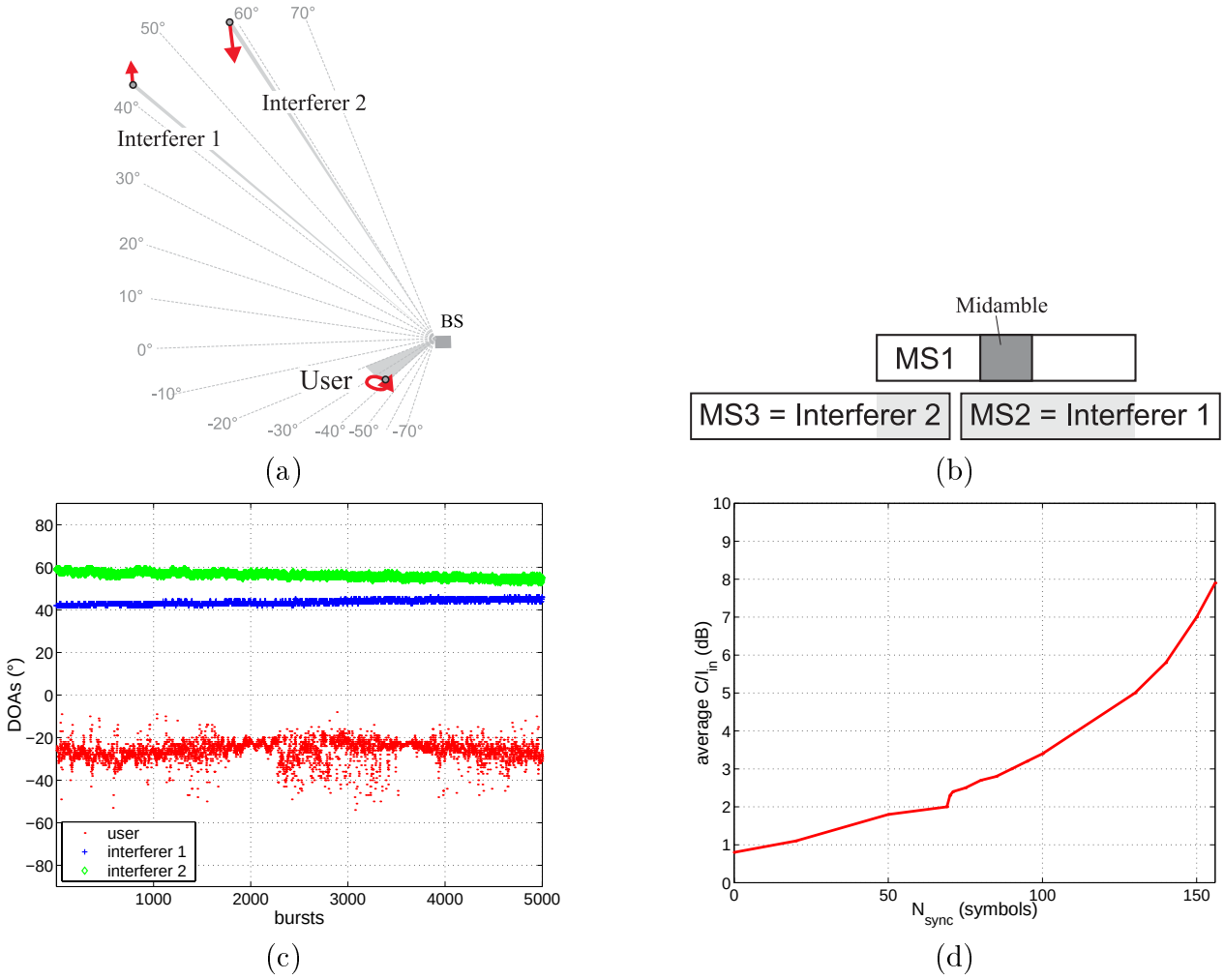

Figure 6.25. Scenario *SFIR 3*: (a) Spatial configuration. (b) Temporal structure. (c) Angular characterization. (d) Average input C/I when asynchronity, N_{sync}, varies.

probability that direction $\phi = 60°$ gives the largest power (when it is erroneously identified as a user DOA) is smaller than in the case of $N_{sync} = 85$ with Interferer 1.

6.3.6 Summary

- Significant asynchronity in an SFIR system degrades the performance of **A**^{3}**P**. A asynchronity of only a few symbols, as it also maybe caused by the timing advance in an SDMA system, does not influence the performance.

- When the change in interference occurs during the midamble, **A**^{3}**P**'s performance does not suffer. **A**^{3}**P** requires a certain minimum overlap of the interference with the midamble to assure identification of the interferer. The minimum overlap depends on the configuration of the **UID** and is in the order of 5 symbols.

of the symbols, of course, assumes that the symbol number 66 is really the first bit in the midamble. However, the symbols might be shifted because of the propagation delay. This delay is not known in the measurement files and therefore the limits can vary within the different measurement files.

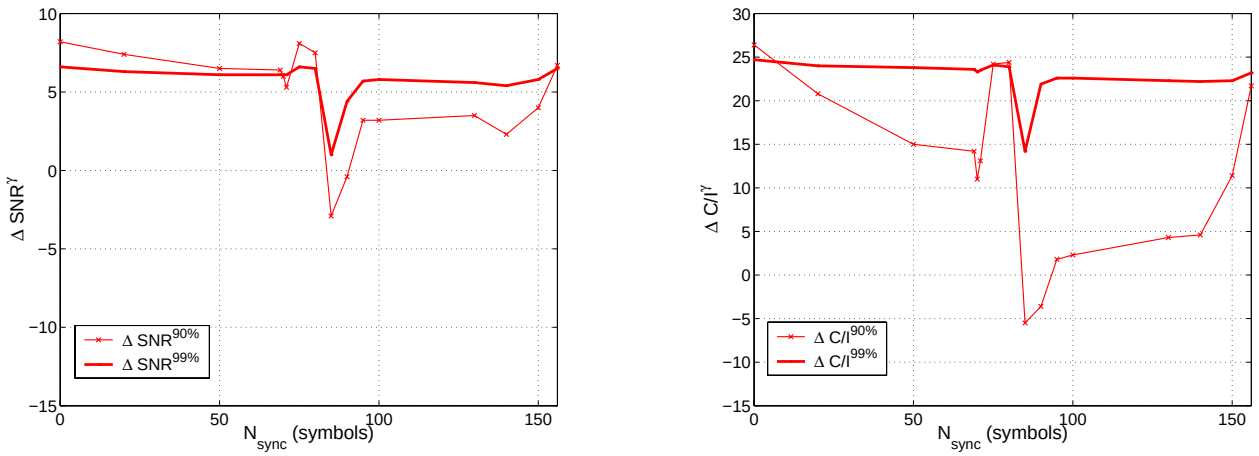

(a) (b)

Figure 6.26. Scenario *SFIR 3*: Influence of synchronization on SNR gain (a) and C/I gain (b).

- The performance degradation is caused by the different data the **DOAE** and the **UID** operate on. The **UID** only senses one interferer, but not the other, while the **DOAE** estimates both interferers. This causes erroneous identifications of supposed user DOAs and then the probability of misdirected main beams is dramatically increased.

- The main beam will only erroneously point into a direction of the interferer, if the interferer power is larger than the user power. Therefore the degradation of the C/I gain strongly depends on the input C/I. As a result the performance drops at a certain level of asynchronity (depending on the current situation, but in the range of $N_{sync} = 90$; when the **UID** cannot identify both interferers) to a minimum. With increasing N_{sync} and thus decreasing C/I the performance gradually increases. The angular characteristic has less influence on the C/I gain degradation than the interference power itself.

- If only a single interferer is present **A**^{3}**P** reaches the optimum performance (of the synchronous case) rather independently of the asynchronity. This will also be the case when interference is low.

6.3.7 Improvements

I suggest two ways to increase the robustness of **A**^{3}**P** against asynchronity:

- Estimate the DOAs from the same data as the **UID** classifies the signals:
  If the **DOAE** is able to estimate the DOAs only from the 26 bits long midamble, it could return only those DOAs that are also sensed by the **UID**. This would avoid the erroneous identifications of interferer signals, because the interference is not present during the midamble.

  Of course, the quality of the **DOAE** would suffer, when only 18% of the entire burst is used. The robustness of **A**^{3}**P** to cope with far–off estimates will help to relax the requirements on the **DOAE**. Still this topic needs further investigation.

- Estimate the DOAs at the beginning and, a second time, at the end of the burst (Fig. 6.27):
  PASTd allows estimating the DOAs from only 50 symbols of a burst (Sect. 4.3). We can repeat this estimation with data from the end of the timeslot to get a second estimate. This allows sensing *all* interferers that are present. The DOAs that are *not* the same at the beginning and at the end can only be interferer DOAs, assuming that the **DOAE** returns the correct DOAs. This additional information will help to improve the decisions of the **UID** and so avoid erroneously identified user DOAs in an asynchronous network.

6.4 Frequency hopping

In the last application I demonstrate a SFIR application *with frequency hopping*. **A**^{3}**P**'s interferer nulling does not have memory. It instantaneously adapts in each burst to the current interferer situation. This is guaranteed because the only subtask that has a memory, the tracking algorithm (Sect. 4.6, p.63), does not include interferer information. Thus **A**^{3}**P** is compatible with frequency hopping and I therefore do not expect a performance degradation whatsoever. Here I do not discuss any other advantageous effects of frequency hopping (reduced fading margin, ...) than the effect on the C/I.

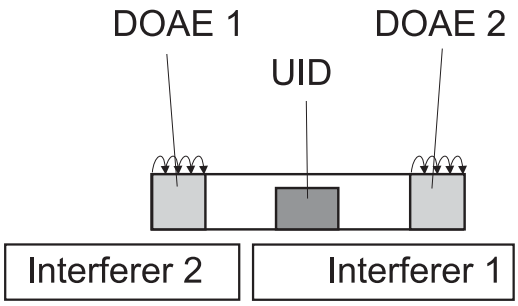

Figure 6.27. Double DOA estimation.

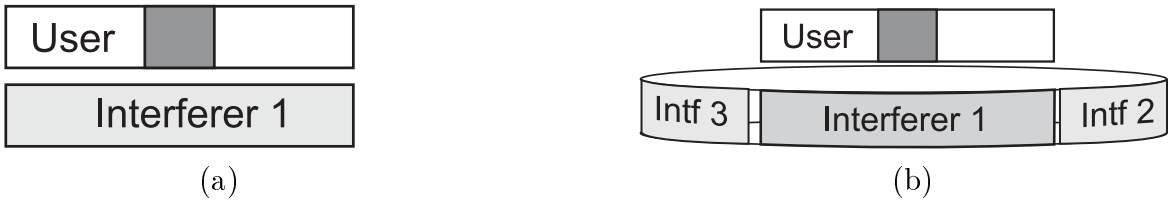

Figure 6.28. Varying interferer situation in a frequency hopping system. (a) No frequency hopping. (b) Frequency hopping. I assume a deterministic hopping sequence.

MVM configuration	Scenario *FH*		
All values in dB	$\overline{C/I}_{in}$	$C/I_{out}^{90\%}$	$C/I_{out}^{99\%}$
only Interferer 1	35.4	17.5	5.9
only Interferer 2	13.6	10.9	2.5
only Interferer 3	11.4	15.7	7.7
Frequency hopping	27.1	14.2	4.9

Table 6.4. Guaranteed output C/I values, $C/I_{out}^{90\%}$ ($C/I_{out}^{99\%}$), in 90% (99%) of the time.

I assume that each interferer is served by a different base station. In a frequency hopping system the frequency channel varies from burst to burst. This causes the co–channel base stations to vary from burst to burst, resulting in burst–wise different interferer situation. Here I model the frequency hopping by three different interferers that, when seen from the user BS, follow in a deterministic sequence (Fig. 6.28)[11].

6.4.1 Scenario SFIR 4

The Scenario *SFIR 4* is a mixture of several other scenarios (Fig. 6.29). It includes a single user and three interfering mobiles. The user signal is taken from Scenario *Urban 1* (MS1). Interferer 1 (MS2) is the signal of Scenario *Environment* I↣N, Interferer 2 (MS3) consists of the first half of Scenario *Highway*, and Interferer 3 (MS4) is the signal of Scenario *Urban 2*. There is partial overlap of signal components of Interferer 1 and the user signal, but Interferer 1 is the weakest. Its average input C/I is $\overline{C/I}_{in} = 35dB$. The other two interferer are much stronger with $\overline{C/I}_{in} < 15dB$. Interferer 3 is well separated in angle, while the LOS direction of Interferer 2 crosses the one of the user.

Results I have calculated the performance of **A**^{3}**P** when no frequency hopping is applied and only one of the three interferers is active (Fig. 6.30). Because the interferer situations differ significantly (compare the average input C/I, $\overline{C/I}_{in}$ in Tab. 6.4), I concentrate on the output C/I and SNR. We find significantly different output C/I statistics. The CDF of the output C/I for the frequency hopping system shows a smaller slope. This is a consequence of the interferer averaging effect. Frequency hopping is implemented to reduce the probability of a

[11]Note that a cyclic frequency hopping sequence, i.e. when *all* BSs follow the same deterministic hopping sequence, will result in a *constant* interferer situation for each BS. Here I assumed that the BSs hop with independent random sequences, thus causing for a certain BS a change in the interferer situation from burst to burst. Because it does not make any difference for **A**^{3}**P** whether the interference situations randomly change or not, I model the frequency hopping with a deterministic change of the *interference situation*.

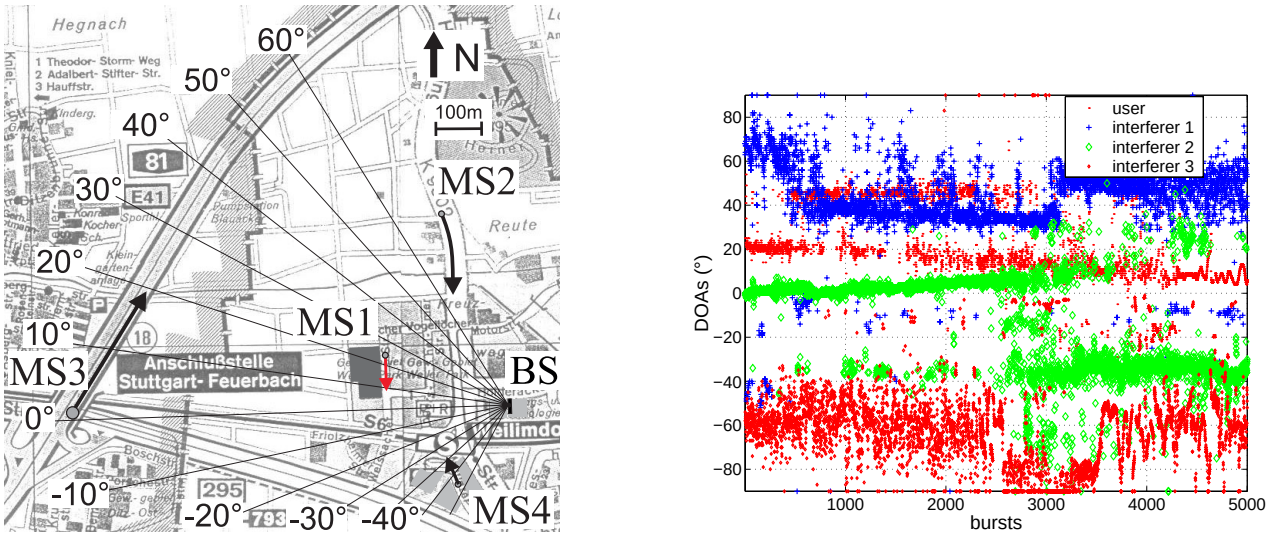

(a) (b)

Figure 6.29. Environment *SFIR 4*. (a) Map of measurement route. MS1 drove in a circle near the railway station with a velocity of about $20km/h$. MS2 drove along a road from north to south with a maximum speed of $60km/h$. (b) DOAs, $\phi_{SB}(n)$, of scanning beam. I include in this diagram the DOAs that scanning beam calculated separately from the user signals (dots) as well as from the interferer signals (crosses).

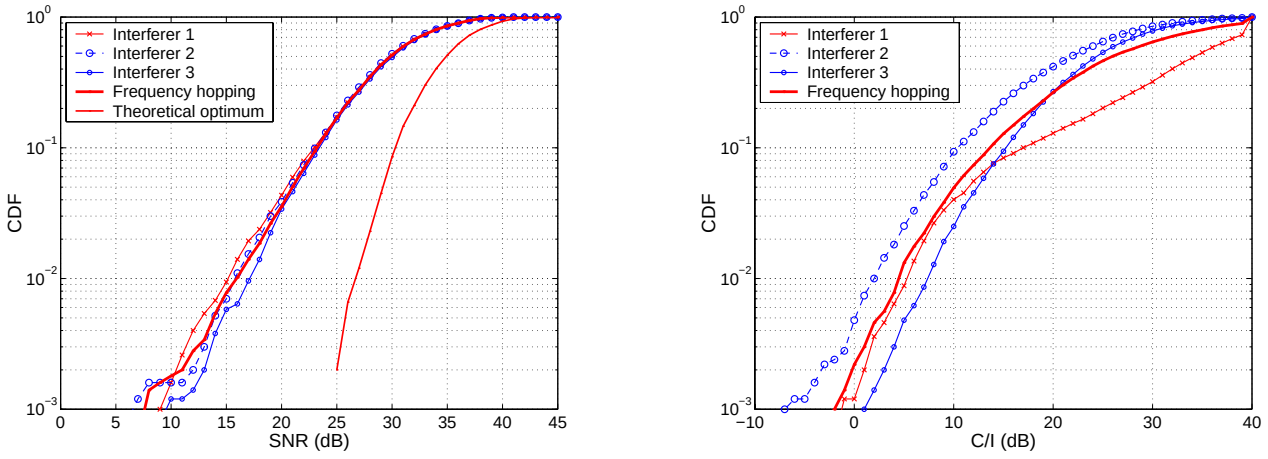

(a) (b)

Figure 6.30. Scenario *SFIR 4*: Influence of frequency hopping on the output SNR (a) and output C/I (b).

MVM configuration	Scenario FH					
All values in dB	$\overline{C/I_{in}}$	$\Delta C/I^{90\%}$	$\Delta C/I^{99\%}$	$\Delta SNR^{90\%}$	$\Delta SNR^{99\%}$	G_b
only Interferer 1	35.4	10.1	8.2	6.2	6.5	5.0
only Interferer 2	13.6	15.3	16.1	6.3	7.3	4.9
only Interferer 3	11.4	21.0	22.2	6.7	8.7	4.9
Frequency hopping	27.1	17.2	17.7	6.5	7.5	4.9

Table 6.5. Frequency hopping.

severe interference situation. Instead the system tries to make the interference situation equally well for all users. In the current result this is evident from the absolute output C/I values, $C/I_{out}^{90\%}$ and $C/I_{out}^{99\%}$. $C/I_{out}^{99\%}$ is the output C/I that is guaranteed in 99% of the cases. In Tab. 6.4 I have summarized those values for the different interferer situations. The smallest output C/I that can be guaranteed is for Interferer 2 where in 10% of the cases $C/I_{out} < 10.9dB$. With frequency hopping this value increases to $14.2dB$.

I have also listed the gain values that can be achieved in the different interferer situations (Tab. 6.5). Again, in case of the frequency hopping the gain is in between the worst and the best situation. The averaging effect is also evident from the smaller slope of the output CDF in case of frequency hopping, i.e. a larger spread of the C/I values (Fig. 6.30).

Conclusions $\mathbf{A}^3\mathbf{P}$ is compatible to frequency hopping. There is no degradation whatsoever because of the rapidly varying interferer situation. This is a consequence of the tracker, which only tracks the user DOAs. As expected from a frequency hopping system with random hopping sequence, an interference averaging effect can be observed and the probability of severe interference situations is reduced. In the current example the guaranteed output C/I in 90% of the time increases by about $3dB$.

Chapter 7

OUTLOOK

The last chapter of this work deals with topics that are not included in the thesis elsewhere, but are closely related to the work and thus need to be mentioned. Additionally I will propose further improvements of the developed **A**^{3}**P** that resulted from the evaluation of the measurements. This gives hints for a future implementation of **A**^{3}**P** in a product.

7.1 Downlink

Here, I present first measurements of the downlink gain [HKTT99]. Still more measurements are important to study the benefits of a smart antenna at the downlink in detail. Especially measurements including interference will be necessary, because this is not included in the first trial. Instead this measurement focussed on the SNR gain achievable on the downlink.

To evaluate the difference between single antenna transmission and array transmission the measurement van was equipped with two mobile stations connected to the same mobile antenna but receiving signals in different time slots. The base station used a single antenna to transmit in time slot 5, while the whole antenna array was used for transmissions in time slot 4.

The power levels received by the two mobile stations were evaluated by analyzing the

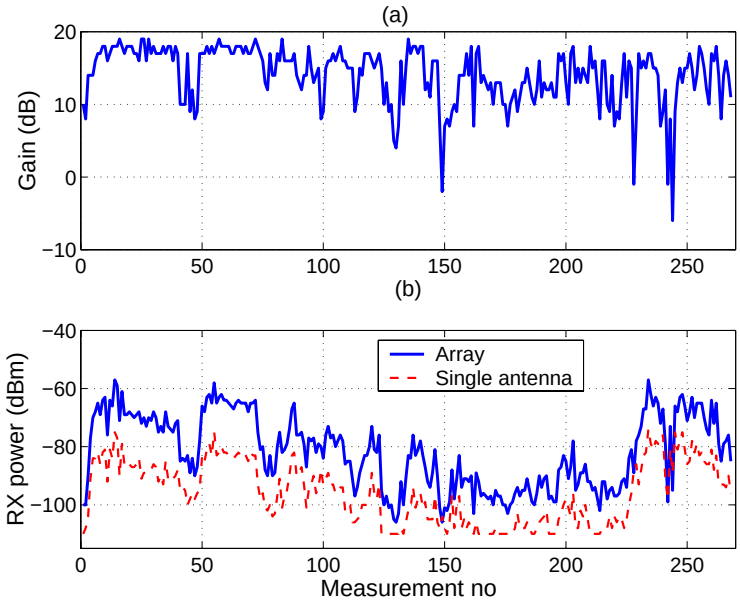

Figure 7.1. Downlink measurements. (a) Downlink gain, (b) received power levels at the mobiles.

SACCH (slow associated common control channel) messages reported back to base station. Theoretically, a gain of $20 \log M$ with M antennas is expected. The base station uses M power amplifiers in the array case and thus transmits M times more power than in the single antenna case. Therefore the expected downlink gain is $18dB$ and not $9dB$. Fig. 7.1 shows that this theoretical gain of $18dB$ with $M = 8$ antennas can be achieved over long time periods, with mainly two exceptions.

The first is that the range of the measurement reports is limited, i.e. when the single antenna power level hits the lower bound, the power difference being reported is smaller than the actual power difference in the field. Thus, this only represents a limitation of the measurement method with no implications on the actual gain.

On the other hand, in some cases the gain is really reduced. This effect is caused by multipath fading leading to an angular spread of the transmit signal larger than the beam width. In this case the single antenna has an advantage by being able to use all possible paths, while the narrow beam is restricted to only the subset of those paths being covered by the beam. However, the implemented algorithmic solution still provides close–to–optimal performance, which is evident when we compare the average gain of $17.4dB$ with the theoretical optimum of $18dB$.

Additionally to the presented measurement result, a downlink connection between MS and BS was active, during all measurements, where we logged data for the uplink. On all these measurement routes the downlink could be maintained. This basically verified the operation of **A**^{3}**P**'s downlink algorithms.

7.2 SDMA

This work has focused on SFIR applications. In an SFIR system, interference is originated from neighboring co–channel cells (*inter*cell interference). In contrast, the main source of interference in an SDMA system is *intra*cell interference. A BS, equipped with an SDMA system, can serve more than one user simultaneously (in the same time slot, at the same frequency). Thus the largest interference will be originated from the users that are simultaneously served inside the same cell, hence the name *intracell* interference.

A GSM system applies a slow power control that adjusts the mobile's transmit power every $480ms$ [MP92] to improve spectral efficiency (because reducing transmission power decreases the interference). This results in a more constant average power of the mobile's signal received at the BS, when measured over $480ms$ [1]. The instantaneous power will still be subject to Rayleigh fading that causes typically signal fluctuations on a time scale (of course this depends on the mobile's speed) smaller than $480ms$.

This origin of the interference and the power control result in another difference: In an SDMA system, the power control will assure a constant average input C/I of $0dB$ for all users served by the BS. This is not the case in an SFIR system. There each user is power controlled but of course by its serving BS. Thus the input C/I in an SFIR system principally will have larger variations than in an SDMA system. Thus in an SFIR system, the *average* C/I is larger, but the slope of the CDF of the C/I is much flatter than for an SDMA system.

Remember that in the current work, no power control was applied during the measurements. Thus the measurements cannot directly be used for the evaluation of an SDMA scenario. This

[1] Actually a constant average power cannot be guaranteed in any situation because the power control has only a dynamic range of $20 - 30dB$.

is another reason why I did not include an evaluation of an SDMA system in this work.

However, the scenarios presented have demonstrated that **A^{3}P** is suitable for an SDMA system. Many of the evaluated scenarios had very low average input C/I values down to 0dB. Especially those severe interference situations were tougher than a typical SDMA scenario, because here no power control was applied that could reduce the variability of the input C/I (especially very low C/I values). On the other hand, I have also demonstrated **A^{3}P**'s performance of different users that where simultaneously served in the same environment. In Scenario A and A', as well as in Scenario *SFIR 2* and *SFIR 3* I have exchanged the role of user and interferer. This corresponds in principle to an SDMA application. In Scenario *SFIR 2* and *SFIR 3* I even studied the influence of asynchronous interference (Sect. 6.3). Here an SDMA system has another advantage over an SFIR system: The intracell interference is synchronous, which relaxes the requirements on the smart antenna.

Still, for a serious assessment of **A^{3}P** under SDMA conditions, power control has to be implemented. Here my expectation is that the quality of the power control will significantly influence the performance of the smart antenna and thus this requires thorough study. Additionally **A^{3}P** is not yet optimized for SDMA application, because it is designed for an SFIR system.

7.2.1 A^{3}P's architecture and SDMA

During the development I kept in mind that **A^{3}P** can be simply upgraded for application in an SDMA mode. I will here summarize which steps have to be taken to make **A^{3}P** fit for SDMA. Additionally I will show how large the increase in the the computational effort is compared to the SFIR case. The following list steps through each of **A^{3}P**'s subtask:

ULBF **A^{3}P**'s algorithmic front end, the DOA estimation, does not require any changes. The DOA estimator already returns all DOAs regardless of their origin (intercell or intracell interference).

ULBF The spatial pre–filter also does not need any upgrade. It returns the spatially resolved signals of each estimated DOA.

UID The user identification detects each of the spatially resolved midambles and compares the resulting bit sequence with the training sequence of the intended user.

In an SDMA system this must be repeated for every user. Because the detection typically includes a user–specific channel estimation (by exploiting the user–specific training sequence), not only the comparison with the training sequence, but also the entire detection process has to be done separately for each user.

The final classification of the signals is different. Here the **UID** not only distinguishes between user and (intercell) interferer, as in the case of SFIR, but between user, *intracell* and *intercell* interference. Actually the reliability of the **UID** can be improved because more information is available when the **UID** distinguishes between the two classes of interferer signals. A DOA can only be a user DOA for the intended mobile station, if it is *not* a user DOA for any other *intracell* interferer, i.e. any other mobile that is served by the same BS (intracell users). Cross–checking the identified user DOAs for the different intracell users will decrease the probability of falsely identified user DOAs.

As a result of this upgrade the **UID** will require approximately K_U times the run–time of the SFIR case. K_U is the number of intracell users.

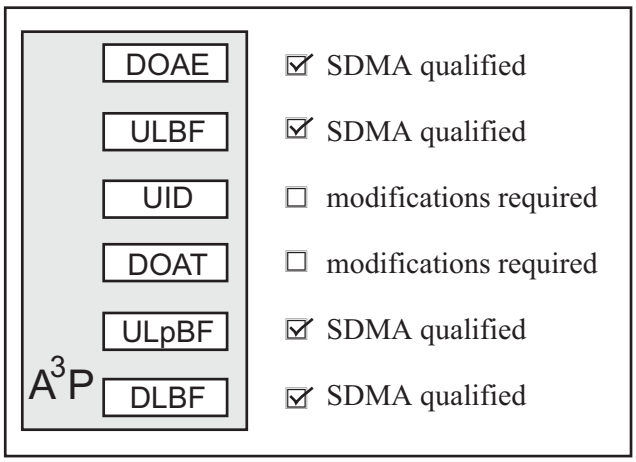

Figure 7.2. Upgrading **A**^{3}**P** for SDMA application. Required changes of the subtasks.

DOAT The straightforward way to upgrade the tracking algorithm to an SDMA system is to duplicate it, i.e. run the **DOAT** separately for each intracell user. From the view point of computational complexity, this is not of concern, because the run–time of the **DOAT** makes up only 6% of **A**^{3}**P**'s total run–time.

But this is not the optimum solution. For the SFIR application I have only tracked the *user* DOAs to be compatible with frequency hopping. In contrast, in an SDMA system we can track *all* intracell users, and only the intercell interferers may not be tracked. This will improve the reliability of **A**^{3}**P** against severe intracell interference.

To fully exploit these possiblities, the **DOAT** requires the largest change. As an upper bound for the run–time of the **DOAT** in SDMA mode I assume that the run–time increases by a factor of K_U.

ULpBF and **DLBF** The final beamforming algorithms do not need any changes. In an SDMA system, they just will be repeatedly applied to each of the intracell SFMA users. Thus the run–time here also increases by a factor of K_U.

In summary, **A**^{3}**P** needs only limited changes to be applied to an SDMA system (Fig. 7.2). To fully exploit the cababilities of **A**^{3}**P**, the most changes are required in the **UID** and the **DOAT** . Still, **A**^{3}**P** can be tested in its current implementation in an SDMA mode by applying **A**^{3}**P** separately for each user.

In Fig. 7.3 I illustrate the increase in complexity of **A**^{3}**P** in SDMA mode compared to the SFIR mode. Here I use the relative effort of each subtask derived in Sect. 4.8 (Fig. 4.40, p.78). Because the run–time depends on the channel situation (number of DOAs) I normalize the run–time to the total run–time of **A**^{3}**P** in SFIR mode, T_{A^3P}.

Because the subtasks of **A**^{3}**P** that spend most of the effort (**DOAE** and **UID**) are not changed, the complexity of **A**^{3}**P** in SDMA operation does not increase strongly (Fig. 7.3). If, for example, $K_U = 3$ intracell users are served by **A**^{3}**P** the computational effort increases only by 70% (Tab. 7.1).

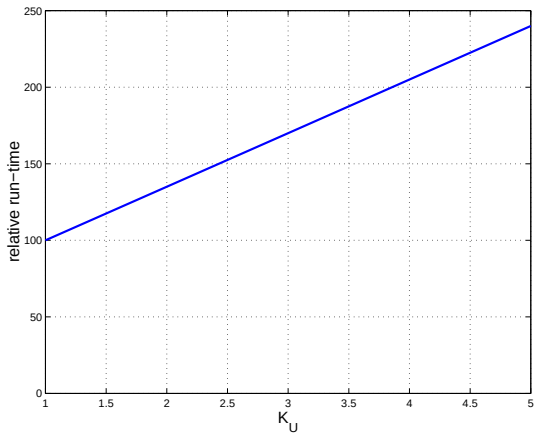

Figure 7.3. Estimated relative run–time of $\mathbf{A}^3\mathbf{P}$ in SDMA mode as a function of the number of intracell users, K_U. 100% corresponds to the run–time in SFIR mode when a single user is served.

Subtask	SFIR mode	SDMA mode
DOAE	$0.45T_{A^3P}$	$0.45T_{A^3P}$
ULBF	$0.2T_{A^3P}$	$0.2T_{A^3P}$
UID	$0.17T_{A^3P}$	$K_U 0.17T_{A^3P}$
DOAT	$0.06T_{A^3P}$	$K_U 0.06T_{A^3P}$
ULpBF	$0.06T_{A^3P}$	$K_U 0.06T_{A^3P}$
DLBF	$0.06T_{A^3P}$	$K_U 0.06T_{A^3P}$

Table 7.1. Relative run–time of **A^{3}P** in SFIR and SDMA mode. T_{A^3P} is the total run–time in SFIR mode, K_U is the number of intracell users.

7.3 Refinements of A^{3}P

Finally I propose some refinements to enhance **A^{3}P**'s performance. The thorough evaluation of **A^{3}P** has exposed the strong and weak spots of the smart antenna system. With this knowledge I propose modifications and suggest topics for further investigation that will enhance **A^{3}P**'s performance.

7.3.1 Beamforming and calibration

The results of Sect. 5.7 have shown that the nulls in the effective antenna pattern are shifted and filled, causing a limitation of the C/I gain. This is a result of hardware imperfections that are not taken into account of the current calibration scheme. One conclusion from this is that for the design of a beamforming based smart antenna the array imperfections have to be taken into account, if reliable conclusions from simulations are required. A first step in this direction is to include the mutual coupling in the simulation environment.

The calibration implemented in the smart antenna base station can cope with imperfections of the receiver trains (gain and phase imbalances), but not with the imperfect array. Especially the mutual coupling, but also the antenna elements that are not exactly the same and not exactly regular antenna spacing, cause the deviations of the measured antenna pattern from theory. In a first step it is important to better understand how the imperfections influence the effective antenna pattern. Further measurements of the antenna pattern will be helpful. If further improvement of the C/I gain is required, a calibration algorithm that can cope with effects of the array imperfections is required. Of course a more complex calibration is possible, but the increased costs must be considered as well. One has to ask whether the increased costs are worth the performance improvement that is achievable. Here further investigations are necessary.

Beamforming to optimize the SNIR In the current implementation of the **ULpBF** and **DLBF** I do not take the actual interferer power into account (except that a null is only placed if the interferer is significantly large). However, the goal of the beamformer is to optimize the output SNIR, thus it would be of advantage to select the null depth for the interferers depending on their power. The **SmearR** beamformer provides this possibility anyway. It is thus just required to set up and solve the optimization problem: Find for each interferer the null depth, ND_l, (null depth parameter of **SmearR**), $l = 1 \ldots \hat{L}_I$, to achieve optimum output SNIR. This would improve the output SNIR, because then a deep null is spent only, where a real strong interferer is present. On the other hand, it will increase the SNR gain: If **A^{3}P** is noise limited, this

approach would avoid placing any nulls and thus optimize the beamforming gain.

Adaptive adjustment of the main beam width **SmearR** allows adapting the main beam width. The next logical step is to increase the main beam width if the angular spread of a multipath becomes larger than the standard main beam width. An estimator of the angular spread of each multipath can, in the framework of the tracker, be realized in a simple way[KTRS98].

It is advisable to increase the main beam width only when the system is noise limited at the output. The adaptive adjustment of the main beam will help to increase the beamforming gain in an environment where the angular spread of the user DOAs is larger than the beam width. But the beamforming gain or SNR gain is only of concern in noise limited environments. Thus increasing the main beam width does make sense in noise limited environments only. Additionally this will avoid any important degradation of the C/I gain, when interference is strong.

7.3.2 Hybrid A³P

In Section 6.2 I have shown that **A³P** can be configured optimally for application to either a noise or an interference limited environment. To guarantee the optimum performance of **A³P** regardless of the environment, I propose to add another level of adaptivity to **A³P**: Adapt the configuration of **A³P** to the current interference situation. The proposed strategy is simple: Activate the tracker when **A³P** is interference limited at the output to optimize the C/I gain. In the case of noise limitation, deactivate the tracker to optimize the SNR gain. The result is **Hybrid A³P**.

To implement this, **Hybrid A³P** needs to estimate what limits the performance at the output. In other words, we need an estimator for the output SNR, $\hat{SNR}_{out}$, as well as an estimator for the output C/I, $\hat{C/I}_{out}$. If $\hat{SNR}_{out} \gg \hat{C/I}_{out}$ **A³P** is noise limited.

Note that it is important to get separate estimates of the SNR and C/I, and not an estimate of the SNIR.

An estimator for $\hat{SNR}_{out}$ is already implemented in **A³P** [KTRS98]. It is a by–product of the DOA estimation. To get an estimate of the output C/I, **A³P** is also already equipped with enough information that only has to be combined properly. The **ULBF** returns spatially resolved signals for each DOA. From that the instantaneous power is calculated and also attributed to a DOA. In other words, the **ULBF** gives a simplified estimate of the APS consisting of Dirac–impulses (Fig. 7.4(a)).

When the **UID** has decided which DOAs are user DOAs and which interferer DOAs, we get a user–specific and an interferer–specific APS (Fig. 7.4(b)). With the weight vector computed by the **ULpBF** that defines the applied antenna pattern, we can estimate the output C/I

$$\hat{C/I}_{out} = \frac{P_U f(\phi_U)}{\sum_l P_{I,l} f(\phi_{I,l})}, \tag{7.3.1}$$

where an estimate for the current antenna element pattern at the direction ϕ is

$$f(\phi) = \mathbf{w}^H \mathbf{a}(\phi). \tag{7.3.2}$$

P_U is the power of the user signal incident from the direction of the main beam ϕ_U. $P_{I,l}$ and $\phi_{I,l}$, $l = 1 \ldots L_I$, are the power and directions of the interferer signals.

A simple way to include the array imperfections is to assume a certain maximum null depth, e.g. $25dB$, and limit $f(\phi)$ accordingly. Additionally a straightforward extension allows including the finite angular spread of each DOA.

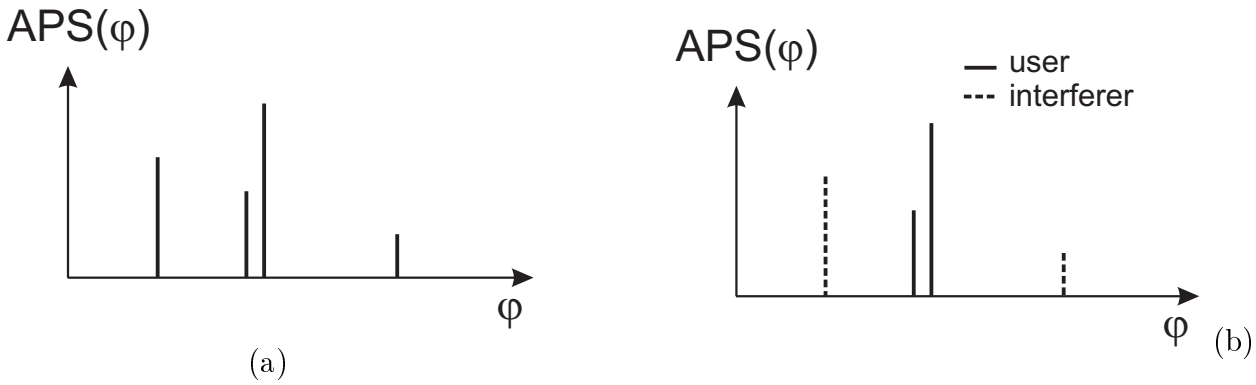

Figure 7.4. Sketch of a sample of an estimated angular power spectrum. (a) Total angular power spectrum. (b) Separate power spectra for user and interferer.

$\hat{SNR}_{out}$ and $\hat{C/I}_{out}$ are estimated in every burst. In the investigations in Sect. 6.2 I have either activated or fully deactivated the tracker. For the hybrid configuration, i.e. when both configurations are needed, it is not advisable to fully deactivate the tracker. The tracker includes averaging over time and thus the initialization phase takes some bursts. Then, activating and deactivating the tracker on a burst basis does not make sense. Instead I suggest not to *deactivate* the tracker fully, but only not to use the tracked DOAs in the case of the noise limited system. Thus I only change the strategy that selects the DOAs:

- In the interference limited case, select the user DOAs from the tracked DOAs. This is the selection strategy when the tracker is activated.
- In the noise limited case, select the user DOAs based directly on the estimated DOAs. This is the selection strategy when the tracker is deactivated.

But in both cases, update the trackers to guarantee a reliable state of the tracker when they are needed.

The decision when to change the selection strategy has to be based on average $\hat{SNR}_{out}$ and $\hat{C/I}_{out}$, because these estimates are only available *after* the selection of the DOAs has been made and the final beamforming vector for the current burst is already calculated. Which averaging constant is best has to be object of further investigations. In general less averaging will improve the SNR gain, while more averaging will increase the system robustness.

Appendix A

REAL–VALUED TRANSFORMATION OF COVARIANCE MATRIX

We derive in [KTRS98] an efficient calculation of the real-valued transformation of the covariance matrix by using the results of [LDD94] and [HN95]. The aim is to transform the complex-valued covariance matrix into a real-valued matrix; this corresponds to forward-backward averaging.

We want to calculate $\mathcal{T}(\mathbf{X})\mathcal{T}(\mathbf{X})^T$ as defined in [HN95] from the covariance matrix $\mathbf{R}$ instead from $\mathbf{X}$, as described in [HN95].

From [LDD94] and [HN95] with using the notation as in [HN95] we find (for M is even)

$$\mathcal{T}(\mathbf{X})\mathcal{T}(\mathbf{X})^T = \mathbf{Q}^H \mathbf{R}_{FB} \mathbf{Q} = \begin{bmatrix} \Re\{\mathbf{R}_A + \Pi \mathbf{R}_B\} & -\Im\{\mathbf{R}_A + \Pi \mathbf{R}_B\} \\ \Im\{\mathbf{R}_A - \Pi \mathbf{R}_B\} & \Re\{\mathbf{R}_A - \Pi \mathbf{R}_B\} \end{bmatrix}, \tag{A.0.1}$$

where $\Re\{\cdot\}$ and $\Im\{\cdot\}$ denote the real and the imaginary part of the argument, respectively.

When $\mathbf{I}$ is the identity matrix and $\mathbf{R}$, $\mathbf{Q}$, and Π are defined as

$$\mathbf{R} = \begin{bmatrix} \mathbf{R}_A & \Pi \mathbf{R}_B^H \Pi \\ \mathbf{R}_B & \Pi \mathbf{R}_A^H \Pi \end{bmatrix}, \tag{A.0.2}$$

$$\mathbf{Q} = \frac{1}{\sqrt{2}} \begin{bmatrix} \mathbf{I} & j\mathbf{I} \\ \Pi & -j\Pi \end{bmatrix}, \text{ and} \tag{A.0.3}$$

$$\Pi = \begin{bmatrix} \mathbf{0} & 1 \\ \dots & \\ 1 & \mathbf{0} \end{bmatrix}. \tag{A.0.4}$$

We calculate the forward-backward averaged covariance matrix

$$\mathbf{R}_{FB} = \mathbf{R} + \Pi \mathbf{R}^H \Pi, \tag{A.0.5}$$

This calculation is efficient ONLY if the covariance matrix $\mathbf{R}$ is already calculated. Otherwise it needs more operations then the method described in [HN95].

Proof From Eq. (26) in [LDD94] we see (note, that $\mathbf{Q}$ and Π in [HN95] corresponds to $\mathbf{K}$ and $\mathbf{J}$ in [LDD94]):

$$\mathbf{B}_{FB} = \mathbf{Q}^H \mathbf{R}_{FB} \mathbf{Q} = \mathbf{Z}_{FB} \mathbf{Z}_{FB}^T, \text{ (26 in [LDD94])} \tag{A.0.6}$$

where

$$\mathbf{Z}_{FB} = \mathbf{Q}^H \, \mathbf{X}_{FB} \, \mathbf{L}, \text{ (24 in [LDD94])}, \tag{A.0.7}$$

$$\mathbf{X}_{FB} = \frac{1}{\sqrt{2}}[\mathbf{X} \;\; \Pi \, \mathbf{X}^H], \text{ (3 in [LDD94])}, \tag{A.0.8}$$

and

$$\mathbf{L} = \frac{1}{\sqrt{2}} \begin{bmatrix} \mathbf{I} & j\mathbf{I} \\ \mathbf{I} & -j\mathbf{I} \end{bmatrix}, \text{ (12, 25 in [LDD94])}. \tag{A.0.9}$$

Now we can split $\mathbf{Q}$ into

$$\mathbf{Q} = \begin{bmatrix} \mathbf{Q}_1 \\ \mathbf{Q}_2 \end{bmatrix}, \; \mathbf{Q}_1 = [\mathbf{I} j\mathbf{I}], \; \mathbf{Q}_1 = [\Pi - j\Pi]. \tag{A.0.10}$$

From Eq. A.0.7 and A.0.8 follows:

$$\mathbf{Z}_{FB} = \mathbf{Q}^H \, \mathbf{X}_{FB} \, \mathbf{L} = \mathbf{Q}^H [\mathbf{X} \quad \Pi \, \mathbf{X}^H] \, \mathbf{L}. \tag{A.0.11}$$

And from Eq. (6) in [HN95] we derive:

$$\mathcal{T}(\mathbf{X}) = \mathbf{Q}^H [\mathbf{X} \quad \Pi \, \mathbf{X}^H \, \Pi] \, \mathbf{Q} = \mathbf{Q}^H \, (\mathbf{X}\mathbf{Q}_1 \; + \; \Pi \, \mathbf{X}^H \, \Pi \mathbf{Q}_2) = \mathbf{Q}^H \, [\mathbf{X} \quad \Pi \, \mathbf{X}^H] \begin{bmatrix} \mathbf{Q}_1 \\ \Pi \, \mathbf{Q}_2 \end{bmatrix} \tag{A.0.12}$$

and finally the identity

$$\begin{bmatrix} \mathbf{Q}_1 \\ \Pi \, \mathbf{Q}_2 \end{bmatrix} = \frac{1}{\sqrt{2}} \begin{bmatrix} \mathbf{I} & j\mathbf{I} \\ \mathbf{I} & -j\mathbf{I} \end{bmatrix} \equiv \mathbf{L} \tag{A.0.13}$$

holds. Thus

$$\mathcal{T}(\mathbf{X}) \equiv \mathbf{Z}_{FB}, \tag{A.0.14}$$

and we see that

$$\mathcal{T}(\mathbf{X}) \mathcal{T}(\mathbf{X})^T \equiv \mathbf{Z}_{FB} \mathbf{Z}_{FB}^T = \mathbf{B}_{FB} = \mathbf{Q}^H \, \mathbf{R}_{FB} \, \mathbf{Q}. \tag{A.0.15}$$

This proofs that we can calculate $\mathcal{T}(\mathbf{X}) \mathcal{T}(\mathbf{X})^T$ from the forward-backward averaged covariance matrix $\mathbf{R}_{FB}$, which itself can be computed from $\mathbf{R}$ (Eq. A.0.5).

Appendix B

LIST OF FREQUENTLY USED ACRONYMS

Acronym	Description
A^{3}P	Adaptive Antenna Array Processor
ABFE	Antenna BeamForming Element
AIC	An Information Criterion
APS	Azimuthal Power Spectrum
AS	Angular Spread
AWGN	Additive White Gaussian Noise
BER	Bit–error ratio
BF	BeamForming
BFCU	Beamforming Control Unit
BS	Base Station
BTS	Base Transceiver Station
BW	Beam Width
C/I	Carrier–to–Interference ratio
CAS	Component angular spread
CCI	Co–channel Interference
CDF	Cumulative Distribution Function
CDMA	Code Division Multiple Access
CW	Continuous Wave
DOA	Direction–of–Arrival
DLBF	DownLink BeamForming
DOAE	DOA Estimation
DOAT	DOA Tracking
ESPRIT	Estimation of Signal Parameters via Rotational Invariant Techniques
FDD	Frequency Division Duplex
FU	Frame Unit
GSCM	Geometry–based Stochastic Channel Model
GSM	Global System for Mobile communications
LOS	Line–Of–Sight

MDL	Minimum Description Length
MMSE	Minimum Mean Square Error
MRC	Maximum Ratio Combining
MS	Mobile Station
MVM	Minimum Variance Method
ND	Null Depth
NLOS	Non–LOS
NW	Null Width
PASTd	Projection Approximation Subspace Tracking and Deflation
PDF	Probability Density Function
OC	Optimum Combining
RF	Radio Frequency
SDMA	Space Division Multiple Access
SFIR	Spatial Filtering for Interference Reduction
SNR	Signal–to–Noise ratio
SNIR	Signal–to–Noise and Interference ratio
TDMA	Time Division Multiple Access
UL	UpLink
ULA	Uniform Linear Array
UID	User Identification
ULBF	UpLink BeamFormer
ULpBF	UpLink Post BeamFormer

Appendix C

LIST OF FREQUENTLY USED SYMBOLS

Symbol	Description	Section
K	number of users served by the BS	1.2
M	number of antenna elements	1.2
$\mathbf{w}_{ul}$	uplink beamforming weight vector	2.1
$\mathbf{w}_{dl}$	downlink beamforming weight vector timeslot	2.1
$\mathbf{T}$	downlink baseband signal	2.1
$\mathbf{X}$	data of a single timeslot	2.1
$\mathbf{a}_{k,l}$	array steering vector of the k–th user and the l–th wave	3.2
$\mathbf{A}_k$	array steering matrix of the k–th user	3.2
B	system bandwidth	3.2
$\mathbf{c}$	(uplink) calibration vector	3.2
c	velocity of light	3.2
Δ	antenna element spacing	3.2
D	number of uplink weight vectors	3.2
f_c	carrier frequency	3.2
$f_{d,l,k}$	Doppler frequency of the l–th scatterer of the k–th user	3.2
$f(\phi)$	single antenna element pattern	3.2
K	total number of users	3.2
K_I	number of interferer	3.2
K_U	number of (intracell) users	3.2
L	number of scatterers	3.2
M	number of antenna elements	3.2
N	number of symbols in a timeslot	3.2
$\phi_{k,l}$	azimuth of the l–th wave of the k–th user	3.2
$\phi_{v,l,k}$	direction of the velocity of the l–th scatterer of the k–th user	3.2
$\rho_{k,l,m}$	complex path coefficient of the l–th scatterer and the k–th user to the m–th antenna element	3.2
$\hat{\mathbf{s}}_d$	estimate for the transmitted downlink baseband signal	3.2

Symbol	Description	Section
$\mathbf{S}^{dl}$	transmitted downlink baseband signal matrix	3.2
$\mathbf{t}^{dl}$	downlink baseband signal vector	3.2
$\tau_{k,l,m}$	delay of wave of the l–th scatterer and the k–th mobile to the m–th antenna element	3.2
T	GSM symbol duration	3.2
$\mathbf{w}_{ul}$	uplink beamforming weight vector	3.2
$\mathbf{w}_{dl}$	downlink beamforming weight vector timeslot	3.2
$\mathbf{W}(n)$	uplink weight matrix	3.2
$\mathbf{w}_d(n)$	uplink weight vector	3.2
$\mathbf{x}(n)$	calibrated received (UL) data vector	3.2
$\mathbf{x}_{uncal}(\tau)$, $\mathbf{x}_{uncal}(n)$	received (uplink) array output data vector at time $\tau(n)$	3.2
$\mathbf{X}(n)$	calibrated received (UL) data matrix of a single timeslot	3.2
$\mathbf{a}_(\phi)$	array steering vector	4.3
$\hat{\mathbf{A}}$	estimated steering matrix	4.4
β	decaying factor of **PASTd**	4.3
β_T	decaying factor of the tracker	4.6
cdf_ϕ	CDF of the estimated DOAs	4.3
γ_b	bottom threshold level of Threshold Criterion	4.3
γ_t	top threshold level of Threshold Criterion	4.3
θ_b	bottom threshold of Threshold Criterion	4.3
θ_t	top threshold of Threshold Criterion	4.3
θ_{BER}	threshold of the **UID**	4.5
$J(\mathbf{Z})$	cost function of PASTd	4.3
K	total number of users	4.3
λ_m	Eigenvalues of covariance matrix	4.3
$\hat{L}$	estimated number of DOAs	4.3
$\hat{L}_I$	estimated number of interferer DOAs	4.5
$\hat{L}_U$	estimated number of user DOAs	4.5
μ_T	instantaneous effective memory length	4.6
$\mu_{T,max}$	maximum effective memory length	4.6
M	number of antenna elements	4.3
$n_{BER,l}$	number of bit errors of the l–th spatially resolved signal	4.5
N	number of symbols in a timeslot	4.3
N_{bursts}	number of bursts	4.3
N_{PASTd}	number of symbols applied to **PASTd**	4.3
$N_{samples}$	number of samples	4.3
ϕ_l	estimated DOA	4.3
$\phi_{I,l}$	classified interferer DOA	4.5
$\phi_{U,l}$	identified user DOA	4.5
$\phi_{I,l}^{UlpBF}$	selected interferer DOA for uplink post beamforming	4.6
$\phi_{U,l}^{UlpBF}$	selected user DOA for uplink post beamforming	4.6
Φ_l	DOA of the tracked multipath	4.6

Symbol	Description	Section
P_l	power of the tracked multipath	4.6
$\overline{P}_l$	average power of the tracked multipath	4.6
$P_{APS}(\phi)$	angular power spectrum at angle, ϕ	4.3
pdf_ϕ	PDF of the estimated DOAs	4.3
Q_{DOAE}	DOA estimation range	4.3
$\hat{\mathbf{R}}(n)$	estimated sample covariance matrix of the n–th burst	4.3
$\mathbf{R}_{FB}$	forward–backward averaged covariance matrix	4.3
R_c	coarse resolution of **MVM**	4.3
$\overline{P}_l$	average power of the tracked multipath	4.6
$P_{APS}(\phi)$	angular power spectrum at angle, ϕ	4.3
pdf_ϕ	PDF of the estimated DOAs	4.3
Q_{DOAE}	DOA estimation range	4.3
$\hat{\mathbf{R}}(n)$	estimated sample covariance matrix of the n–th burst	4.3
$\mathbf{R}_{FB}$	forward–backward averaged covariance matrix	4.3
R_c	coarse resolution of **MVM**	4.3
R_f	fine resolution of **MVM**	4.3
σ_{DOAE}	DOA estimate variation	4.3
$\hat{\mathbf{S}}_{TS}$	spatially resolved signals (midamble)	4.4
$\hat{\mathbf{W}}_{ULBF}$	weight matrix of the **ULBF**	4.4
$\mathbf{X}(n)$	uplink data matrix of the n–th burst	4.3
$\mathbf{X}_{TS}$	midamble part of the uplink data matrix	4.4
$C/I_{in,m}(n)$	input C/I at the m–th antenna element	5.2
$C/I_{out}(n)$	output C/I	5.2
$\mathcal{C}_{in,m}^{C/I}$	CDF of input C/I at the m-th antenna	5.2
$\mathcal{C}_{out}^{C/I}$	CDF of output C/I	5.2
$\mathcal{C}_{in,m}^{SNR}$	CDF of input SNR at the m-th antenna	5.2
$\mathcal{C}_{out}^{SNR}$	CDF of output SNR	5.2
$\Delta SNR^\gamma(n)$	SNR gain at probability level γ averaged over all antenna elements	5.2
$\Delta C/I^\gamma(n)$	C/I gain at probability level γ averaged over all antenna elements	5.2
G_b	beamforming gain	5.2
G_{div}^γ	diversity gain at probability level γ	5.2
K_I	number of interferers	5.2
L_{tap}	tapering loss	5.2
N_{bursts}	number of bursts	5.2
$\mathbf{N}_{intf,k}(n)$	interferer noise data matrix of the k–th interferer	5.2
$\mathbf{N}_{user}(n)$	user noise data matrix	5.2
$N_{symbols}$	number of symbols of a burst (timeslot)	5.2
ϕ_{SB}	DOA of scanning beam	5.1
P_N	noise power	5.2

Symbol	Description	Section
$P_{N,I}$	interferer noise power	5.2
$P_{N,U}$	user noise power	5.2
$P_{I,m}$	interferer power at the m–th antenna element	5.2
$P_{S,m}$	signal power at the m–th antenna element	5.2
$SNR_{in,m}(n)$	input SNR at the m–th antenna element	5.2
$\overline{SNR}_{out}(n)$	average output SNR	5.2
$SNR_{out}(n)$	output SNR	5.2
$\overline{SNR}_{in}(n)$	average input SNR	5.2
$SNIR(n)$	input/output SNIR	5.2
$\mathbf{w}(n)$	uplink weight vector	5.2
$\mathbf{X}(n)$	received uplink data matrix	5.2
$\mathbf{X}_{intf,k}(n)$	interferer data matrix of k–th interferer	5.2
$\tilde{\mathbf{X}}_{intf,k}(n)$	received data matrix of the k–th interferer	5.2
$\mathbf{X}_{user}(n)$	user data matrix	5.2
$\tilde{\mathbf{X}}_{user}(n)$	received user data matrix	5.2
AS	angular spread	6.1
APS	angular power spectrum	6.1

BIBLIOGRAPHY

[AB99] H. Aroudaki and K. Bandelow. Static simulations of radio networks equipped with adaptive array antennas. In *European Personal Mobile Communications Conference (EPMCC'99)*, pages 328–333, Paris, France, March 1999.

[Ada93] F. Adachi. Postdetection optimal diversity combiner for DPSK differential detection. *IEEE Trans. Vehicular Technology*, 42:326–337, 1993.

[AFK+97] S. Anderson, U. Forssen, J. Karlsson, T. Witzschel, P. Fischer, and A. Krug. Ericsson/mannesmann GSM field–trials with adaptive antennas. In *IEEE Vehicular Technology Conference (VTC'97)*, volume 3, pages 1587–1591, Phoenix, AZ, May 1997.

[Aka74] H. Akaike. A new look at the statistical model identification. *IEEE Transactions on Automatic Control*, 19(6), December 1974.

[AMVW91] S. Anderson, M. Millnert, M. Viberg, and B. Wahlberg. Adapative antenna array for mobile communication systems. *IEEE Trans. Vehicular Technology*, 40(1):230–236, February 1991.

[And98a] J. Bach Andersen. High–gain antennas in a scattering environment. In *International Symposium on Personal, Indoor and Mobile Radio Communication (PIMRC'98)*, volume 3, pages 1275–1279, Boston, MA, September 1998.

[And98b] J. Bach Andersen. Transmit–receive diversity in a scattering environment. In *COST 259*, volume TD(98) 011, Bern, Switzerland, February 1998.

[APC+98] R. Arnott, S. Ponnekanti, F. Cesborn, C. Taylor, and D. Greenaway. Application of adaptive antennas in a DCS1800 mobile network: Performance analysis of the TSUNAMI (II) field trial data. In *Intelligent Antennas Symposium*, Gillford, UK, July 1998.

[BBJ95] J. J. Blanz, P. W. Baier, and P. Jung. A flexibly configurable statistical channel model for mobile radio systems with directional diversity. In *Proc. 2nd ITG Fachtagung Mobile Kommunikation*, pages 93–100, 1995.

[BJ95] G.E. Bottomley and K. Jamal. Adaptive arrays and MLSE equalization. In *IEEE Vehicular Technology Conference (VTC'95)*, pages 50–54, May 1995.

[Bon98] E. Bonek. Smart antennas — current issues. In *MTT–S European Wireless '98*, Amsterdam, The Netherlands, October 1998.

[Boo93] C.J. Booth, editor. *The New IEEE Standard Dictionary of Electrical and Electronic Terms*. IEEE Press, fith edition, 1993.

[BPW99] J. Boccuzzi, S.U. Pillai, and J.H. Winters. Adaptive antenna arrays using subspace techniques in a mobile radio environment with flat fading and CCI. In *IEEE Vehicular Technology Conference (VTC'99)*, volume 1, pages 50–54, Houston, TX, May 1999.

[CC91] C.K. Chui and G. Chen. *Kalman Filtering with Real–Time Applications*. Springer Verlag, 1991.

[CGK67] J. Capon, R.J. Greenfield, and R.J. Kolker. Multidimensional maximum–likelihood processing of a large aperture seismic array. *IEEE Proceedings*, 55:192–211, February 1967.

[ECS+98] R.B. Ertel, P. Cardieri, K.W. Sowerby, T.S. Rappaport, and J.H. Reed. Overview of spatial channel models for antenna array communication systems. *IEEE Personal Communications*, pages 10–22, February 1998.

[Egg95] P.C.F. Eggers. Angular dispersive mobile radio environments sensed by highly directive base station antennas. In *International Symposium on Personal, Indoor and Mobile Radio Communication (PIMRC'95)*, volume 1, pages 522–526, Toronto, Canada, September 1995.

[FG98] G. J. Foschini and M. J. Gans. On limits of wireless communications in a fading environment when using multiple antennas. *Wireless Personal Communications*, 6:311–335, February 1998.

[FKB97] J. Fuhl, A. Kuchar, and E. Bonek. Capacity increase in cellular PCS by smart antennas. In *IEEE Vehicular Technology Conference (VTC'97)*, volume 3, pages 1962–1966, Phoenix, TX, May 1997.

[FKJ+94] U. Forssen, J. Karlsson, B. Johannison, F. Kronstedt, F. Lotse, M. Almgren, and S. Anderson. Adaptive antenna arrays in GSM900/DCS1800. In *IEEE Vehicular Technology Conference (VTC'94)*, pages 605–609, Stockholm, Sweden, June 1994.

[FMB98] J. Fuhl, A.F. Molisch, and E. Bonek. Unified channel model for mobile radio systems with smart antennas. *IEE Proc.-Radar, Sonar Navigation*, 145(1):32–41, February 1998.

[FTHD98] B. Fleury, M. Tschudin, R. Heddergott, and D. Dahlhaus. Channel parameter estimation in mobile radio environments using the SAGE algorithm. *accepted by IEEE J. Select. Areas in Commun. (JSAC)*, 1998.

[Fuh97a] J. Fuhl. Efficient computation of the weights of a wideband antenna structure. *IEE Electronic Letters*, 33(13):1109–1111, June 1997.

[Fuh97b] J. Fuhl. *Smart Antennas for Second and Third Generation Mobile Communications Systems*. PhD thesis, Technische Universität Wien, 1997.

[GBe98] D. Greenaway, M. Beach, and P. Mogensen et.al. TSUNAMI (II) — final report. Technical report, ACTS Program, August 1998.

[God97a] L.C. Godara. Applications of antenna arrays to mobile communications, part i: Performance improvement, feasibility, and system considerations. *Proceedings of the IEEE*, 85(7):1031–1061, July 1997.

[God97b] L.C. Godara. Applications of antenna arrays to mobile communications, part ii: Beam–forming and direction–of–arrival considerations. *Proceedings of the IEEE*, 85(8):1195–1245, August 1997.

[Haa91] M. Haardt. *Efficient One, Two–, and Multidimensional High–Resolution Array Signal Processing*. PhD thesis, Technical University Munich, 1991.

[HKTT99] C. Hoek, A. Kuchar, M. Taferner, and M. Tangemann. Uplink and downlink field trial with a GSM/DCS1800 smart antenna base station. In *MTT–S European Wireless '99*, page to be published, Munich, Germany, October 1999.

[HLB99] K. Hugl, J. Laurila, and E. Bonek. Downlink beamforming for frequency division duplex systems. In *IEEE Global Telecommunications Conference (GLOBECOM '99)*, Rio de Janeiro, Brazil, December 1999.

[HN95] M. Haardt and J.A. Nossek. Unitary ESPRIT: How to obtain increased estimation accuracy with a reduced computational burden. *IEEE Transactions on Signal Processing*, 43(5):1232–1242, May 1995.

[HÖMB97] B. Hagerman, T. Östman, K. J. Molnar, and G. E. Bottomley. Field test performance results for D–AMPS in PCS bands with array processing. In *IEEE Vehicular Technology Conference (VTC'97)*, volume 3, pages 1582–1586, Phoenix, AZ, May 1997.

[HP99] R. W. Heath and A. Paulraj. Multiple antenna arrays for transmitter diversity and space–time coding. In *IEEE International Conference on Communications (ICC'99)*, volume 1, pages 36–40, Vancouver, Canada, June 1999.

[Hug98] K. Hugl. Downlink beamforming using adaptive antennas. Master's thesis, Technische Universität Wien, 1998.

[Jak74] W. C. Jakes. *Microwave Mobile Communications*. IEEE Press, 1974.

[JD91] D.H. Johnson and D.E. Dudgeon. *Array Signal Processing, Concepts and Techniques*. Prentice–Hall Signal Processing Series, 1991.

[Joh98] W. Johnston. Europe's future mobile telephony systems. *IEEE Spectrum*, pages 49–53, October 1998.

[JXLV98] S.-S. J. Jeng, G. Xu, H.-P. Lin, and W.J. Vogel. Experimental studies of spatial signature variation at 900mhz for smart antenna systems. *IEEE Trans. on Antennas and Propagation*, 46(7):953–962, July 1998.

[KFB97] A. Kuchar, J. Fuhl, and E. Bonek. Spectral efficiency enhancement and power control in smart antenna systems. In *European Personal Mobile Communications Conference (EPMCC'97)*, Bonn, Germany, October 1997.

[KFK97] W. Konrad, J. Fuhl, and A. Kuchar. Influence of quantization and channel imbalances on direction finding algorithms. In *Proc. International Conf. on Telecommunications (ICT'97)*, Melbourne, Australia, June 1997.

[KNKB97] W. Konrad, H. Novak, A. Kuchar, and E. Bonek. Advance antenna demonstrators for umts data rates. In *ACTS Mobile Communications Summit '97*, pages 303–307, Aalborg, Denmark, October 1997.

[KRB99] A. Kuchar, J.-P. Rossi, and E. Bonek. Directional macro–cell channel characterization from urban measurements. *to appear in February 2000 in IEEE Trans. on Antennas and Propagation*, 1999.

[KTP98] A. Kuchar, M. Taferner, and G. Pospischil. Project SFIR: Test specification for pre–integration. Deliverable D4.1a, Institut für Nachrichtentechnik und Hochfrequenztechnik, TU Wien, Wien, February 1998.

[KTRS97a] A. Kuchar, M. Taferner, W. Rauscher, and Martin Strasser. Project SFIR: Performance evaluation with synthetic data and test data. Deliverable D1.2d, Institut für Nachrichtentechnik und Hochfrequenztechnik, TU Wien, Wien, December 1997.

[KTRS97b] A. Kuchar, M. Taferner, W. Rauscher, and Martin Strasser. Project SFIR: Software structure. Deliverable D2a, Institut für Nachrichtentechnik und Hochfrequenztechnik, TU Wien, Wien, September 1997.

[KTRS98] A. Kuchar, M. Taferner, W. Rauscher, and Martin Strasser. Project SFIR: Description of each algorithm of **A**^{3}**P** . Deliverable D1.2c, Institut für Nachrichtentechnik und Hochfrequenztechnik, TU Wien, Wien, February 1998.

[KTT+99a] A. Kuchar, M. Taferner, M. Tangemann, C. Hoek, and E. Bonek. A run–time optimized adaptive antenna array processor for GSM. In *European Personal Mobile Communications Conference (EPMCC'99)*, pages 307–312, Paris, France, March 1999.

[KTT+99b] A. Kuchar, M. Taferner, M. Tangemann, C. Hoek, W. Rauscher, M. Strasser, G. Pospischil, and E. Bonek. Real–time smart antenna processing for GSM1800 base station. In *IEEE Vehicular Technology Conference (VTC'99)*, pages 664–669, Houston, TX, May 1999.

[KTT+99c] A. Kuchar, M. Taferner, M. Tangemann, C. Hoek, W. Rauscher, M. Strasser, G. Pospischil, and E. Bonek. A robust DOA–based smart antenna processor for GSM base stations. In *IEEE International Conference on Communications (ICC'99)*, pages 11–16, Vancouver, Canada, June 1999.

[KTTH99] A. Kuchar, M. Taferner, M. Tangemann, and C. Hoek. Field trial with a GSM/DCS1800 smart antenna. In *IEEE Vehicular Technology Conference (VTC'99 Fall)*, page to be published, Amsterdam, The Netherlands, September 1999.

[KV96] H. Krim and M. Viberg. Two decades of array signal processing research. *IEEE Signal Processing Magazine (Special Issue on Array Processing)*, 13(4):67–94, February 1996.

[LDD94] Linebarger, DeGroat, and Dowling. Efficient direction–finding methods employing forward/backward averaging. *IEEE Transactions on Signal Processing*, 42(8):2136–2145, August 1994.

[Lev47] N. Levinson. The Wiener RMS criterion in filter design and prediction. *J. Math. Phys.*, 25:261–278, January 1947.

[LKB99] J. Laurila, K. Kopsa, and E. Bonek. Semi–blind separation and detection of co–channel signals. In *IEEE International Conference on Communications (ICC'99)*, pages 17–22, Vancouver, Cananda, June 1999.

[LMB98] J. Laurila, A.F. Molisch, and E. Bonek. Influence of the scatterer distribution on power delay profiles and azimuthal power spectra of mobile radio. In *IEEE International Symposium on Spread Spectrum Techniques and Applications (ISSSTA'98)*, pages 267–271, Sun City, South Africa, September 1998.

[LR96] J.C. Liberti and T.S. Rappaport. A geometrically based model for line-of–sight multipath radio channels. In *IEEE Vehicular Technology Conference (VTC'96)*, volume 1, pages 844–848, Atlanta, GA, April 1996.

[LT98] Bell Labs Lucent Technologies. Bell labs scientists shatter limit on fixed wireless transmission. In *press release*, http://www.lucent.com/press/0998/980909.bla.html, September 1998.

[LTB99] J. Laurila, R. Tschofen, and E. Bonek. Semi–blind space–time estimation of co–channel signals using least squares projections. In *IEEE Vehicular Technology Conference (VTC'99 Fall)*, pages 17–22, Amsterdam, The Netherlands, September 1999.

[MFD+96] P. Mogensen, F. Frederiksen, H. Dam, K. Olesen, and S.L. Larsen. TSUNAMI (II) stand alone testbed. In *ACTS Summit '96*, volume 1, pages 517–527, Granada, Spain, November 1996.

[MFG+99] U. Martin, J. Fuhl, I. Gaspard, M. Haardt, A. Kuchar, C. Math, A.F. Molisch, and R. Thomä. Model scenarios for intelligent antennas in cellular mobile communication systems - scanning the literature. *Wireless Personal Communications Magazine 11, Special Issue on Space Division Multiple Access*, pages 109–129, 1999.

[MH99] T.L. Marzetta and B.M. Hochwald. Capacity of a mobile multiple–antenna communication link in rayleigh flat fading. *IEEE Trans. on Information Theory*, 45(1):139–157, January 1999.

[MKL+99] A. F. Molisch, A. Kuchar, J. Laurila, K. Hugl, and E. Bonek. Efficient implementation of a geometry-based directional model for mobile radio channels. In *IEEE Vehicular Technology Conference (VTC'99 Fall)*, page accepted for publication, Amsterdam, The Netherlands, September 1999.

[MKL+ed] A.F. Molisch, A. Kuchar, J. Laurila, K. Hugl, and R. Schmalenberger. Geometry–based directional model for mobile radio channels — principles and implementation. *ETT European Transactions on Telecommunications*, submitted.

[MLKS98] A.F. Molisch, J. Laurila, A. Kuchar, and R. Schmalenberger. Test scenarios for mobile radio systems with adaptive antennas. In *First COST 252/259 Joint Workshop*, pages 162–170, Bradford, UK, April 1998.

[MP92] M. Mouly and M.-B. Pautet. *The GSM System for Mobile Communications.* Cell & Sys, France, 1992.

[MPFF99] P. Mogensen, K. Pedersen, B. Fleury, and F. Frederiksen. Measurements, channel statistic, and performance of adaptive base station antennas. In *COST259/260 Joint Workshop — Spatial Channel Models and Adaptive Antennas*, pages 65–72, Vienna, Austria, April 1999.

[MPLE+97] P. Mogensen, K. Pedersen, P. Leth-Espensen, B. Fleury, F. Frederiksen, K. Olesen, and S. Larsen. Preliminary measurement results from an adaptive antenna array testbed for GSM/UMTS. In *IEEE Vehicular Technology Conference (VTC'97)*, Phoenix, AZ, May 1997.

[MSH99] Carol C. Martin, Nelson R. Sollenberger, and Jack H.Winters. Field test results of downlink smart antennas and power control for IS–136. In *IEEE Vehicular Technology Conference (VTC'99)*, pages 453–459, Houston, TX, May 1999.

[MTC+98] J.-J. Monot, J. Thubault, P. Chevalier, F. Pipon, S. Mayrargue, and A. Levy. Smart antenna prototype for the SDMA experimentation in UMTS and GSM/DCS1800 networks. In *Proc. International Conf. on Telecommunications (ICT'98)*, volume 1, pages 333–337, Porto Carras, Greece, July 1998.

[NNK98] H. Novak, H. Nord, and A. Kuchar. A single–layer 8x8 butler matrix with patch antenna. In *MTT–S European Wireless '98*, pages 25–29, Amsterdam, The Netherlands, October 1998.

[NNK99] H. Novak, H. Nord, and A. Kuchar. Switched beam adaptive antenna demonstrator for UMTS data rates. In *Virginia Tech Symposium on Wireless Personal Communications 1998*, Blacksburg, VA, June 1999.

[Nov99] H. Novak. *Switched–Beam Adaptive Antenna System.* PhD thesis, Technische Universität Wien, November 1999.

[OSMS93] T. Ohgane, T. Shimura, N. Matsuzawa, and H. Sasaoka. Space–time modems for wireless personal communications. *IEEE Trans. Vehicular Technology*, 42(3):282–288, August 1993.

[Pet96] L. Pettersson. An experimental s–band digital beamforming antenna. In *Radio Vetenskap och Kommunikation '96*, pages 440–444, Lulea, Sweden, June 1996.

[PMF97] K.I. Pedersen, P.E. Mogensen, and B.H. Fleury. Power azimuth spectrum in outdoor environments. *IEE Electronic Letters*, 33(18):1583–1584, August 1997.

[PN98] A.J. Paulraj and B.C. Ng. Space–time modems for wireless personal communications. *IEEE Personal Communications*, pages 36–48, February 1998.

[PP97] A.J. Paulraj and C.B. Papadias. Space–time processing for wireless communications. *IEEE Signal Processing Magazine*, 14(6):49–83, 1997.

[PW98] H.V. Poor and G.W. Wornell. *Wireless Communications — Signal Processing Perspectives.* Prentice–Hall Signal Processing Series, 1998.

[Rau98] W. Rauscher. User identification in mobile radio systems with adaptive antennas. Master's thesis, Technische Universität Wien, 1998.

[RPK86] R. Roy, A. Paulraj, and T. Kailath. ESPRIT — a subspace rotation approach to estimation of parameters of cisoids in noise. *IEEE Trans. Acoustics, Speech, and Signal Processing*, 34(5):1340–1342, October 1986.

[Sch95] T. Schuetz. BTS digital signal processing specification. Technical spec., Alcatel Corporate Research Center Stuttgart, Stuttgart, November 1995.

[Str98] M. M. Strasser. Direction–of–arrival estimation for real–time processing. Master's thesis, Technische Universität Wien, 1998.

[SWR+97] J. Strandell, M. Wennström, A. Rydberg, T. Öberg, O. Gladh, L. Rexberg, E. Sandberg, B.V. Andersson, and M. Appelgren. Experimental evaluation of an adaptive antenna for a tdma mobile telephony system. In *IEEE Vehicular Technology Conference (VTC'97)*, volume 1, pages 79–84, Phoenix, AZ, May 1997.

[TBHH97] M. Tangemann, U. Bigalk, C. Hoek, and M. Hother. Sensitivity enhancements of GSM/DCS1800 with smart antennas. In *European Personal Mobile Communications Conference (EPMCC'97)*, pages 87–97, Bonn, Germany, October 1997.

[TGM96] J. S. Thompson, P. M. Grant, and B. Mulgrew. Smart antenna arrays for CDMA systems. *IEEE Personal Communications Magazine*, pages 16–25, October 1996.

[THR94] M. Tangemann, C. Hoek, and R. Rheinschmitt. Introducing adaptive array antenna concepts in mobile communication systems. In *Proc. RACE Mobile Communications Workshop*, pages 714–727, Amsterdam, The Netherlands, May 1994.

[TKL+99] M. Taferner, A. Kuchar, M.C. Lang, M. Tangemann, and C. Hoek. A novel DOA–based beamforming algorithm with broad nulls. In *International Symposium on Personal, Indoor and Mobile Radio Communication (PIMRC'99)*, Osaka, Japan, September 1999.

[TMB98] G. V. Tsoulos, J. P. McGeehan, and M. Beach. Space division multiple access (SDMA) field trials. part 1: Tracking and BER performance. *IEE Proc. Radar, Sonar and Navigation*, 145(1):73–78, February 1998.

[TSC98] V. Tarokh, N. Seshadri, and A.R. Calderbank. Space–time codes for high data rate wireless communication: Performance criterion and code construction. *IEEE Trans. on Information Theory*, pages 744–760, March 1998.

[Win84] J. H. Winters. Optimum combining in digital mobile radio with cochannel interference. *IEEE Journal in Selected Areas in Communications*, 2(4):528–539, July 1984.

[Win93] J. H. Winters. Signal acquisition and tracking with adaptive arrays in digital mobile radio system IS–54 with flat fading. *IEEE Trans. Vehicular Technology*, 42(4):377–384, November 1993.

[Win94] J. H. Winters. The impact of antenna diversity on the capacity of wireless communication systems. *IEEE Trans. Communications*, 42(¨2/3/4¨):1740–1751, ¨February/March/April¨ 1994.

[Win98a] J. H. Winters. The diversity gain of transmit diversity in wireless systems with Rayleigh fading. *IEEE Trans. Vehicular Technology*, pages 119–123, February 1998.

[Win98b] J. H. Winters. Smart antennas for wireless systems. *IEEE Personal Communications Magazine*, pages 23–27, February 1998.

[WK85] M. Wax and T. Kailath. Detection of signals by information theoretic criteria. *IEEE Transactions on Acoustics, Speech, and Signal Processing*, 33(2), April 1985.

[WMZ98] J. H. Winters, C. C. Martin, and T. Zhang. A two–element adaptive antenna array for IS–136 PCS base stations. In *Proc. USCD Conference*, March 1998.

[WTFH98] R. Weinmann, M. Tangemann, S. Fritsch, and C. Hoek. Beamforming performance measurements in a DCS 1800 smart antenna testbed. In *IEEE Vehicular Technology Conference (VTC'98)*, Ottawa, Canada, May 1998.

[Yan95a] B. Yang. An extension of the PASTd algorithm to both rank and subspace tracking. *IEEE Signal Processing Letters*, 2(9), September 1995.

[Yan95b] B. Yang. Projection approximation subspace tracking. *IEEE Transactions on Signal Processing*, 43(1):95–107, January 1995.

[Yli99] J. Ylitalo. Performance of a digital beamforming concept in a gsm1800 downlink: A simulation study. *Wireless Personal Communications*, 11:31–43, August 1999.

CURRICULUM VITAE

Personal data

Address:	A-2232 Deutsch-Wagram, Friedhofallee 4a/11, Austria
Email:	Alexander.Kuchar@nt.tuwien.ac.at
Date of birth:	10. March 1971 in Vienna
Marital status:	Married since 1997, one daughter
Nationality:	Austria

Employment history

4/1993 - 3/1995	Hewlett Packard Wien, Free-lance software developer
4/1995 - 2/1996	Part time researcher at the Institut für Nachrichtentechnik und Hochfrequenztechnik (INTHF) at the Technische Universität Wien as member of the Mobile Communications Group of Prof. Bonek.
3/1996 - 9/1999	Research engineer at the INTHF Research topics: smart antennas, directional channel measurements and modeling,microstrip antennas
10/1999-5/2000	Military service

Education

9/1981-6/1985	High–school
9/1985-5/1990	Technical (EE) high–school in Vienna (TGM Wien 20)
10/1990-2/2000	Technische Universität Wien
3/1996	Graduation (Dipl.–Ing.) in EE with highest honours Masters thesis: Aperture–coupled Microstrip Antenna Array
2/2000	Graduation (Dr. techn.) in technical sciences

Awards

4/1994	Scholarship "Leistungsstipendium" of the EE faculty for excellent study performance 1993
6/1995	Scholarship "Förderungsstipendium" of the EE faculty
11/1996	"GIT-Förderpreis 1996" of the Öster. Verbandes für Elektrotechnik (Organization of Austrian EE) for outstanding diploma thesis
3/1999	"Best Paper Award" at the European Personal Mobile Communications Conference (EPMCC '99), Paris
10/1999	"Best Paper Award" at the European Wireless Conference '99, Munich